Study on the creep behavior of clay under complex triaxial loading in relation to the microstructure

Dan Zhao

Dissertation presented to obtain the doctor's degree of

University of Lorraine

by

Dan ZHAO

Special field: **Geotechnique**

Study on the creep behavior of clay under complex triaxial loading in relation to the microstructure

To be defended on 18 December 2017

In front of the jury:

Irini Djeran-Maigre	Professor	INSA Lyon	Reviewer
Yujun Cui	Professor	Ecole des Ponts ParisTech	Reviewer
Pierre-Yves Hicher	Professor	Ecole Centrale de Nantes	Examiner
Christophe Dano	MCF	Université Grenoble Alpes UGA	Examiner
Mohamad Jrad	MCF	Université de Lorraine	Examiner
Mahdia Hattab	Professor	Université de Lorraine	Supervisor
Zhenyu Yin	MCF-HDR	Ecole Centrale de Nantes	Co-Supervisor

Laboratoire d'Étude des Microstructures et de Mécanique des Matériaux

LEM3 UMR CNRS 7239 - Université de Lorraine

Île du Saulcy - 57045 Metz Cedex 01- France

Thèse présenté pour obtenir le grade de

Docteur de l'Université de Lorraine

par

Dan ZHAO

Spécialité: **Géotechnique**

Étude du comportement au fluage de l'argile sous chargements triaxiaux complexes en relation avec la microstructure

Soutenue le 18 Décembre 2017

Devant le jury composé de :

Irini Djeran-Maigre	Professor	INSA Lyon	Rapporteur
Yujun Cui	Professor	Ecole des Ponts ParisTech	Rapporteur
Pierre-Yves Hicher	Professor	Ecole Centrale de Nantes	Examinateur
Christophe Dano	MCF	Université Grenoble Alpes UGA	Examinateur
Mohamad Jrad	MCF	Université de Lorraine	Examinateur
Mahdia Hattab	Professor	Université de Lorraine	Directeur de thèse
Zhenyu Yin	MCF-HDR	Ecole Centrale de Nantes	Co-Directeur de thèse

Laboratoire d'Étude des Microstructures et de Mécanique des Matériaux

LEM3 UMR CNRS 7239 - Université de Lorraine

Île du Saulcy - 57045 Metz Cedex 01- France

Abstract

With the growing emergence of constructions concentrated in densely populated urban areas, there is an increasing need to construct geotechnical structures on soft clay materials, which usually produce significant creep deformation. The prediction of the time dependent deformation of clay is generally very problematic due to the complex elasto-viscoplastic properties of the clayey materials. The objective of this research is to analyze the creep behavior of a typical clay along triaxial tests, moreover, to analyze the microstructural mechanisms of creep in order to provide a better understanding of this behavior.

At the macroscopic scale, the method is based on a series of drained triaxial creep tests under constant mean effective stress, where the volumetric creep strain is caused by the sole deviatoric stress variation. Tests are conducted on a saturated reconstituted clayey material by the use of a GDS stress path control apparatus. The development of the axial and volumetric creep strains is studied with respect to time, stress level and overconsolidation ratio.

At the microscopic scale, the study is based on a thorough microstructure analysis using in particular scanning electron microscope (SEM), coupled to an adapted method for the identification of preferential orientations of particles, the pore area and pore shape. This microscopic study is complemented by mercury intrusion porosimetry (MIP) analysis, a method which allows quantifying the pore space and characterizing the local void ratio. The microscope research is developed on two kinds of samples after mechanical loading: one is after shear and another is after creep. Consequently, we can observe the evolution of microstructure of the soil within creep by comparing the results after shear and after creep.

Analysis on the macroscopic results ascertained that both dilatancy and contractancy phenomena could occur during creep. The magnitude of the dilatancy/contractancy during creep was guided by the test conditions: stress level (*SL*) and the over consolidation ratio (OCR), which specifically governed the direction of the volumetric strain variations. The position of the stress level located in different volumetric domains, defined by monotonic triaxial tests in the (p'-q) plane, controls the evolution of the creep strain and creep strain rate. The three creep

stages were identified in different tests. The failure (or tertiary creep) of an overconsolidated specimen could be observed for a stress level located under the maximum strength envelope, but above the critical state line in the (p'-q) plane, accompanied by a significant dilative behavior during creep.

The results of SEM indicated that the microstructural evolution of the clay after the mechanical loading depend on the stress history. Afterwards, the structural evolution in creep phase depends on the structural pattern developed in monotonic loading. The creep contractancy/dilatancy in the macroscopic level were related to the variation of pore size and pore shape at the microscope level.

Keywords: Clay, Kaolinite, Drained creep, Triaxial test, Microstructure, Mercury intrusion porosimetry (MIP), Scanning Electron Microscopy (SEM)

Résumé

Dans les zones urbaines à fortes populations, le besoin de plus en plus fort en construction amène à concevoir et à réaliser des ouvrages géotechniques sur des sols argileux mous. Ces argiles se caractérisent souvent par des déformations de fluage importantes. Ces déformations, qui se développent en fonction du temps, sont complexes et difficiles à prévoir in-situ. Cette question nécessite donc une réflexion approfondie autour des propriétés elasto-viscoplastiques des argiles, et pour leur identification, une démarche expérimentale rigoureuse.

Cette recherche vise à analyser et à identifier, par des essais, le comportement au fluage d'une argile de type kaolinite sous un état de contraintes triaxial. Une investigation fine de l'état microstructural, avant et après fluage, a par ailleurs été réalisée, ce qui a permis de fournir un éclairage complémentaire pour une meilleure compréhension du comportement.

A l'échelle macroscopique, la méthode expérimentale consiste à réaliser une série d'essai de fluage triaxial drainé, les échantillons ayant subi au préalable des chargements purement déviatoriques (sous contrainte moyenne effective constante), à des degrés de surconsolidation différents. L'intérêt de type de chargement se situe dans le fait que la déformation volumique obtenue n'est causée que par la seule variation du déviateur des contraintes.

Les essais sont réalisés sur l'argile reconstituée saturée, au moyen d'un système triaxial automatisé. Les déformations de fluage, axiales et volumiques, sont obtenues en fonction du temps, chaque essai se caractérise par un niveau de contrainte donné et à un degré de surconsolidation donné.

L'étude de la microstructure est basée sur l'analyse de photos de microscope électronique à balayage (MEB), couplée à une méthode adaptée pour l'identification des orientations préférentielles des particules argileuses, et de la distribution et orientation des pores.

Cette étude microscopique est soutenue par des résultats d'essais au porosimètre de mercure (PAM), une méthode qui permet de quantifier et de caractériser l'espace poral, et la distribution des pores.

L'identification de l'état microstructural (MEB et PAM) est réalisée sur des petits échantillons extraits d'éprouvettes (centimétriques) ayant été au préalable sous chargement mécanique. L'investigation est systématiquement menée après le chargement purement déviatorique d'une part, et après le chargement purement déviatorique suivi de l'essai de fluage d'autre part. Cette méthode permet, par la comparaison des résultats, d'observer comment varie la microstructure au cours du fluage.

Les résultats macroscopiques ont permis de constater que des phénomènes de dilatance et de contractance s'amplifient pendant le fluage. Les résultats montrent également que la position, sur le plan des contraintes (p'-q), du niveau de contrainte vis-à-vis des différents domaines volumétriques, contrôle le développement de la déformation au fluage et du taux de déformation.

Ces travaux ont permis de mettre en évidence les trois modes de fluage : primaire, secondaire et tertiaire. Ce dernier apparaît sous forme d'un effondrement de l'échantillon surconsolidé, dont le niveau de contrainte se situe sous l'enveloppe de résistance maximale mais au-dessus de la ligne d'état critique dans le plan (p'-q). Ce comportement de fluage est accompagné d'une forte dilatance qui se développe avant effondrement.

Les résultats de MEB ont montré que l'évolution microstructurale de l'argile, après le chargement mécanique, dépend fortement de l'histoire du chargement.

Mots-clefs: Argile, Kaolinite, Fluage drainé, Microstructure, Essai triaxial, Prosimètre au mercure (PAM), Microscope Electronique à Balayage (MEB)

List of symbols and abbreviations

Symbols:

The most commonly used symbols are listed. A description of other used symbols not described in this list can be found in the text.

Greek:

δ	Deformation
ε	Normal strain
ε_1	Axial strain
ε_d	Deviatoric strain
ε_v	Volumetric strain
ε_z	Vertical strain
$\varepsilon_{1,creep}$	Axial strain during creep phase
$\varepsilon_{d,creep}$	Deviatoric strain during creep phase
$\varepsilon_{v,creep}$	Volumetric strain during creep phase
$\delta\varepsilon_v^e$, $d\varepsilon_v^e$	Elastic volumetric strain increment
$\delta\varepsilon_d^e$, $d\varepsilon_d^e$	Elastic deviatoric strain increment
$\delta\varepsilon_v^p$, $d\varepsilon_v^p$	Plastic volumetric strain increment
$\delta\varepsilon_d^p$, $d\varepsilon_d^p$	Plastic deviatoric strain increment
$\dot{\varepsilon}$	Strain rate
$\dot{\varepsilon}_1$	Axial strain rate
$\dot{\varepsilon}_v$	Volumetric strain rate
$\dot{\varepsilon}_d$	Deviatoric strain rate
φ	Friction angle
σ, σ'	Normal stress, effective normal stress
σ_1, σ'_1	Axial stress, effective axial stress in triaxial test condition
σ_3, σ'_3	Radial stress, effective radial stress in triaxial test condition
σ'_z	Vertical consolidation pressure
$\sigma'_{z,pc}$	Initial consolidation pressure
η	Stress ratio $\eta=q/p'$

γ	Unite weight
ζ	The maximum strength envelope

Latin:

C_c	Compression index
C_s	Swelling index
C_α	Secondary compression coefficient (C_α=Δe/Δlg t)
$C_{\alpha e}$	Secondary compression coefficient ($C_{\alpha e}$=Δe/Δln t)
e, e_0	Void ratio, initial void ratio
e-creep	Void ratio at the end of creep observation in triaxial test
e_M	Void ratio per gram in mercury intrusion porosimetry
e_S	Void ratio per μm^2 by SEM images
e-shear	Void ratio at the end of shear loading in triaxial test
H, H_0	Height of the soil, initial height of the soil
I_{or}	Structural or void isotropic index
I_p	Plastic index
m	Slope of the $lg\dot{\varepsilon}$-$lg\ t$ curve
m_1	Slope of the $lg\dot{\varepsilon}_1$-$lg\ t$ curve
m_v	Slope of the $lg\dot{\varepsilon}_v$-$lg\ t$ curve
M	Inclination of critical state line
p'	Mean effective stress
p'_0	Preconsolidation pressure
q	Deviatoric stress
q_f	Deviatoric stress at failure
Rs	Roundness of pores
t_{100}	Time of the primary consolidation
t_{creep}	Creep time
u,Δu	Pore water pressure, excess pore water pressure
w	Water content
w_L	Liquid limit
w_P	Plastic limit
υ	Poisson's ratio

Abbreviations:

BP	Back pressure
EOP	End of primary consolidation
GDSTTS	GDS Triaxial Testing System
MIP	Mercury intrusion porosimetry
NC	Normally consolidated
OC	Over-consolidated
OCR	Over consolidation ratio
PDST	Purely deviatoric stress path
PWP	Pore water pressure
SEM	Scanning Electron Microscopy

Contents

General introduction

Background of this study

In fact, every soil ‘‘lives’’ in all properties undergo changes with time, this time-dependent mechanical process may lead to composition and structural changes that result in stiffening, strength gain, softening or strength loss, etc. Clayey soils are complex materials that consists of more than 30% of fine particles whose size is less than 2 μm (Lambe & Whitman, 1969) which have a great influence on the physical, mechanical and physicochemical properties inside these materials.

When soil is subjected to a constant load, it deforms over time, and this is usually called creep. Clayey soils exhibit all the time-dependent properties, where creep is the most typical, pronounced and readily observed. Clayey soils usually display large creep deformations, in the form of prolonged settlements, tilts of buildings and geotechnical structures, or slowly slippage of slopes and embankments, influenced by the composition, stress history, change in temperature, and biochemical environment of these soils.

Large amount of researches have been conducted on creep of soil since the middle of 19^{th} century due to the intensive building activities; the first highlighting phenomenon of the creep in clay can be found in “Bases and Foundation” by V. Karlovich in 1869. Afterwards, a lot of creep tests have been performed. Most of the previous laboratory experimental studies on creep, performed on clay, have focused on the stress-strain-time relationship through drained and undrained oedometer and triaxial tests. This time-dependent relationship should be based on drained, rather than on undrained, test results because pore water pressure build-up in an undrained creep process results in the decrease of the mean effective stress. This is contradictory to the condition of constant stress during creep. From this point of view, experimental studies on drained creep conditions can provide a better understanding of the creep phenomenon.

In reality, time-dependent deformations are significantly resulting from the time-dependent or viscous adjustment of the soil structure to reach a new equilibrium under the external stress. Microstructure of soils remained largely unknown until suitable optical, X-ray diffraction, and electron microscope techniques made direct observations possible starting in the mid-1950s. Thereafter, there are some proposed theories to elucidate the mechanisms of creep, for instance,

the creep mechanisms explained by the breakdown and/or sliding between particles, changes in pore structures and structural viscosity.

The very pronounced time-dependent macroscopic behavior of clayey soils is due to their viscous properties. On the microscope level, the cohesion between clay particles is related to the pore size at different scales. Consequently, it is clear that the study of the mechanical behavior of clays from the structural standpoint, i.e., the variation of particles and pores, is an absolute necessity. The structural interpretation of the mechanical behavior of soil may be expected to give a proper understanding of its time-dependent constitutive relation. At present, the study on microscopic mechanism of creep for soft clay is still in its infancy due to the limitations of experimental technique and a lack of experimental data.

The study on creep of soils are important not only due to the direct application of the results to solve practical problems, but also because the results can be used to obtain fundamental information about soil structure, inter particle bonding, and the mechanisms that controll the strength and deformation behavior.

Thus, attempts were made to introduce the creep mechanism of clay from first the view of phenomenological approach and macromechanics, and then the micromechanics endeavors to deduce its structural properties. Emphasis in this research is on how time under stress changes the deformation, strength and structural properties of clay, what can be learned from knowledge of these changes, as well as their quantification for predictive purposes.

Objectives and organization of the thesis

The aim of this study is to try to understand how the creep evolve, in clayey materials at macroscopic scale under a given stress path, and how the corresponding microstructural changes within time.

The investigation consists in conducting a literature review, a laboratory experimental program and an analytical program. Experimental research are conducted on normally consolidated and overconsolidated saturated reconstituted clay under different constant sustained stresses in a certain creep duration. The microscope study is based on a thorough microstructure analysis using in particular scanning electron microscope, coupled to an adapted method for the identification of preferential orientations of particles. This microscopic study is complemented by mercury

intrusion porosimetry analysis, a method that allows quantifying the pore space and characterizing the local void ratio.

The detailed organizational list of the thesis is as follows:

A general introduction to the time-dependent deformation of clay is provided.

Chapter 1 contains a summary of the existing state-of-the-art on the creep of clayey soils, including macroscopic studies and microscopic studies.

Chapter 2 presents the clayey materials and experimental methods that are used in this study.

Chapter 3 gives the results of macroscopic experiments, which includes three groups of drained triaxial creep tests under different preconsolidated pressures (p'_0=200 kPa, 800 kPa and 1000 kPa). The evolution of creep strains as well as strain rates with respect to time, stress level and overconsolidation ratio are presented.

Chapter 4 proposes the results of the microscopic experiments of two groups of samples: six samples from creep test series with p'_0=1000 kPa and six samples in conventional shear tests that follows exactly the same stress path as in creep tests. Results of scanning electron microscopy and mercury intrusion porosimetry are compared on soils after shear and after creep.

The conclusions derived from this study and perspectives on future research are given.

Chapter 1 Literature review

Research on literatures are reviewed from the soil science, geology and mineralogy concerning the problem of creep in clayey soils. The information provided by the soil scientists concerns the physical characterization of creep in soils, the geologists deal with the physical observation of creep deformation. There is also information derived from the mineralogy that considers the mechanical characteristics of creep in the view of soil mineralogy.

A lot of creep tests have been performed (Bishop & Lovenbury, 1969; Mesri, 1973; Tavenas et al., 1978; Tian et al., 1994; Fodil et al., 1997; Yin, 1999; Zhu et al., 1999). The problem of creep in clayey soils has not been completely assessed. The treatment of creep remains problematic due to the complex elasto-viscoplastic properties of the clayey materials. The literature review given in this chapter provides some insight into the behavior of creep in soils.

1.1 Macro approach to creep of clay

When soil is subjected to a constant load, it deforms over time, and this is usually called creep. Figure 1.1 shows a schematic diagram of a typical creep curve of soil: from point A to B is the stress path, the creep starts when the soil sample is deformed to point A (Figure 1.1a), meanwhile, the stress is kept constant (Figure 1.1b). As time goes on, the strain of soil increases gradually (Figure 1.1c).

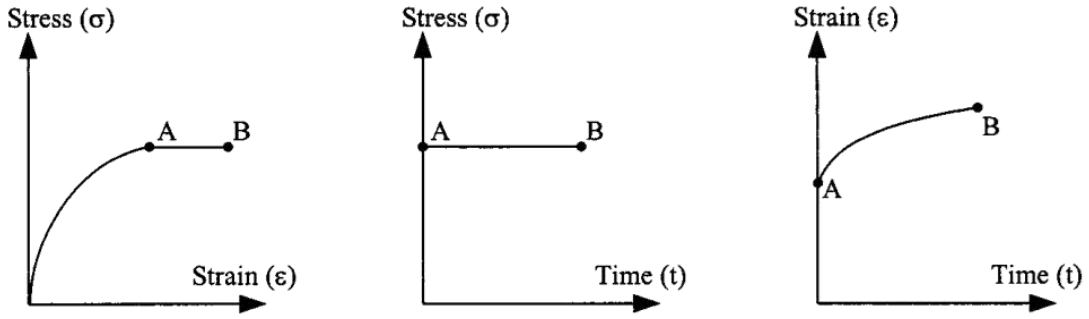

(a) (b) (c)

Figure 1.1 Creep test:(a) stress-strain; (b) stress-time; (c) strain-time

Creep properties of clay under different stress conditions are summarized in the following: one-dimensional compression, triaxial shear, unconventional complex stresses, and large-scale field tests. Among which, laboratory creep tests are the main approach to understand the creep characteristics of soil. Compared with the field test, the laboratory test has characteristics of easy

long-term observation, strict controlling in test conditions, repeated trials and less cost. Therefore, the in-door testing methods are more used in the current research for creep.

1.1.1 One-dimensional creep test

In one-dimensional creep test, the effective vertical stress, σ_v', is maintained constant, and the vertical deformation with the development of time can be measured directly. One-dimensional creep characteristics are the simplest and most basic, which mainly answering the following questions: (1) what is the secondary compression and the secondary compression coefficient; (2) how the compression coefficient evolves; (3) how to determine the secondary compression coefficient.

1.1.1.1 Secondary compression and the secondary consolidation coefficient

In the conventional one-dimensional consolidation test, for each stage of loading, the deformation of soil is mainly due to the compression in primary consolidation, the pore water pressure dissipation and the secondary compression (Bjerrum, 1967; Graham et al., 1983; Fodil et al.,1997). Yin (1999) summarizes the volumetric creep strain mechanism under the drainage condition: (a) the primary stage, under the vertical load, the compression deformation causes the volume to decrease whereas an increase in pore water pressure. The deformation of the soil caused by the dissipation of the pore water pressure is much less than that caused by compression. (b) the secondary stage, the pore water pressure dissipated to its initial value and the volume variation of soil is mainly caused by dissipation of pore water pressure. (c) the third stage, deformation of soil after the dissipation of the pore water pressure, i.e., the pure creep stage.

Buisman (1936) pointed out that the relationship between deformation and the logarithm of time is essentially linear in the secondary compression stage, moreover, he presented that creeping of clays never ends. A 43 years' oedometer creep test performed by Vienna University of Technology on an organic clayey silt proved his point of view (Figure 1.2). It is seen that, under a final 163 kPa constant vertical stress, the settlement of soil continued to develop within 43 years and didn't show a stable state at the end of test.

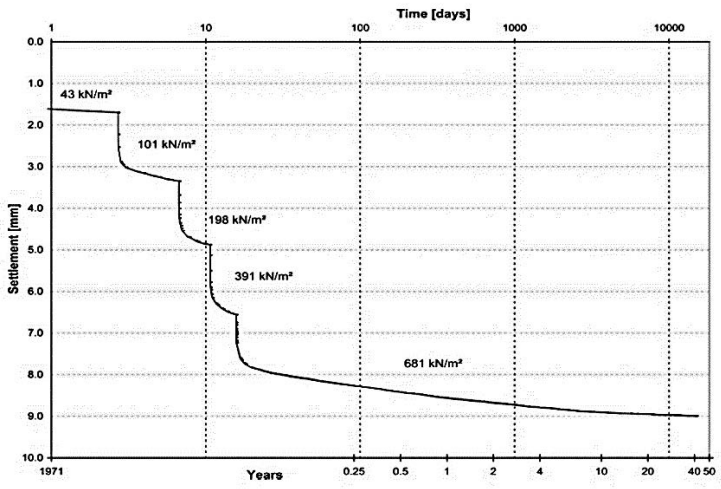

Figure 1.2 Relationship of settlement as a function of logt of an organic clayey silt in oedometer test by Vienna University of Technology (1971-2013), Brandl (2013)

Figure 1.3 shows a typical relationship between void ratio and the logarithmic time in the one-dimensional creep test. The curve is in the S-shape, which can be divided into two parts: the main consolidation stage and the secondary consolidation stage. The time t_{100} (or t_{EOP}) at the transition is the approximate time of the end of the primary consolidation. The subsequent deformation is the secondary consolidation, that is, creep under constant effective vertical stress. In the secondary consolidation stage, the slope of the void ratio versus logarithmic time is defined as the secondary consolidation coefficient:

$$C_\alpha = -\frac{\Delta e}{\Delta \log t} \quad \text{or} \quad C_{\alpha e} = -\frac{\Delta e}{\Delta \ln t} \tag{1.1}$$

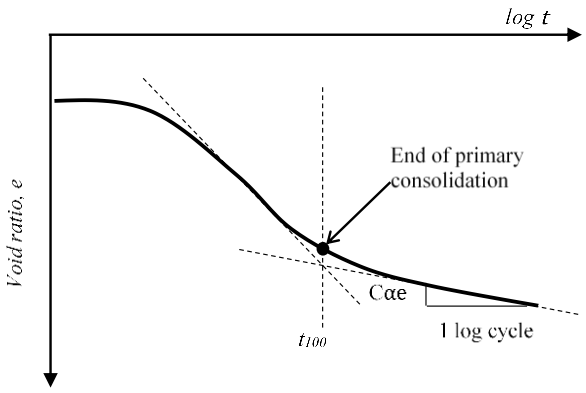

Figure 1.3 Identification of secondary compression coefficient

It is noteworthy in literatures that many attentions have been paid to the evaluation of the referenced time, t_{100}. The concern is to decide when the creep deformation starts, and the referenced time is especially crucial to estimate creep deformation in low permeability clay. The approaches, i.e. hypotheses A and B (Ladd et al., 1977), are as follows:

- Hypothesis A assumes that the secondary compression (creep) occurs only after the primary compression. The strain at EOP is a unique value, which means that the soil show time-independent creep behavior during dissipation of pore pressure in a manner that affects the strains at EOP. The reference time is taken as an intrinsic parameter for a given soil and independent of drainage condition and soil thickness (Ladd et al., 1977; Mesri & Choi, 1985).

- Hypothesis B assumes that creep take places within the whole consolidation process, which implies that the value of strain at EOP is not unique. The time-dependent strain occurs since the primary compression. The t_{100} is taken as the time at EOP, its value thus varies with the drainage condition of the sample (Suklje, 1957; Wahls, 1962; Bjerrum, 1967; Barden, 1969; Crawford, 1986; Kabbaj et al., 1986).

The assumed strain versus time relationships based on the two hypotheses are shown in Figure 1.4, and general agreement on whether there is a combination of primary and secondary compression during the dissipation of pore pressure is still not reached (Berre & Iversen, 1972; Leroueil et al., 1985; Duncan et al., 1996). It is agreed to some extent that the real soil behavior is most likely in a middle state other than the extreme cases in the two hypotheses (Augustesen et al., 2004). Aboshi (1973) performed different scales of experimental oedometer creep tests on muddy clay, which the thickness of samples varies from 2cm to 100 cm, whose results confirmed that the strain developed at EOP gradually increased with thickness: denial of hypothesis A; meanwhile, the secondary curves do not converge to a single line: denial of hypothesis B.

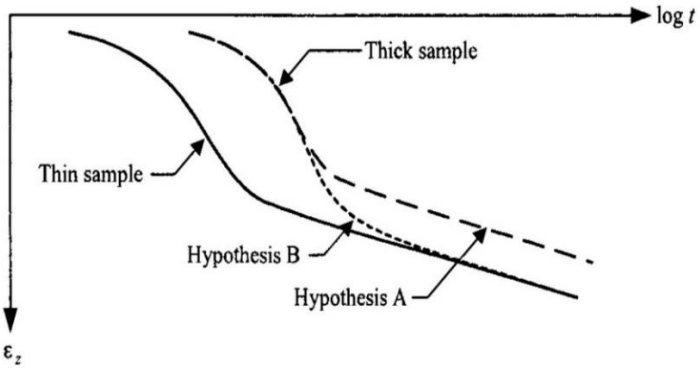

Figure 1.4 Strain versus time for hypotheses A and B (Augustesen et al., 2004)

In all the above researches related to secondary compression, whether hypothesis A or B is adopted, numerous investigations have shown that the void ratio (or vertical strain) as a function of time after the primary compression (hypothesis A) or instantaneous compression (hypothesis B) in oedometer test can be fitted by a logarithmic function (Liingaard et al., 2004). The problem of the reference time does not change the fact that secondary compression exists, and that the magnitude of creep strain is concerned not the evolution of creep strain or creep strain rate.

The traditional understanding of the creep behavior within oedometer creep test in shown in Figure 1.3, i.e., the secondary compression (or creep) follows a linear function in plot of *e-logt* or ε_v-*log t*. This type of curve may be valid for several log cycles of time, but the results of long term (140 days) creep tests by Leroueil et al. (1985) on Batiscan clay under different vertical stress showed a general non-linear strain-time behavior. It is seen in Figure 1.5 that:

- Type I corresponds to the overconsolidated soil, the vertical stress is less than the preconsolidation stress, no significant cross-point is between the primary consolidation and secondary consolidation.

- Type II corresponds to a normally consolidated sample which the vertical consolidation pressure is close to the preconsolidation stress, and the slope of ε_v-*logt* during secondary compression is significantly larger that of type I.

- Type III is a normally consolidated sample and vertical consolidation pressure is much higher than the preconsolidation pressure, and the slope of ε_v-*logt* curve is gradually reduced, showing by an obvious anti-S shape as shown in Figure 1.3.

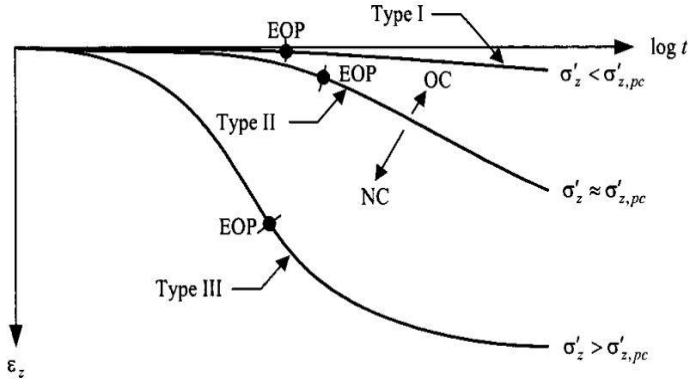

Figure 1.5 Types of strain versus time relations by Leroueil et al. (1985)

The general strain-time behavior has also been observed by Leonards & Girault (1961), Bjerrum (1967), Berre & Iversen (1972), and Yin (1999). However, Yin et al. (2013) considered that the classification method shown in Figure 1.5 is open to objection, that is, no discrimination has been made between remolded soil and the structural undisturbed soil. Only the strain-time relations of structural soil can be divided into these three types. Moreover, the ε_v-*logt* curve of type II is most likely corresponds to the destruction of soil structure and this deformation pattern is independent of the preconsolidation pressure (Yin et al., 2011; Yin & Wang, 2012). The deformation pattern of remolded normally consolidated soil should be similar to type III in Figure 1.5.

Oedometer creep tests were also performed by the author on remolded normally consolidated Kaolin and Shanghai clay (see details in Annex Chapter 1), and the strain-time relation is consistent with type III in Figure 1.5. The time note, t_{100} that identified by the linear part of the anti "*S*" shape *e-logt* curve, was found to be stress-dependency (Figure 1.6), similar results were obtained for other experimental results on Shanghai clay after Zhu (2014), Hong Kong marine deposits (after Yin J-H, 1999) and Vanttila clay (after Yin, et. al., 2011).

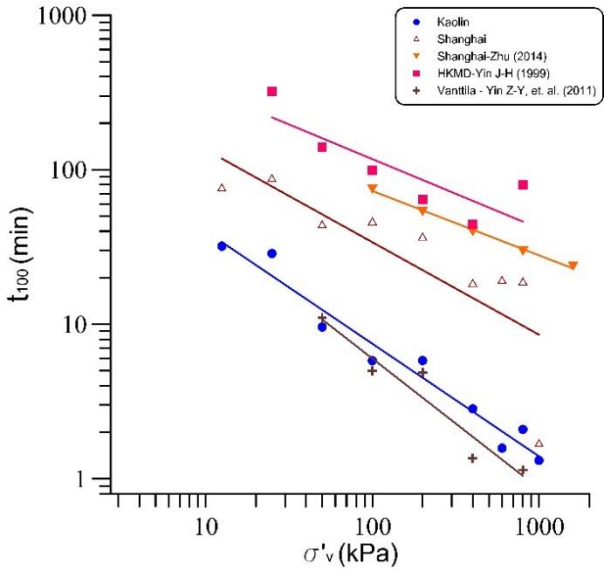

Figure 1.6 Relationship of t100 as a function of vertical stress

1.1.1.2 Evolution of secondary compression coefficient

The parameter $C_{\alpha e}$ has been used as a reference to describe the creep characteristics of clay in one-dimensional tests, the stress dependency and time dependency of $C_{\alpha e}$ has been subjected to numerous investigations in previous literatures.

a) Stress dependency

Bjerrum (1972) considered that $C_{\alpha e}$ was related to the preconsolidation pressure. Leroueil et al. (1985) noted that $C_{\alpha e}$ was associated with vertical stress. Fodil et al. (1997) found that $C_{\alpha e}$ increased with the increase of σ'_z. However, when σ'_z was above the preconsolidation pressure the increase was less significant, which was consistent with the conclusions of Murayama & Shibata (1961).

Mesri & Godlewski (1977) conducted one-dimensional consolidation tests of remolded soil and natural soil with different OCRs. The results indicated that $C_{\alpha e}$ was related to the state of soil: for natural undisturbed soil, $C_{\alpha e}$ increased gradually with the increase of σ'_z then decreased after reaching a peak; whereas the parameter $C_{\alpha e}$ for remolded soil varied in a small range, thus can be regarded as independent with vertical stress. Experimental results on remolded Kaolin and Shanghai clay (Figure 1.7) also shows the stress-dependency.

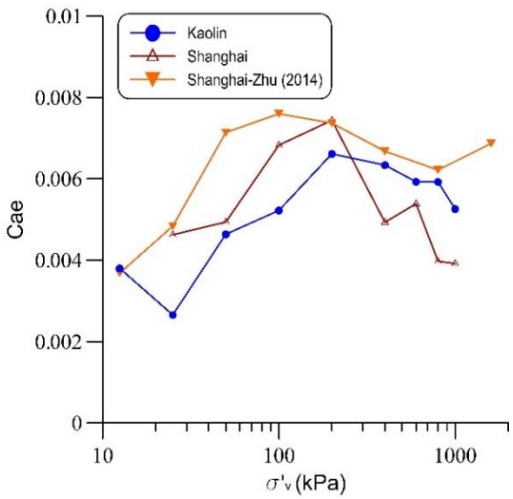

Figure 1.7 Parameter Cαe as a function of vertical stress

It can be concluded, to some extent, that $C_{\alpha e}$ depends not only on the applied effective stress but also on the preconsolidation pressure. The value of $C_{\alpha e}$ increases while σ'_z approaches initial consolidation pressure $\sigma'_{z,pc}$, reaching a maximum around $\sigma'_{z,pc}$ then shows a decrease tendency and

remain constant (Ladd & Preston, 1965; Tavenas et al., 1978; Graham et al., 1983; Länsivaara & Nordal, 2000; Augustesen et al., 2004).

Yin et al. (2010, 2011) considered that the creep behavior of a soil must be analyzed separately being intact or remolded: for natural soft clay, the analysis of $C_{\alpha e}$ should integrate the over consolidation, density or void ratio, particularly the structure of soil and other status characteristics, the relationship of $C_{\alpha e}$ with the vertical stress is more likely superficies. They also summarized values of $C_{\alpha e}$ for 24 typical remolded and undisturbed clays, and found that the values of $C_{\alpha e}$ varied from 0.004 to 0.137. It is considered that the secondary compression coefficient of soft clay is associated with many factors and thus it is difficult to obtain a constant value. Therefore, a certain value of $C_{\alpha e}$ should correspond to a specific condition.

Walker & Raymond (1968) pointed out that the secondary compression rate appeared to be linearly to the compression index. Mesri (1973) have suggested to represent the results in terms of the $C_{\alpha e}$ -Cc relation, which makes it possible to highlight the relation of stress-compressibility with time. Based on the results of 22 natural soil deposits, Mesri & Godlewski (1977) proposed that there was a unique relationship between $C_{\alpha e}$ and Cc. They found a range of values for $C_{\alpha e}$ /Cc was between 0.025 and 0.1 and the magnitude of $C_{\alpha e}$ /Cc seems to related to the type of soil. The values of $C_{\alpha e}$ /Cc were small for some clays and silts, medium for organic silts and clays, and in general high for peats. For a majority of inorganic clays, the value of $C_{\alpha e}$ /Cc equals 0.04 ± 0.01, and 0.05 ± 0.01for highly organic plastic clays (Mersi & Castro, 1987).

Secondary compression occurs after the dissipation of pore water pressure, and is mainly caused by un-recovered inelastic deformation of the solid skeleton due to creep. The parameter $C_{\alpha e}$ represents inelastic deformation in secondary compression, whereas the compression index C_c indicates both elastic and non-elastic deformations. Therefore, the ratio of $C_{\alpha e}/C_c$ may lead to inaccurate understanding on the secondary compression behavior. Yin et al. (2011) proposed to represent the secondary compression behavior on the $C_{\alpha e}$ - (C_c -C_s) plane instead of $C_{\alpha e}$-C_c, where the term (C_c -C_s) only includes non-elastic deformation similar to $C_{\alpha e}$. Yin et.al (2012) further showed that the parameter (C_c -C_s) can be considered as constant from results on 5 types of remolded clays, and the variation of $C_{\alpha e}$ as a function of (C_c -C_s) is considered to be caused by the evolution of $C_{\alpha e}$ with applied stress or soil density. The experimental results performed on Kaolin and Shanghai clay by the author of this thesis showed that the values of $C_{\alpha e}$ - (C_c -C_s) were not constant and close to the lower limit values of $C_{\alpha e}/C_c$ by Mesri and Godlewski (1977).

b) Time dependency

Some authors (Feda, 1992; Wu et al., 2011), Mesri and Godlewski (1977) were also included, questioned the uniqueness of the constant concept of $C_{\alpha e}/C_c$ in which $C_{\alpha e}$ and C_c are assumed to be independent of time. They concluded that both $C_{\alpha e}$ and C_c changed with time, and the variation of $C_{\alpha e}$ with time might reflect the changes of C_c with time.

Similar experimental results on remolded Kaolin and Shanghai clay by the author of the thesis were also obtained (Figure 1.8). It is seen that the value of $C_{\alpha e}$ shows a decrease tendency with time, after one day, a recommended duration to perform oedometer test, the decrease tendency is slowed down but have not terminated at a constant value.

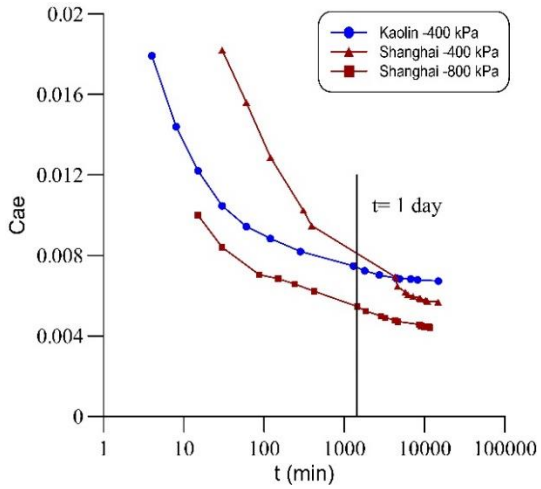

Figure 1.8 Parameter Cαe as a function of time for kaolin clay and Shanghai clay

1.1.2 Triaxial creep test

In triaxial creep test, the axial stress and radial stress are maintained constant, the evolution of deformation with time can be measured directly. According to the drainage conditions, triaxial creep test can be divided as (Figure 1.9): (a) drained creep, where the main effective stress p' and deviatoric stress q remain constant; (b) undrained creep, in which the deviatoric stress is constant while p' decreases caused by a building up of pore water pressure. Triaxial creep properties are the basis of three-dimensional constitutive model of creep, in which the main problems can be answered: strain-stress-time evolution.

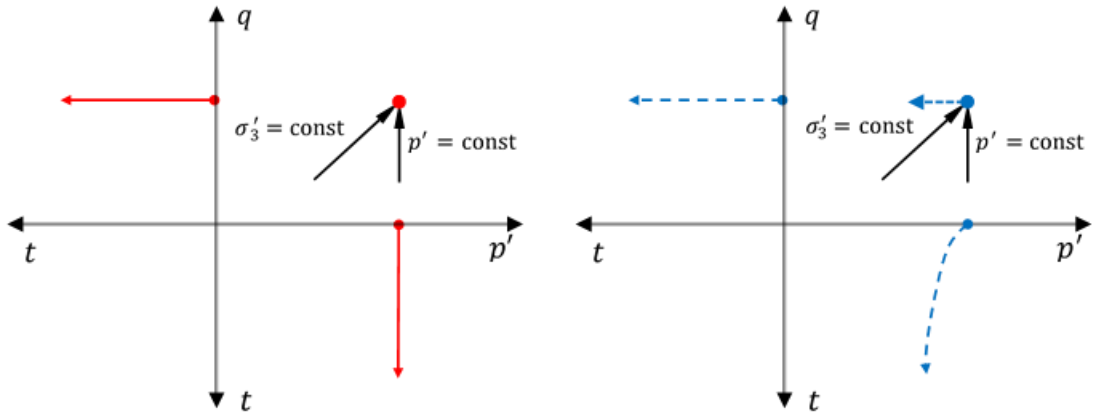

Figure 1.9 Triaxial creep tests under drained and undrained conditions (a) drained creep; (b) undrained creep

1.1.2.1 Undrained creep test

It is well-known that the typical strain-time relationship observed in triaxial creep test can be divided into three phases (Mitchell, 2003; Sheahan, 1995), as illustrated in Figure 1.10. The primary, secondary and tertiary creep, which sequentially corresponds to a decrease strain rate with time, following by a nearly constant creep rate, and then an accelerating rate eventually leading to failure of the soil (donated as creep rupture).

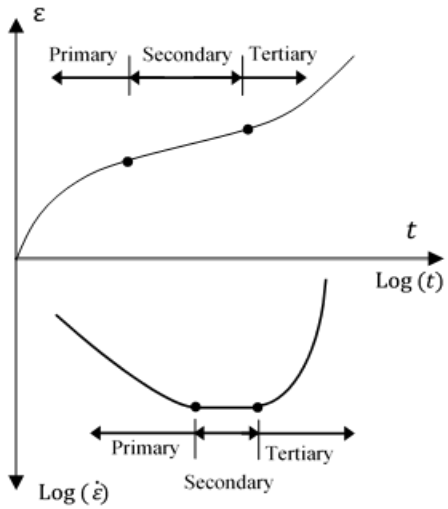

Figure 1.10 Definition of primary, secondary and tertiary creep

In the primary phase of creep, the strain rate decreases with time, and the relationship of $log\dot{\varepsilon}$ *-logt* is linear. Under low stress level (q_1 in Figure 1.11), the primary creep may last a certain

period of time then cease (Zhu, 2007). For creep test performed under high stress level (SL=q/q_f), the creep strain rate decreases linearly at first and then increases till a creep rupture as soon as reaches a minimum (point A and B in Figure 1.11). The higher the stress level, the earlier the creep rupture (Murayama & Shibata, 1958; Liam Finn & Snead, 1973; Vaid et al., 1979). The time of the creep rupture was also studied within the undrained creep (Saito, 1965, 1969; Snead; 1970; Kwan, 1971; Campanella & Vaid, 1973), empirical equations to estimating the rupture time were proposed. For soils subject to failure during undrained creep, the time to failure is usually a negative exponential function of the stress. For stresses greater than some limiting values below which no failure develops even after very long times.

Many tests show that the three phases of creep are difficult to be wholly observed under single load stage. Basically, most soils have the primary creep following application of a stress, and turn to the tertiary creep directly in the case of high stress level, without showing of the secondary creep phase (Singh & Mitchell, 1968; Arulanandan et al.; 1971; Stepanian, 1975; Hicher, 1985; Vyalov, 1986; Augustesen et al.,2004). Mitchell (2003) considered that the secondary creep was rarely being observed in laboratory tests because of a true steady state can exist only within constant structure and stress conditions, which conditions are likely only for a fully destructured soil. Additionally, a constant rate of strain must be identified within the limits of the measuring instrument as well as the strain rate calculation.

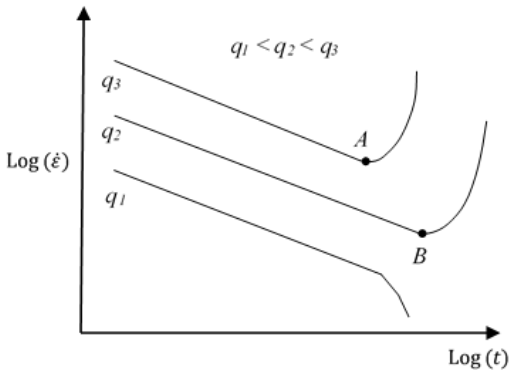

Figure 1.11 Typical relationship of creep strain rate with time under different stress level in undrained creep (after Zhu, 2007)

Singh & Mitchell (1968) proposed a phenomenological equation to describe the linear relationship of creep strain rate versus time after investigating a number of creep test results, to

describe the primary phase of creep in the range of stress levels commonly encountered in engineering practice. They defined the creep parameter *m,* controlling the rate at which the strain rate decreases with time, which was the absolute value of slope of the straight line on the log strain rate versus log time plot, being

$$m = -\frac{\Delta \log \dot{\varepsilon}}{\Delta \log t} \tag{1.2}$$

The values of *m* were found to fall between 0.75 and 1.0 whatever the tests conditions of the soil: undisturbed or remolded, normally or overconsolidated, drained or undrained. Furthermore, they suggested that for a given soil, the value of *m* was independent of stress level. Consequently, a semi experimental equation of the interrelation among creep strain rate, stress level and creep duration was developed, being:

$$\dot{\varepsilon} = Ae^{\alpha D}(\frac{t_1}{t})^m \tag{1.3}$$

where *A*, α and *m* are soil creep parameters (Singh & Mitchell,1968; Mitchell, 2003), D can be deviatoric stress or stress level. t_1 is a reference time (e.g., 1 minute) and *t* is the elapsed time after creep. The scope of the application of this formula was discussed by Walker (1969a), Tavenas et al.1978, Borja & Kavazanjian (1985), Li & Lin (2000) and Zhu (2007).

a) Strength softening in undrained creep

In general, during the undrained creep, the undrained strength of saturated clay is reduced within long-term test condition (Saito & Uezawa, 1961; Singh & Mitchell,1969; Hicher, 1985; Yin & Karstunen, 2011). The long-term undrained shear strength is generally lower than that obtained in conventional undrained shear test. Casagrande & Wilson (1961) showed that the shear strengths of 6 brittle undisturbed soils were found to be reduced to 40-80 percent of their normal values in 30 days, similar tendency was also reported by Goldstein & Ter-Stepanian (1957), Vialov & Skibitsky (1957) and Yin et al. (2013) on natural soft clays.

Loss of strength during creep is important in clays within undrained conditions, because it's in connection with the stability of constructions on clay. Mitchell (2003) pointed out that the strength loss during creep may be explained as follows:

- If a significant portion of soil strength is due to cementation, and then creep deformation causes the failure of cemented bonds, thus, the strength will be lost.
- The strength depends on effective stress, if creep causes changes in effective stress then the strength changes will also occur.

- Changes in pore pressure during undrained deformation, the influence of pore pressure on strength may be highlighted especially in heavily overconsolidated clays. Shear deformations cause dilation and the development of negative pore pressure, which concentrate along planes where the greatest shearing stresses and strains develop. Under sustained loading, water migrates into zones of high negative pore pressures, leading to strength decrease relative to the strength in normal undrained shear test. This leads to the formation of shear band.

b) Water pressure evolution

Another investigation related to the undrained creep is the excess porewater pressure. Holzer et al. (1973) preformed undrained creep test on San Francisco Bay mud, they found that the magnitude of the increased pore pressure was a function of the initial consolidation stress, except the amount that occurred immediately after the shear stress is applied. The undrained creep test on Leda clay by Walker (1969b) showed that the excess pore pressure could reached 20% of the cell pressure. Moreover, the creep strain, i.e., the secondary compression effect, and pore pressure are directly related. Two equations were derived to describe the proportional relation between pore pressure and mean effective stress. Similar result was found by Shen et al. (1973) on a soft marine clay. Arulanandan et al. (1971) pointed out that the pore pressure developed during undrained creep was due to not only the secondary compression but also to the deviatoric stress. The magnitude of pore water pressure built up in secondary compression was found to be time and structure dependent, based on the experimental results of a costal organic silt clay.

1.1.2.2 Drained creep test

Deep understanding of stress-strain-time relationship within creep phenomenon allows to enrich the constitutive models. Tavenas et al. (1978) proposed that the time dependent constitutive model should be based on drained test results rather than undrained tests, considering the decrease of p' caused by building up of pore water pressure in undrained creep process, which conflicts with the postulate of constant stress conditions for creep. The creep behavior is required first to be understood then can be used to develop constitutive model. The experimental research on drained creep behavior is of fundamental importance for understanding and modelling the time-dependent stress strain behavior of soil.

One of the main acquisition in drained creep test is to reveal the evolution of creep strain and strain rate. Under the drained condition, volume change of soil is allowed within the creep process. Tavenas et al. (1978) concluded that the development of volumetric strain rate with time for a lightly overconsolidated clay could also be represented by means of parameter m with reference to the work of Singh & Mitchell (1968). For more clarity, we choose to define the creep parameter m in the form of m_1 and m_v, which are the slopes of the straight lines on log axial and volumetric strain respectively rates versus log time.

a) Axial creep strain

A general axial strain versus time behavior during drained creep is similar as within the undrained creep test shown in Figure 1.10, and the magnitude of axial creep strain is generally increased with stress level. The evolution of axial creep strain rate thus be subject to numerous investigations.

Based on the drained triaxial creep tests on intact Pancone clay, Bishop & Lovenbury (1969) noted that m_1 increased with deviatoric stress level. Augustesen et al. (2004) reproduced the test data of Bishop & Lovenbury (1969) on drained triaxial tests and oedometer tests (Figure 1.12a), an "abrupt" change in the strain rate between 20 and 100 days was highlighted, which was interpreted as a limited instability causing by a fundamental modification in soil structure. Kabbaj et al. (1986) pointed out that the abruption in strain rate within oedometer test might corresponds to a creep delay, which occurs at a transition state from overconsolidated to normally consolidated. The strain rate for remolded normally consolidated Kaolin and Shanghai clay, in drained oedometer creep tests performed by the author of the thesis, also exhibits fluctuation after 2 days.

Tavenas et al. (1978) concluded that m_1 increased slightly with the shear stress with an average value of 0.76. D'Elia et al. (1991) performed long-term drained triaxial creep tests on Santa Barbara clay, and found that the strain rate was negligible up to a stress level of 0.65, and the value of m_1 was small, typically between 0.45 and 0.6. Based on drained triaxial creep tests on undisturbed marine sediments, Tian et al. (1994) pointed out that m_1 was a function of the deviatoric stress. The authors also indicated that m_1 appeared strongly dependent on the plastic properties of the clayey material. For high-plasticity clays, the value of m_1 increased with deviatoric stress, while no significant variation was observed for low-plasticity clays. Den Haan & Edil (1994) reported that the common value of m_1 was between 0.7 and 0.9, and seems to be independent of deviator stress level for drained or undrained triaxial tests on low permeability soils.

Zhu (2007) found that, for remoulded Hong Kong marine deposits in drained triaxial tests, the values of m_1 were in the range of 1.03 to 1.39, and whose value reflected the intensity of viscous effect, with larger value of m_1 corresponds to a weaker viscous effects. Augusttesen et al. (2004) summarized the parameter of m_1 for clays and noted that typical range of m_1 varies for normally consolidated soils from 0.7 to 1.2 with most values less than 1.0, and m_1 seems to be less than 1.0 in the overconsolidated range. The general observation shows that m_1 is stress-dependent most of the time, and the axial strain rate increases with deviator stress or stress level.

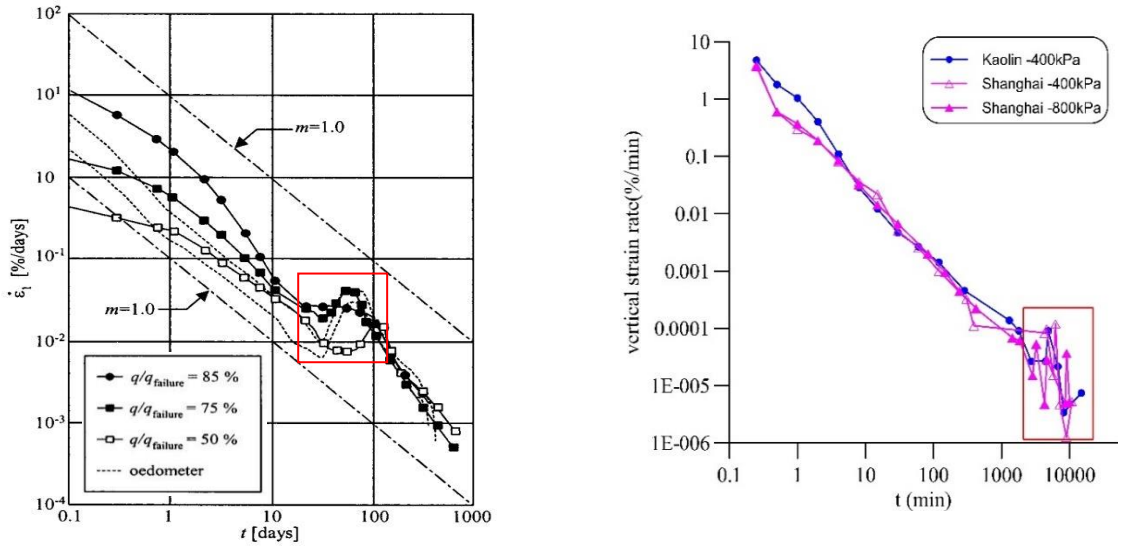

(a) (b)

Figure 1.12 Axial strain rate as a function of time: (a) reproduced results of drained creep tests and oedometer tests on Pancone clay by Bishop & Lovenbury (1969) (Augustesen et al., 2004); (b) oedometer tests on remolded Kaolin and Shanghai clay

b) Volumetric creep strain

It is generally accepted that under drained triaxial loading on saturated clays, the normally consolidated and lightly overconsolidated clays exhibit contractant behaviour (Bishop & Lovenbury, 1969; Shibata & Karube, 1969), whereas heavily overconsolidated clays can exhibit dilatant behaviour (Henkel, 1956; Roscoe & Burland, 1968; Shimizu, 1982; Biarez & Hicher, 1994; Hattab & Hicher, 2004). In most of the experimental approach to the creep of soil, the analyses have been focused mainly on the axial strain and axial strain rate. Little analyses have been

conducted on the evolution of volumetric strain, so does for the dilatant behavior, especially in large range of overconsolidation ratios.

In the conventional triaxial test, where the confining pressure σ'_3 is constant, the contractant creep behaviour was observed by Tian et al. (1994) on normally consolidated undisturbed marine sediments. The results show that ε_v varied in positive correlation with different stress level (i.e., ε_v increases with the increase of the stress level), and the values of parameter m_v referring to volumetric strain rate were different with m_1 referring to axial strain rate. The contractant results were also obtained by Zhu (2007) on normally consolidated remolded Hong Kong marine deposits. However, the evolutions of ε_v within creep were quite close in spite of variations of the stress level. Kong et al. (2011) found that the overall volumetric creep strain for undisturbed normally consolidated Zhanjiang clay was contraction under constant σ'_3 stress path, while a certain contraction and dilatancy alternately appear during creep when σ'_3 was within the material's structural yield stress (Figure 1.13). It can be seen that the contractant/dilatant behaviour during creep relates to the loading condition before creep and this relation was highlighted on structural soils.

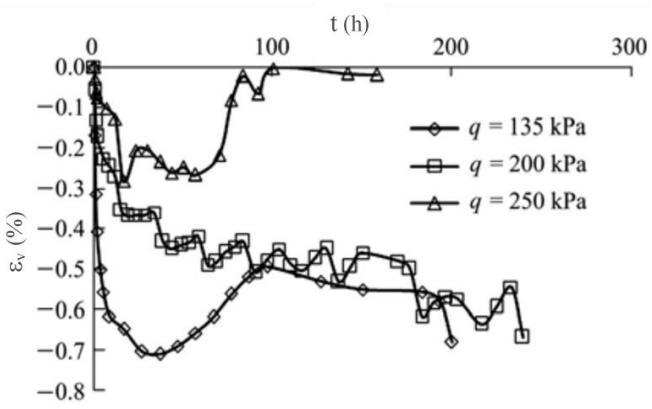

Figure 1.13 Volumetric strain curves time in drained creep of Zhanjiang clay (Kong et al., 2011)

Tavenas et al. (1978) performed drained creep triaxial tests on undisturbed lightly overconsolidated Saint-Alban clay along different stress paths. The authors observed that ε_v was obviously influenced by the mean effective stress p'. Under the increased p' stress path (line 1 and line 2 in Figure 1.14, which line 2 translates σ'_3 constant stress path) a contractive creep was detected and the magnitude of ε_v increased with the stress level, whereas values of m_v decreased with the increase of stress level. Similar tendency was obtained by Yin (2006) for Saint -Herblain

clay, and the values of m_v decreased from 0.7 to 0.36 while the stress level was increased from 0.53 to 1.0.

Under constant p' stress path (line 3 in Figure 1.14) very small volume change was detected. Furthermore, an obvious dilatancy occurred continuously and up to failure after the decrease p' stress path (line 5 in Figure 1.14).

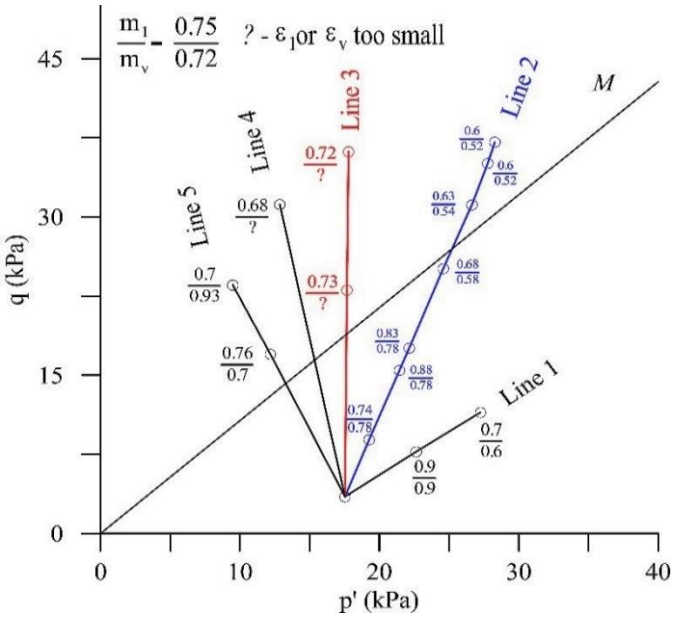

Figure 1.14 Variations of the creep parameter m for volumetric and axial strains with the stress condition, reproduced from Tavenas et al.,1978

Contraction related to creep was detected by Sekiguchi (1973) on normally consolidated remolded Fujinomori clay through constant p' creep tests, and the variation of ε_v was found to be dependent on the increment and magnitude of effective stress level. Similar to the decrease p' stress path test performed by Tavenas et al. (1978), D'Elia et al. (1991) performed long-term drained triaxial creep tests on intact Santa Barbara clay under a stress path with σ'_3 decreasing and σ'_1 constant. The results show a dilatancy phenomenon for low confining pressure. The dilatant creep was observed for dense sand under high deviatoric stress by Murayama et al. (1984) under p'=constant loading.

The overconsolidation condition is not the only factor that influences the volumetric performance (contractancy/dilatancy) during creep, the stress path or stress condition before creep under progressive stress seem to also matter. Thus, it is necessary to develop a clear understanding on the effects of the stress conditions before creep on the volumetric behavior. Afterwards, the

evolution of volumetric creep strain rate can be investigated. Augustesen et al. (2004) also noted that the determination of m_v was associated with some uncertainty compared with the determination of m_1. Yin et al. (2013) pointed out that the value of m_v implied the concept of strain acceleration, and the relationship between the creep rate and the characteristic parameters of clay needed to be further studied.

c) Deviatoric creep strain

Due to the known coupling effects between shearing and volumetric plastic deformations in soils, an increase in either mean pressure or deviator stress can generate both types of deformations. Creep behavior is no exception. Time-dependent shear deformations are usually referred to as deviatoric creep or shear creep. Time-dependent deformations under constant stress referred to as volumetric creep, which the secondary compression is a special case of volumetric creep. Deviatoric creep is often accompanied by volumetric creep.

The relationship between deviatoric strain, and axial and volumetric strains can be obtained:

$$\varepsilon_d = \varepsilon_1 - \frac{\varepsilon_v}{3} \tag{1.4}$$

Kavazanjian & Mitchell (1977, 1980) suggested that the time-dependent strains be described by separated but not independent consideration of deviatoric and volumetric stains. Tavenas et al. (1978) confirmed the validity of the separation of volumetric and deviatoric strain components, and proposed an equation to describe the deviatoric strain with time:

$$\dot{\varepsilon_d} = Ag(\sigma')(\frac{t_1}{t})^m \tag{1.5}$$

where parameter A and m are defined as in Equation 1.3 by Singh & Mitchell (1968). The stress function g(σ′) may be expressed with the reference to the stress level.

Similar work was conducted by Tian et al. (1994), the time-dependent deviatoric strain and strain rate could be described by the power law as in Equation 1.3 by Singh & Mitchell (1968) and Equation 1.5 by Tavenas et al. (1978). The evolution of deviatoric strain and strain rate with time indicated limited variations compared with the axial strain rates for two undisturbed marine sediments. Zhu (2007) proposed an empirical hyperbolic equation to fit the development of deviatoric strain with time:

$$\dot{\varepsilon_d} = \frac{\eta}{M-\eta}\frac{a_1^2 a_2}{(a_1+a_2 t)^2} \tag{1.6}$$

where M is the slope of critical state line and η is stress ratio; a_1 and a_2 are soil parameters.

Although a number of investigations on drained creep have been made, indeed that equation proposed by Singh & Mitchell (1968) has been commonly used, but mainly by the axial strain versus time of soil without acceleration creep in undrained creep. The quantitative empirical expression for the evolution of creep strain with time is still limited, especially the volumetric characteristics in overconsolidated range, still need to be characterized.

1.1.3 Other creep tests

The stress states in actual projects are much more complicated than the one-dimensional and triaxial stress state. Therefore, it is necessary to perform some creep tests within other stress condition, especially under complex stress, such as unconventional laboratory test and field tests.

1.1.3.1 Direct shear creep test

Tests under direct shear are widely used in geotechnical laboratories. The special condition in which shear of soil structure is possible to be reviewed under direct shear. If the drainage conditions are maintained properly, the test results can be consisting with those obtained from compressive tests in triaxial apparatus (Maslov, 1935).

General procedure of this test on soil can be divided into the two parts: the first part is the application of stress for the consolidation of soil; after (the primary) consolidation during which the pore water pressure is supposed to dissipate, shear is gradually applied.

Under a constant shear stress τ, the general shear strain γ and time curves within direct shear creep test is shown in Figure 1.15, where the primary, secondary and tertiary parts of direct shear creep are illustrated as OA, AB and BC segments. Results of Meschyan (1995) showed that under lower shear stress mobilization τ/τ_f (where τ_f is the shear strength of the tested soil); only primary creep phase was observed. The secondary creep phase was recorded with shear mobilization was 0.5- 0.9 with up to 60% of deformation occurred in the primary phase. The τ/τ_f - γ curves can be approximated by a bilinear diagram, as suggested by Geuse & Tjong-Kie (1953). Luo & Chen (2014) performed direct sheer creep on a marine sediment and found that γ increased with τ, when τ was increased to a peak strength, the soil was damaged in quite short time. The direct shear creep failure was mainly controlled by shear stress rather than the accumulation of shear strain. Similar tendency was obtained by Zhu et al. (2014).

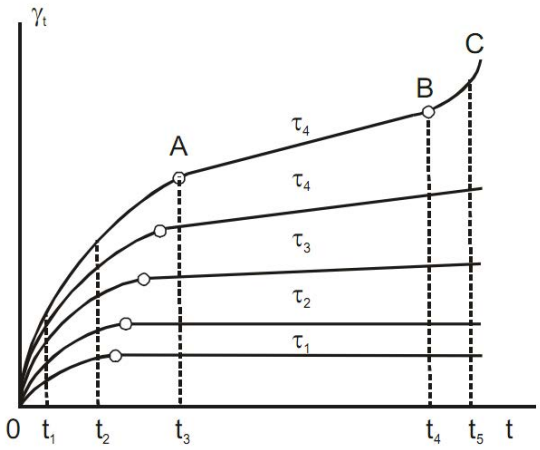

Figure 1.15 Shear strain γ and time curves under different shear stress τ in direct shear creep test (Meschyan, 1995)

Although the direct shear creep test is easy to operate, its shortcomings are also obvious. Within the direct shear condition, the shear failure surface is artificially fixed by the shear boxes, rather than the weakest damage surface of the specimen. Moreover, the shear stress distribution on the shear plane is not uniform, the drainage condition is hard to control as well as the measurement of pore water pressure, thus, limited investigations on creep behavior of soil by direct shear test have been made.

1.1.3.2 Pressuremeter creep tests

A pressio-triax creep test is performed by setting a cylindrical pressuremeter vertically into the tested material, pressure is applied into the pressuremeter resulting in the expansion of the surroundings film. Thus, the surrounding material is compressed and deformed under the stress transferred from the expanded film. The mechanical properties can be obtained through the relationship between the applied pressure and deformation of tested material.

Several methods based on pressuremeter testing have been proposed to determine the creep properties of frozen soils (Baguelin et al.,1978; Ladanyi & Johnston,1973; Kjartanson et al. 1988; Bahar et al. 1995). A research team of Hicher (Rangeard et al., 2003; Yin, 2006, Yin & Hicher, 2008) developed a laboratory pressio-triax apparatus for soils with better controlling of boundary conditions and soil uniformity than the general tightly controlled laboratory conditions by Zentar (1999) and Rangeard (2002). The pressuremeter test conditions can be reproduced in a triaxial cell, one special function is that the evolution of pore water pressure along the hole of pressuremeter

can be detected. The radial displacement along the pressuremeter wall can be measured within a constant side pressure, as well as the variation of pore pressure caused by the expansion of pressuremeter cell.

Experimental results on Saint-Herblain clay by Yin & Hicher (2008) revealed that under the constant radial stress, the radial displacement increased fast in the beginning, accompanied by a rapid decrease of pore water pressure. Afterwards, a stable tendency was obtained on both radial displacement and pore water pressure. Values of the parameters obtained from pressuremeter tests agreed with those obtained from triaxial and oedometer tests.

1.1.3.3 Rheometer creep test

The application of rheometer techniques in soil mechanics is uncommon, but they have key advantages: short test time, small size of samples and simple specimen preparation. The rheological approach is based on a mixed behavior of elasticity, viscosity and plasticity (Ghezzehei & Or, 2001).

In soil creep analyses by rheometry, the soil and its structure are possible to be changed in a certain constant stress states. The rheometer creep test on Mio-Pliocene clay performed by Kaczmarek (2016) showed that all the 3 creep stages were identified as in triaxial creep test. Soil strength during single stage rheometer creep process was reduced to 35% with respect to that under steady state stress; however, soil tended to be more resistant to shear stress in multi-stage creep, which might be resulting in shortening of the distance between clay particles and bond formation in soil structure. Similar as the direct shear creep test, one of the main disadvantages of rheometer technique is the lack of pore pressure control.

1.1.4 Field creep tests

In order to study the field characteristics of clay creep, a number of field measurements of time-displacement investigations have been made, for different structures and natural slopes. A classical one is the differential settlement of the Tower of Pisa in Italy, the tower settled about 1.5 meter and tilted to one side with an inclination of 5.5 degrees over 600 years and the settlement is still continued. The long-term settlement of buildings was also recorded by Feda (1992). He found that up to 60% of the total settlement were detected after construction, and the settlement was not

stabilized after 40 years of measurements. Thus, the forecasted settlement of structural building would be very inaccurate if the time-dependent compression of soil foundation was neglected.

Many experimental test embankments were constructed during the last century, among which the most famous are highway embankments at New Liskeard (Raymond, 1965), Sackville embankment in Canada with geo-reinforced (Rowe & Hinchberger, 1998), the Gloucester embankment in UK (Hinchberger & Rowe, 1998) and the Murro embankments in western Finland (Karstunen &Yin, 2010; Yin et al., 2010; 2011). The field test data show globally that: the long-term settlement of embankment is far greater than that just after construction; excess pore water pressure will exist in the embankment within quite a long time after the construction if the pore pressure is not allowed to dissipate quickly because of restricted drainage condition.

In addition, the long-term settlements of soil foundations of metro, especially soft and high compressibility soil foundations of tunnels, are also remarkable. Based on numerous investigation on the measured date of long-term settlement of tunnels, Shirlaw (1995) concluded that the long-term settlement took up to 30%-90% of the total settlement. Research of O'Reilly et al. (1991) confirmed this conclusion through a 11 years' observation Grimsby tunnel in British. Apparent settlement of metro foundation in Shanghai was also found during 10 years of operating (Cui &Tan, 2014).

As illustrated by the above filed examples, the creep deformations of clays are generally in unneglectable magnitude and often continue for tens even hundreds of years. The extrapolation tests on experimental and structural interpretation of the time-dependent behavior of clay are still needed.

1.2 Shear dilatancy/contractancy related to creep

The experimental investigations on time-dependency behavior of clay aiming at mainly characterizing the stress-stain-time evolution, and then incorporating into constitutive model to fit and to predict its development. Shear dilatancy/contractancy (plastic flow or hardening plasticity) is an important characteristic and the basis for the constitutive model of soil. The relationship of shear dilatancy/contractancy for sands has been investigated by many researchers (Bishop & Henkel, 1957; Murayama et al, 1984; Mejia et al.,1988). However, few researches have been performed on clay, especially the time-dependency of shear dilatancy/contractancy.

1.2.1 Typical shear dilatancy/contractancy equations

Physical performance of shear dilatancy was first discussed by Reynolds (1885), Rowe (1962) and Roscoe et al. (1963) introduced two critical dilatancy equations.

The equation proposed by Rowe (1962) assumed the rate of increment of input energy and increment of output energy was constant, which could be expressed with variables in soil mechanics under critical state, being

$$\frac{d\varepsilon_v^P}{d\varepsilon_d^P} = \frac{9(M-\eta)}{3M-2M\eta+9} \tag{1.7}$$

Where $d\varepsilon^P_v$ and $d\varepsilon^P_d$ are the increment of plastic volumetric and deviatoric strain, respectively. M and η are the slope of critical state line and stress ratio as in Cam Clay Model.

Roscoe et al. (1963) proposed a dilatancy equation based on dissipation of stress energy, i.e., the plastic incremental equals to the dissipation of friction energy, which consists with the plastic flow rule proposed by Schofield & Worth (1968), being

$$\frac{d\varepsilon_v^P}{d\varepsilon_d^P} = M - \eta \tag{1.8}$$

Another widely used dilatancy equation was proposed by Roscoe & Burland (1968) in developing the Modified Cam Clay Model, being

$$\frac{d\varepsilon_v^P}{d\varepsilon_d^P} = \frac{M^2-\eta^2}{2\eta} \tag{1.9}$$

Wheeler et al. (2003) propose an dilatancy equation develop in anisotropic constitutive model, being

$$\frac{d\varepsilon_v^P}{d\varepsilon_d^P} = \frac{M^2-\eta^2}{2(\eta-\alpha)} \tag{1.10}$$

Where α is a measure of the degree of plastic anisotropy of the soil, with $\alpha = 0$ the soil behaviour is isotropic and Equation 1.10 corresponds to the Modified Cam Clay yield curve in Equation 1.9.

1.2.2 Evolution shear dilatancy/contractancy during creep

The experiments show that the nature of creep strains is similar to that of plastic strains. They may be predicted from the framework provided by the hardening plasticity theory (Lade & Liu, 1998).

As discussed in Section 1.1.2.2, deviatoric creep is often accompanied by volumetric creep, the rate of volumetric to deviatoric during creep thus follows a plastic dilatancy rule as well.

Walker (1969c) investigated the time-dependent interaction of these two coponents in multi-stage drained triaxial creep tests on normally consolidated kaolinite. Followed by an instantaneously increase of deviatoric stress, an immediate increase was detected for ε_d accompanied by a constant ε_v (section AB in Figure 1.16a). Afterwards, under the constant deviatoric stress, the primary compression (controlled by the dissipation of pore pressures) and then the secondary compression (creep) were observed, shown by section BD and DE in Figure 1.16a, separately.

The linear relation tendency of $d\varepsilon_v/d\varepsilon_d$ implied that the dilatancy rule was time-independent, which was similar to the dilatancy rule described in Section 1.2.1. Moreover, the strain increment ratio decreased with increasing stress ratio as shown in Figure 1.16b. A linear relationship of between ε_v and ε_d was proposed by Sekiguchi (1973) through drained incremental creep tests on normally consolidated Fujinomori clay

$$\frac{d\varepsilon_v}{d\varepsilon_d} = 1.21 - 0.77\eta \tag{1.11}$$

The linear relation of $d\varepsilon_v/d\varepsilon_d$ during creep was confirmed by Tian et al. (1994) through drained creep tests on marine sediments at lower stress level, while piecewise linear relation was detected at higher stress level emphasizing a significant magnitude of microstructural adjustments.

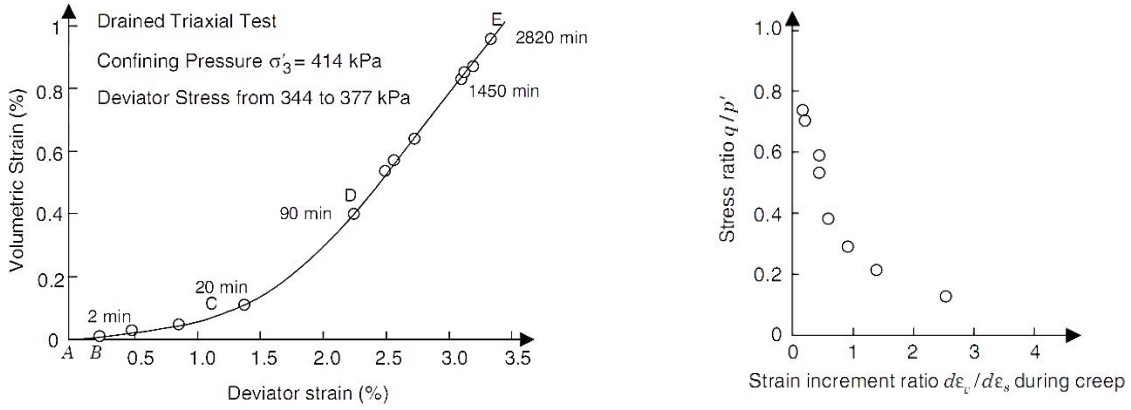

(a) (b)

Figure 1.16 Dilatancy relationship obtained from drained creep test on kaolinite: (a) evolution of volumetric strain and deviatoric strain with time; (b) effect of stress ratio on strain increment ratio (Walker, 1969c)

Wang &Yin (2015) performed undrained triaxial creep tests on K_0-consolidated and isotropically consolidated samples of marine clay with different stress levels. They demonstrated

that the dilatancy Equation 1.7-1.10 can describe the stress-dilatancy relationship during undrained creep. The authors also proposed a modified dilatancy equation with the inclination of potential surface

$$\frac{d\varepsilon_v^P}{d\varepsilon_d^P} = D * f(M,\eta) \tag{1.12}$$

Where D is a material constant as used in dilatancy equations for sand (Jefferies, 1993; Gajo & Muir Wood, 1999).

Yin et al. (2013) reproduced the results of drained triaxial creep tests on normally consolidated Hong Kong marine sediments performed by Zhu (2007) and pointed out that dilatancy rule was not always time-independent. It can be seen in Figure 1.17 that the values of strain increment ratio $d\varepsilon_v/d\varepsilon_d$ decrease with increasing of stress ratio, which consists with the tendency described in Equation 1.7-1.10. Nevertheless, the values of $d\varepsilon_v/d\varepsilon_d$ are constant in creep condition based on these equations, which conflicts with the fluctuating curves. The time-dependent curves in Figure 1.17 confirms that the anisotropy may be induced along the evolution of plastic strain (Yin & Chang, 2009; Yin et al., 2013). Further theoretical analysis and experimental verifications are still needed to accurately summarize its evolution.

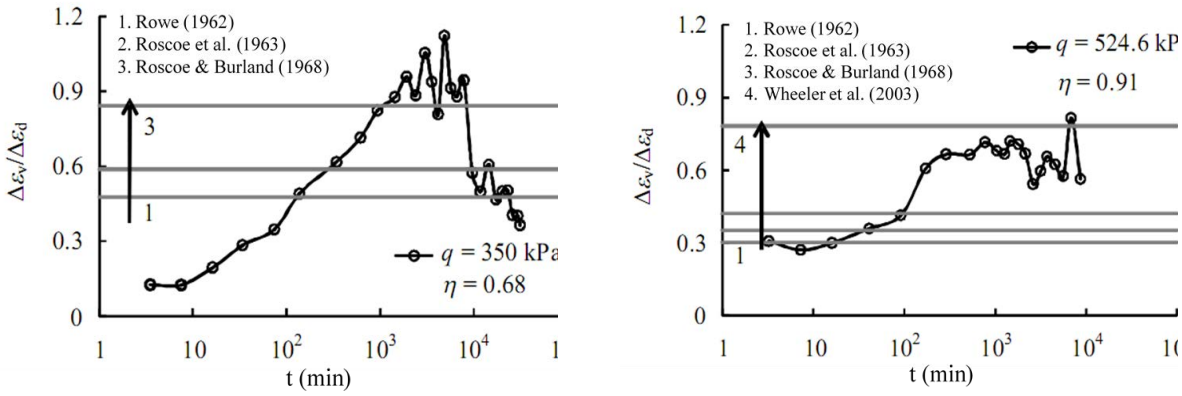

(a) (b)

Figure 1.17 Evolution of plastic strain increment ratio with time during drained creep under different stress conditions: (a) η=0.68; (b) η=0.91 (Yin et al.2013)

1.3 Micro approach to creep of clay

Microstructural investigations are increasingly used for a better understanding of the macroscopic behavior and physical properties of clay. The microstructure of clays has been studied

by many researchers (Diamond, 1971; Moon, 1972; Collins & McGown, 1974; Sergeyev et al., 1980; Griffiths & Joshi, 1990; Hattab et al., 2010). These studies involve the determination of the properties of clays at microscopic level and analyzing in the arrangement and distribution of particles, particle aggregates and pores, as well as their contact and connectivity under different stress conditions. Microscopic research in the time-dependency of clay is supplemental important to understand the creep mechanism that hides behind the macro stress-stain-time behaviors.

1.3.1 Structural mineralogy of clays

Mineralogy is the primary factor that controls the size, shape, and properties of soil particles. A priori knowledge to the minerals in soil may provide a direct insight into its behavior. It is already known that clayey soil consists of mixed groups of minerals, primarily hydrous aluminum silicates, whose sizes are usually less than 2μm (Lambe & Whitman, 1969; Velde, 1995; Mitchell, 2003; Sparks, 2003). Introductions thus starts progressively from the atomic structure to crystal then to particle and its aggregations of typical clay minerals in the following.

1.3.1.1 Atomic structure and bonds

An atom may be simplified represented by a small nucleus surrounded by diffuse concentric of electrons clouds. Based on the localization of bonding electrons in space, the inter-atomic bonding can be divided into 3 categories: covalent, ionic, and metallic (Mitchell, 2003; Pacios, 1991; Gould et al., 2008).

The combination of ionic and covalent bonding is typical in most non-metallic solids. For instance, the inter-atomic bond in silica (SiO_2) is about half covalent and half ionic, and silicate minerals are the most abundant constituents of most soils (Schulten & Schnitzer, 1997).

Besides the strong ionic and covalent bonding, a weaker secondary bonds are usually formed, which probably are sources of attraction between very small particles as well as between liquids and solid particles (Horowitz &Trievel, 2012). Two typical secondary bonds are the hydrogen bond and Van der Waals bonds (Mitchell, 2003):

Hydrogen bond: if the hydrogen ions form the positive side of the dipole, then its attraction to the negative end of the adjacent molecule is called the hydrogen bond. Hydrogen bonds are important in determining the interaction between soil particle surfaces and water.

Van der Waals bonds: fluctuating dipole bonds exist commonly termed as van der Waals bonds. Since the van der Waals bonds are non-directional and additive between atoms, consequently, when there are large groups of atoms they decrease less rapidly with distance than hydrogen bonds. The van der Waals bonds are strong enough to determine the final arrangements of groups of atoms in some solids, and they may be responsible for small cohesions in fine grained soils.

1.3.1.2 Crystal structures and bonds

A crystal is a homogeneous body bounded by smooth surfaces, which are the external expression of the internal atomic arrangement. The soil particles, which are the maximum proportion of soil solids, are composed of mineral crystals. Structure characteristics of crystal are used to distinguish different groups of minerals. The crystal structures do not organized by chance but in a way with stable arrangement of atoms in a crystal which minimizes the energy. Figure 1.18 gives some possible arrangements of silica tetrahedral in silicate mineral structures (Gillott, 1968). Many of the clay minerals contain silica in a sheet structure, and framework silicates are most common in quartz.

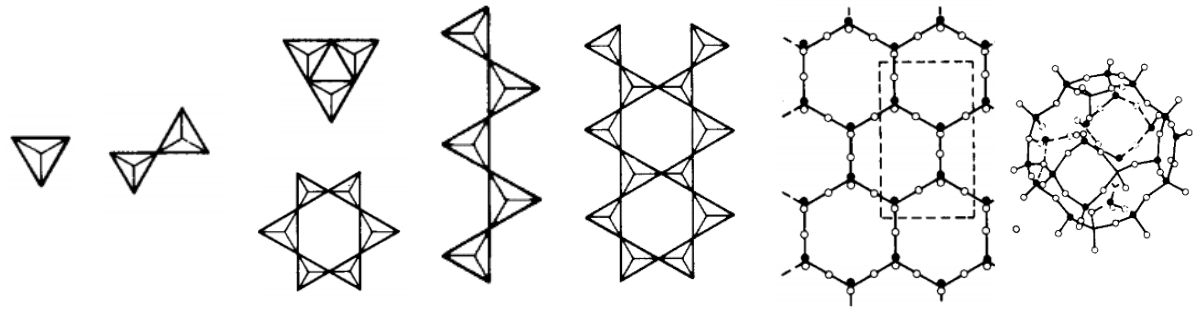

Figure 1.18 Silica tetrahedral arrangements in different silicate mineral structures (Gillott, 1968)

The sheets structure, consists of tetrahedral and octahedral units of oxygens and silicons, oxygens and aluminum etc., respectively (Grim, 1962), stack to form layers that combine to produce the different clay mineral groups (Figure 1.19).

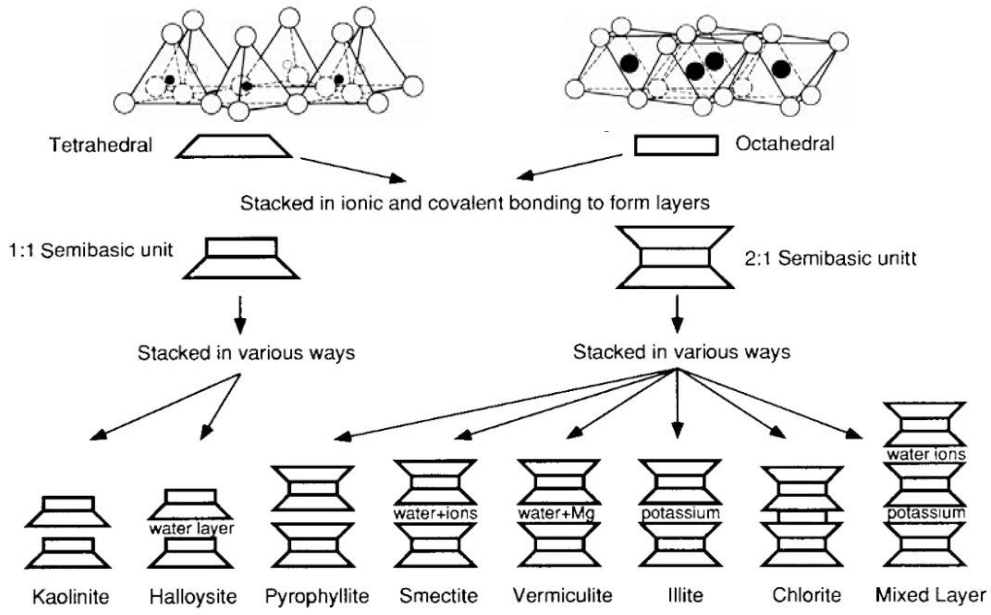

Figure 1.19 Synthesis pattern for the clay minerals (reproduced after Mitchell, 2003)

Bonding between tetrahedral and octahedral sheets is very strong, but the bonds connecting the unit layers together are different and may be vulnerable to changes in environmental conditions, such as changes of water content, type and concentration of aqueous solution (Marshall, 1964; Evans & Guggenheim, 1988; Mitchell & Soga,2005).

1.3.1.3 Morphology and surface area

Most common clay minerals are in shape of flake, lath, needle and 2 μm in size (Velde, 1995). Figure 1.20 shows the electron photomicrograph of clay minerals. The well-crystallized kaolinite particles (Figure 1.20a) are six-sided plates and often group into large crystals which may reach up to 20 μm (Beaufort et al., 1998). The tubes of halloysite (Figure 1.20b) range in length from one micrometer to several micrometers, and drying of halloysite may result in splitting or un rolling of the tubes. Montmorillonite (Figure 1.20c) tend to form smaller crystals with average crystal size in less than 0.5 μm; well-crystallized illite (Figure 1.20d) may have a hexagonal outline and usually occurs as very small, flaky particles mixed with other clay and non-clay materials.

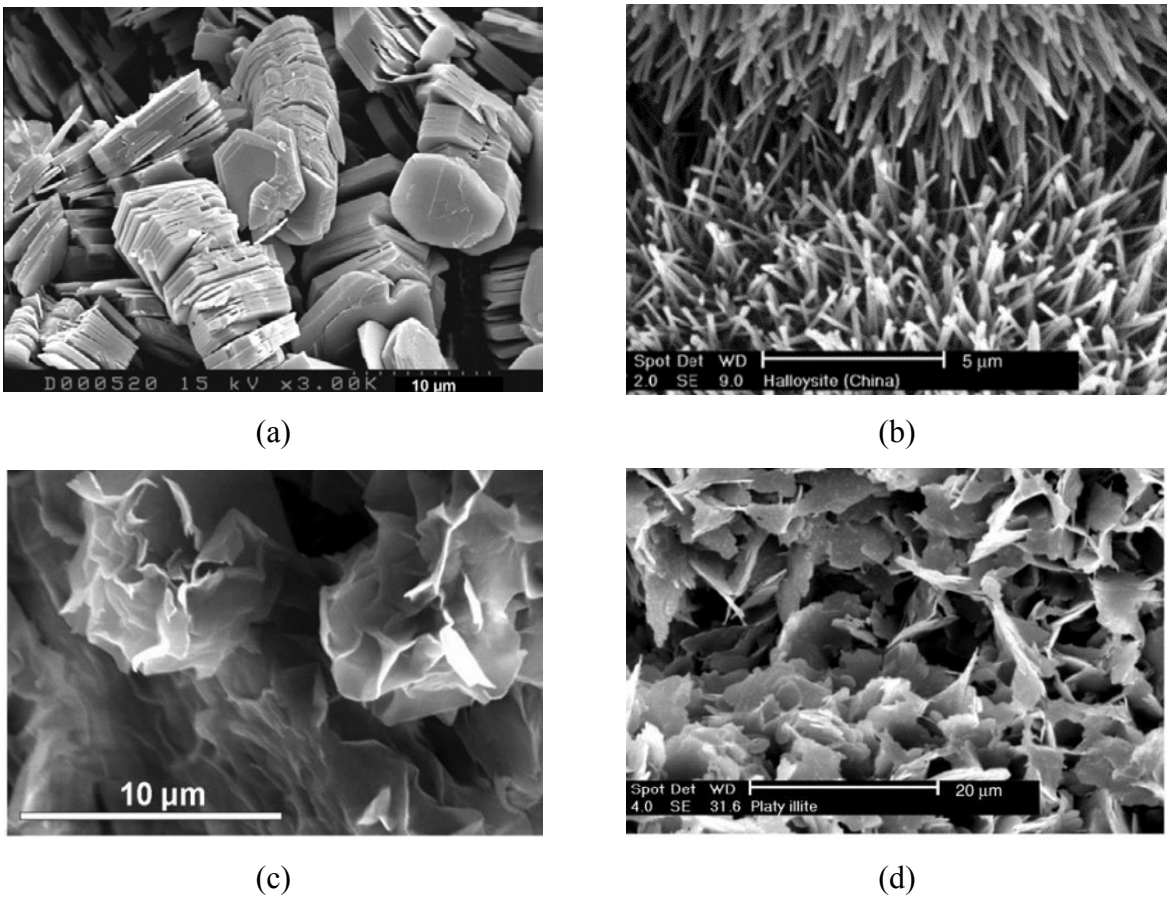

(a) (b)

(c) (d)

Figure 1.20 Electron photomicrograph of clay minerals: (a) crystals of kaolinite (Wilson et al.,2014) (b) tubular crystals of halloysite (Christidis, 2011) (c) subhedral montmorillonite crystals (Fesharaki et al., 2007) (d) flaky illite crystals (Christidis, 2011)

However, even in the same mineral group, the shap of crystal may changes. For example, the kaolin group minerals form euhedral to hexagonal crystallites (Pruett & Murray, 1993; Beaufort et al.,1998), and tubular, spherical or flake in halloysite (Giesse, 1988).

For clay minerals, the small crystal size resulting in a large specific surface area both in external and internal. The large specific surface area creates significant degree of surface reactivity, which can be increased by acid activation (Myriam et al.,1998; Nguetnkam et al., 2005).

1.3.1.4 Clay mineral aggregates and pores

After the recognizing of the formation, size, shape and structure of clay minerals, a following research can be the arrangement of the solid particles, which together with the associated pores, constitute the structure of a soil.

The common arrangements of clay mineral may be from simple to complex in forms of layers (particles), aggregates and clusters (or assembly of aggregates) (Bergaya & Lagaly, 2006). Due to the aggregation of particles, all clay minerals are therefore porous, including pores of varied sizes and shapes (Figure 1.21).

Generally, the void of clay refers to the void of particles, which is the sum of interparticle void and the interaggregate void. When soil is subjected to stress or shearing, the soil particles are recombined or dislocated, i.e., the microstructure changes of the soil. Therefore, the shape and/or size of one or more of the three types of pores will change (Yin et al.,2013).

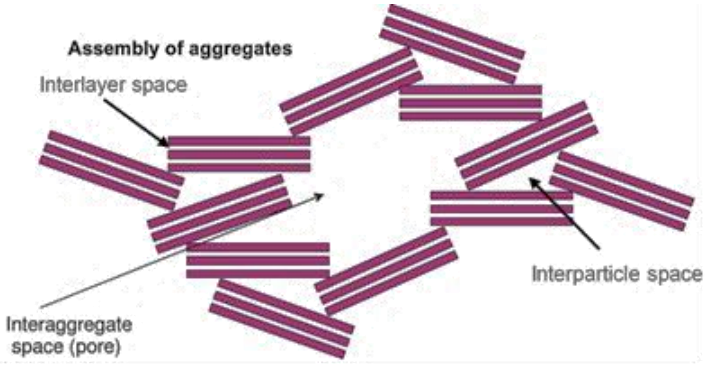

Figure 1.21 Aggregates of clay mineral particles and pores (after Bergaya & Lagaly, 2006)

1.3.1.5 Plasticity and viscosity

The clay particle is surrounded by water molecules adsorbed on the clay mineral surfaces by double electronic layer film (Figure 1.22a), which gives the nature of plasticity for clays (Grimshaw, 1971). The clay particles are connected in different texture forms, which can deform by rotation of particles or shifting coherently under stress, and retain their shapes after unloading (Lagaly, 2006). The plasticity is increased by clay minerals, while non-clay minerals productive on the contrary. The plasticity of clays is comprehensive affected by the type of clay mineral, surface area of the clay particles and the arrangement of clay aggregates, as well as the water content (Grimshaw, 1971).

The water content can be critical for the development of plasticity, i.e., when water content is lower than the plastic limit, the clay particles contact resulting in the loss of plasticity; while a higher water content will lead to weak connection between water molecules and clay surface thus plasticity is reduced (Grimshaw, 1971). Therefore, the plasticity limit can be used for classification of different clay minerals (Figure 1.22b).

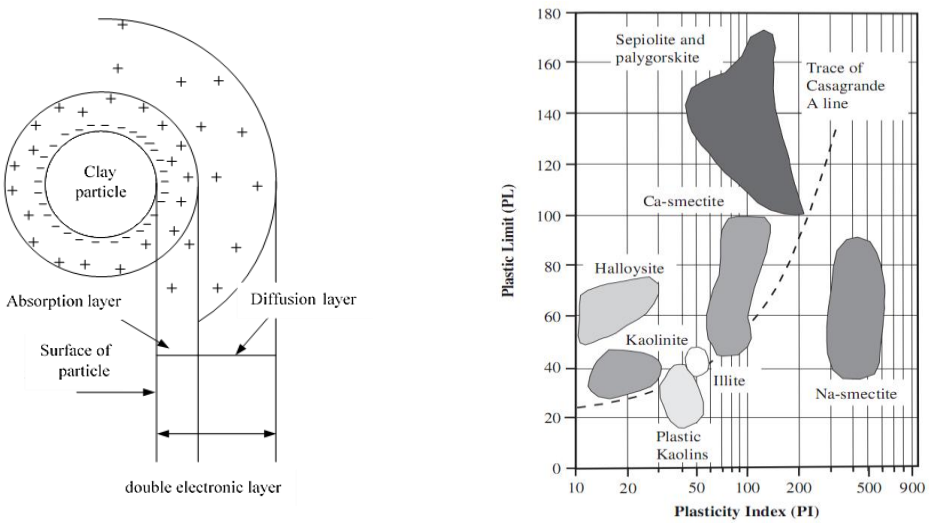

(a) (b)

Figure 1.22 Plastic charatcteristic of clay minerals: (a) double electronic layer of clay particle (Yin et al., 2013) (b) identification of clay minerals using plastic parameters (Christidis, 2011)

Viscosity is generally defined as the resistance of fluid to deform or flow under stress. Taylor (1942) pointed out that the structural viscosity of clay could be a plastic structural resistance to compression stress due to double electronic layers surronded by clay particles. As shown in Figure 1.22a, the absorption layer contains cations and anions, which makes the water layer exhibit electro-chemical properties (Sridharan, 2001; Reeves et al., 2006).

The water absorbed within microstructure of clay is generally formed in 3 types (Figure 1.23): (1) water held on mineral particle surfaces; (2) the double layer water; (3) capillary water held in micro and macro pores between clay particles. The water held on mineral surfaces can be considted in solid state, which will be changed with the distance to the mineral surface (Winkerkorn, 1943). In addation, the viscosity of double layer water was considered higher than that of free water in pores, and the viscosity of double layer water was found to be increased when close to the clay surfaces (Grim,1962).

Except for distance factors, the viscosity of adsorbed water can also be affected by tempreture. According to Grim (1962), when soil was heated above the room tempreture, the adsorbed water and free water in micropore were removed. Moreover, the interlayer water in montmorillonite minerals could be completely removed when the temperatures in over 100˚C, while clay mineral structure could be altered or destroyed by heating over 400˚C.

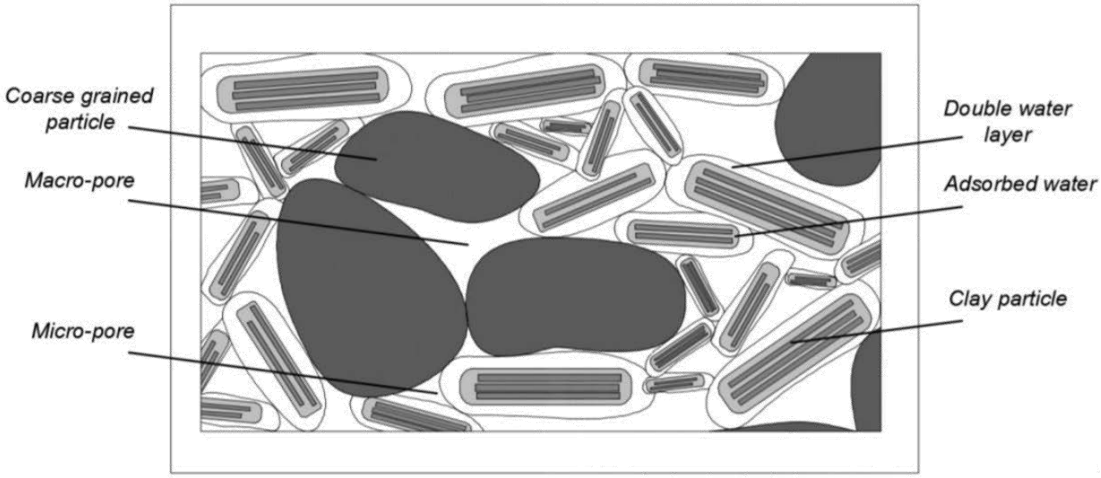

Figure 1.23 Clay-water system (Kaczmarek & Dobak, 2016)

1.3.2 Methods for identification of clay microstructure

Technique methods are of the same importance for the microstructure research of material as the theoretical knowledge presented in Section 1.3.1. Thus, some commonly used methods in literatures are presented here.

1.3.2.1 X-ray diffraction

X-ray diffraction (XRD) is the most widely used method for identification of minerals and crystal structure of fine-grained soils. The wavelength of X-rays varies from 0.01 to 100 Å, where the wavelength of 1Å is about the same magnitude of atomic plane space in crystalline material. When high-speed X-ray strike a crystal, the scattered intensity was found to be a function of incident angle, the wavelength and polarization.

Figure 1.24 shows a parallel X-rays beam striking a crystal at an angle which parallels to the atomic planes spaced at distance *d*. The wave reflected from A is supposed to be reinforced by the wave reflected wave from C, then the path length difference between these two waves (BC+CD) should be an integral number of wave lengths nλ, with $BC=CD=d\sin\theta$, thus, the Bragg's law is verified:

$$2d \cdot \sin\theta = n\lambda \tag{1.12}$$

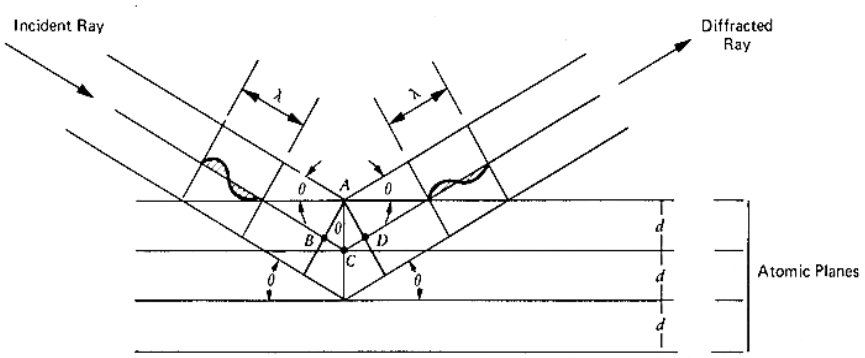

Figure 1.24 Geometrical conditions for X-ray diffraction according to Bragg's law

The stereoscopic spacing of inter-atomic planes of different minerals are different, the angle at which the diffractions occur are different, thus XRD can be used to identify different types of minerals (Whittig & Allardice,1986). Soils containing only two or three well-crystallized mineral components are easier analyzed than those with multimineral compositions. Some non-clay minerals, includes feldspar, quartz, and carbonates, can also be identified by strong X-ray diffraction reflections (Brindley & Brown,1980).

The application of XRD in clay is made by powder method and of oriented aggregates of particles rather than of single crystals because difficulties in manipulating with single small particle. (Carroll, 1970; Moore & Reynolds,1997), to determine the phase composition, epitaxy, preferred orientation and other structural properties.

1.3.2.2 Optical and electron microscope

The orientations of clay group particles can be studied by binocular and petrographic microscopes.

While the research of thin section of soil greater than a few hundreds is difficult because the observed field will be out of focus sharply as magnification increases. Thus, identification of single clay particle is impractical using an optical microscope. The optical microscope method works better on silt and sand grains. Cady et al. (1986) gave relatively simple diagnostic criteria for identify over 80% of coarse grains in most soils, by color, refractive index, cleavage, and particle morphology.

The properties of surface textures and coatings, decomposition layers and so on identified by optical microscope are useful both for understanding of the soil history, as well as for guiding the soundness and durability of the particles.

With the development of technology, the study of single particle is possible with modern electron microscopes, which can resolve distances less than 100 Å. Electron diffraction is similar to X-ray diffraction except an electron beam instead of an X-ray beam is used. One advantage of electron diffraction over X-ray diffraction is that the specimen does not need to be single crystal or even polycrystalline powder.

Based on operating principle, the electron microscopes can be classified as: transmission electron microscope (TEM); scanning electron microscope (SEM); environmental scanning electron microscopes (ESEM). A general disadvantage of electron diffraction is that the sample largely has to be viewed in vacuum, because the molecules that make up air would scatter the electrons. An exception is liquid-phase electron microscopy (De Jonge & Ross, 2011) using either a closed liquid cell or an environmental chamber. For example, in the ESEM, which allows hydrated samples to be viewed in a low-pressure (up to 20 Torr) wet environment. Various techniques for in situ electron microscopy of gaseous samples have been developed as well (Gai & Boyes, 2009).

1.3.2.3 X-ray microtomography

X-ray tomography is originally used in medical radiography for obtaining a slice through the body (Hounsfield, 1973; Swindell & Barrett, 1977). X-ray microtomography (or X-ray CT) is a radiographic imaging technique that can produce 3D images of the internal structure at a spatial resolution, which process is schematically illustrated in Figure 1.25. The specimen is rotated about a single axis and is scanned by computed tomography, thereafter, a series of 2D X-ray absorption images are obtained. A 3D digital image is produced using mathematical principles of tomography on this series of images, displayed as a series of 2D slices. The 3D internal structure can be inferred from the images based on the relationship between X-ray absorption and material density, thus a virtual model is recreated without destroying the original sample.

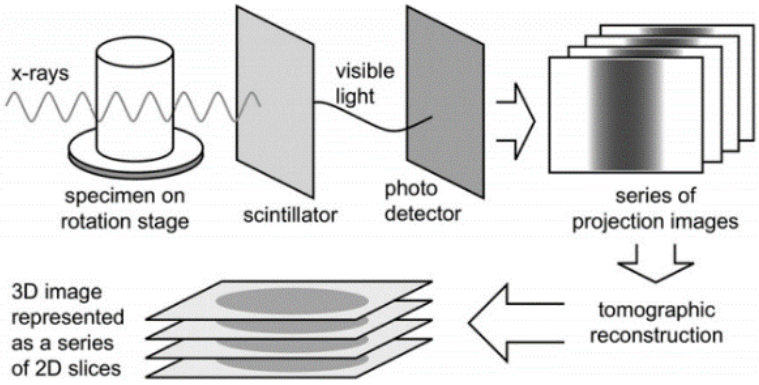

Figure 1.25 Schematic illustration of X-ray tomography acquisition and reconstruction process (Landis & Keane, 2010)

In the application of X-ray microtomography, the relations between the external load, specimen deformation and damage, and internal specimen damage are followed. Since the resolution of CT devices ranges in a few μm (Brunke et al., 2008), it is particularly suitable for studying sandstones, soils, or rocks with large particles and less suitable for the characterization of clay particles (Landis et al, 1999; Lenoir et al., 2007). However, the local crack is still possible to be detected in clay. The fractures and continuous cracks due to expansion of gas bubbles in marine clays through X-ray CT by Yang et al. (2010). Kaufhold et al. (2016) founded that within a clay-rich shear failure area, there was a so-called mylonitic zone of two main fractures, in which the clay particles were reduced and were pulled apart from the original matrix and rearranged near the surface by X-ray CT and SEM (Figure 1.26).

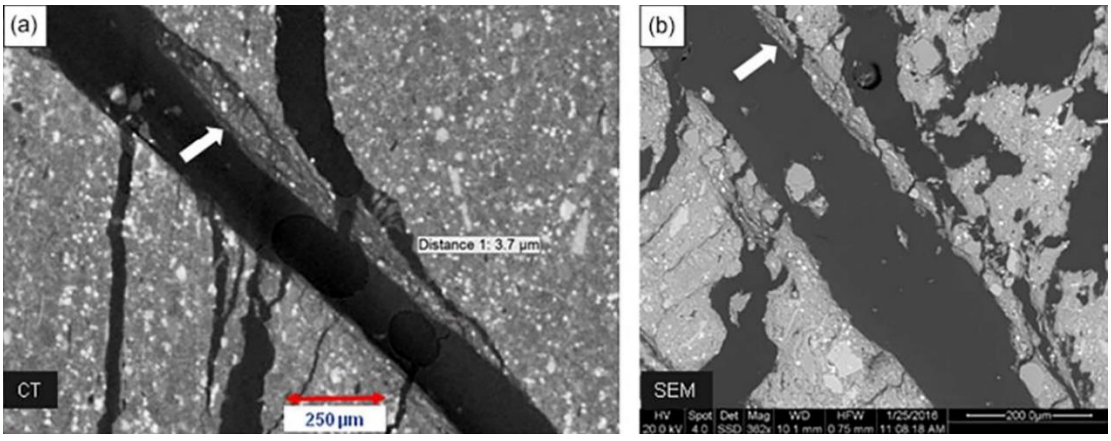

Figure 1.26 Magnified view of the shear failure: (a) X-ray CT image (b) SEM image (Kaufhold et al.,2016)

The limitations for X-ray microtomography include the penetrating ability of the X-rays relative to the sample density, and very high-energy X-rays or very small specimens is required for dense material. Additionally, the method suffers when the material phases have large differences in X-ray absorption, and within the less absorptive phases the images will have very poor contrast.

1.3.2.4 Pore size distribution

The pore size distribution of soil relates to soil properties in a complex and useful way, it indicates complexity of structure far more than porosity itself. Large pores can be associated with both large particles but also clays aggregation (Nimmo, 2013).

The pore size distribution (PSD) analysis can give supplementary pore volume information in addition to 2D mage information of soil, and has been under numerous investigations on clays. Moreover, the PSD curves were founded to be related to the states of clay, for example, natural or remolded, saturated or unsaturated. Oualmakran et al. (2016) found that the under saturated conditions, the pore size distribution varied more significant with loading. The unimodal PSD curves were identified on some remolded clays by Penumadu & Dean (2000) and Hammad (2010). However, the bimodal PSD curves were obtained in natural sediments and structured clays (Sun et al., 2016; Oualmakran et al., 2016).

1.3.3 Evolution of clay microstructure under different stresses

1.3.3.1 Evolution of clay particles

The most widely used investigations on particle orientation of clay is by means of SEM images. Hicher et al. (2000) assumed an ellipsoidal shape of the particle or aggregate based on the analysis of SEM images of a kaolinite and a bentonite, and proposed three parameters to describe the microstructural properties of clay:

- Shape index (or sometimes called aspect ratio), which represents the ratio between the length and width of the individual particles or aggregates element.
- The mean surface, assuming the element an ellipse.
- Particle concentration represents the number of individual particles by surface unity.

The orientation of the particles can be generally considered as the orientation of the main axis of the ellipse or particles with respect to the horizontal.

The general organized terms of clay particles are "flocculated" and "dispersed" (Collins & McGown, 1974; Prashant & Penumadu, 2007; Sachan & Penumadu, 2007). The "flocculated" describes the soil that has an open-ended structure with edge-to-face contacts or random orientation of particle platelets (Figure 1.27a); "dispersed" means a soil with closed structure which consists of face-to-face contacts or preferred orientation of particles (Figure 1.27b).

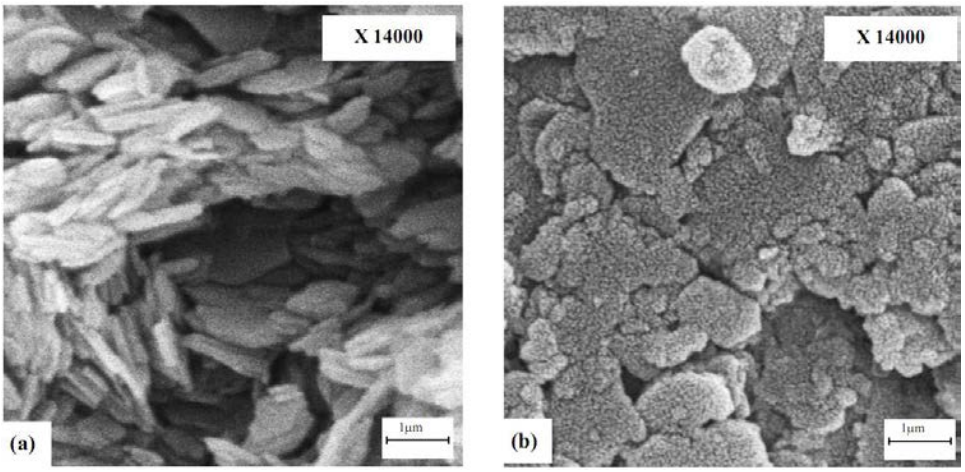

Figure 1.27 SEM images of a kaolin clay specimen with two extreme structures: (a) flocculated (b) dispersed (Sachan & Penumadu, 2007)

a) Direct shear stress path

Morgenstern & Tchalenko (1967) analyzed the effect of direct shear tests on specimens of kaolin using polarized light microscopy, and an obvious orientation of the clay particles in the direction of shear was observed.

b) Oedometric stress path

The clay particles tend to be oriented isotropically to the direction of deposit if it is hydrated. Under the one-dimensional compression, an induced anisotropy was developed with the loading (Pusch, 1970; Delage & Lefebvre, 1984; Hicher et al 2000; Mitchell, 2003). Hammad (2010) analyzed the orientations of clayey materials under oedometric path, and concluded that the initial oedometric loading would lead to a preferential orientation of the particles. Similar results were observed by Hattab& & Fleureau (2011) on Kaolin P300 after one-dimensional compression of 120kPa (see Figure 1.28). The clay particles were tending to orientate perpendicularly to the vertical compression stress.

Additionally, a breakage of the aggregates was found which leading to a more homogeneous size distribution. At large deformations, the big aggregates disappeared almost completely (Pusch, 1970; Hicher et al 2000). Following by the breakage of aggregates, the mean value of the particle concentration is increased with the increase of deformation.

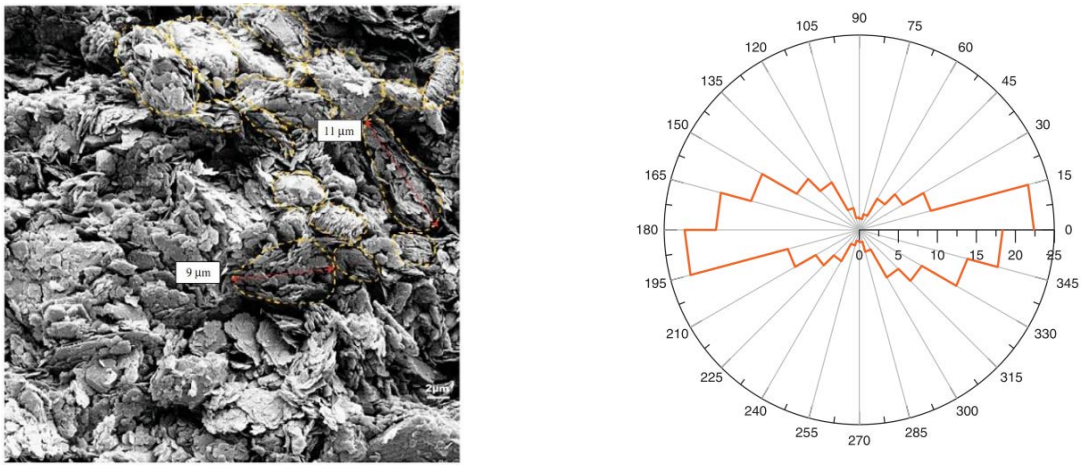

(a) (b)

Figure 1.28 SEM observation of kaolinite after one-dimensional compression at σ'_v=120kPa: (a) SEM photos on vertical plane (b) global rose diagram of angular distribution of the particles (Hattab& & Fleureau, 2011)

c) Isotropic stress path

Within the isotropic stress path, the structure of soil is supposed to be isotropic without preferential organization. The clays particles were rearranged in flocculated (face-to-edge) structure (Hicher et al. 2000 in Figure 1.29). The mean particles size is lower when subject to a higher maximum stress, which caused some aggregates to break. The studies by Bouziri (2007) and Hattab & Fleureau (2011) on kaolinite also shows a tendency toward isotropy after isotropic consolidation.

But this is not always true, Sivakomar et al. (2012) found that the particle orientation of reconstituted kaolin clay on isotropically path related to the loading history. Scanning Electron Microscope (SEM) images indicated that the monotonically compressed samples exhibited an anisotropic microstructure. Whereas the preferential orientation was destroyed when the kaolin slurry was first isotropically compressed to a low pressure and then completely remoulded.

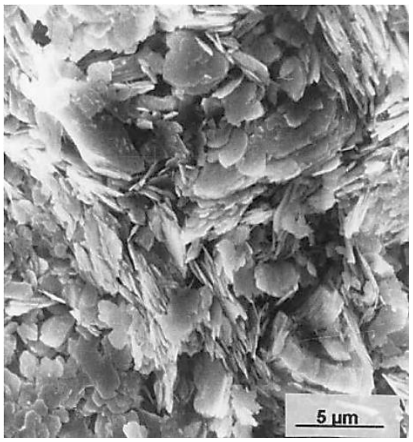

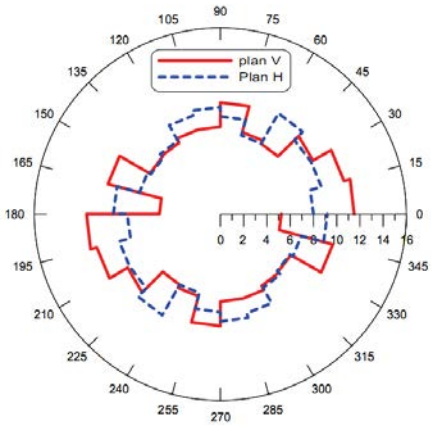

Figure 1.29 Structure of Kaolin P300 isotropically consolidated at 300 kPa (Hicher et al., 2000)

d) Triaxial stress path

The shear stress tends to orient the particles and the aggregates in a direction parallel to the shear direction, and the failure mode is the rotation and slip between clay units in the damage zone (Mckyes & Yong, 1971; Delage & Lefebvre, 1984; Kirby & Blunden, 1991; Sachan & Penumadu, 2009). Beyond the critical state, under a certain shear stress in triaxial test, the microstructure anisotropy of clay is usually observed. Bai & Smart (1997) observed an increase in the anisotropy of kaolin with strain, followed by a decrease on undrained axisymmetric triaxial paths. Hicher et al. (2000) reported the creation of structural anisotropy of normally consolidated and overconsolidated kaolin during drained loading using scanning and transmission electron microscope photographs. They pointed out that the mechanical behaviour is largely dependent on the changes that occur at the micro scale. Same conclusion was drawn by Dudoignon et al. (2001) on normally consolidated kaolinitic matrices during shearing.

Based on the orientation properties of a lightly overconsolidated kaolin clay in drained triaxial test, Hattab & Fleureau (2011) proposed two models of orientation:

- The **D** model that shows the structural isotropy of a fictional material. All the orientations are represented by the same percentage (see Line D in Figure 1.30b).

- The principal orientation mode (**P**) is a preferential orientation in which the percentage of orientation P is significant.

The strong anisotropy (**P** model) is observed under higher shear strain (Ob_3 in Figure 1.30). This phenomenon is considered to be linked, at the marcoscope scale, to the deviaotoric mechanism activation.

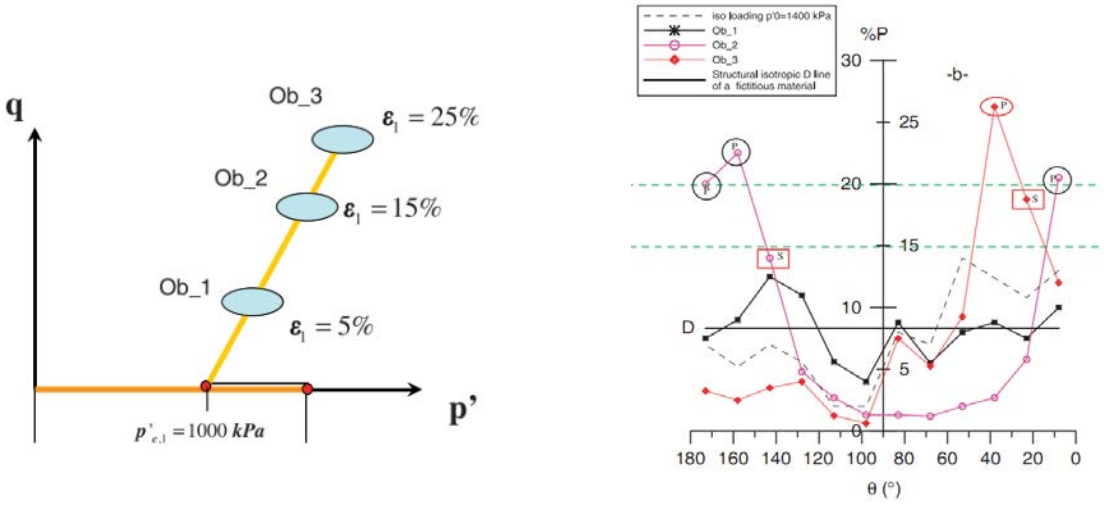

(a) (b)

Figure 1.30 Microstructural evolution of kaolin clay in triaxial test: (a) stress condition in (p′-q) stress plane (b) orientation modes under different stress levels (Hattab & Fleureau, 2011)

1.3.3.2 Evolution of pores

Delage & Lefebvre (1984) investigated changes in pores of a sensitive natural clay during one-dimensional compression. The results revealed that the interaggregate pores decreased in size and varied in shape after consolidation, whereas the intra-aggregate pores remained unchanged. The interaggregate pores that are perpendicular to stress became narrower (see Figure 1.31). Electron microscopy and mercury intrusion porosimetry studies conducted by Olsen (1962), Pusch (1970), Yong & Sheeran (1973), Griffiths & Joshi (1990), Shear et al. (1992) and Monroy et al. (2007). on clays after consolidation give support to the findings of Delage & Lefebvre (1984). Al-Mukhtar et al. (1996) pointed out that both the applied mechanical and hydraulic stress state conditions were related to the pore space variations. Based on the mercury porosimetry results for bentonite after one-dimensional loading, Hicher et al. (2000) noticed the progressive disappearing of the big pore family (around 8 μm) during mechanical loading. This corresponds to a simultaneously breakage of the biggest aggregates under the same mechanical conditions.

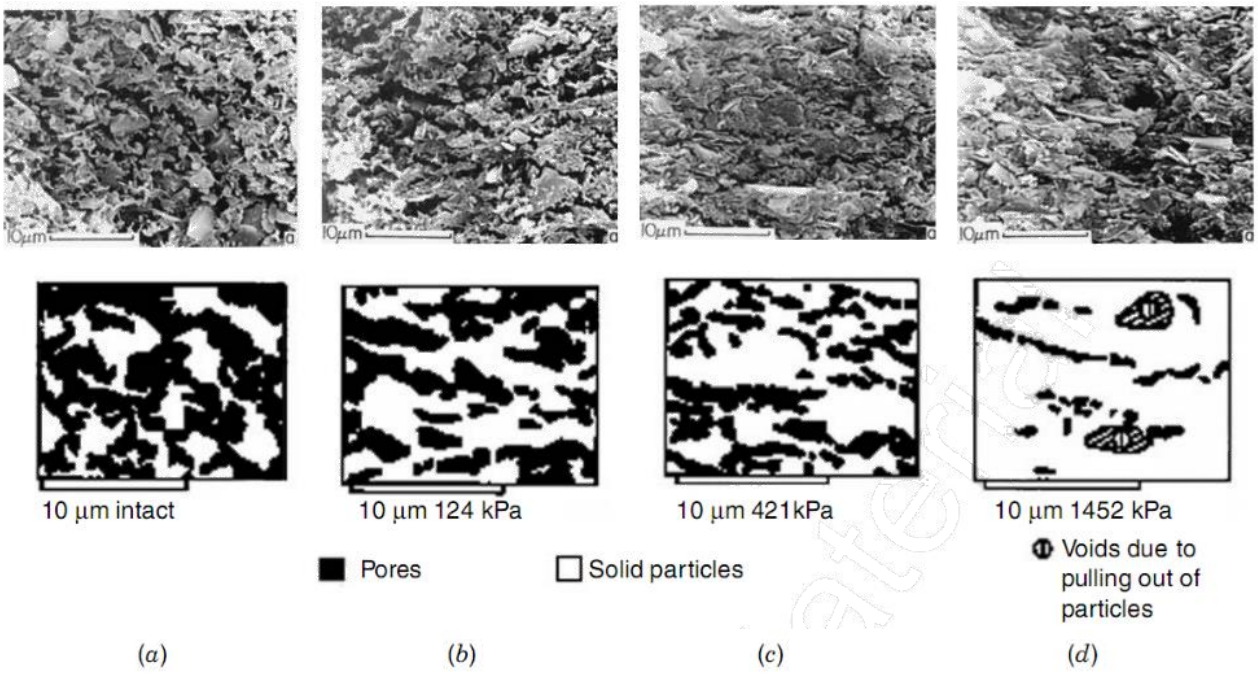

Figure 1.31 SEM photographs of a sensitive Champlain clay under consolidation at (a) intact state (b) 124 kPa (c) 421 kPa (d) 1452 kPa. The preconsolidation pressure of the clay is 54 kPa (Delage &Lefebvre, 1984).

1.3.4 Evolution of clay microstructure related to creep

The presence of clay particles in soils is one of the main reasons for soil creep deformation. Le et al. (2012) conclude that the causes of soil creep can be categorized into 5 groups, namely

- the breakdown of the inter-particle bonds;
- sliding between the soil particles;
- water flow from micro-pores to macro-pores;
- deformation due to the structural viscosity;
- deformation due to the jumping of bonds.

1.3.4.1 Breakdown of the inter-particle bonds

According to Taylor & Merchant (1940) and Terzaghi (1941), the compression processes including both primary and secondary (or creep) settlement are explained based on the transfer of stress and the rearrangement of soil particles. Under the effect of the applied stress, free water flows out of the soil element, resulting in the rearrangement of the soil structure. The contacts between particles gradually increase with the increase in the effective stress with time, causing

from the total stress transferring from pore water to the contacts between particles. Therefore, the bonds between particles may be broken or destroyed by the increase in the effective stress. The breakdown of bonds between soil particles may cause further rearrangement of soil particles, consequently further settlement or compression called creep (Taylor & Merchant, 1940; Terzaghi, 1941; Mesri, 1973, 2003; Crooks et al., 1984). Microscopically, creep is likely to occur in the weak clusters because the contacts in them are at limiting frictional equilibrium (Mitchell, 2003). Any small perturbation in applied load at the contacts or time-dependent loss in material strength can lead to sliding, breakage or yield at asperities.

1.3.4.2 Sliding between soil particles

Grim (1962) explained creep as the reduction in volume mainly due to slipping between soil grains, while primary consolidation is caused by squeezing out water with insignificant slippage between grains. The increase in bonding forces causes the increase in the frictional resistance of particles against slipping relative to each other. Therefore, the reduction in the volume during creep occurs slowly. Gupta (1964) pointed out that creep was caused by the relative sliding movement of clay particles under the external load. This relative movement between particles was delayed by the bonds of water molecules existing in adsorbed water layer, and can gradually cause the change in the orientation of soil particles. To examine the effects of particle rearrangement, Kuhn (1987) developed a discrete element model that considers sliding at interparticle contacts to be visco-frictional. The mechanistic representations of the contact normal and shear forces are shown in Figure 1.32. Small changes in the tangential and normal force ratio at a contact can have a very large influence on the sliding rate at that contact. These changes, when summed over all contacts in the shear zone, result in a decrease or increase in the overall creep rate.

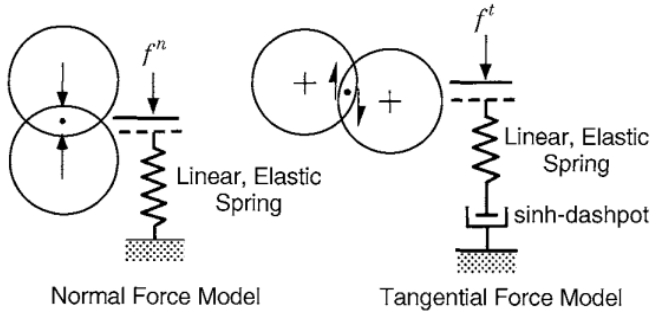

Figure 1.32 Normal and tangential interparticle force models (Kuhn & Mitchell, 1993)

1.3.4.3 Water flows in pores

Creep compression is explained as the reduction in micropore water and the relative reduction in pores in the microstructure (Figure 1.23), which was originally proposed by De Jong & Verruijt (1965) and supported lately by Berry &Poskitt (1972), Zeevaart (1986), Navarro & Alonso (2001), Mitchell (2003), Wang & Xu (2006) and Le et al., 2012. Akagi (1994) concluded that the mechanism of the consolidation is based on the drainage of pore fluids and the deformation of pores. And the creep is the result of the delayed deformation of micropores within the clay particles induced by the viscous flow of micropore fluid.

1.3.4.4 Structural Viscosity

Terzaghi (1941) considered that the viscosity of adsorbed water causes the decrease in speed of the rearrangement of soil structure. Therefore, the structural viscosity has significant impact on soil creep. This theory is also supported by Barden (1969), Bjerrum (1967), Garlanger (1972), Christie & Tonks (1985) and Graham & Yin (2001). Moreover, the viscosity of pore water was considered as the factor causing the delay in the pore water pressure dissipation (Garlanger, 1972; Yin & Graham, 1989). Sridharan & Rao (1973) considered that viscosity of pore fluid affect the coefficient of secondary compression. According to Yin (2002), creep mainly results from the combination of two processes: viscous flow of adsorbed water in double layers on clay particles and viscous adjustment of clay structure to reach a new equilibrium to balance with the external effective stresses. Therefore, creep occurs as long as the effective stress exists in the soil.

1.4 Conclusions

This chapter contains an outline of the existing literatures concerning macroscopic and microscopic researches of time-dependent behavior in clayey materials. At the macroscopic level, creep (or secondary compression) is defined and characterized in laboratory experiments and in-situ observations. The creep behavior and its relations with stress path, stress level, loading history and drainage condition etc. are presented. The mineralogy of clays, different techniques for studying the microstructure of clays, the influence of stress condition on the arrangement of particles and pores, their orientations and evolution with time in microscopic level are introduced.

Based on the numerous experimental investigations on the creep of clay material, the following conclusions were drawn:

1.4.1 Macroscopic study of creep

Soils deform continuously in response to the sustain constant external load. This time-dependent deformation depends on the state of soil, drainage condition, the loading history and stress state.

At present, there are some problems in analyzing the secondary compression characteristics of clay based on one-dimensional consolidation test. The evolution the secondary consolidation coefficient should be studied in combining with the over-consolidation ratio, the density or void ratio, the soil structure and its destructive characteristics.

Under drained condition, the creep rate of clay decreases with time, while the undrained creep will lead to long-term shear strength softening. In addition to one-dimensional and triaxial test, some unconventional laboratory test and field creep tests are also used to investigate the time-dependent deformation of clay.

Simple constitutive equations can reasonably describe time-dependent behavior under limited conditions. This behavior is considered related to the viscoplastic properties of clay, much remains to be learned, however, about the development of shear contractant and shear dilatant plastic strains during drained creep.

1.4.2 Microscopic study of creep

Clay consists of different types of minerals. The microstructure of clay, its fabric, arrangement, surface area as well as bonding capacity influence the appearance of the time-dependent properties of clays.

From the experimental point of view, the microstructure of clayey materials was investigated under various stress conditions. These studies require the use of several techniques at particles and aggregates scales (<100 μm) to analyze the organization and orientation of particles, particle assemblies and pores: (a) optical microscopic observation (b) scanning electron microscopy (c) X-ray diffraction (d) mercury intrusion porosimetry etc.

Time-dependent deformations and that result from the viscous rearrangement of the soil structure may be responsible for a significant part of the total creep deformation response. Macroscopic stress applied to a soil mass induces both tangential and normal forces at the interparticle contacts is essential for understanding the creep behavior.

Theoretical studies of particle bonding and water flows in pores as well as structural viscosity have been used to explain the macroscopic creep behavior. However, in the case of direct microscopic observations, the literature is scarcer and the subject needs more investigations.

Chapter 2 Material and Experimental Techniques

In this chapter, we present all the techniques used in this research, at the global (macroscopic) scale, which is the scale of the specimen, and at the local (microscopic) level that represents the scale of the clay particle. The preparation of the sample, the experimental program for this study also presented.

2.1 Material properties and specimen preparation

2.1.1 Mineralogy and kaolinite properties

The soil selected for the present investigation is an industrial clay named Kaolin K13, supplied by Sibelco, France. The natural state of Kaolin is loose powder, variable color from white to beige, and the melting point is 1500° C. The characteristics of the remolded Kaolin and its mechanical behavior were identified in the LEM3, University of Lorraine.

2.1.1.1 Mineralogy analysis of Kaolin K13

The Kaolin powder contents mainly Kaolinite (Alumina silicate hydrate) and a little quartz (Table 2.1 Table 2.2). Kaolinite has a low shrink-swell capacity and a low cation-exchange capacity (1-15 meq/100 g). It is a soft, earthy double-structure silicate mineral; the crystal structure formula is $Al_4(Si_4O_{10})\ (OH)_8$. Each crystal layer consists of a layer of silicon-oxygen tetrahedron (SiO_4) and a layer of aluminum oxygen octahedron, linked by the common oxygen, as shown in Figure 1.19.

Table 2.1 Ingredients of Kaolin K13

Name	Chemical	EINECS	CAS
Kaolinite	Al2 Si2 O5 (OH)4	310-127-6	1332-58-7, 1318-74-7
Quartz Alpha	Silica (SiO2)	238-878-4	14808-60-7

Table 2.2 Chemical type composition of Kaolin K13

Chemical type	SiO_2	Al_2O_3	Fe_2O_3	K_2O	CaO
Content (%)	60	28	1.0	0.6	0.5

The observation by scanning electron microscopy (Figure 2.1) reveals that the original Kaolin particles are mostly in shape of separate serrated thin plates, and a bit of particles composed of superimposed sheets, which are both typical structures of kaolinite clay particles.

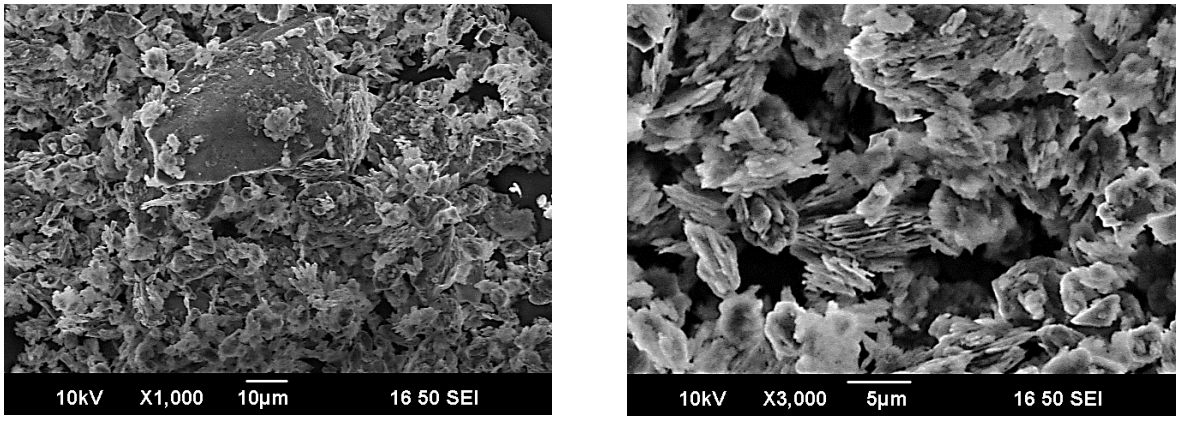

(a) (b)

Figure 2.1 Photo of SEM of Kaolin powder: (a) ×1000 times; (b) ×3000 times

2.1.1.2 Physical properties of Kaolin K13

Table 2.3 gives the physical property parameters of Kaolin, using fall cone test for Atterberg limits and pycnometer for density, both the values of w_L and w_P are normal values for low plasticity soils.

Table 2.3 Physical properties of Kaolin K13

Material	Liquid limit $w_L(\%)$	Plastic limit $w_P(\%)$	Plastic index $I_P(\%)$	Density of the solid grains ρ_s (cm^2/s)
Kaolin K13	42	21	21	2.63

The grain size distribution of Kaolin determined by laser granulometer through three parallel measurements is represented in Table 2.4 and Figure 2.2, which shows that the mean dimensions of Kaolin K13 falls in the range of 2.5 μm to 20 μm, the distribution curve provided by the manufacturer, Sibelco, shows approximate trend. A quite similar and more known Kaolin P300 is also represented in Figure 2.3 which has been analyzed for instance by Wei (2014), Hammad (2010) etc. by laser granulometry. The particle size of the Kaolin P300 is smaller with 65% of particles less than 1 μm. The larger size (for example >5mm) in the distribution curve for Kaolin K13 may

indicate aggregates rather than particles. Thus, other distribution tests should be performed on the K13 to more accurate approach the representative curve of the material.

Table 2.4 Identification of grain size distribution of Kaolin K13

Granulometry (μm)	≥50	50>D≥20	20>D ≥10	10>D ≥5	<5
Cumulative Results (%)	5.1	16.8	16.3	20.2	41.6

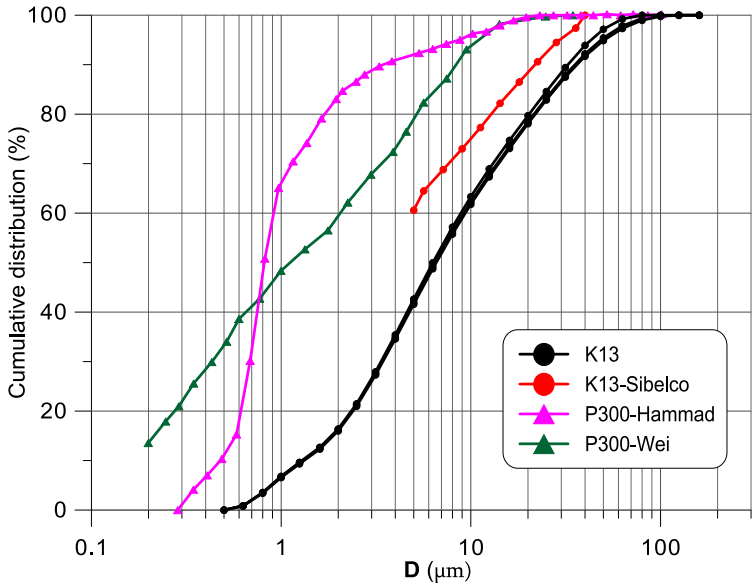

Figure 2.2 Grain size distribution of Kaolin

2.1.2 One-dimensional consolidation and sample preparation

2.1.2.1 Slurry preparation

The clay powder was mixed with an amount of de-aired water corresponding to 1.5 times of its water content ($w = 1.5\, w_L$), and then was mechanically stirred for 15 minutes (Figure 2.3a), under a velocity of 280 revolutions per minute, into a homogeneous slurry (Figure 2.3b). The slurry was sealed by film paper and aluminum foil, and then rest for 24 hours in room temperature for a better homogeneity (Figure 2.3c). Afterwards, the prepared slurry was filled into the consolidometer for preconsolidation.

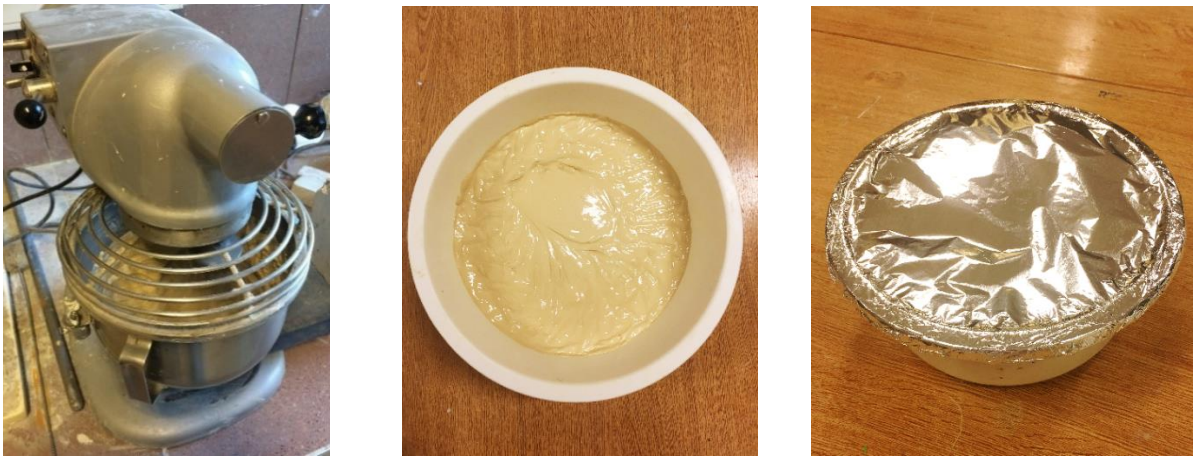

(a) (b) (c)

Figure 2.3 Preparation of Kaolin slurry: (a) stirrer; (b) slurry; (c) conservation of slurry

2.1.2.2 One-dimensional consolidation

The slurry was manually filled layer by layer into a double drainage consolidometer with diameter of 95 mm (Figure 2.4a). The material was preconsolidated under one-dimensional compression by steps until a final stress of 120 kPa for at least 3 weeks for a good preconsolidation quality. A cylindrical section can then be cut (Figure 2.4b) from the obtained core for triaxial tests.

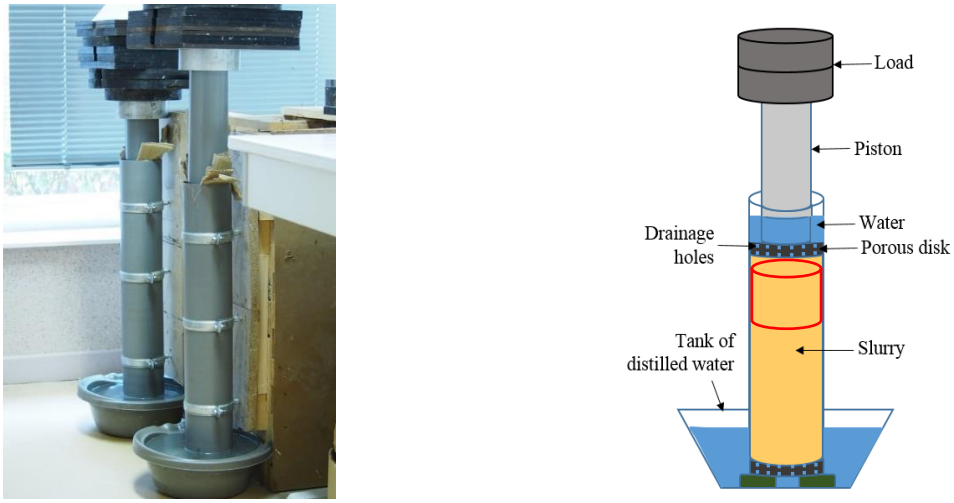

(a) (b)

Figure 2.4 Preconsolidation of Kaolin slurry: (a) photo of consolidometer; (b) specimen section after preconsolidation

Then the soil section was trimmed gently into cylindrical specimen of 75 mm in height and 50 mm in diameter by coulter knife on a rotary cutting base (Figure 2.5a), and then was moved into the triaxial cell through two cylindrical molds quickly (Figure 2.5b).

(a)

(b)

Figure 2.5 Sample preparation: (a) cutting tools; (b) triaxial specimen

2.2 Macroscopic research techniques

2.2.1 Axisymmetric triaxial tests

Focusing on the stress-strain relationship and the measurements of volumetric change, a reliable experimental apparatus with automatic recording and controlling is required. The GDS triaxial testing system is a fully automated triaxial testing system, based on the classic Bishop's & Wesley's (1975) hydraulic triaxial cell. All triaxial loading following stress paths, and creep tests maintaining a given stress level, in this thesis performed on this GDS system.

2.2.1.1 The GDS Triaxial testing system and measurements

The fundamental system hardware elements of the used GDS Triaxial Testing System (GDSTTS) shown in Figure 2.6. The whole system includes one triaxial cell, three automatic controllers, one data acquisition pad and PC software control terminal, connected by a closed loop.

The GDSLAB control and acquisition software starts with the Kernel module and Version 2.5.4.4 is used to perform the triaxial tests, which is connected with PC resident via IEEE card. The standard GDS data acquisition device, known as the "serial data pad", has 8 computer controlled gain ranges, specifically designed to suit the pressure and displacement transducers.

The GDS Advanced Pressure/Volume Controller (ADVDPC) is a microprocessor-controlled screw pump for the precise regulation and measurement of fluid pressure and volume change, which offers the highest level of accuracy, resolution and control. The optional volumetric capacity is 1000cc (for pressure ranges < 2MPa); the resolution of measurement and control is pressure ≤0.1% full range, volume = 0.5 mm^3 (<8MPa); the ambient temperature range is 10°C to 30°C.

After filling with de-aerated water into the cylinder of ADVDPC, the de-aerated water is pressurized and displaced by a piston moving in the cylinder. The piston is actuated by a ball screw turned in a captive ball nut by an electric motor and gearbox that move rectilinearly on a ball slide (Figure 2.7). An integral solid-state transducer measures pressure. Control algorithms are built into the onboard microprocessor to cause the controller to seek to a target pressure or step to a target volume change. Volume change is measured by counting the steps of the incremental motor.

Radial stress is applied by controlling the water pressure into the triaxial cell through ADVDPC 1 (Figure 2.6). ADVDPC 2 linked to the specimen by a capillary tube can acquire backpressure and volume change. Pore pressure transducer is connected to the base of the pedestal, which shows the local pore pressure at the bottom of the sample, and it can react the whole pore pressure through the soil if the sample is well saturated. Axial displacement/strain is achieved by applying a strain increment on the base of soil specimen in the cell. The measurements obtained directly from GDSTTS are summarized in Table 2.5.

Table 2.5 Measurements obtained by GDSTTS

Apparatus	Measurement item	Notation
ADVDPC 1	Cell pressure (kPa)	σ_3
ADVDPC 2	Back pressure (kPa)	BP
	Volume change (mm^3)	ΔV
ADVDPC 2	Load cell (kN)	F
	Axial displacement (mm)	Δh
Pore pressure transducer	Pore pressure (kPa)	PWP

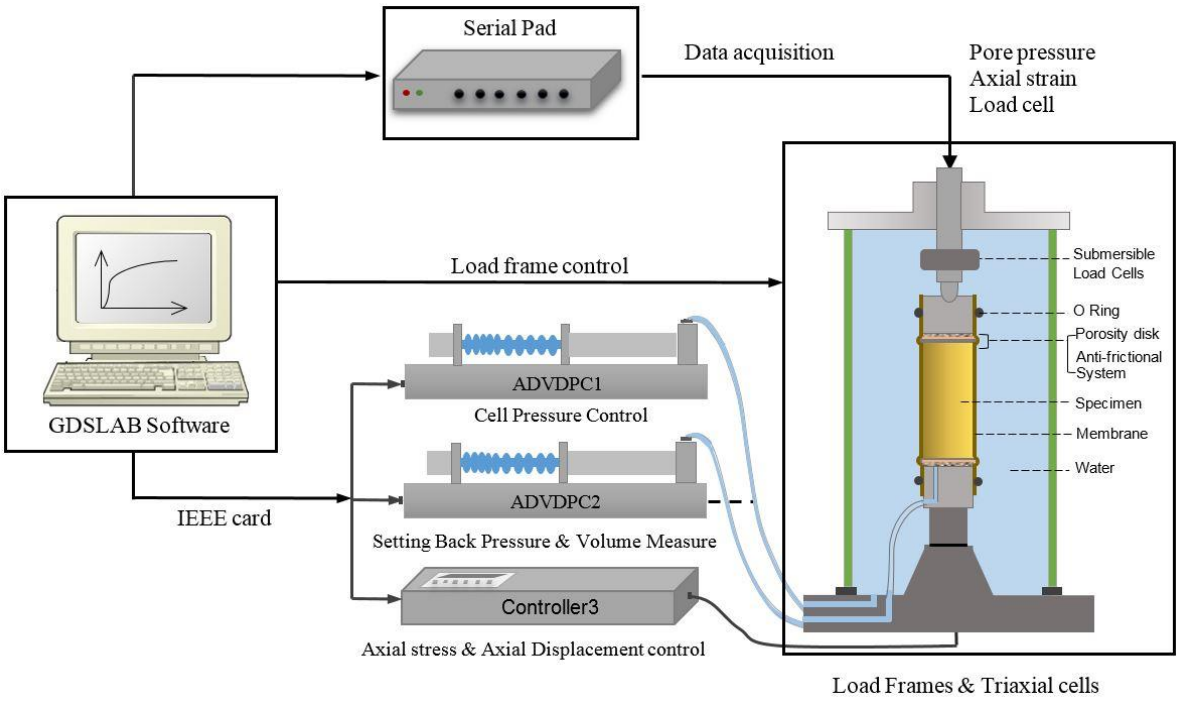

Figure 2.6 GDS testing control and acquisition system

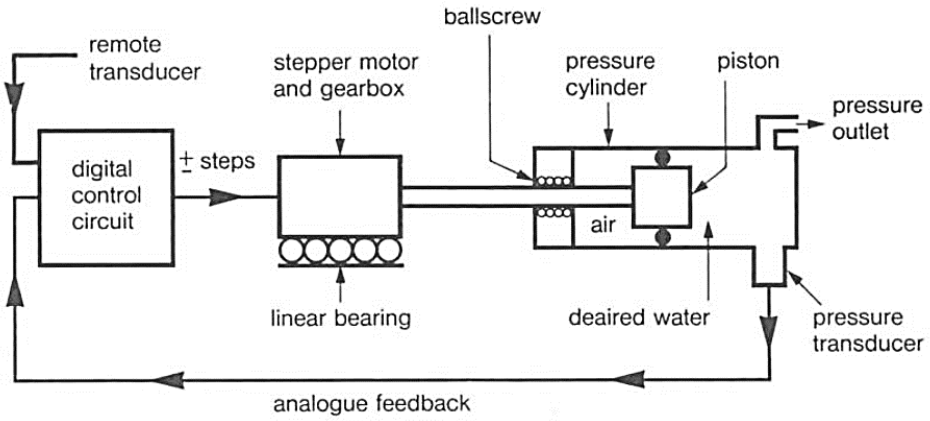

Figure 2.7 Operational schematic of ADVDPC

All transducers, volume change unit and load cell, which are connected to the serial pad are calibrated carefully before test. All the load cell and connections parts were checked under a pressure of 500 kPa to prevent the leakage in the whole system.

2.2.1.2 GDS testing techniques

For creep test performed by the triaxial apparatus, the leakage of membrane between the cell water and the specimen can be an important aspect that controls the accuracy of test. Since the volume change is obtained by measuring the amount of pore water that circulated from and to the

soil specimen by GDS controllers, the detecting accidental leakage of water through the membrane is highly significant.

To perform the creep test in a long time duration, we need membrane of high quality; meanwhile, to reduce the restraining effect of the membrane, the thickness of the membrane should not be too large. According to the British Standard (BS 1377: Part 8, 1990), the membrane thickness shall not exceed 1 % of the specimen diameter, otherwise the calculated deviator stress need to be corrected to allow the effects of the rubber membrane (Head, 1992; Havel, 2004). After tested with several types of membranes, a customized membrane made of latex which thickness is 0.35 mm, marked by Piercan.fr was used in this research and performed well in the long-term creep tests.

In the classical triaxial test, the non-uniformity of the specimen due to end restraint is an important problem. Lanier (1989) pointed out that the end restraints and the slenderness of the sample were the main points that should be taken into account. The end restrains due to the friction between the loading plates and the material becoming too large, meanwhile, the radial displacement of the specimen is restrained at the boundary. Consequently, the stress state is non-homogeneous and the maximum shear strength is usually overestimated. In order to decrease the friction, Rowe & Barden (1964) used greased membranes on the two ends of soil specimen, between the specimen and the platens. Hattab & Hicher (2004) used similar technique; they used a "sandwich" device that was made of two smooth plates lubricated by a thin layer of grease and latex layers. In the research of this thesis, we chose the same "sandwich" anti-frictional device (see Figure 2.8).

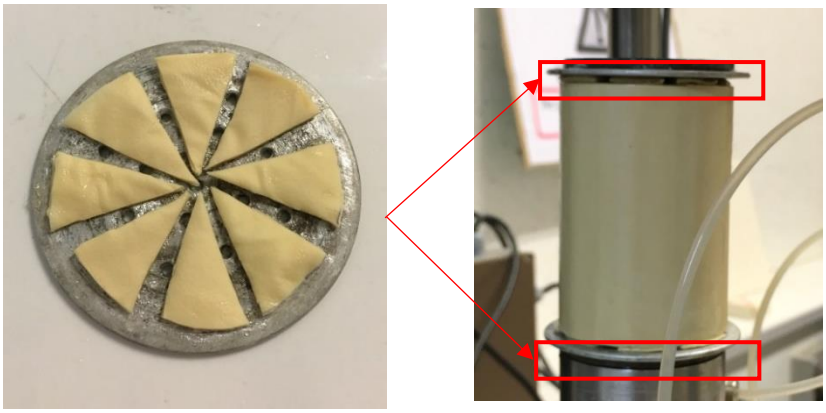

Figure 2.8 Anti-friction device used on the two ends of specimen

The stability of the specimen decreases and the shear-bands develops more easily while the slenderness (ratio of H/D) increases, especially for the overconsolidated specimen presented in large strain condition. Combining with the "sandwich" anti-friction system, a slenderness of H/D=1.5 was selected for the research of this thesis to maintain the homogeneity throughout the specimen.

Since the distance between the piston and the loading ends on the top, together with the membranes flatten of the anti-friction system, which will add an extra deformation to the whole deformation of specimen when the specimen is truly loaded. A correction is necessary at the beginning of the compression for both axial strain and volume strain. Figure 2.9 shows the corrections of the strains verses stress, the fluctuation part of the original strain at the beginning arises from the connection of loading piston and the membranes flatten. A fitting function was drawn from a section of the real compression curve, we re-calculated the corresponding strain at the beginning (marked by the red dotted line) by deviatoric stress using the fitting function, and a parallel movement of the corrected curve gave the final strain curve (marked by the black dotted line).

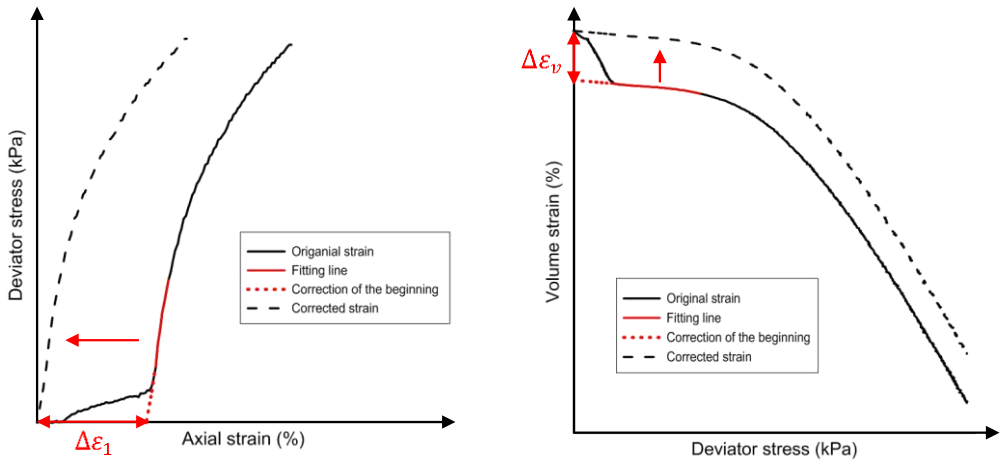

(a) (b)

Figure 2.9 Correction at the beginning: (a) axial strain; (b) volume strain

Murayama & Shibata (1966) and Mitchell et al. (1968) pointed out that the temperature did influence the creep of soil, that the higher the temperature the test was performed, the higher the creep rate. In addition, the ratio of increment of strain and increment of logarithm time appears to be proportional to the absolute temperature. As discussed by Zhu (1999), the temperature greatly influenced the viscosity of soil and hence, the results of creep test and stress relaxation test affected

by temperature. In the tests of soils related to creep behavior, the environment temperature should be controlled with the greatest care. Therefore, the entire test in this thesis performed in the lab where the temperature was maintained constant at 20°.

2.2.1.3 Triaxial testing program

After saturating the whole triaxial system, the tests were managed progressively in four phases as illustrated in Figure 2.10: the saturation stage, the isotropic consolidation stage (at normally consolidated or overconsolidated condition), the monotonic loading stage along purely deviatoric stress path up to a given stress level, and then to the creep stage.

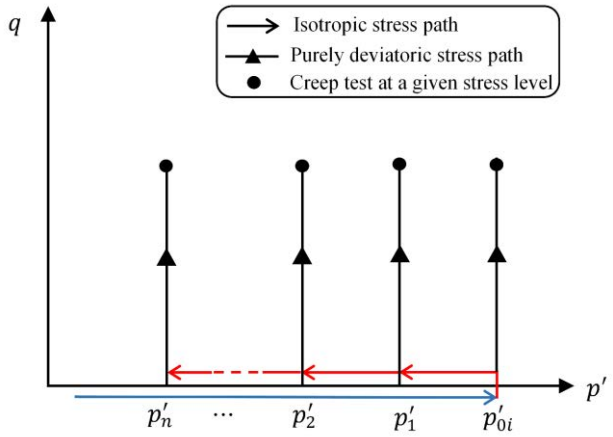

Figure 2.10 Experiment procedures of different tests stages

a) Saturation phase

After the soil specimen was well settled in the triaxial cell, all the system was saturated, and then a value of radial stress σ_3 = 40 kPa and backpressure BP = 10 kPa was applied to provide an initial pressure for the saturation stage. The radial stress and backpressure were slowly increased simultaneously with a constant difference (Δ = 30 kPa) until a certain target for at least 2 days. The average duration of this phase depends on the material, the experienced duration for the Kaolinite clay was estimated for 48 hours, and had been verified by Ighil Ameur (2016) in his thesis with the same material for a good saturation.

At the end of the saturation, the Skempton coefficient B need to be checked and the value of B should approaches 100% to ensure the good quality of saturation (Figure 2.11). If the value of B was unqualified, σ_3 and BP would be increase a little manually (10 kPa, for instance) at the same time and then were maintained constant for another 24 hours, following by B check in the end for

a second time until B ≈ 100% was reached. Afterwards, the backpressure was kept constant during the whole following phases to ensure the saturated state.

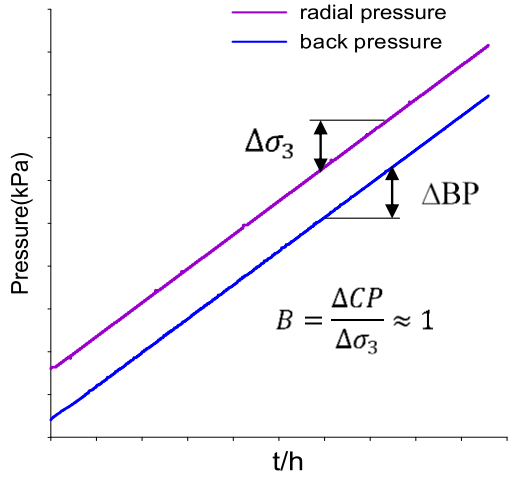

Figure 2.11 Saturation ramp of Kaolin K13

b) Isotropic consolidation phase

In order to obtain the initial normally consolidated or over consolidated state, the specimen was isotropically loaded up to a maximum pressure p'_0, and then was isotropically unloaded by steps to a pressure $p'_j = p'_{0i}/\mathrm{OCR}$ (Figure 2.12), similar operation modes were conducted by different authors among them Shimizu (1982), and Hattab and Hicher (2004).

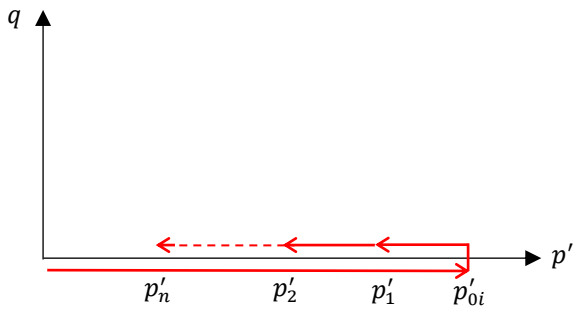

Figure 2.12 Isotropic loading and unloading in p'- q plane

Three groups of creep tests have been performed on normally and overconsolidated samples with a maximum consolidation stresses of p'_{0i}=1000 kPa, 800 kPa or 200 kPa. The details of each test series are listed in Table 2. The name of the test takes the form of $P_{0(x)}$-OCR(y)-q(z), where (x) reflects the abbreviation of preconsolidation pressure, (y) is the value of OCR and (z) refers to the deviatoric stress at which the creep test is performed. For example, the test named P_{010}-OCR1.5-q200 presents a specimen which was isotropically consolidated until p'_{0i} = 1000 kPa, and

then was unloaded to 666 kPa giving an OCR=1.5. Afterwards, the deviatoric stress was increased to 200 kPa and was maintained constant for creep observation.

The identification of t_{100} is shown in Figure 2.13, where the turning point of Δv- $\sqrt{t}$ curve can be regarded as the end of primary consolidation according to Norm France P 94-071.

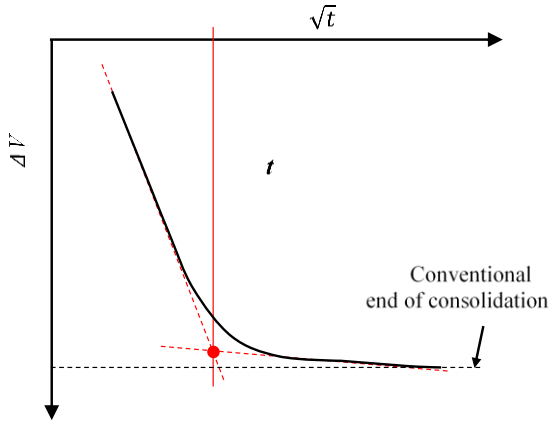

Figure 2.13 Identification of t_{100} during consolidation in triaxial test

Figure 2.14 gives an example of the identification for t_{100} by typical root time methods; an upper limit value of 200 was obtained and was selected as referenced value of t_{100} for the kaolin. Hence, the duration for each consolidated step should be over than 200 minutes and the time interval for data recording should be short enough for an accurately capture of volume changes.

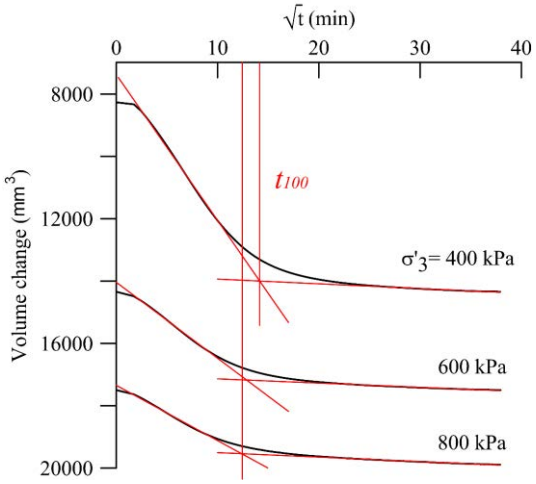

Figure 2.14 Determination of t_{100} during consolidation phase (example of test P_{010}-OCR1.5)

Figure 2.15 presents the isotropic path of test P_{010}-OCR1.5 where OCR = 1.5 and p'_{0i} = 1000 kPa. The volume changes were recorded every 3 minutes, the variation of loading was 200 kPa and the duration of each stage was at least 1000 minutes. Both the last stages of loading and

unloading were prolonged until no volume changes were detected. This kind of consolidation process ensures the detection of accidental leaks, and the porosity of the membrane.

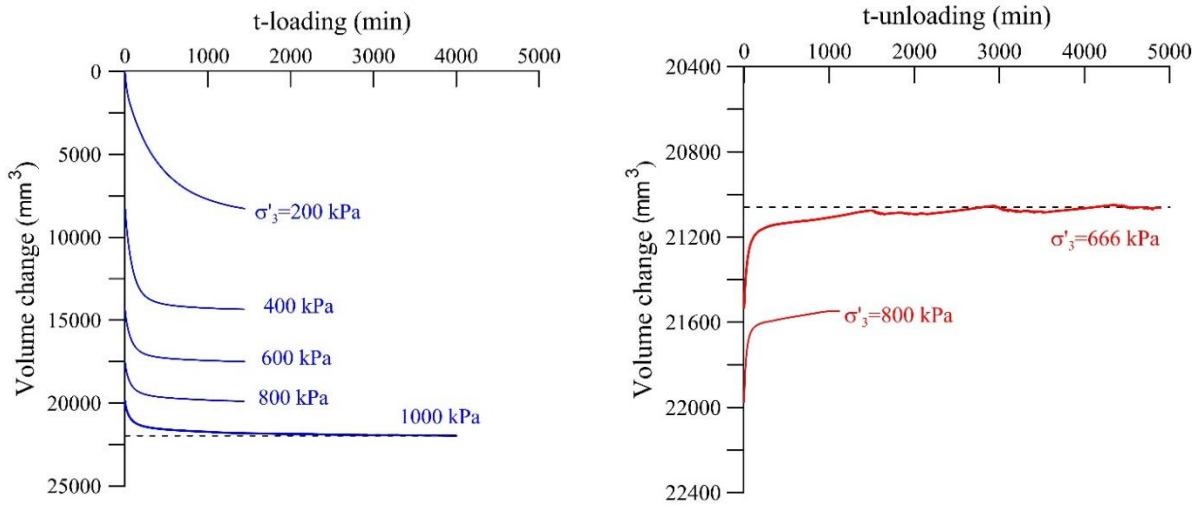

(a) (b)

Figure 2.15 Volumetric variation during isotropic consolidation (example of test P_{010}-OCR1.5) (a) in loading phase (b) in unloading phase

Additionally, the variation of calculated volumetric strain ($\varepsilon_v=\Delta V/V_0$) is represented in Figure 2.16, which was found to be varied within 0.001% at the end of consolidation. Hence, the final equilibrium state of ε_v confirmed a quite well consolidation process.

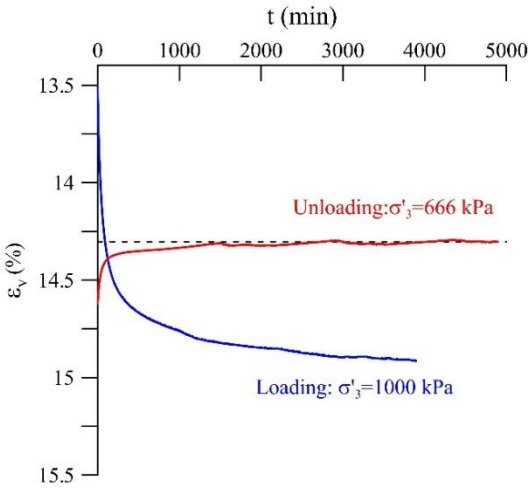

Figure 2.16 Variation of volumetric strain in last stage of isotropic consolidation (example of test P_{010}-OCR1.5)

This consolidation process ensures the detection of accidental leakage that relates to the porosity of the membranes, particularly in the unloading stage. The whole consolidation technique imposes a high-precise measurement of volume changes.

c) Purely deviatoric loading phase

In general, there are two typical ways to perform the purely deviatoric stress path, the load control and strain control methods, both of these two control methods have been used in performing the drained triaxial tests (Nicholson et al., 1996; Flavigny and Reveillet, 1983; Zhu, 2007).

Special attention should be paid to the mode of loading during the drained triaxial test. A too rapid loading would be inappropriate for controlling of the drainage conditions, arousing a possible development of excess pore water pressure which would be dissipated during the creep phase, leading thus to wrong results.

The loading phase was performed by a strain control method. The Formula (2.1) following NF-P 94-074 was used to calculate the maximum velocity of strain during loading

$$V_{max} = \frac{h_0 \cdot \varepsilon_f}{a \cdot t_{100}} \tag{2.1}$$

where h_0 is the initial height of sample; ε_f is the estimated failure strain which depends on the type of soil (6% for soft soil); parameter a depends on the type of drainage (8.5 for simple drainage).

From the data of test P_{010}-OCR1.5, the calculated loading velocity is 0.0025 mm/min. This value, which is quite consistent with that used by other researchers on quite similar materials (e.g., on Kaolin P300 by Hattab and Hicher, 2004), has been used as representative value of loading velocity to perform the triaxial tests in this research.

The purely deviatoric loading procedure and the obtained results are represented in Figure 2.17 and Figure 2.18, taken the example of test P_{010}-OCR1.5. In this test, the constant mean effective stress of p' = 666 kPa (named p'_{target}) was maintained, meanwhile, the deviatoric stress of q = 200 kPa (named q_{target}) was supposed to be reached. Hence, the name of this test is noted completed as P_{010}-OCR1.5-q200. The results show how the measured values of both the deviator and the mean effective stresses evolve in reaching the target values. In Figure 2.18, $t_{loading}$ represented the duration of monotonic loading, and BP_{target} is the target backpressure that was maintained constant. The pore pressure transducer at the bottom of the sample measured the pore water pressure (PWP). This procedure permits to follow correctly the measurement of all parameters during the purely deviatoric stress path. As it can be seen in Figure 2.17, the scattering of mean effective stress was within ±1.5 kPa, within 0.2% of the target value. In Figure 2.18, one can see that the pore water pressure and backpressure were maintained closely constant around its target value, which is the

intrinsic adaptation of the GDS system. These results show clearly that during the purely deviatoric loading there is no generation of excess pore water pressure. Therefore, the drained condition can be well maintained by using the calculated velocity.

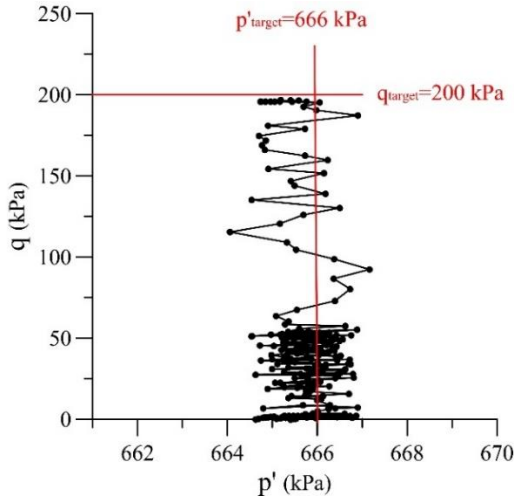

Figure 2.17 Loading process on the purely deviatoric stress path (example of test P_{010}-OCR1.5-q200)

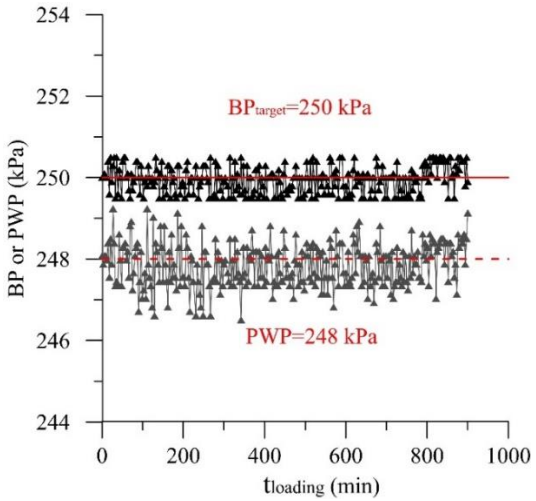

Figure 2.18 Pore pressure response on the purely deviatoric stress path (example of test P_{010}-OCR1.5-q200)

Based on the detected volume changes, the calculated volumetric strain is shown in Figure 2.19, where q_v is the deviatoric stress corresponding to the onset of variation in volumetric strain. For q lower than q_v, no volume change was detected ($\varepsilon_v \approx 0$). For q beyond q_v, the progressive contraction was observed. Consequently, the volumetric change can be detected precisely in the purely deviatoric loading program, which provides a reliable approach to the volumetric strain changes in the following creep phase.

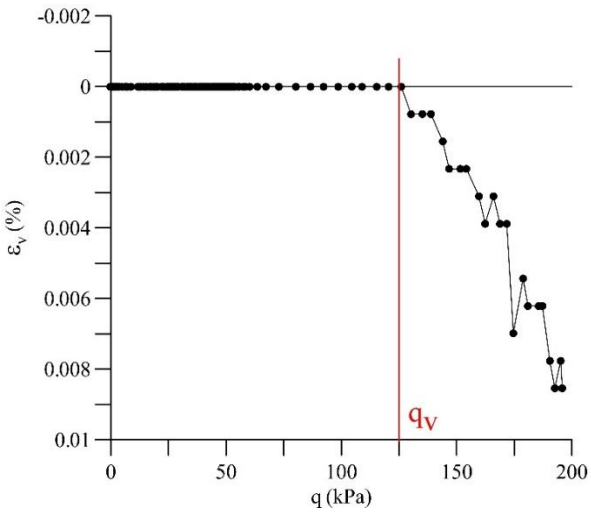

Figure 2.19 Pore pressure Volumetric strain variation as a function of q on purely deviatoric stress path

d) Creep phase

After reaching a given stress level, both the mean effective stress and deviatoric stress are maintained constant at least 7 days for creep observation. Since the deformation of soil specimen has been evolving within the whole test, how to maintain the constant stress targets in this active process could be a vital issue to the success of the creep test.

For the general software control loading program, the test will terminate while reaching the target value, so does the GDSLAB. After failing several times, we tested with higher version of GDSLAB software and advanced controllers. We found that with the strain control loading method in the higher version of software, meanwhile, the terminate condition should only relate to time, the software could always search and keep the given creep target within the whole process.

Figure 2.20 gives the constant stress procedure during creep measurement on an overconsolidated sample with OCR = 1.5. The creep phase was performed under a constant deviatoric stress of q = 200 kPa, the duration for creep is represented by t_{creep}. It can be observed that the whole fluctuation of q was within 2% of its target value. Meanwhile, the measured PWP and BP were constant as in the monotonic loading stage. Consequently, the deformation development obtained since the beginning of this phase reflects the logical creep phenomena.

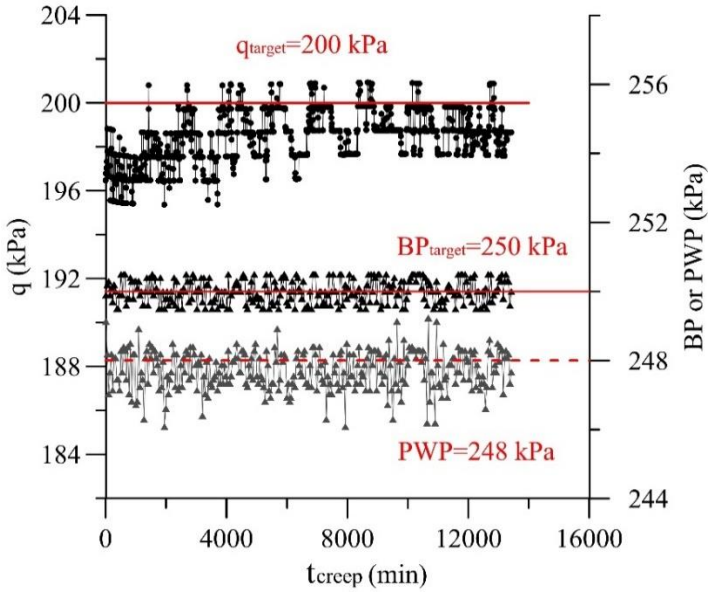

Figure 2.20 Constant stress procedure in creep phase (example of test P_{010}-OCR1.5-q200)

The variation of volumetric strain versus time during creep is illustrated in Figure 2.21, where some representative values are selected to show the main tendency of ε_v with time. Under sustained stresses (see Figure 2.20), the evolution of volumetric creep strain was well detected by GDS data acquisition per 3 minutes. Considering its highly automaton and precision, the whole experimental technique allows us to obtain quite reliable experimental results in a long-term duration and to well investigate the creep behavior.

Following up this experimental method explained above, three groups of creep tests have been performed on normally and overconsolidated samples with a maximum consolidation stresses of p'_{0i}=1000 kPa, 800 kPa or 200 kPa. The details of each test series are listed in Table 2.6. The name of the test takes the form of $P_{0(x)}$-OCR(y)-q(z), where (x) reflects the abbreviation of preconsolidation pressure, (y) is the value of OCR and (z) refers to the deviatoric stress at which the creep test is performed.

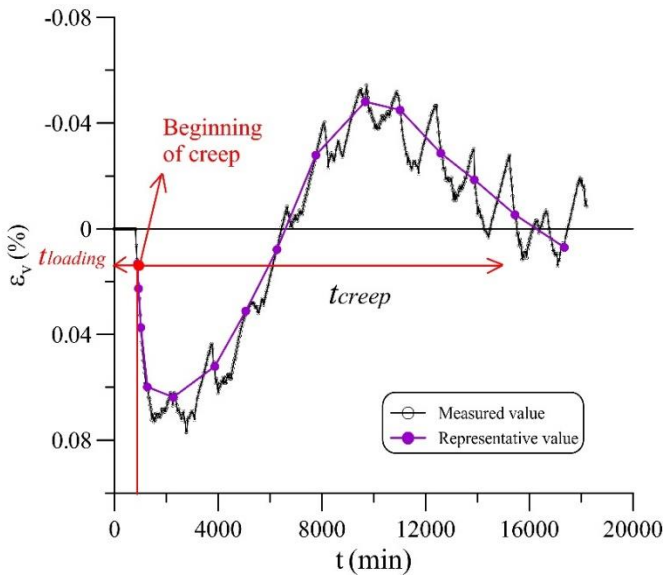

Figure 2.21 Volumetric strain variation during creep measurement (example of test P_{010}-OCR1.5-q200)

Table 2.6 Drained triaxial tests on Kaolin K13

Test No.	$p'_{0i}(kPa)$	$p'_j(kPa)$	$q_{creep}(kPa)$	OCR
P_{010}-NC-q670	1000	1000	670	1
P_{010}-NC-q200		1000	200	1
P_{010}-OCR1.5-q445		666	445	1.5
P_{010}-OCR1.5-q200		666	200	1.5
P_{010}-OCR2.5-q200		400	200	2.5
P_{010}-OCR4-q200		250	200	4
P_{02}-OCR4-q43	200	50	40	4
P_{02}-OCR5-q30		40	30	5
P_{02}-OCR5-q43		40	43	5
P_{08}-OCR16-q43	800	50	43	16

2.2.2 Calculation of test parameters

a) Initial parameters

After the pre-consolidation of the saturated specimen, we can calculate the initial void ratio e_{00} of soil

$$e_{00} = w\, G_s = G_s \cdot \frac{M_w - M_d}{M_d} \tag{2.2}$$

where M_w and M_d are the wet and dry masses of the specimen; G_s is the density of the solid grains;

The initial dimension are H_{00}=75 mm, D_{00}=50 mm, and the initial volume of the cylindrical specimen is $V_{00}=\frac{\pi \cdot D_{00}^2}{4} \cdot H_{00}$.

b) Parameters during consolidation

After the isotropic consolidation, the new void ratio can be calculated through the measured volume change ΔV:

$$e_0 = e_{00} - (1 + e_{00}) \cdot \frac{\Delta V}{V_{00}} \tag{2.3}$$

And for the isotropic unloading stage

$$e_0 = e_{0i} + (1 + e_{0i}) \cdot \frac{\Delta V}{V_{0i}} \tag{2.4}$$

where e_{0i} and V_{0i} are the void ratio and the volume of the specimen respectively after isotropic loading at consolidation stress p'_0.

The height and sectional area at the end of consolidation are:

$$H_0 = H_{00} - \frac{1}{3} \cdot \frac{\Delta V}{V_{00}} \tag{2.5}$$

$$S_0 = \frac{V_0}{H_0} \tag{2.6}$$

c) Parameters during purely deviatoric loading

The effective radial stress $\sigma'_3=\sigma_3$-BP, and the effective axial stress $\sigma'_1=\sigma_1$-BP, the deviatoric stress $q=\sigma'_1-\sigma'_3$, the mean effective stress $p'=\frac{1}{3}(\sigma'_1+2\sigma'_3)$, where the axial stress

$$\sigma_{1i} = \frac{F_i}{S_i} + \sigma_{3i} \tag{2.7}$$

And the sectional area of soil specimen

$$S_i = \frac{V_0 - \Delta V_i}{H_0 - \Delta H_i} \tag{2.8}$$

The calculation of axial strain $\varepsilon_1= \frac{\Delta H}{H_0}$ and the volumetric strain

$$\varepsilon_{vi} = \frac{\sum \Delta V_i}{V_0} \tag{2.9}$$

And the corresponding void ratio

$$e_i = e_0 - (1 + e_0) \cdot \varepsilon_{vi} \tag{2.10}$$

2.3 Microscopic research techniques

The widely used laboratory microscopic approach for the analysis on soils includes the mercury intrusion porosimetry (MIP) test and scanning electron microscopy (SEM) observations. These microscopic techniques provide a supplementary and deeper way to investigate the mechanical behavior of clay, which have been used in this research and are presented in the followings.

2.3.1 Preparation of specimens for MIP and SEM

To perform the MIP test and SEM observation, the specimens must be completely dry; meanwhile, the drying technique plays an important role in the quality of the results. As summarized by Guillot et al., 2002; Hammad, 2010; Wei 2014, the general drying techniques are:

- Air drying
- Evaporation of water
- Freeze-drying

Among which the air drying in an oven is the simplest way to dry the soil specimen, which usually takes a long period and can lead to a certain amount of shrinkage of the sample and the pore size could be changed consequently (Delage and Lefebvre, 1984).

The evaporation of water should be in the condition of the critical point, and then the liquid water is transformed into vapor directly. Since the critical point of water should be under a circumstance of 375°C and 22 MPa, which is difficult to manage physically, this technique usually consists of 2 stages: exchange of water by ethanol and then replace ethanol by CO_2 progressively. The critical point of CO_2 is 31°C and 7.6 MPa, which is much more accessible.

The freeze-drying method is a dehydration process, which principle can be explained briefly using the phase diagram of water (Figure 2.22). If the atmospheric pressure is higher than 6.11 mbar, water passes through all three phases (solid, liquid, gas) when the temperature is lowered or raised. At 6.11 mbar the melting pressure curve, vapor pressure curve and sublimation pressure curve meet in one point called triple point. At this point, all three phases occur in parallel. Below this point, the ice is converted directly from a solid to a gaseous phase on reaching the sublimation pressure curve.

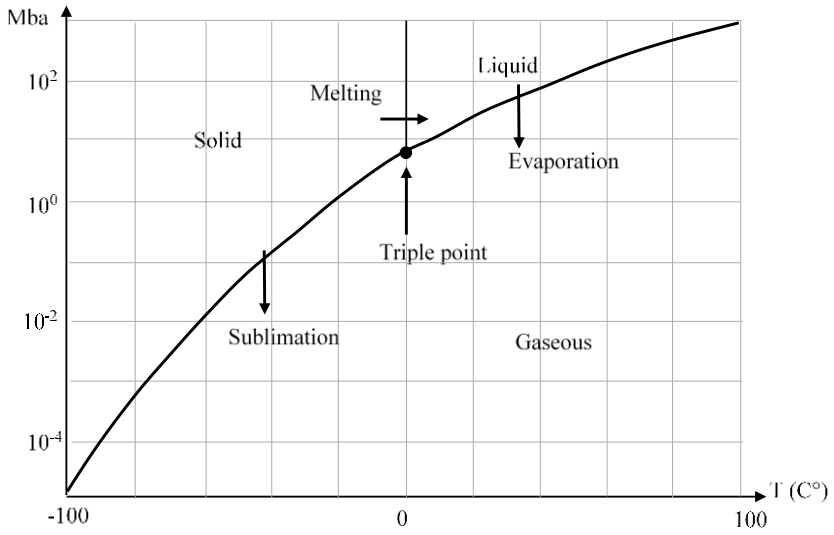

Figure 2.22 Vapor pressure curve for ice and water

The advantages of freeze-drying method are no introduction of new material into the sample; an increase of the strength in the sample; can obtain a fracture plan that does not correspond to the weakness plan of the sample structure. Considering the disadvantages of the other two techniques, the freeze-drying method is better thus is adopted for this thesis.

Based on this principal, the drying process works by freezing the clay material and then reducing the surrounding pressure to allow the frozen water in the material to sublimate directly from solid phase to gas phase (red line in Figure 2.23).

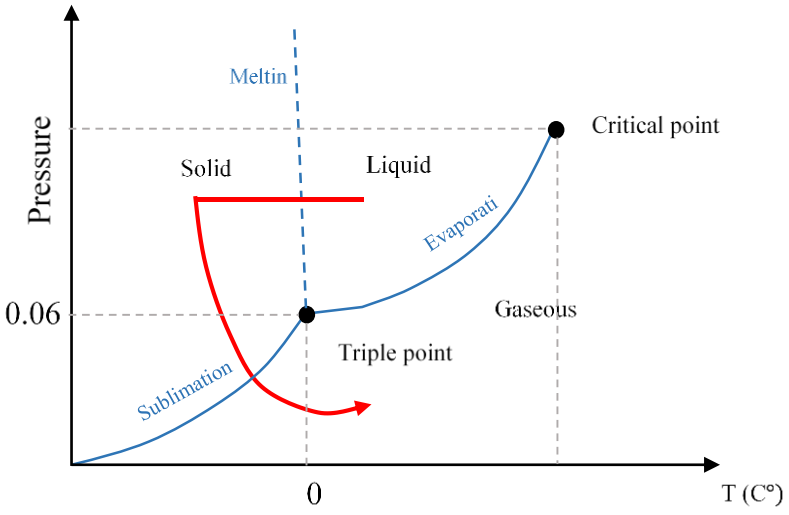

Figure 2.23 Freeze-drying technique

Freezing should be carried out in a rapid manner to prevent the crystallization of water particles (Tovey & Wong, 1973). Ahmed et al. (1974) recorded a very slight reduction in the size of the

clay sample using the freezing method, the authors concludes that the shrinkage during freezing is negligible.

To process the freeze-drying, several delicate operations, which consist in preserve the quality of the samples for the microstructural study, these operations are: pretreatment, freezing, main drying, and final drying.

a) Pretreatment

After removing from the triaxial cell, all the specimens were reserved by film paper, tin foil and paraffin sequentially. Thereafter, each core zone of specimen was cut into a beam in dimension of 30 mm ×30 mm ×10 mm, and then 3 pieces of strips were taken from the beam for drying, as shown in Figure 2.24. The region of interest for observation is the surface of the vertical plane, which is in parallel with vertical stress σ_1'. Slight nicks were carved outside of the strips before drying, aiming at easier obtaining as well as reducing perturbations of the cross section for SEM observation. The dimensions of the MIP samples for freezing are 10 mm ×10 mm ×10 mm, we chose this size, as recommended by Hammad (2010) and Wei (2014), to accelerate freezing.

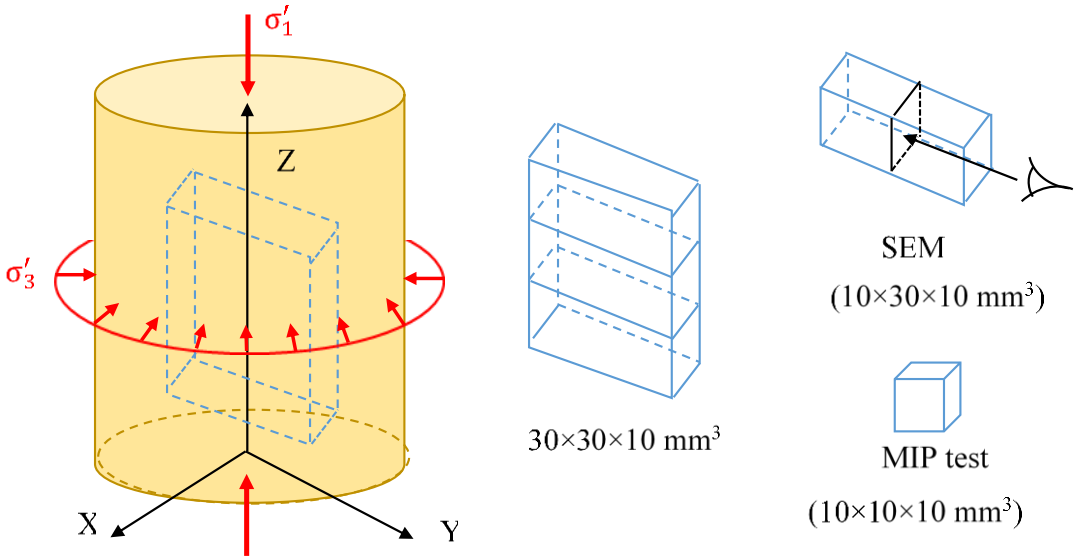

Figure 2.24 Cutting of small specimens for microscopic research

b) Freezing

The freezing phase is the most critical in the whole freeze-drying process, because the soil sample can be spoilt for improper operation. The pre-cut samples are immersed into the liquid

nitrogen until the air bubbles completely disappear. It is important to cool the material below its triple point, which ensures that sublimation rather than melting will occur in the following steps. The next step consists in transferring the samples to the sublimation apparatus, the plates carrying the samples are cooled beforehand in liquid nitrogen in order to avoid the melting of ice, and then sublimated in the freeze dryer, which allows generating a vacuum up to 104 kPa at a temperature of -70°. Freeze Dryer used in this research is ALPHA 2-4 LSC, made by Martin Christ, located at Central Supelec, in MSSMat Laboratory.

c) Main drying

During the main drying phase, the moisture is removed by sublimation, as soon as sublimation of the water vapor from the frozen sample begins, heat is extracted and consequently the samples continues to cool down. The pressure is lowered and enough heat is supplied to the material for the water to sublimate.

This phase may be slow, if too much heat is added, the material structure could be altered. The duration of the main drying phase depends mainly on the layer thickness of the sample, the solid content of the sample, the heat supplied during the drying, and the pressure inside the drying chamber. In this research, the main drying phase takes about 24 hours, and about 95% of the water in the material is sublimated according to the typical drying curve in Figure 2.25.

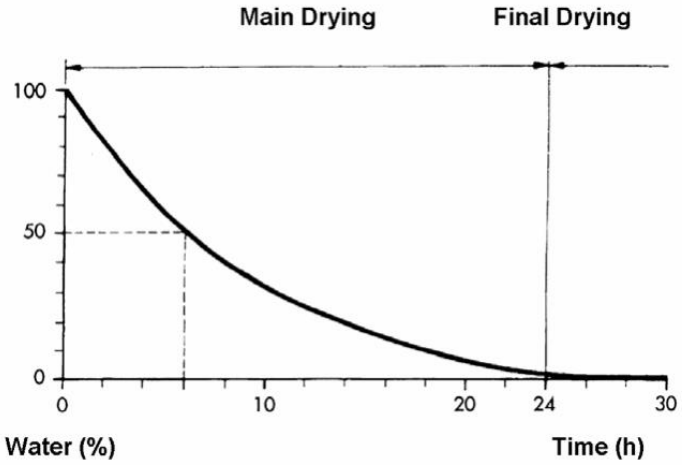

Figure 2.25 Residual moisture with time during drying

In this phase, pressure is controlled through the application of partial vacuum, which speeds up the sublimation. The ice condenser collects the generated water vapor. The vacuum pump is to lower the partial pressure of the non-condensable gases so that the water vapor can be transported

from the product to the ice condenser. Furthermore, a cold condenser chamber provides a surface for the water vapor to re-solidify on.

d) Final drying

The secondary drying phase aims to remove the unfrozen water molecules, and the bound moisture is removed by desorption. In this phase, the temperature is increased higher than that in the main drying phase (20~30 °C), in order to break the physico-chemical interaction between the water molecules and the frozen samples.

Usually the pressure is also lowered in this stage to encourage desorption. The end of the drying process is reached when the temperature of the sample and that of the shelves are about 15 to 20°C. The residual water content is extremely low, below 1%. After the final drying, the samples are transferred to reserve in a vacuum desiccator for the following observations (Figure 2.26).

Figure 2.26 Reservation of the drying specimens

2.3.2 Mercury intrusion porosimetry (MIP)

2.3.2.1 Principle of MIP

Mercury does not wet most substances and will not spontaneously penetrate pores by capillary action, it must be forced into the pores by the application of external pressure.

Mercury porosimetry analysis is the progressive intrusion of mercury into a porous structure under stringently controlled pressures. The required equilibrated pressure is inversely proportional to the size of the pores. From the pressure versus intrusion data, the instrument generates volume

and size distributions using the Washburn equation (1921). The pressure P and the intrusion of the non-wetting fluid into cylindrical pores and their radius "r" (Carlos A, 1998, Griffiths and Joshi, 1989)

$$P = -2\gamma \cdot \frac{\cos\theta}{r} \tag{2.11}$$

where γ is the liquid surface tension (N/m), and the value for Hg in this research is 0.485N/m; θ the angle of contact between liquid and solid (°), which θ=130° of Hg and soil.

An externally applied pressure tending to force mercury into the opening acts over the surface of the interface bridging the opening. The externally applied force, therefore, is the product of the pressure (P) and area (A) over which the pressure is applied. For a pore of circular cross-section

$$F_{EXT} = PA = P \cdot \frac{\pi D^2}{4} \tag{2.12}$$

At equilibrium, just before the resistive force is overcome, the equation is

$$-\pi D\gamma \cos\theta = P \cdot \frac{\pi D^2}{4} \tag{2.13}$$

Therefore, at any pressure, the pores into which mercury has intruded have diameters greater than

$$D = -4 \cdot \frac{\gamma \cos\theta}{P} \tag{2.14}$$

By measuring the volume of mercury that intrudes into the sample material with each pressure change, the volume of pores in the corresponding size class is known.

2.3.2.2 MIP apparatus

MIP tests were carried out on a Micrometrics Autopore IV analyzer located at Centrale Supelec, in MSSMat Laboratory. In order to avoid the broken of the sample during the tests, the rate of pressure increase must be low and the equilibrium times on each step must be long enough (Diamond, 1970).

Two loading units were used in this research: the low-pressure apparatus, the intrusion pressure P ranges from 0.003 MPa to 0.17 MPa, measuring the pore diameters D larger than 7.3 μm. During which the dry sample is initially evacuated by applying a vacuum and surrounded by mercury; the

high pressure unit, where the mercury pressure P is raised continuously between 0.17 MPa to 200 MPa, measuring the apparent pore diameters D from 6.3 nm to 7.3 μm.

The volume of mercury that enters pores is measured by a mercury penetrometer (Figure 2.27). The specimen is sealed into the sample cup on the top and mercury is applied through the stem capillary tube under pressure. This device is very sensitive and can detect the magnitude of change in mercury volume under 0.1μL.

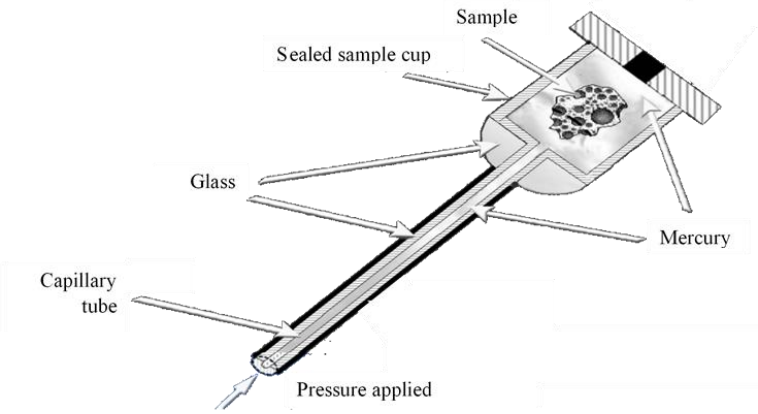

Figure 2.27 Cross-sectional view of a mercury penetrometer

2.3.2.2 Data interpretation

The validity of this characterization technique is more or less discussed because of the assumptions regarding the shape of the pores and their accessibility. However, despite its imperfections, this technique remains to analyze the diameters of pore sizes from nanometers to hundred micrometers.

a) Pore size

The mercury porosimetry mainly determine the connection from the sample surface towards the core of the specimen rather than the internal pore size. The calculated pore sizes through the intrusion pressure using Washburn equation are smaller than those identified through Scanning Electron Microscopy (SEM), which will be presented in Chapter 4.

b) Volume pore size distribution

Same as Ritter & Drake (1945), the volume pore size distribution *D(d)* is based on a cylindrical pores model open at ends, and is defined as the pore volume per unit interval of pore diameter by Equation 2.15

$$D(d) = \frac{P}{D} \cdot \frac{dV}{dP} \tag{2.15}$$

where P and D is the pressure and pore diameter, as in Equation 2.14, and V is the pore volume.

c) Total surface area

The total pore surface area is the area above the intrusion curve, and it is independent of the geometrical pore shape (Rootare & Prenzlow 1967). Thus, it can be calculated integral through the total intrusion volume V_{intru}

$$S = \frac{1}{\gamma \cdot |\cos\theta|} \int_0^{V_{intru}} P dV \tag{2.16}$$

d) Mean pore diameter

The mean pore diameter D_{mean} is calculated by Equation 2.17

$$D_{mean} = 4 \cdot \frac{V_{intru}}{S} \tag{2.17}$$

While the median pore diameter, D_{median} is the pore diameter at which 50% of the total intruded mercury injected into the sample (Dees & Polderman, 1943), the mean pore diameter D_{mean} implies smaller pores rather than median pore diameter.

e) Void ratio

The calculation of void ratio generally being $e = V_v/V_s$, for the interpretation of porosimetry results, the volume of void (V_v) could be represented by the intrusion volume V_{intru}, which is an eigenvalue per gram. Thus, the void ratio identified in MIP (e_M) can be calculated by Equation 2.18, which demonstrates a unit value of per gram for the sample.

$$e_M = V_{intru} \cdot \rho_s \tag{2.18}$$

The total intrusion volume versus pore diameter for creep test P_{010}-OCR1.5-q200 is represented in Figure 2.28 as an example. With the increase of pressure, the intruded volume of Hg is cumulating, meanwhile, the pores of sample are filled from large pores to small ones. The cumulative intrusion and the void ratio identified in MIP (Equation 2.18) can be obtained.

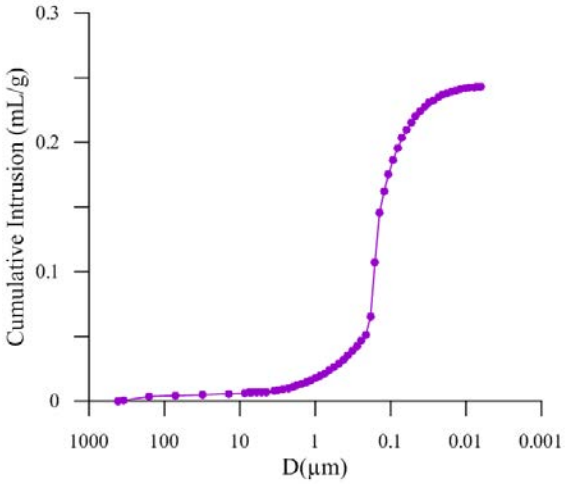

Figure 2.28 Cumulative intrusion curve for test P_{010}-OCR1.5-q200

Based on the intrusion volume, the differential curve of pore size can be plotted, as illustrated in Figure 2.29. Based on the differential curve, we can clearly identify the major pore peak, D_{peak}. which is 0.16 μm in this example.

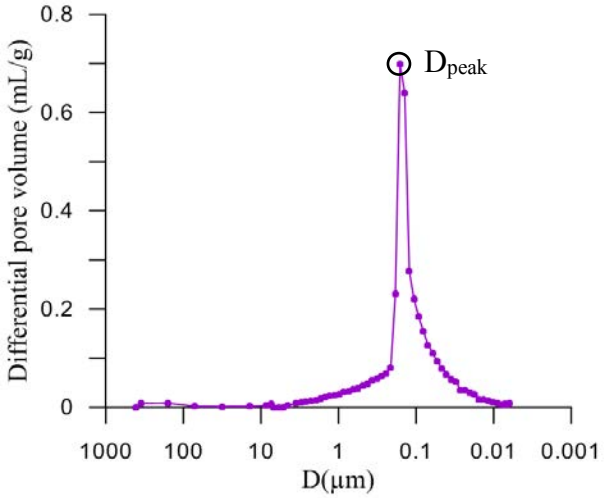

Figure 2.29 Volume pore size distribution for test P_{010}- OCR1.5-q200

2.3.3 Scanning Electron Microscope (SEM) technique and method of analysis

The scanning electron microscope is an analytical device, which is able to capture quickly information on the morphology and chemical composition of a solid object.

2.3.3.1 Principle of SEM

The principle of the scanning electron microscope based on the detection of the signals coming from the interaction of the electrons emitted by a cathode with the sample. The electrons interact with atoms in the sample, producing various signals that contain information about the sample's surface topography and composition. The electron beam is scanned generally in a raster scan pattern, and the beam's position is combined with the detected signal to produce an image.

The most common SEM mode is detection of secondary electrons emitted by atoms excited by the electron beam. The number of secondary electrons that can be detected depends, among other things, on specimen topography. By scanning the sample and collecting the secondary electrons that are emitted using a special detector, an image displaying the topography of the surface is created.

As shown in Figure 2.30, all these radiations are produced simultaneously and make it possible both to observe and to analyze a chosen object.

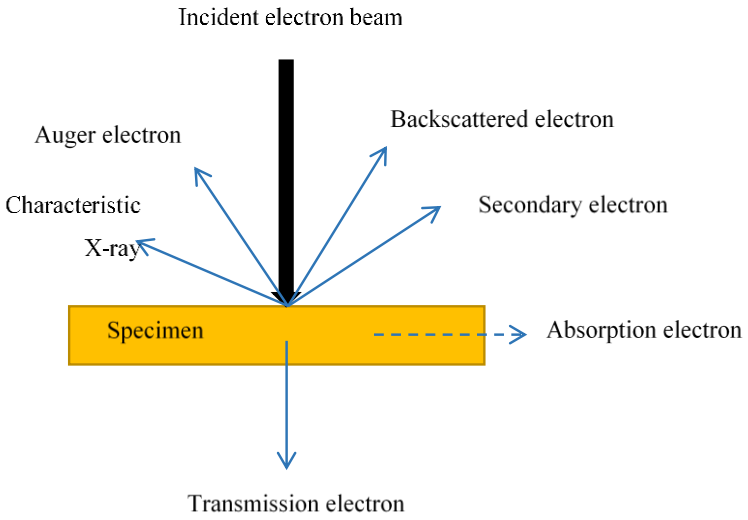

Figure 2.30 The radiation between the beam and the material

2.3.3.2 Observation of SEM images

The observations of surface structures were achieved through secondary electrons, the backscattered electrons, which were generated simultaneously with secondary electrons, carry information on orientation of clay particles and the shape of pores. To operate the SEM observation, the specimens should be pretreated carefully before scanning.

a) Preparation

The cross-sections used for the SEM observations were obtained by fracturing the freeze-dried samples through the pre-engraved abrasion on the surface to create an intact observation plane.

In order to observe conductivity, the specimen surfaces must be covered with a thin layer of metal, which is called metallization.

The metallization consists in evaporating the metal of a heated filament in a high vacuum, the atoms of this metal are deposited on the sample, as in a mist. The metal used is gold, given that its ease of emitting secondary electrons. The apparatus used in this preparation is Sputter Coater 108auto, marked by Cressington Scientific Instruments, which can offer rapid pump down times, fine-grain coatings and negligible sample heating. All these surfaces of specimens after creep and shear were metalized with gold and were reserved intact for image observation.

b) SEM observation

The morphology of specimen surfaces was observed by the apparatus of JSM-6490LV Scanning Electron Microscope by JEOL USA located at the LEM3. In order to obtain a better resolution of the image, the related parameters were: accelerating voltage of 10 kV, working distance 11 mm, and the image format is in Tiff.

Since the SEM observation can only gather the image information at the local level, theoretically, images of quite large qualitative of points should be obtained statistical for identifying the typical morphology of specimen surfaces. In fact, this identification will imply a laborious manual work and is difficult to manage. In the research of this thesis, 20 points for each specimen were selected randomly internal of the cross-section (Figure 2.31), afterwards, a qualitative and semi-quantitative analysis were used for the image processing.

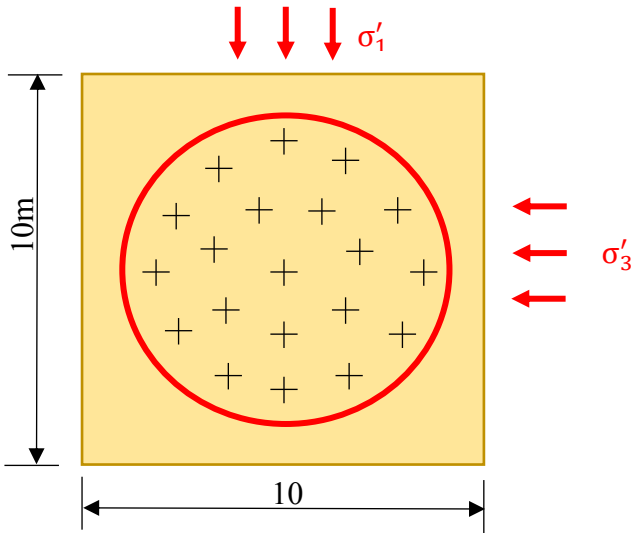

Figure 2.31 Selection of points for SEM observation on specimen surface

2.3.4 Method of analysis of particles and void

The identification of particle orientation and void carried on the SEM images. The key issue is how to identify a clay particle on an optical image, and to define its' orientation. Meanwhile, to separate the void apart from the particle and to fitting the void area simultaneously.

2.3.4.1 Identification of particle orientation

As shown in Figure 2.1, the natural kaolinite particles are rigid platelets, which can be considered as ellipse flakes, especially on the vertical surface from the horizontal point of view on SEM image (Figure 2.32a). Thus, the particles were manually represented by lines having the same dimension and orientation as the particle edge, reproduced on sheet layers by Photoshop (Figure 2.32b). What should be mentioned here is that the particles show by face, zone A and B in Figure 2.34a for example, are not marked here. Because these kind of particles behave general isotropically under external load without showing preferential orientation.

Thereafter, the orientations of the fitted lines on the particles showing by edge could be measured directly through a free access software named Image J.

Image processing of the obtained fitted lines allows the orientation of all the represented particles, with respect to the X-axis (perpendicular to the axial stress) to be calculated. In connection to the fitted picture, the plane was divided into a given number of quadrants, each of them equal to 15˚ referenced to the work by Hicher et al. (2000) and Hattab & Fleureau (2010).

We then counted the number of particles oriented within a given quadrant. By dividing this number by the total number of particles, we obtained a percentage of particles for a given orientation. The angular distribution diagram to be drawn as a rose diagram (Figure 2.32c), giving the percentage of particles showing by edge as a function the orientation (Figure 2.32d). The work of Lafeber (Barton, 1974) has suggested that 400-500 measurements would give a good representation of the distribution on a rose diagram

With this construction, we could see that, for any given isotropic structure, all the radii would have the same length (equal to 1/12= 0.083), shown by the structural isotropic D line in Figure 2.32d.

Following the quantitative statistics analysis on a series of SEM pictures by the method presented above, we could have the global information of the structural orientation inside the soil sample.

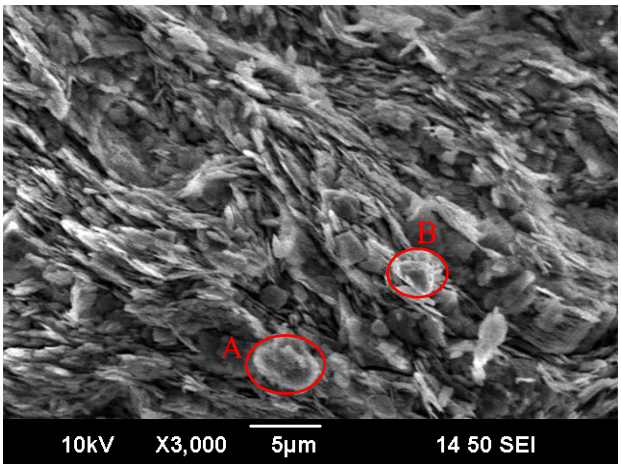

(a)

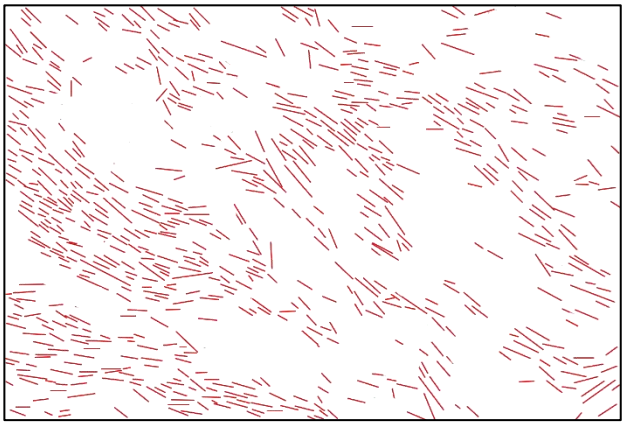

(b)

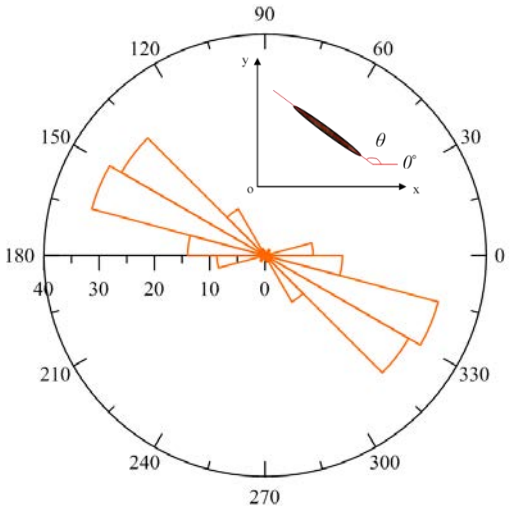

(c)

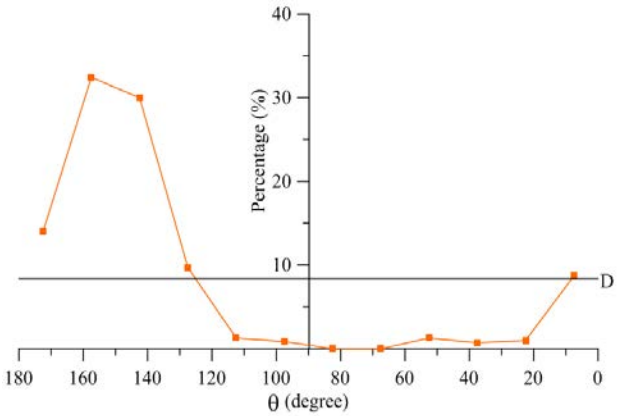

(d)

Figure 2.32 Method of analysis and image treatment for particle orientation (single picture of test P_{010}-NC-q200): (a)SEM image (b) particle characterization (c) rose diagram of angular distribution of particles (d) particles orientation on the vertical plane

In order to quantify the anisotropy of the structure, the parameter of orientation index I_{or} (Hicher et al., 2000) can be defined by in the rose diagram, given by

$$I_{or} = (K + L + M)/(P + Q + R) \tag{2.19}$$

where Q is the zone of maximum orientation intensity Q(%) in a rose diagram, the neighbouring zones P and R and zone L directly perpendicular to Q and its neighbouring zones K and M (Figure 2.33). I_{or} can vary from 1 for an isotropic structure to 0 for a perfectly anisotropic structure.

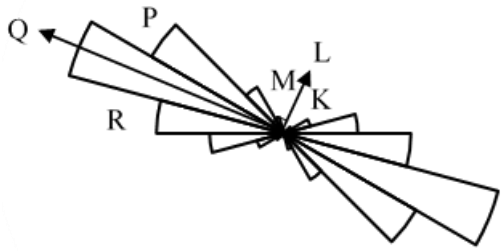

Figure 2.33 Identification of orientation index I_{or}

2.3.4.2 Image processing related to void

On the SEM images, pores show in black, thus Image J can identify the pore properties, such as orientation and mean diameter through a semi-automated process on the original image. Figure 2.34 presents the main process for the identification of pore spaces by Image J on one SEM picture of creep test P_{010}-NC-q200.

By choosing a best threshold value, the identical pores (Figure 2.34c) are obtained according to the original image (Figure 2.34a). However, some pore spaces identified in Figure 2.34c can be blurted together, which will present pore information as a whole space other than individual pores. We thus construct the mage after threshold with classic watershed by Image J, through which more clear boundaries are characterized (Figure 2.34c).

The identified individual pore spaces are shown by ellipses (Figure 2.34e), which the area of each fitted ellipse equal to the corresponding area of the irregular pore space in black. The area of single pixel is 0.001μm^2. Only pore space whose area is over 0.05 μm^2 was used in this research, to avoid introducing errors in identifying too small ellipse that may be image noise.

Through this process, the void information is extracted from the 2D SEM image, thereafter, qualitative and quantitative analyses can be processed on the evolution of pores.

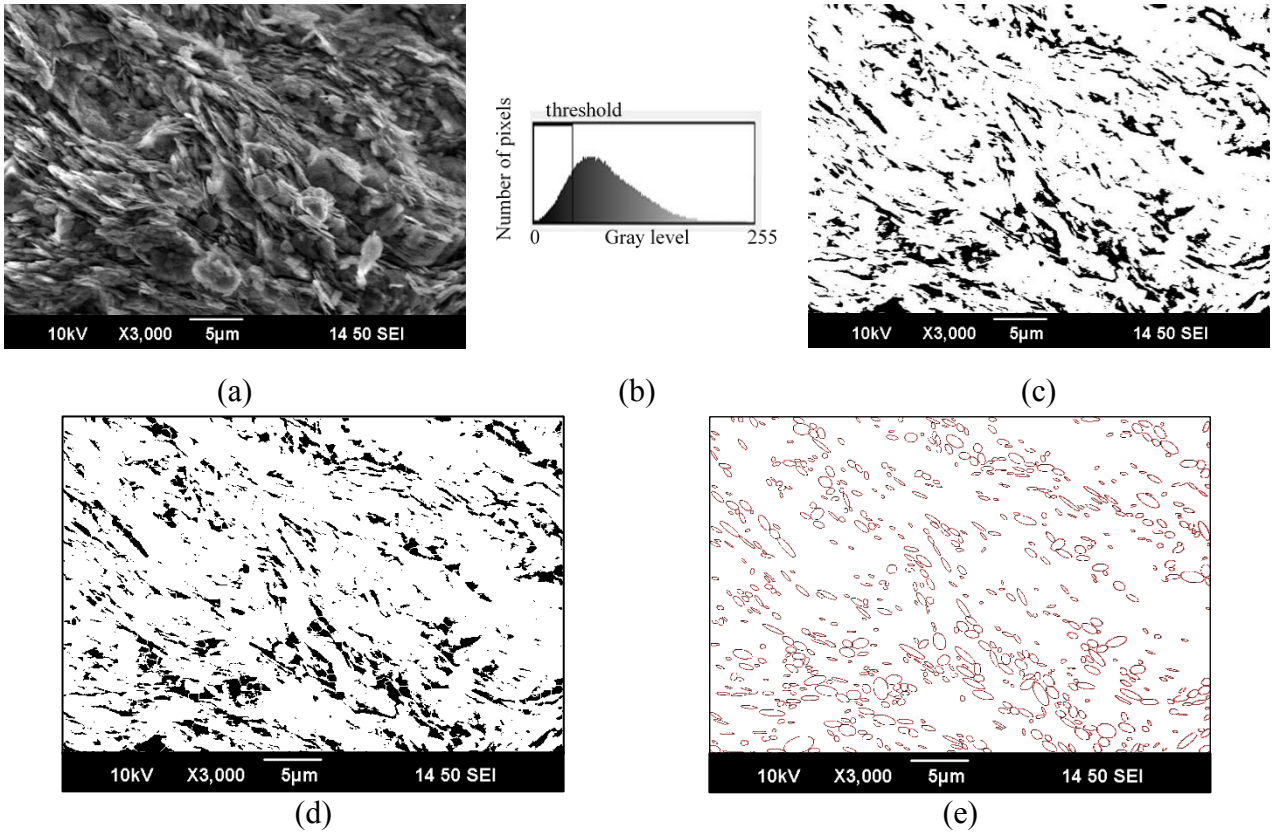

Figure 2.34 Pore space identification (example of test P_{010}-NC-q200): (a) SEM image (b) threshold histogram (c) pore space identification (d) watershed histogram (e) fit with ellipse

Similar with the definition with particle orientation, the orientation of the pores (Figure 2.35) is defined by the angle between the main axis and the X-axis. The length of the secondary axis B. defines the pore diameter here.

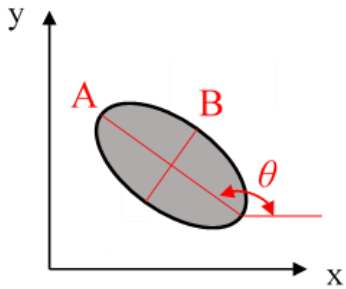

Figure 2.35 Schematic plot of pore dimension

Based on the dimensions of pore by ellipse, we can have the roundness properties of the pores, expressed as

$$R_s = B/A \tag{2.20}$$

The parameter R_s is between 0 to 1, this value gives the shape characteristic of the pores.

According to the area of pore space, we can plot the pore area distribution curves (see Figure 2.36).

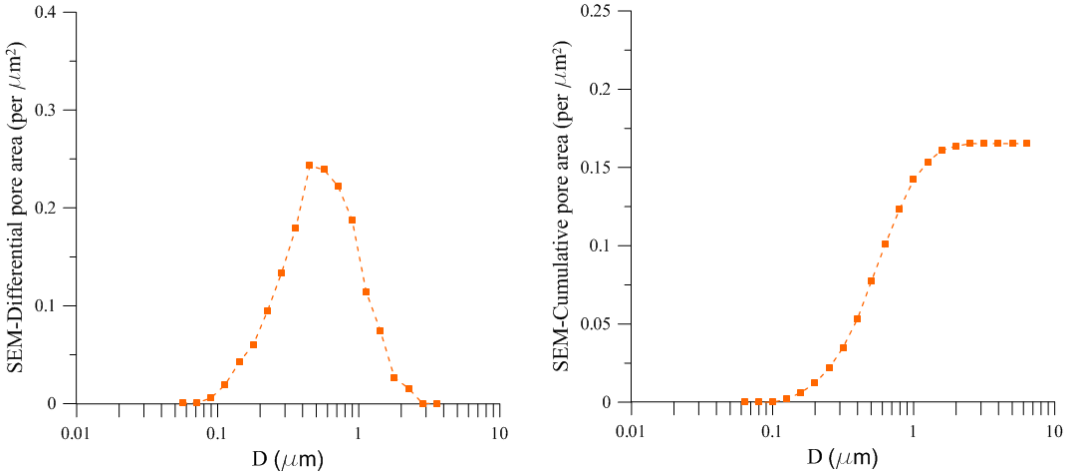

(a) (b)

Figure 2.36 Pore area distribution curve (example of test P_{010}-NC-q200)

Through the cumulative pore area in Figure 2.36b, we can calculate the porosity of the sample, n, given by the pore area divided by the solid area. Thereafter, the void identified by pore space on SEM images (e_S) can be calculated

$$e_S = \frac{n}{1-n} \tag{2.21}$$

2.4 Conclusions

In this chapter, we have presented all the methods and techniques used in this research.

The triaxial creep tests are performed through the advanced GDS testing system on remolded saturated Kaolin K13. The volumetric variation are detected precisely under constant stress condition.

The microscopic research are conducted through scanning electron microscope and mercury intrusion porosimetry to identify the pore space and the local void ratio. The evolution of clay particles are also conducted through SEM.

Chapter 3 Creep behavior and strain mechanisms

We present in this chapter the creep behavior of kaolinite after purely deviatoric triaxial stress paths. In the first step, the aim is to try to understand and to characterize the mechanical behavior under the purely deviatoric stress path, and then to identify the evolution of creep with the variation of stress history.

3.1 Strain mechanisms along purely deviatoric stress path

3.1.1 The 3 domains of deformation on (p'-q) plane

3.1.1.1 Basic notion of purely deviatoric stress path

In axisymmetric triaxial loading the effective stress tensor σ'_{ij} can be divided into two parts, an isotropic part and a deviatoric part expressed as

$$\sigma'_{ij} = p' \cdot c_{ij} + q \cdot \delta_{ij} \tag{3.1}$$

where the mean effective stress $p' = (\sigma'_1 + 2\,\sigma'_3)/3$ and deviatoric stress $q = \sigma'_1 - \sigma'_3$, δ_{ij} is the unit matrix, and c_{ij} is an identity matrix, defining as

$$c_{ij} = \begin{bmatrix} 2/3 & 0 & 0 \\ 0 & -1/3 & 0 \\ 0 & 0 & -1/3 \end{bmatrix}$$

Furthermore, the total generated triaxial strain tensor can also be expressed through the combination of volumetric part and deviatoric part:

$$\varepsilon_{ij} = \varepsilon_v \cdot \delta_{ij} + \bar{\varepsilon}_{ij} \tag{3.2}$$

where $\bar{\varepsilon}_{ij}$ is the deviatoric strain tensor. The total generated strain tensor can be also expressed as:

$$\varepsilon_{ij} = \frac{\varepsilon_v}{3} \cdot \delta_{ij} + \varepsilon_d \cdot d_{ij} \tag{3.3}$$

where ε_d is the deviatoric strain, and d_{ij} is a constant matrix (see Hattab and Hicher, 2006), being:

$$d_{ij} = \begin{bmatrix} 1 & 0 & 0 \\ 0 & -1/2 & 0 \\ 0 & 0 & -1/2 \end{bmatrix}$$

In clayey soils, an increase of isotropic stress always generates a positive contractive volumetric strain ($d\varepsilon^{(p')}_v > 0$), and the increase of deviatoric part products a volumetric strain $d\varepsilon^{(q)}_v$,

which can be positive ($d\varepsilon^{(q)}_v > 0$ for contractant material) or negative ($d\varepsilon^{(q)}_v < 0$ for dilatant material). The sign of $d\varepsilon^{(q)}_v$ depends on the overconsolidated condition. The dilatancy phenomenon is here defined as the negative variation of volume increment $d\varepsilon^{(q)}_v$ caused by the increase of deviatoric stress tensor.

The used method to perform the creep test is to load the specimen up to a given stress level at first, and then to maintain constant stress condition. There are numerous stress paths possibilities to reach a certain stress level, among which σ'_3=constant path and p'=constant path are two typical ones, as illustrated in Figure 1.9 in Chapter1. In the conventional triaxial stress path (at σ'_3=constant) there will be an increment of the deviatoric stress dq accompanied by the increment of dp'. Thus, the obtained total volumetric strain increment $d\varepsilon^{(T)}_v$ during loading could be the combination effects of these two stress increments

$$d\varepsilon_v^{(T)} = d\varepsilon_v^{(p')} + d\varepsilon_v^{(q)} \tag{3.4}$$

Pure deviatoric stress path, wherein the deviatoric stress is applied progressively to a certain creep stress level with p'=constant, allowing us to make a direct measurement of the dilatancy phenomenon. Thus, we can obtain directly the volumetric strain solely caused by the deviatoric part:

$$d\varepsilon_v^{(T)} = d\varepsilon_v^{(q)} \tag{3.5}$$

Once the dilatancy behavior is clearly identified since monotonic loading, the obtained total volumetric strain after stress is maintained constant can be written as the combination of strain occur during loading and creep

$$\mathrm{d}\varepsilon_{\mathrm{v}}^{(\mathrm{T})} = \mathrm{d}\varepsilon_{\mathrm{v,load}}^{(\mathrm{q})} + \mathrm{d}\varepsilon_{\mathrm{v,creep}} \tag{3.6}$$

By removing the component in loading phase $d\varepsilon_{v,load}$, one can have directly the values of creep deformation, thus, the contractancy or dilatancy trend during creep can directly be identified by the sign of the second component of the volumetric strain, $d\varepsilon_{v,creep}$.

3.1.1.2 Volume change condition in the (p'-q) plane

Based on the purely deviatoric stress path tests on remoulded Kaolinite, Hattab & Hicher (2004) gave transformation boundaries of different volumetric strain domains (see Figure 3.1). In the p'-q plane, the M line corresponds to the critical state, ς is the maximum strength envelop. The

contraction domain for OCR≤2.5 is limited by the critical state line M, and the dilatancy domain is obtained for OCR≥2.5 which is limited by the maximum strength envelop ς. Moreover, these two domains are limited by a third domain of no-volume change, wherein M^*, m^*_2 and m^*_1 are the boundaries correspond to the beginning of dilation or contraction.

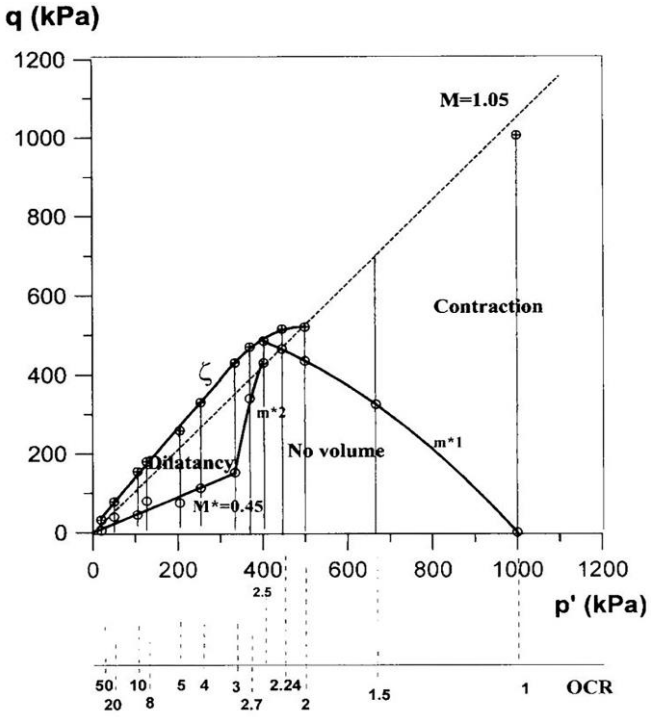

Figure 3.1 Volume change condition in the (p'-q) plane (Hattab and Hicher, 2004)

Hattab & Hicher (2004) demonstrated that the obtained no-volume change zone, in the purely deviatoric stress path tests, corresponds to the pseudoelastic volumetric domain defined by Biarez & Hicher (1994), where the volumetric strain depends only on the mean effective stress variation. Beyond the pseudoelastic domain, the development of volumetric strain variation depends on both the deviatoric stress and the mean effective stress changes.

3.1.2 The Kaolin K13 clay behavior

Three groups of drained triaxial creep tests, distinguished by different preconsolidated pressures and different OCRs shown in Table 2.6, were performed on remolded Kaolin K13. The mechanical behavior on isotropic and monotonic loading phases (before creep phase) were represented here.

3.1.2.1 On isotropic loading phase

From the results obtained on isotropic consolidation, as the example illustrated in Figure 2.15, the evolution of void ratio with mean effective stress in triaxial loading for test P_{010}-OCR1.5-q200 is shown in Figure 3.2.

Based on the *e-log p′* curve, the compression index thus being:

$$C_c = \frac{\Delta e}{\Delta \log p'} = 0.293 \tag{3.7}$$

And the swelling index is computed by Equation 3.8:

$$C_s = -\frac{\Delta e}{\Delta \log p'} = 0.078 \tag{3.8}$$

The obtained value of C_c is consistent with the compression index proposed through the correlation with liquid limit and plastic limit proposed by Biarez & Favre (1975) through Equation 3.9, with w_L=42% and w_p=21% for kaolin.

$$C_c = 0.009(w_L - 13) = 0.12\, w_P = 0.26 \tag{3.9}$$

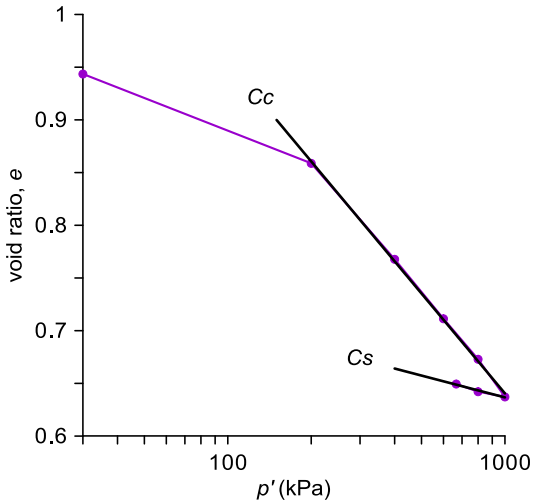

Figure 3.2 Evolution of void ratio in isotropic path of Kaolin for test P_{010}-OCR1.5-q200

Figure 3.3 shows the curves obtained in isotropic loading in *e-log p′* plane for test series P_{010} which the preconsolidation pressure p'_{0i} =1000 kPa. The compression curves dispersion exists, principally because of the minor dispersion of initial void ratios. The compression index C_c can be calculated through Equation 3.10, which indicates an average value of all linear slopes of the compression curves:

$$C_c = \frac{\sum_{i=1}^{n=6} C_{ci}}{n} = 0.288 \tag{3.10}$$

Each isotropic loading curve ends in the point (e_{fi}, p'_{0i}=1000 kPa). Hence, the C_c line can be obtained through the line which slope equals to 0.288, passing through the point (e_f, p'_{0i}) illustrated in Figure 3.4:

$$e_f = \frac{\sum_{i=1}^{n=6} e_{fi}}{n} = 0.677 \tag{3.11}$$

For the identification of *Cs* line:

$$C_s = \frac{\sum_{i=1}^{n=4} C_{si}}{n} = 0.085 \tag{3.12}$$

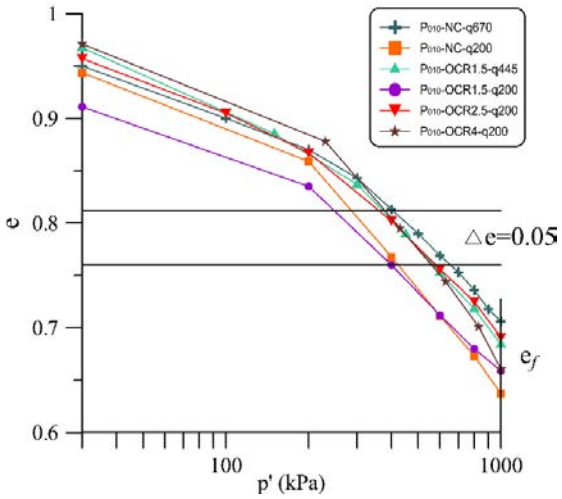

Figure 3.3 Identification of Cc for test group P_{010} during isotropic path

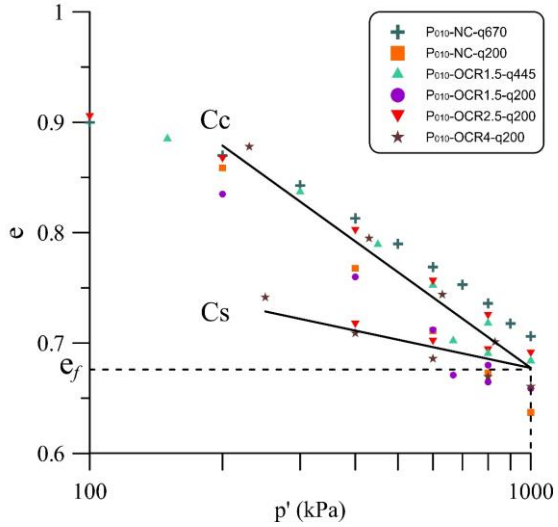

Figure 3.4 Identification of Cs for test group P_{010} during isotropic path

Similarly, the parameter C_c and C_s deduced in *e-log p'* plane with test p'_{0i} = 200 kPa and 800 kPa shown in Figure 3-1 and Figure 3-2 in Annex Chapter 3. All these parameters identified through different groups of tests are summarized in Table 3.1. We can see that the behavior on isotropic path with different preconsolidation pressure is quite similar. Therefore, the average value of C_c=0.283 and C_s=0.088 from the three groups of compression curves were taken as the representative compression index and swelling index of the Kaolin. These values are consistent with the values identified by Ighil-Ameur (2016) in the same material on both oedometric loading and isotropic loading.

Table 3.1 Compression index C_c and swelling index identified C_s on isotropic path

Test	p'_{0i} (kPa)	C_c	C_s
P_{010}	1000	0.288	0.085
P_{02}	800	0.292	0.091
P_{08}	200	0.268	0.089
Average value		0.283	0.088

3.1.2.2 On purely deviatoric stress path

After the isotropic consolidation, the deviatoric stress q is applied instantly from zero to the target value, meanwhile, the mean effective stress is maintained constant. The loading procedure consists in decreasing of the lateral stress σ'_3 and increasing of the axial stress σ'_1 (Figure 3.5).

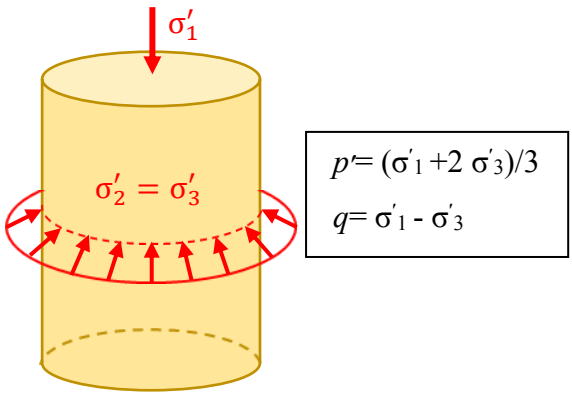

Figure 3.5 Contract condition in classic triaxial test

The loading velocity for test group P_{010} is 0.0025mm/min through constant strain control loading program. For test groups P_{02} and P_{08}, the stress control loading method was used, and an equivalent loading velocity is calculated by Equation 3.13

$$V = \frac{h_0 \cdot \varepsilon_{1,loading}}{t_{loading}} \tag{3.13}$$

where h_0 is the height of sample after consolidation, $t_{loading}$ is time duration to perform the purely deviatoric loading, and $\varepsilon_{1,loading}$ is the axial strain at the end of the purely deviatoric loading.

The loading velocity for all these three group of tests are summarized in Table 3.3. It is seen that the computed equivalent stress control loading velocities for test groups P_{02} and P_{08} are in general no more than that for test P_{010} by strain control loading. Thus, the drainage condition is considerable well maintained under both loading programs.

With the calculated loading velocity, the deviatoric stress was increased to the target value (q_{creep} in Table 2.6). And most of the final values of deviatoric stress are supposed to within the critical state. Thus, in order to determine the critical state stress condition which corresponds to the deviatoric stress at ultimate state (q_f), a conventional drained shear test was performed on a normally consolidated sample with preconsolidation pressure p'_{0i} = 200 kPa, the test results were represented in Figure 3.6.

With the increase of q, the axial strain develops with q until the critical state. A value of q_f = 163 kPa was identified through the peak strength in the plane of (ε_1-q) and (p'-q), giving the plasticity state which corresponds to the line of $M = q_f / p'_{0i}$ = 0.815. Results of q_f by Ighil-Ameur (2016) on the same material under σ'_3= constant loading gave a value of M = 0.857, which is close to the value obtained in purely deviatoric stress path. Therefore, value of 0.857 is taken as the representative value for M in the research of this thesis.

The M line is an intrinsic property of the clay relating to the internal friction φ by the relationship in compression

$$M = \frac{6 \sin \varphi}{3 - \sin \varphi} \tag{3.14}$$

The internal friction of Kaolin K13 is equals to 22°, slightly smaller but close to those obtained in literatures (Table 3.2). The small value of φ here is most likely due to the deviatoric stress path, where the sample could not reach a perfect plasticity.

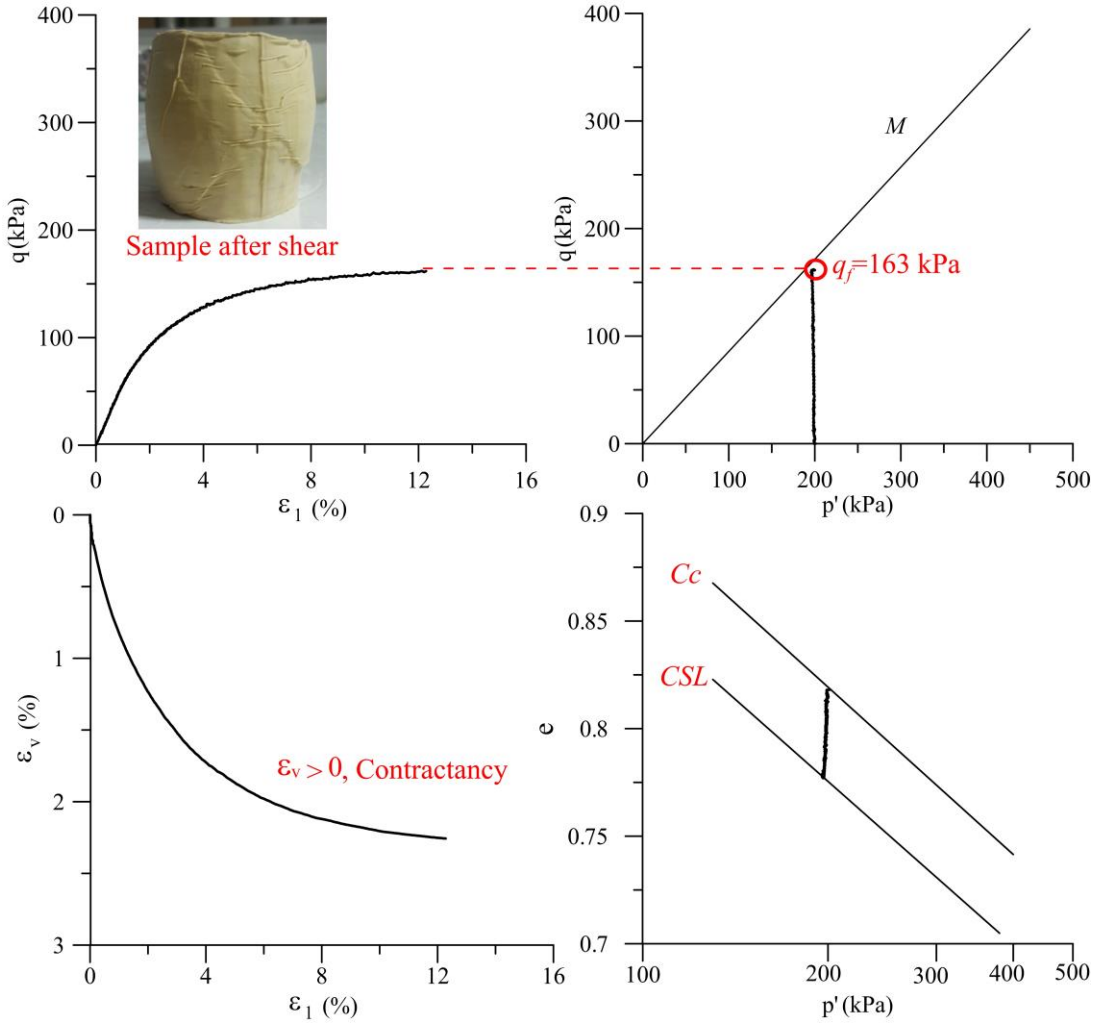

Figure 3.6 Mechanical behavior of Kaolin K13 under *p'*= constant loading

In the (*e-logp'*) plane in Figure 3.6, the difference of Δ*e* represents the difference between the isotropic consolidation line and the perfect plasticity line, which equals to 0.057. The value of Δ*e* used in this research is very close to the values found in the literature for Kaolin (Table 3.2).Thus, a referenced value of 0.06 is taken as the difference between *Cc* and *CSL* lines in (*e-logp'*) plane for the 3 groups of tests in this research.

Table 3.2 Parameters of critical state for Kaolin material

	Φ (°)	Δ*e*
Hattab (1994)	26.5°	0.05
Bouziri (2007)	25°	0.056

Hammad (2010),	25.8°	0.06
Ighil-Ameur (2016)	22°	0.051

With the referenced critical state, the deviatoric stress at ultimate state for each test is taken as $q_f = p'_j \cdot M$, and the stress level being $SL = q_{creep}/q_f$. Thus, all the triaxial tests were loaded, on constant p' stress path with corresponds loading velocity, until a certain stress level. The loading program is shown in Table 3.3.

Table 3.3 Constant p' loading triaxial tests

Test No.	p'_{0i} (kPa)	p'_j (kPa)	q_{creep} (kPa)	*Velocity* (mm/min)	$t_{loading}$ (min)	$\eta = \frac{q_{creep}}{p'_j}$	$SL = \frac{q_{creep}}{q_f}$
P_{010}-NC-q670	1000	1000	670	0.0025	2370	0.67	0.78
P_{010}-NC-q200		1000	200		620	0.20	0.23
P_{010}-OCR1.5-q445		667	445		2140	0.67	0.78
P_{010}-OCR1.5-q200		667	200		900	0.30	0.35
P_{010}-OCR2.5-q200		400	200		880	0.50	0.58
P_{010}-OCR4-q200		250	200		720	0.80	0.93
P_{02}-OCR4-q43	200	50	40	0.0012	1000	0.79	0.93
P_{02}-OCR5-q30		40	30	0.0010	1000	0.70	0.83
P_{02}-OCR5-q43		40	43	0.0029	1000	1.08	1.26
P_{08}-OCR16-q43	800	50	43	0.0009	1000	0.86	1.0

The mechanical behavior for each group of tests is analyzed in the following planes:

ε_1-q: evolution of axial strain as a function of deviatoric stress

p'-q: loading path in the plane of invariants

ε_1- ε_v: evolution of axial strain as a function of volumetric strain

e-log p': evolution of void ratio as a function of the mean effective stress

- Test group P_{010}

Results of 6 creep tests after purely deviatoric stress path of group P_{010} are presented in Figure 3.7. It is seen in that the mean effective stress was well maintained constant along the purely deviatoric stress path, and the deviatoric stress was well reached the target value.

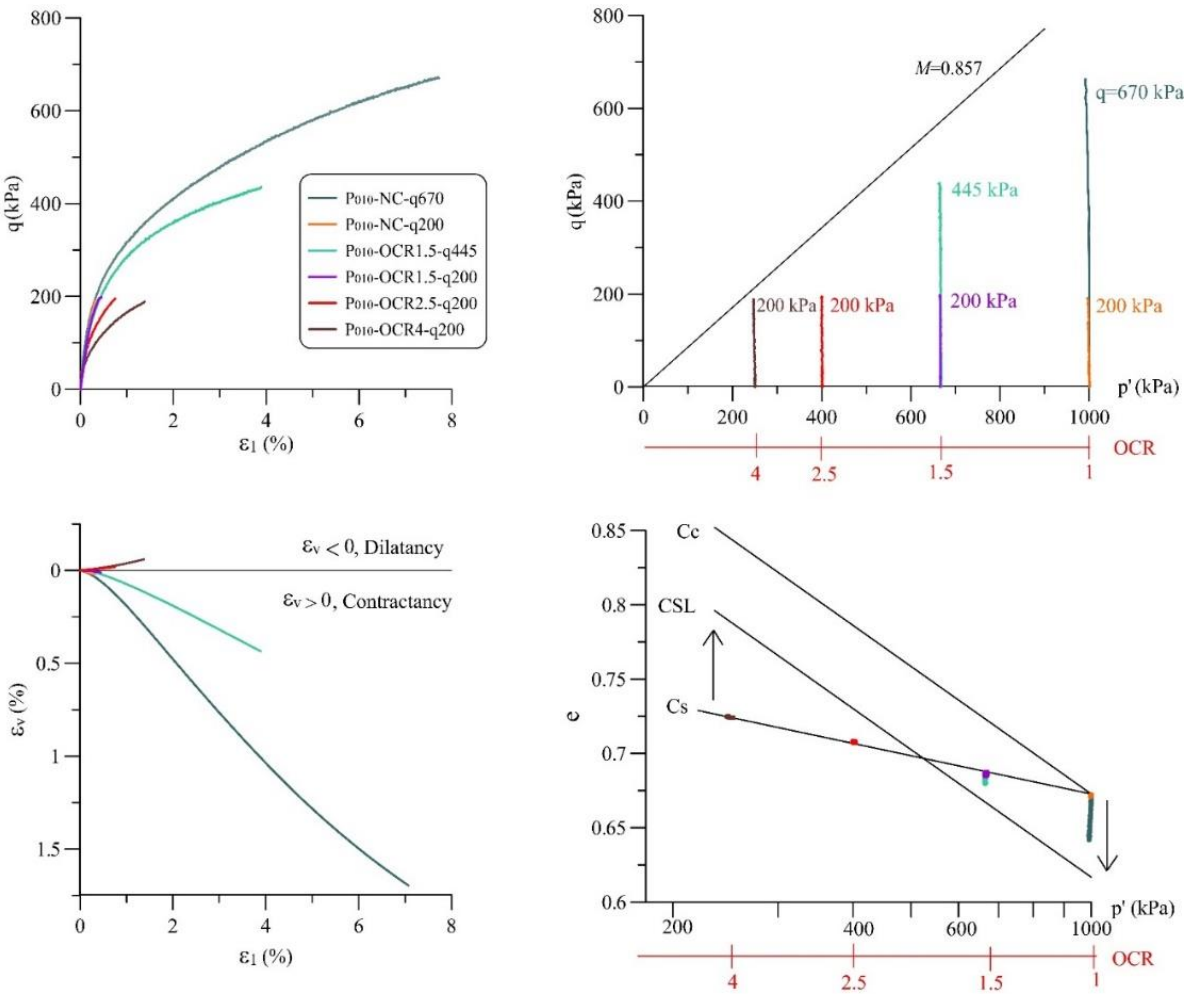

Figure 3.7 Triaxial tests of test P_{010} (p'_{0i} = 1000 kPa) for Kaolin along p' constant stress paths

The evolution of volumetric strain as a function of axial strain in the plane of (ε_1- ε_v) shows different tendencies with variations of stress conditions. For normally consolidated and lightly overconsolidated specimens (OCR<2.5), contractancy was detected corresponding to a decrease of void ratio towards the critical state line in (*e-log p'*) plane. While for the highly overconsolidated samples, dilatancy was observed accompanied by an increase in void ratio heading to the critical state in the plane of (*e-log p'*). Moreover, quite consistent curves were obtained for tests with the same OCR and greater deformation was developed under higher stress level (e.g., test P_{010}-NC-q200 and P_{010}-NC-q670).

The mechanical behaviors identified here on Kaolin K13 are consistent with those identified by Hattab & Hicher (2004) on Kaolin P300, Ighil-Ameur (2016) on Kaolin K13 and by Shimizu (1982) on Fujinanori clay through *p'*= constant loading triaxial tests.

- Test group P_{02} and P_{08}

Experimental results with different preconsolidation pressures (p'_{0i}= 200 kPa and 800 kPa) were represented in Figure 3.8 and Figure 3.9.

It can be seen that for highly overconsolidated specimens, a clear dilatancy evolved for both two group of tests, illustrated in (*e-log p'*) plane in Figure 3.8 and Figure 3.9. Moreover, the same dilatation tendency was identified here for highly overconsolidated samples as for group P_{010}.

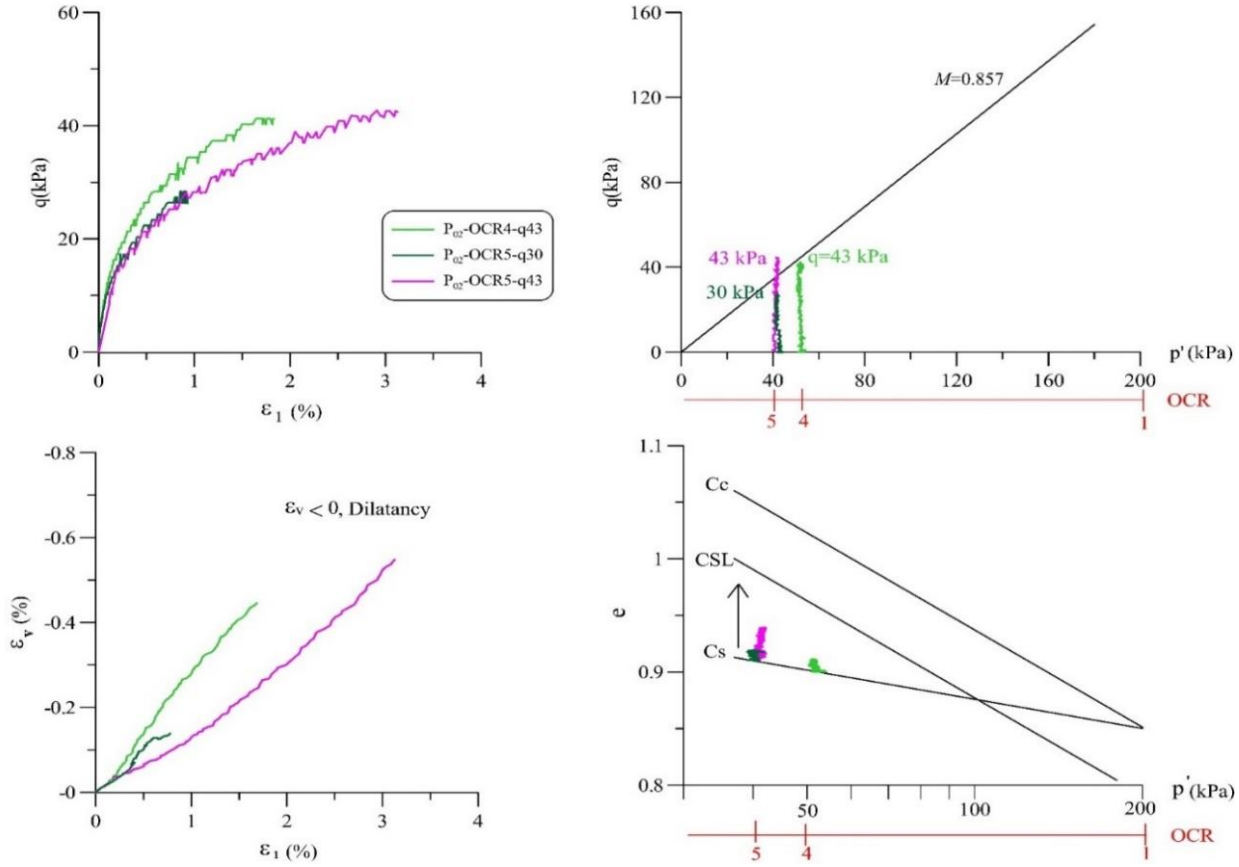

Figure 3.8 Triaxial tests of test P_{02} (p'_{0i} = 200 kPa) for Kaolin along p' constant stress path

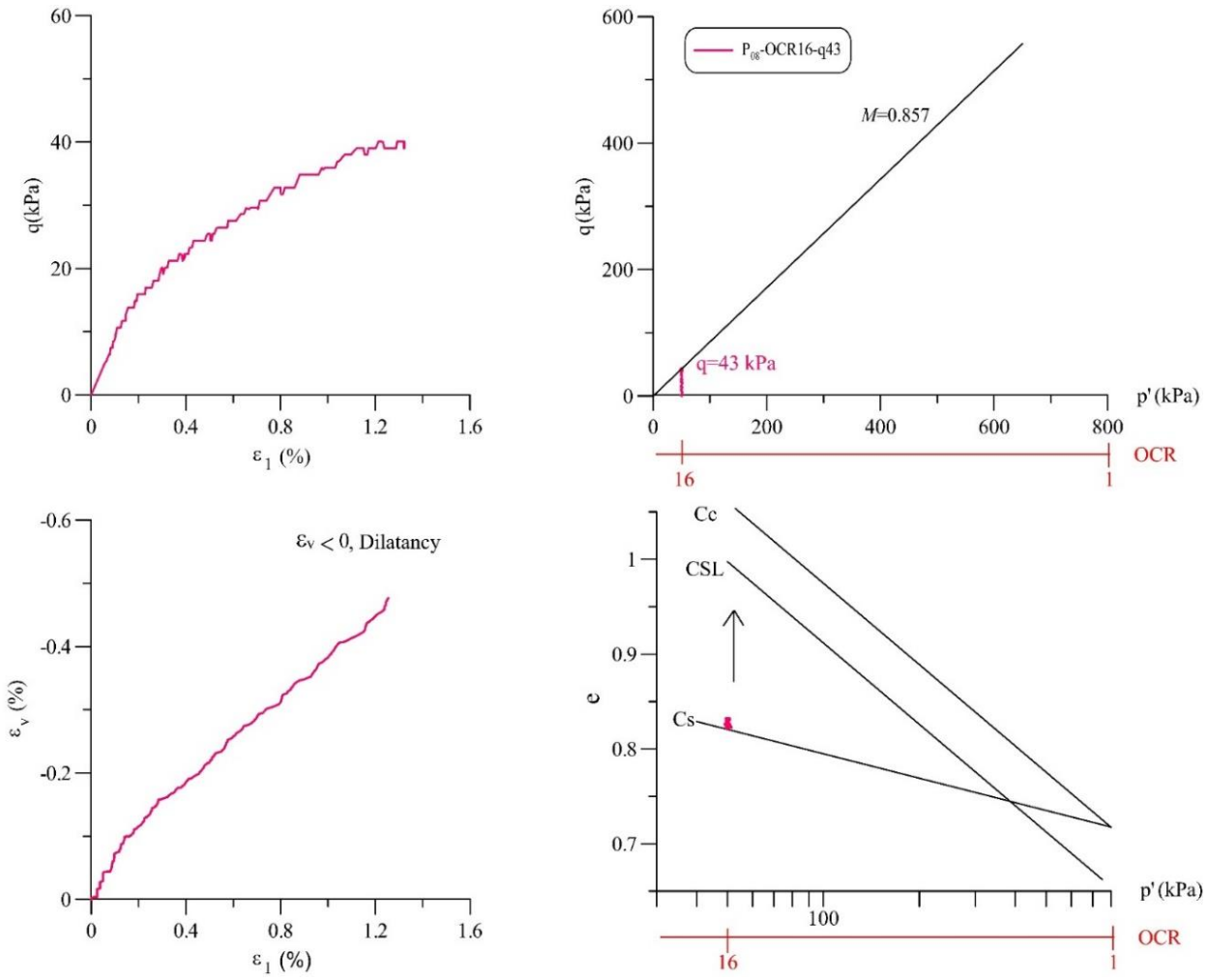

Figure 3.9 Triaxial tests of test P_{08} (p'_{0i} = 800 kPa) for Kaolin along p' constant stress paths

3.1.2.3 Volumetric evolution and the strain domains in (p'-q) plane

In order to identify more precisely the evolution of volumetric strain under the purely deviatoric stress path, the experimental results were further plotted in the plane of (q-ε_v), shown from Figure 3.10 to Figure 3.12.

- Test P010

The volumetric strain evolution as a function of the deviatoric stress along the purely deviatoric stress loading for OCR values between 1 and 4 of group P_{010} was represented in Figure 3.10. The results show globally that:

For normally consolidated sample, contractancy was detected from the beginning of the loading, where positive value of ε_v was obtained in the plane (q-ε_v). The contraction is greater under higher stress level with ε_v = 0.024% under q = 200 kPa, and ε_v = 1.80% under q = 670 kPa.

For lightly overconsolidated samples (1.5< OCR<2.5), slight volume changes were obtained, the final volume strain of the plane (q-ε_v) for test P_{010}-OCR1.5-q200 was measured about 0.008% at the end of monotonic loading. When the deviatoric stress was increased (case of P_{010}-OCR1.5-q445 test), more obvious deformation in contraction was observed, with ε_v = 0.44% at the end of loading.

For highly overconsolidated sample (case of OCR = 4), a slight dilatancy was observed after q_v reaches about 90 kPa following by a clear dilatancy trend, with ε_v = -0.06% at the end of loading.

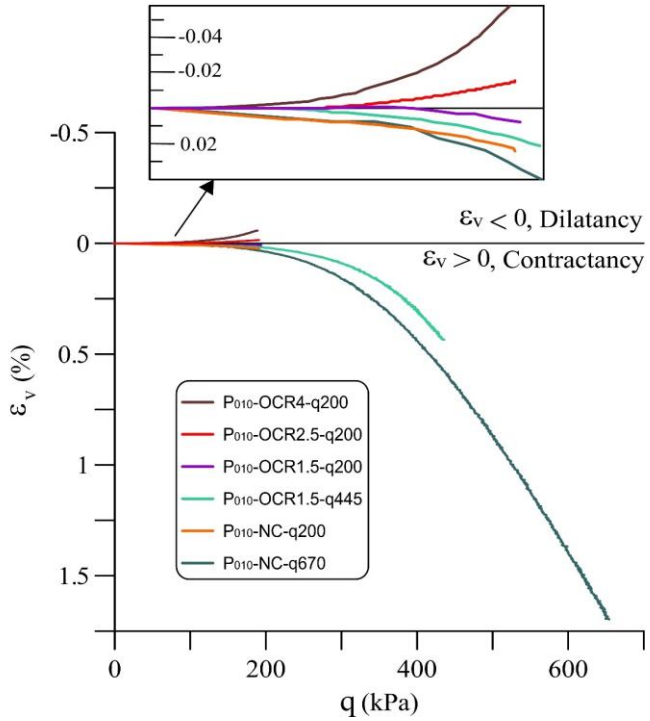

Figure 3.10 Volumetric strain versus q on purely deviatoric stress paths of test P_{010}

- Test P_{02} and P_{08}

The evolution of volumetric strain as a function of deviatoric stress is shown in Figure 3.11 and Figure 3.12 when the isotropic consolidation stress changes (p'_{0i} = 800 kPa and 200 kPa).

Similar dilatancy trends were detected in high OCR values for p'_{0i} = 800 kPa and 200 kPa as for p'_{0i} = 1000 kPa. For test P_{02}-OCR4-q43 in Figure 3.11, the deviatoric stress starting to introduce the dilation is about 13 kPa and after $q_v \approx$ 13 kPa a clear dilatancy trend was detected with ε_v =-

0.51% at the end of loading. While for test P_{08}-OCR16-q43 in Figure 3.12, the dilatancy was increased clearly after $q_v \approx 8$ kPa.

Even though the test results scattered slightly with lower preconsolidation pressure ($p'_{0i} = 800$ kPa and 200 kPa) than that with higher pressure, the dilatancy phenomenon was still well detected along all the purely deviatoric loading phase.

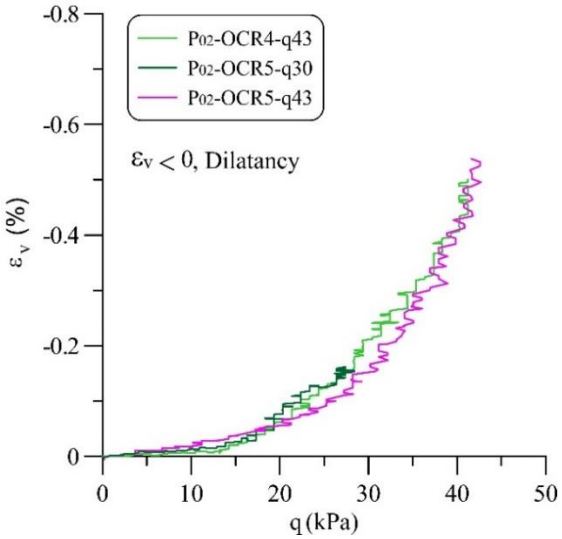

Figure 3.11 Volumetric strain versus q on purely deviatoric stress paths for test P_{02}

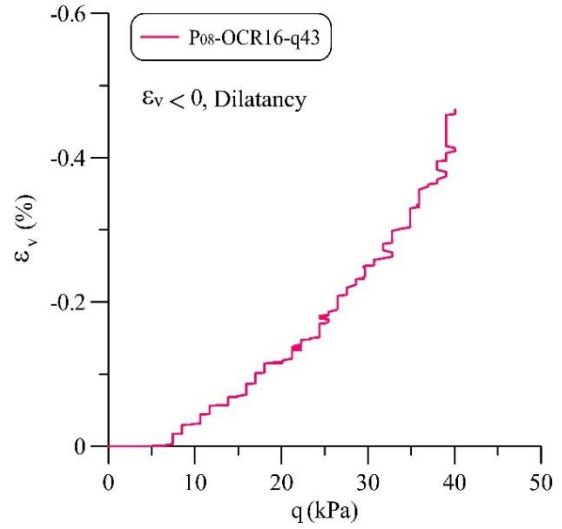

Figure 3.12 Volumetric strain versus q on purely deviatoric stress paths for test P_{08}

Overall, when subjected to a pure deviatoric loading, the overconsolidated specimens show dilation after having reached a given value of deviatoric stress (q_v), while for normally consolidated and lightly overconsolidated samples are contractant. These results demonstrate that the variation

of volumetric strain for Kaolin K13 in this research is generally consistent with the different volumetric domains identified by Hattab and Hicher (2004) presented here in Figure 3.1.

Therefore, for this study, referenced boundaries of these strain mechanism domains were introduced and superimposed in (p'-q) plane, see Figure 3.13 to Figure 3.15. Where M^* is a straight line for OCR≥3, representing the transition between the no volume change and the dilatancy behavior in the high overconsolidated domain. The values of q_v identification for three group of tests gives an average stress level corresponding to the characteristic state of M^*= 0.3; m^*_1 characterizing the beginning of contraction, and its shape is similar to the shape of the yield surface in Cam Clay Model; the m^*_2 connects the M^* line and the ζ envelope.

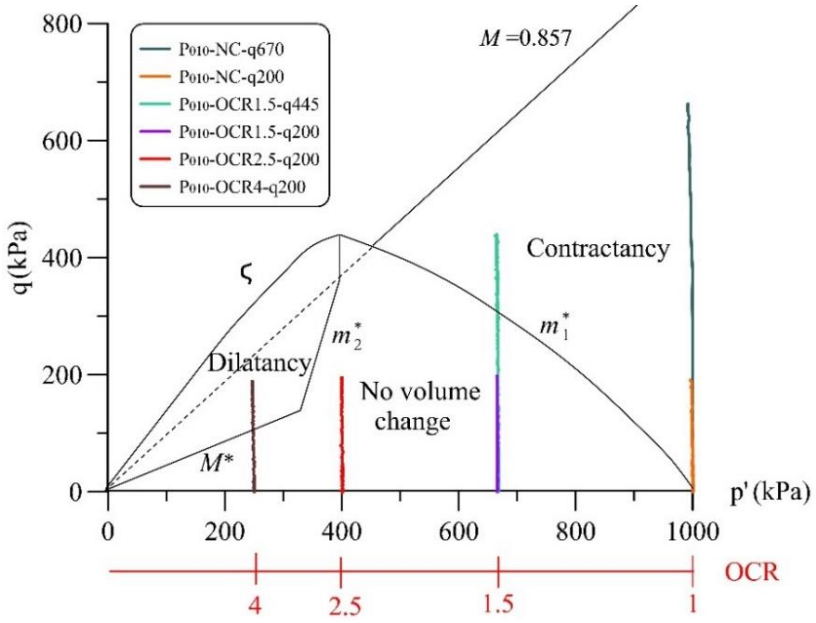

Figure 3.13 Volume change condition in the (p′-q) plane for test P_{010}

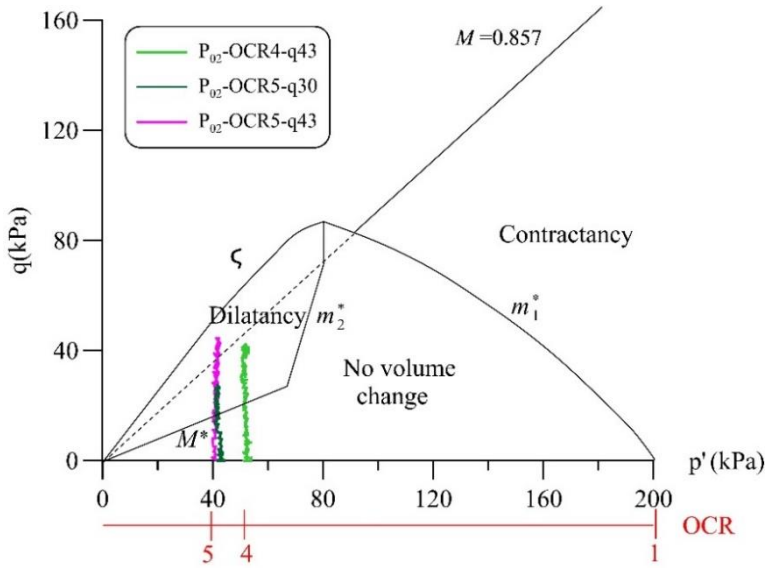

Figure 3.14 Volume change condition in the (p′-q) plane for test P_{02}

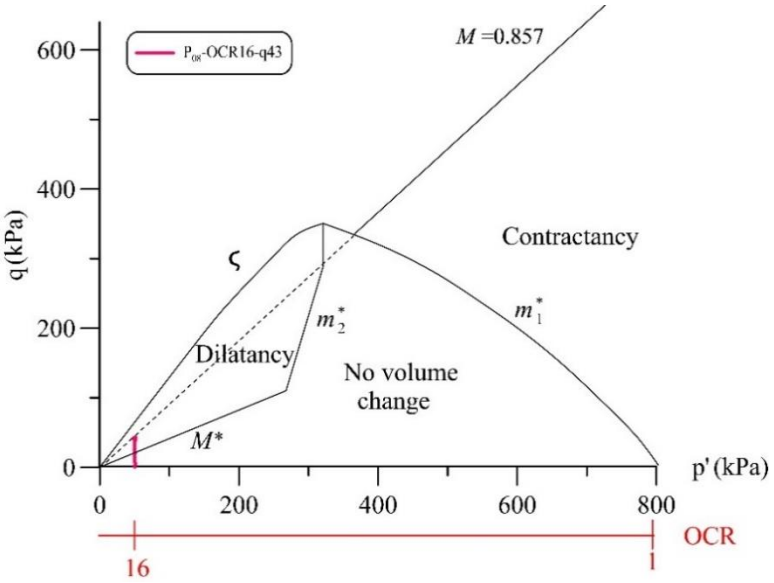

Figure 3.15 Volume change condition in the (p′-q) plane for test P_{08}

3.1.3 Discussions

Given the three domains of the behavior defined above, the approach to follow the creep process was to perform different creep tests on Kaolin K13, with different stress levels located in the identified volumetric domains.

For test P_{010} with p'_{0i}=1000 kPa, the purely deviatoric loading phase was terminated in 3 strain domains. Thus, the evolution of creep deformation in each domain is supposed to be followed.

Moreover, with the variation of stress condition, the stress-dependency of creep behavior may be detected.

Test series P_{02} and P_{08} with p'_{0i}=200 kPa and 800 kPa presents the highly overconsolidated samples creep in dilatancy domain. The dilative creep phenomenon was supposed to be highlighted in these tests.

In this manner, through an experimental method, the creep mechanism is analyzed deeply via the strain-stress-time changes.

3.2 Identification of creep behavior related to the dilatancy phenomenon

3.2.1 Introduction of the creep phase

After q is loaded up to the target value in a single stage, both p' and q are maintained constant, the creep phase start thereafter. The duration for creep observation for all the 3 groups of tests were at least 7 days.

Based on the strain mechanism domains identified along purely deviatoric loading from Figure 3.13 to Figure 3.15, the constant stress condition of creep phase were marked in the plane of (p'-q) illustrating from Figure 3.16 to Figure 3.18.

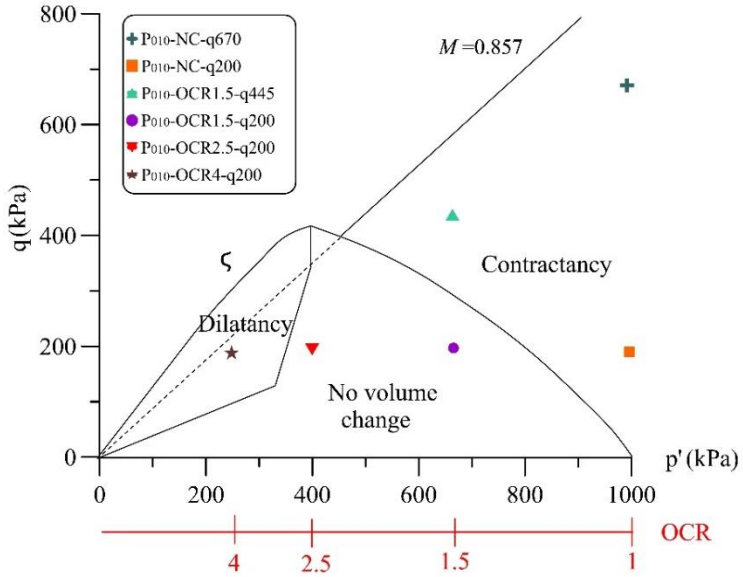

Figure 3.16 Creep stress conditions in strain domains for test P_{010}

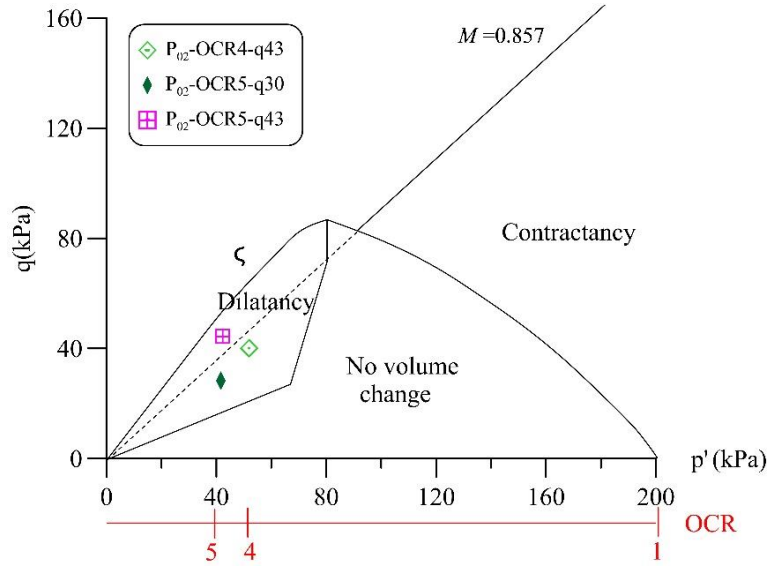

Figure 3.17 Creep stress conditions in strain domains for test P_{02}

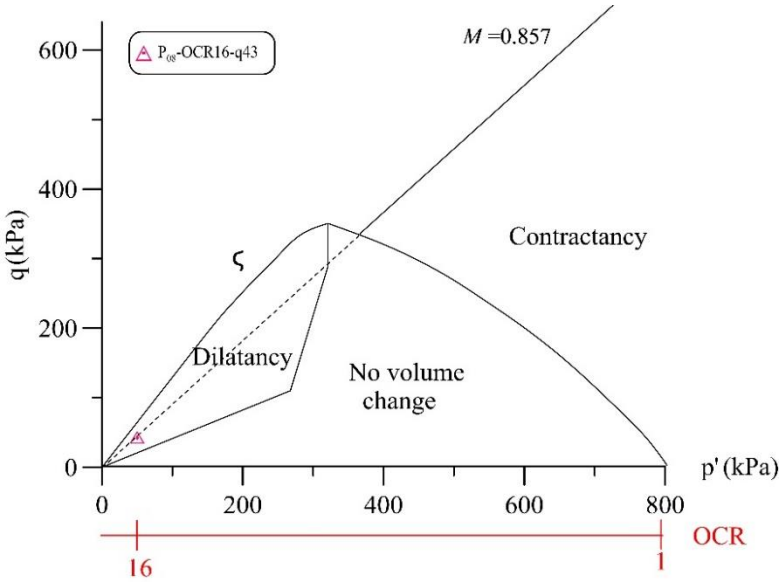

Figure 3.18 Creep stress conditions in strain domains for test P_{08}

The evolution of creep strain thus would be represented according to different strain domains and stress levels. The mechanical behavior during creep for each group of tests is analyzed in the following planes:

ε_1- ε_v- q: evolution of volumetric strain as a function of axial strain and deviatoric stress

e-log p': evolution of void ratio as a function of the mean effective stress

3.2.2 Creep analyses in (ε_1- ε_v- q) and (*e-log p'*) plane

- Test P_{010}

Figure 3.19 to Figure 3.21 give the results of 6 creep tests performed after purely deviatoric stress paths for group P_{010} with p'_{0i} = 1000 kPa. Under the constant sustained stress, all specimens exhibited creep deformation, both in axial and volumetric aspects. It can be seen that:

In the contractancy domain for normally consolidated (P_{010}-NC-q667 and q200) and lightly overconsolidated samples (P_{010}-OCR1.5-q445), contraction was obtained (Figure 3.19). Which corresponds to a decrease of void ratio towards to the critical state line in the plane of (*e-log p'*) in Figure 3.21. The results in creep phase clearly highlighted that the deformation tendency followed that obtained in the purely deviatoric stress path phase.

In dilatancy domain, for highly overconsolidated soil (case of P_{010}-OCR4-q200 in Figure 3.20), an obvious dilatancy was detected from the beginning of creep. The final value of volumetric strain during creep measurement was ε_v = -0.547%, which is almost 10 times the value at the end of monotonic loading (ε_v = -0.057%). Similar dilatancy trends were also observed in high OCR values for tests with p'_{0i} = 800 kPa and 200 kPa. Due to the dilation in this creep phase, a continuously increase of void ratio was obtained heading to the critical state line (see Figure 3.21).

More complex volumetric strains tendency was obtained within the pseudoelastic volumetric domain for lightly overconsolidated specimens (cases of P_{010}-OCR1.5 and 2.5-q200 in Figure 3.20). This result, showing the form of alternating very small contractancy/dilatancy or dilatancy/contractancy, is most likely due to the monitoring system trying to maintain the constant stress in the (p'- q) plane within a narrow variation band.

Figure 3.22 and Figure 3.23 show the different steps of stress variation in maintaining p' and q constant for these two tests. As we can observe, the scattering of the stresses induces fluctuation in the obtained volumetric strain. At the early stages of creep, the global slight decrease of stress ratio η induces weak contraction for OCR=1.5 (see Figure 3.22), while a tiny increase of η induces small magnitude of dilation for OCR=2.5 (see Figure 3.23). Thereafter, almost no-volume change was observed when the stresses were maintained idealized constant in the later part of creep measurement. This tendency is especially obvious for OCR = 2.5 test in Figure 3.23. Consequently, in this work, we may assume that a no volume change is developed at these two stress levels located in the pseudoelastic volumetric domain.

Therefore, after the purely deviatoric stress path, the domain in which the creep test is conducted obviously governs the development of volumetric creep deformation.

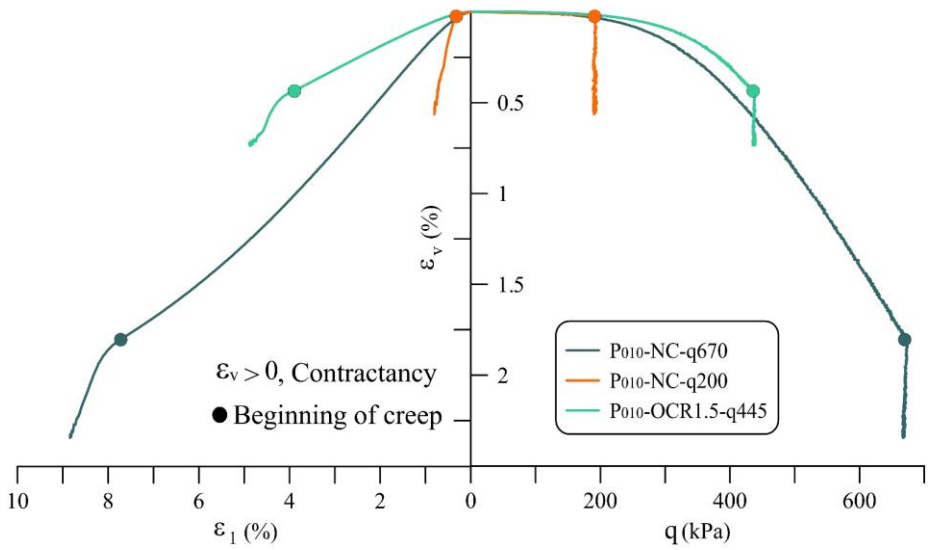

Figure 3.19 Evolution of strains in contractancy domain for the P_{010} tests

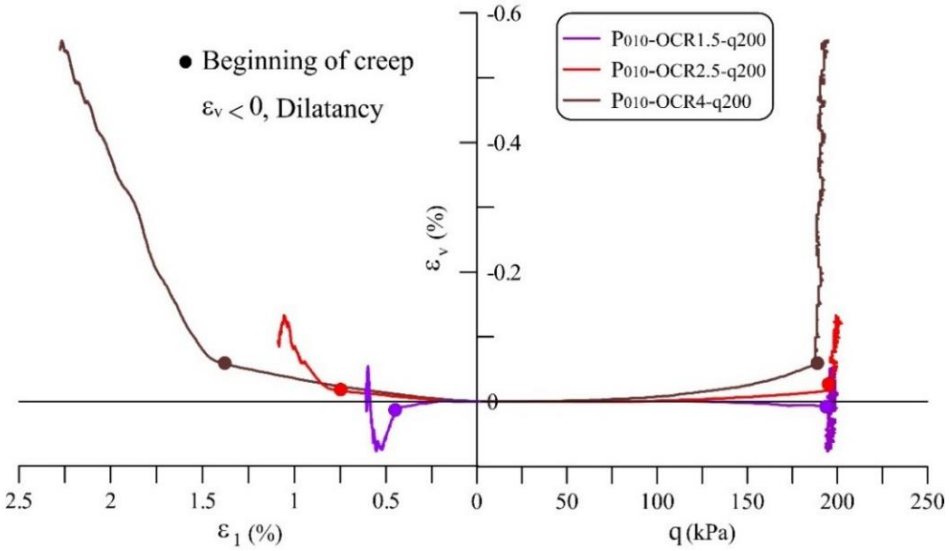

Figure 3.20 Evolution of strains in the no-volume and dilatancy domains for P_{010} tests

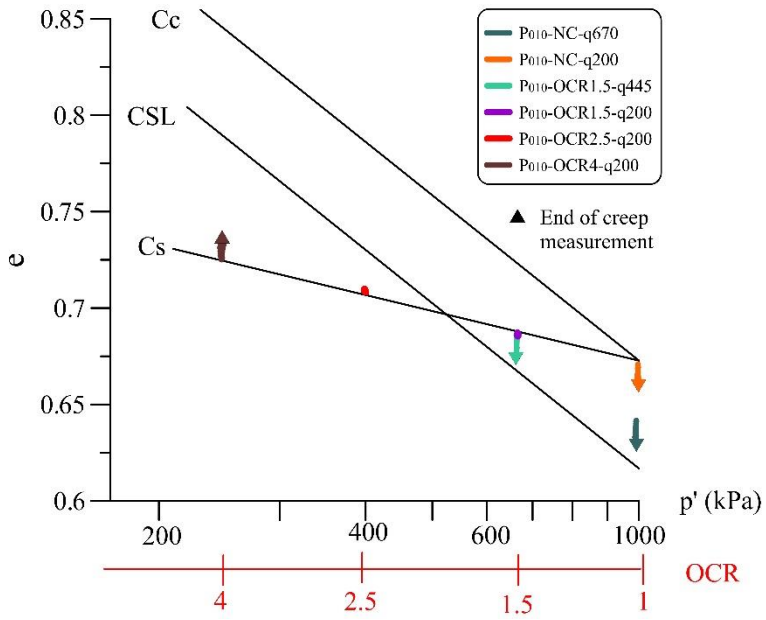

Figure 3.21 Evolution of void ratio during creep phase for P_{010} tests

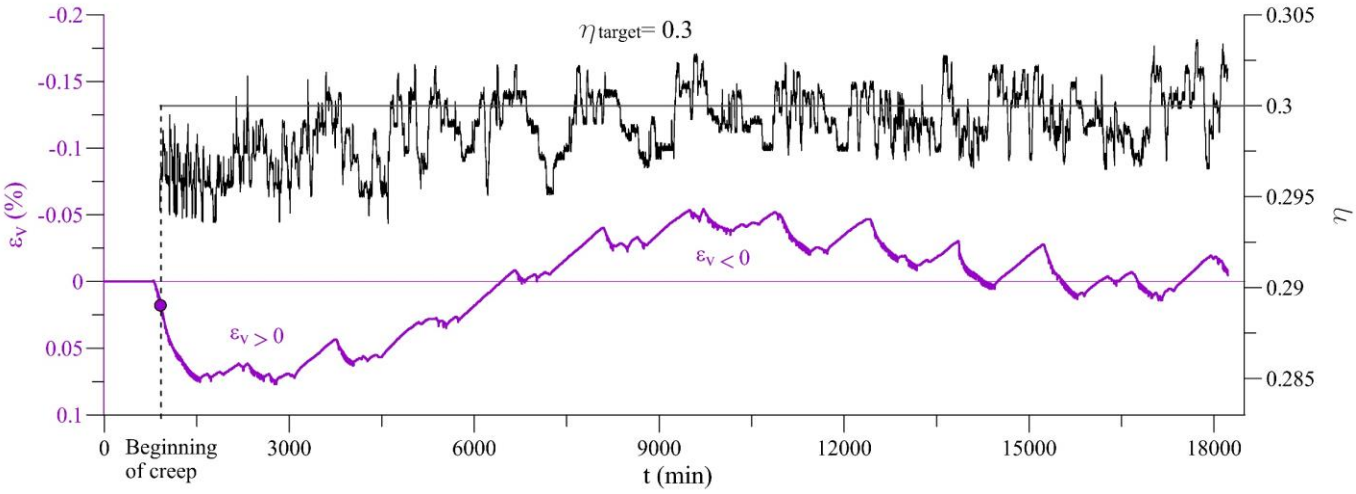

Figure 3.22 Kinematic constant stress and volumetric strain response of test P_{010}-OCR1.5-q200

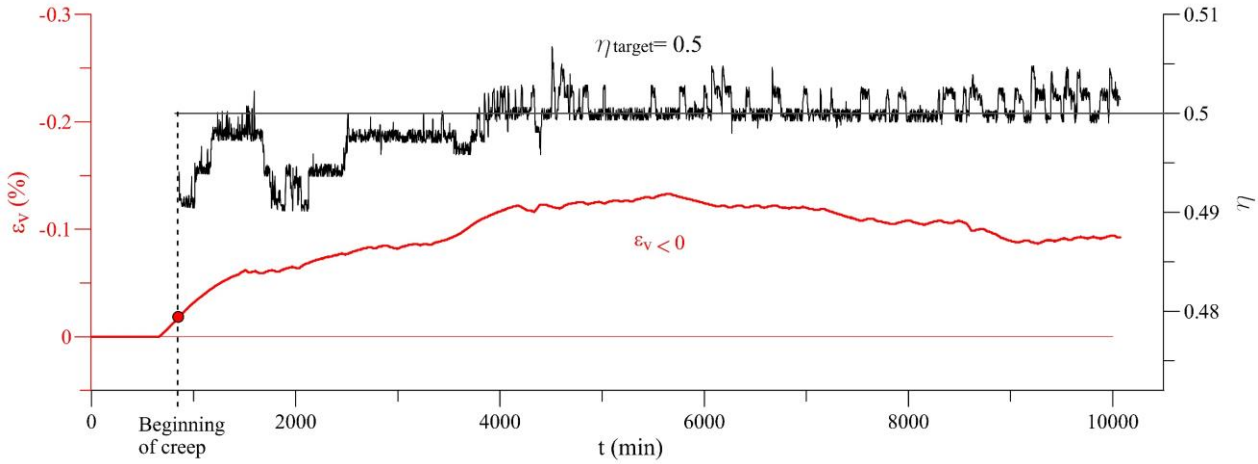

Figure 3.23 Kinematic constant stress and volumetric strain response of test P_{010}-OCR2.5-q200

- Test P_{02}

Figure 3.24 and Figure 3.25 gives the 3 creep tests performed after purely deviatoric stress paths for test P_{02} with p'_{0i} = 200 kPa. It is seen that in (ε_v-*q)* plane in Figure 3.24, there is scattering (within ±2 kPa from the target value of *q*) on deviatoric stress during creep phase. This scattering is mainly due to the adjustment by GDS control software, and this scatter seems to be amplified under lower stress condition than that under higher stress for test group P_{010} with p'_{0i} = 1000 kPa.

Within the constant sustained stress, all specimens exhibited creep deformation, both in axial and volumetric aspects. The results show that in dilatancy domain, an obvious dilatancy was detected from the beginning of creep for all the 3 highly overconsolidated samples (see Figure 3.24), which is in consist with tendency that identified for highly overconsolidated specimens in dilatancy domain for test P_{010}.

For test P_{02}-OCR5-q43 performed at high stress level (*SL* = 1.26) over the critical state line, the dilatant volumetric deformation developed quickly, with large ε_1 = 23%, ε_v = -2.5% at the end of creep measurement and then was totally collapsed. The collapsed result could be further verified in (*e-log p')* plane in Figure 3.25, wherein the void ratio was increased and headed towards the critical state.

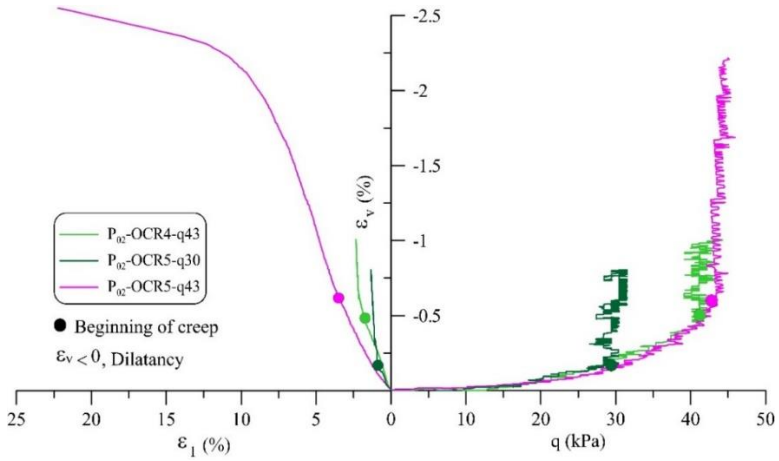

Figure 3.24 Evolution of stains during creep phase for test P_{02}

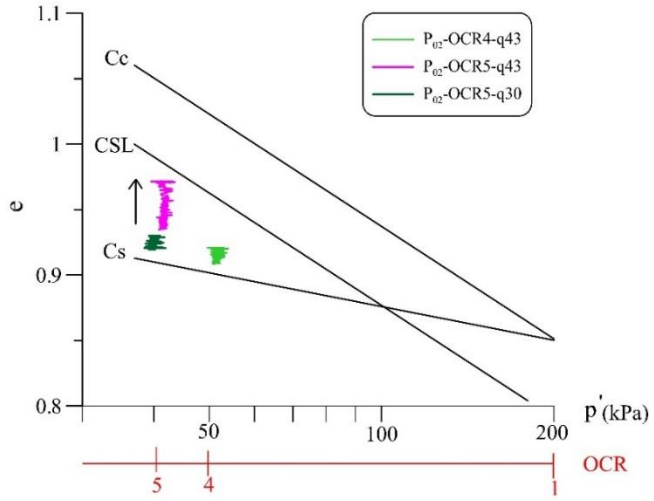

Figure 3.25 Evolution of void ratio during creep phase for test P_{02}

- Test P_{08}

Test performed after purely deviatoric stress paths with p'_{0i} = 800 kPa is shown in Figure 3.26 and Figure 3.27.

From Figure 3.26, it is seen that when the stress condition of creep phase was ended in the dilatancy domain, the creep deformation for test P_{08}-OCR16-q43 follows the tendency that was identified in monotonic loading, i.e., the sample was dilatant continuously under constant stress. Moreover, the evolution of volumetric strain increased more rapidly than the evolution of axial strain, resulting in a sharper slope of (ε_1- ε_v) curve than that in purely deviatoric loading phase.

Correspondingly, a slight increase of void ratio was detected within this creep phase in the plane of (*e-log p'*) in Figure 3.27 while the specimen was dilatant continuously.

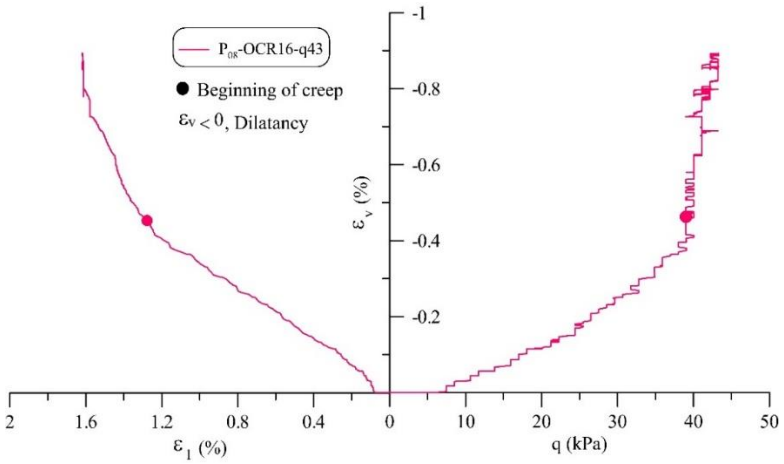

Figure 3.26 Evolution of stains during creep phase for test P_{08}

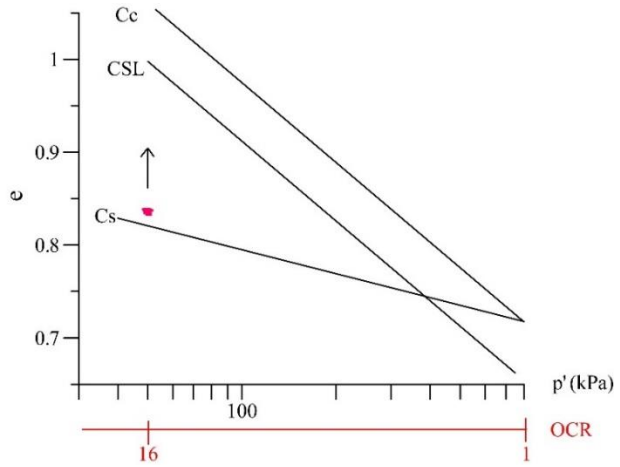

Figure 3.27 Evolution of void ratio during creep phase for test P_{08}

One can see that, when the preconsolidation pressure changes, quite similar dilatancy trends were observed for highly overconsolidated specimens in dilatancy domain, which further reveals that the sense of the volumetric creep deformation is dominated by the domain in which the creep test is conducted.

3.3 Influence of stress condition on creep evolution

In order to identify clearly the creep evolution with the variation of stress, volumetric strains and axial strains during creep phase were separated from the strains obtained in purely deviatoric loading phase. And the evolution of creep strains was thus replotted as a function of creep duration (t_{creep}) according to the different creep stress conditions. The experimental results were first analyzed by test P_{010} with p'_{0i} = 1000 kPa and then were further studied by tests when

preconsolidated pressures were changed (tests p'_{0i} = 200 kPa and 800 kPa) for normalized mechanisms.

3.3.1 Case of test P_{010}

The tests performed under certain common stress conditions are marked by numbered lines in Figure 3.28, are here considered. Line ① represents four tests at the same q under different OCRs, distributed in 3 volumetric domains; line ②/③ translates two tests under different SL with the same OCR in contractancy/no-volume change domain; line ④ connects two tests under the same η with variation in OCRs in contractancy domain. The evolution of creep strains located in different volumetric domains thus are plotted and discussed below.

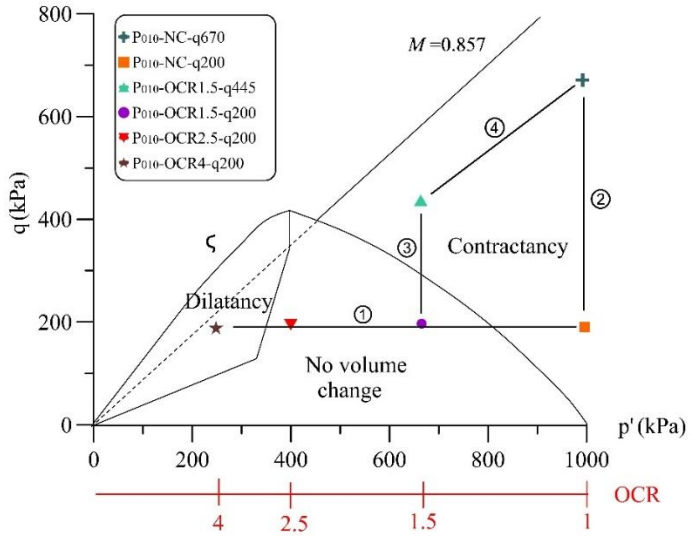

Figure 3.28 Creep under a given stress condition in strain domains for test P_{010}

3.3.1.1 Under the same deviatoric stress

Under the same deviatoric stress (q = 200 kPa), along line ① in Figure 3.28, tests with OCR = 1, 1.5, 2.5 and 4 show, in Figure 3.29, confirm that the creep strains development mainly depends on the volumetric strains domain where the phenomenon is observed. The results along the ① line condition clearly show that the creep deformations are more obvious for normally consolidated samples in contractancy domain, and for highly overconsolidated specimens within dilatancy domain. On the other side, in the pseudoelastic volumetric domain (for OCR =1.5 and 2.5), the volumetric creep strains remain very small and can be considered as zero as explained above.

As consequence, the results show that the strain mechanisms activated during the triaxial loading stage (along the purely deviatoric stress path) seems to control completely the tendency of creep volumetric strain.

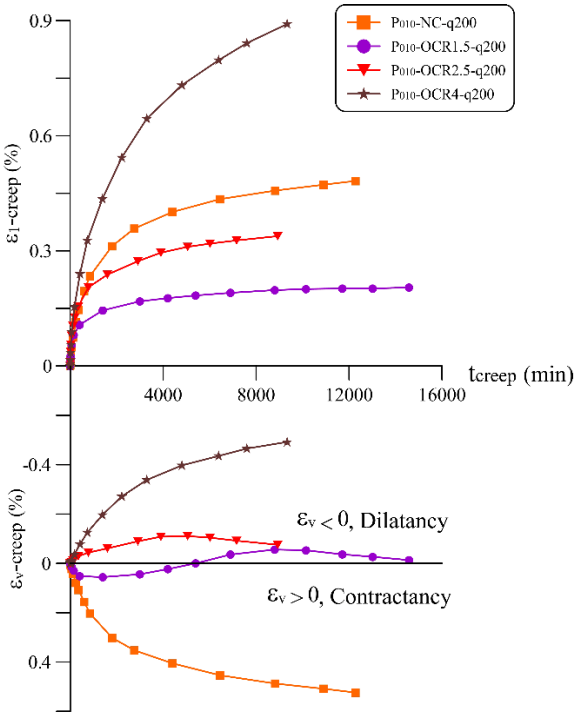

Figure 3.29 Strains versus time during creep phase with the same q (line ① in Figure 3.28)

3.3.1.2 Under the same OCR

The stress level dependency of creep strains versus time is shown in Figure 3.30 and Figure 3.31, translating by line ② and ③ in Figure 3.28.

As it could be expected, the creep deformation is isochronous greater under higher stress level:

Line ② condition: for normally consolidated specimens (Figure 3.30), the values of $\varepsilon_1 = 0.43\%$ and $\varepsilon_v = 0.48\%$ under $q = 200$ kPa were observed at $t_{creep} = 7000$ min, while $\varepsilon_1 = 1.11\%$ and $\varepsilon_v = 0.53\%$ were detected when $q = 670$ kPa after the same elapsed duration.

Line ③ condition: for lightly overconsolidated samples (Figure 3.31), the stress level dependency was highlighted when q was increased from the pseudoelastic volumetric domain up to the contractancy domain. Relatively quite small evolution of ε_v was detected with $q = 200$ kPa in the pseudoelastic volumetric domain, whereas obvious contraction ($\varepsilon_v = 0.29\%$ at the end of creep observation) was obtained when q was increased into the contractancy domain.

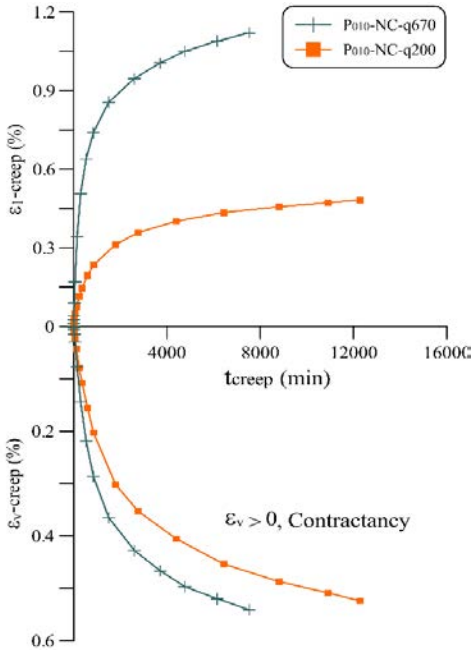

Figure 3.30 Influences of stress level on creep evolution for normally consolidated specimens (line ② in Figure 3.28)

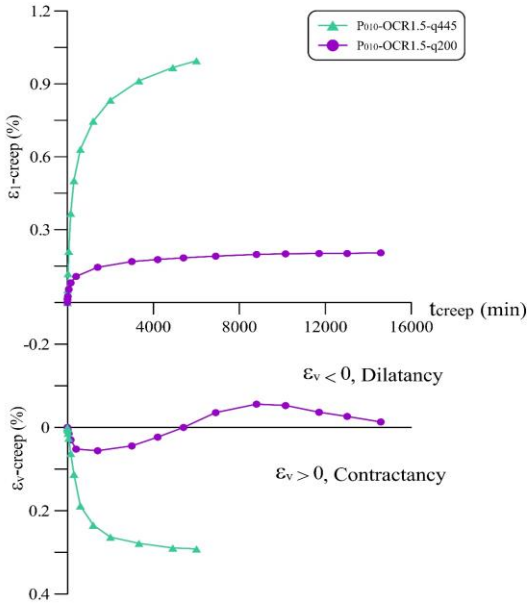

Figure 3.31 Influences of stress level on creep evolution for overconsolidated specimens (line ③ in Figure 3.28)

3.3.1.3 Under the same stress ratio

The volumetric strains evolve in obvious difference for the two tests creeping under the same stress ratio (η = 0.67), see Figure 3.32. The same η condition in the contractancy domain seems to

not enough to induce the same volumetric strains under different OCRs. This phenomenon highlights the influence of loading history, i.e., the influence of the isotropic loading/unloading paths and then constant p' path.

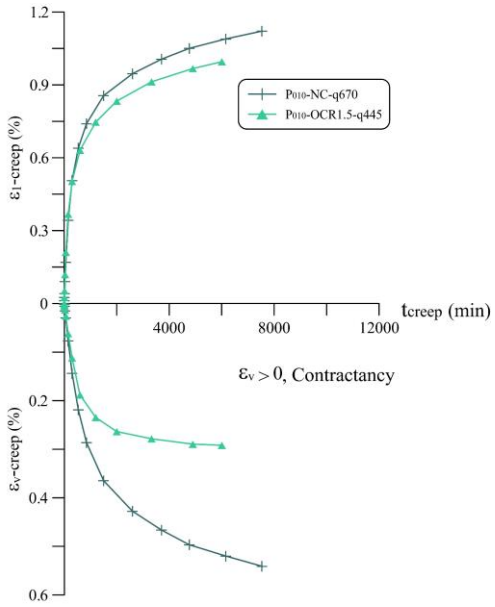

Figure 3.32 Creep strain evolution under the same stress ratio (line ④ in Figure 3.28)

3.3.2 Creep evolution in normalized (p′-q) plane

The results of group P_{010} showed that the creep behavior was dominated by the strain mechanism domains, that is, the location of stress level condition in volumetric domains where the creep test is performed. In order to obtain more general creep mechanism on the purely deviatoric stress path, the other two groups of tests (P_{02} and P_{08}) are superimposed and plotted in the (p'_i/p'_{0i} -q/p'_{0i}) normalized plane of the Figure 3.33. The locations of creep stress conditions are supposed to be normalized dimensionless by eliminating the effects of preconsolidation pressure p'_{0i}. Thus, for tests with the same OCR and the same stress level can be represented in the same location in volumetric domain. In Figure 3.33, line ⑤ series connects 4 tests of close high stress ratio (η = 0.75~0.86) with OCR varies from 4 to 16 (similar to line ④ in Figure 3.28); line ⑥ translates 2 tests performed under different stress level, in the dilatancy domain, with the same OCR (similar to line ② and ③ in Figure 3.28).

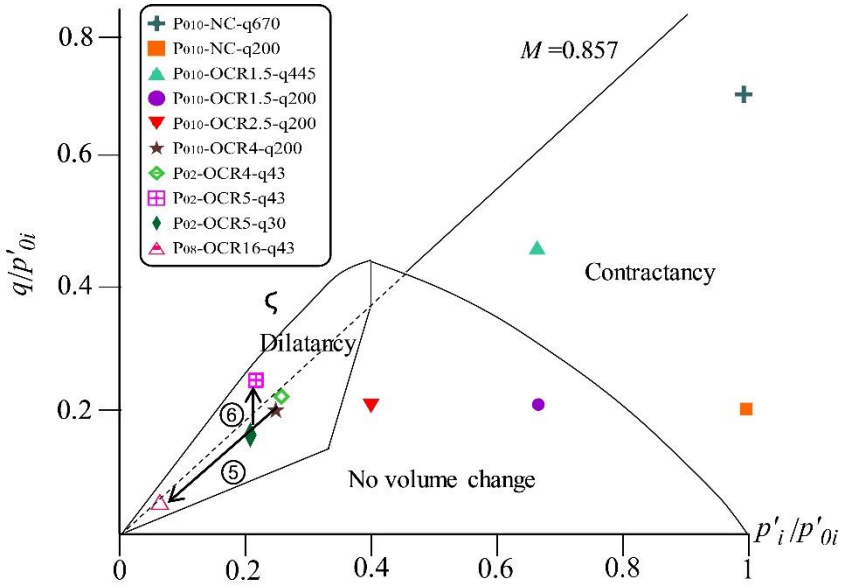

Figure 3.33 Creep tests under different stress conditions in the normalized plane

From Figure 3.34, one can see that in the dilatancy domain the volumetric deformation of tests with similar high stress levels exhibits unanimously dilatancy, and varies from each other within a narrow band. It also can be seen that in spite of different absolute values of p'_{0i}, p' and q, quite close volumetric strains were obtained for specimens with the same OCR (=4) for P_{010} and P_{02}, at a very close stress level in the normalized plane. This consistency on ε_v of tests P_{010}-OCR4-q200 and P_{02}-OCR4-q43 in turn verified that the location of stress condition in volumetric domain, which is associated by both OCR and stress level, is the main parameters that characterizes the creep evolution.

Unlike the consistent tendency that identified for volumetric strains, the evolution of axial strain seems to more susceptible to the variation of stress. It is likely that the axial strain evolves greater under higher deviatoric stress, resulting in ε_1 = 0.87% for test P_{010}-OCR4-q200 while ε_1 = 0.59% for test P_{02}-OCR4-q43 at t_{creep}= 9000 min. On the other hand, the evolution of ε_1 seems to be slowed down under higher OCR (=16), where the isochronous smaller value of ε_1 was detected and the axial creep strain seems to reach the equilibrium after t_{creep}= 4800 min.

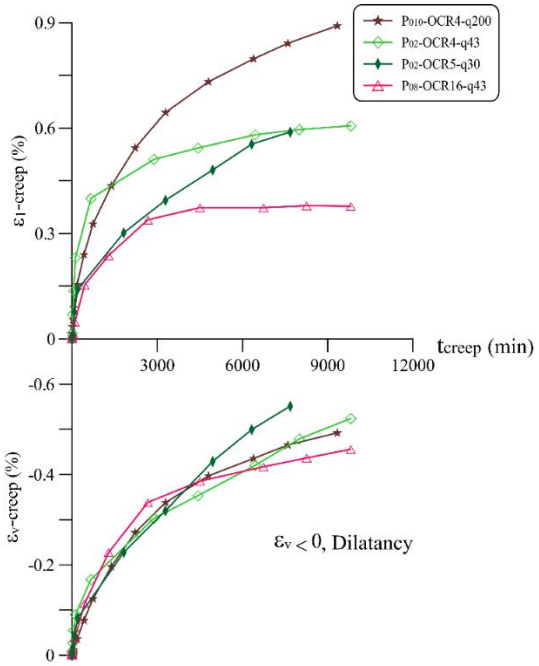

Figure 3.34 Creep strain evolution under similar normalized stress ratio (line ⑤ in Figure 3.33)

3.3.3 Creep rupture

The creep test P_{02}-OCR5-q43 is performed, after the purely deviatoric stress path, at a stress level above the critical state line in the dilatancy domain and near to the maximum strength envelope. As it is seen in Figure 3.35, quite pronounced increase of dilatancy was detected under this high stress level condition (along line ⑥ in Figure 3.33). This dilation tendency in creep phase held about 600 minutes, with large final values of ε_1=4.42% and ε_v=-2.31%. Afterwards, the sample totally collapsed rapidly, see the photo in Figure 3.35.

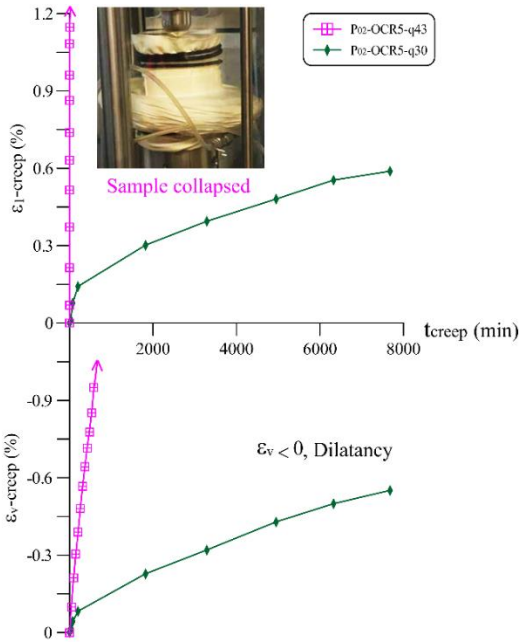

Figure 3.35 Creep evolution for overconsolidated specimen in critical state zone (line ⑥ in Figure 3.33)

3.4 Evolution of creep strain rate

Based on the identified strains within creep phase, the evolution of strain rate is possible to be computed. The strain rates, creep parameter *m* and its relationship with OCR and the stress level (or stress ratio η) will be discussed. In this section we try to characterize how the creep develop within different volumetric domains after the purely deviatoric stress path, aiming to provide more experimental data in cooperating into the constitutive model.

3.4.1 Axial strain rate

3.4.1.1 Evolution of axial strain rate with time

Figure 3.36 represents the variation of axial strain rates ($\dot{\varepsilon}_1$) versus time in double logarithmic plot. The results show globally that: for the tests performed at stress levels under critical state, the primary stage of creep is highlighted; for the stress level beyond the critical state (P_{02}-OCR5-q43 in Figure 3.36c), the secondary then the tertiary creep stage are detected till the sample totally collapsed. This phenomenon is rather rare to see in this soil.

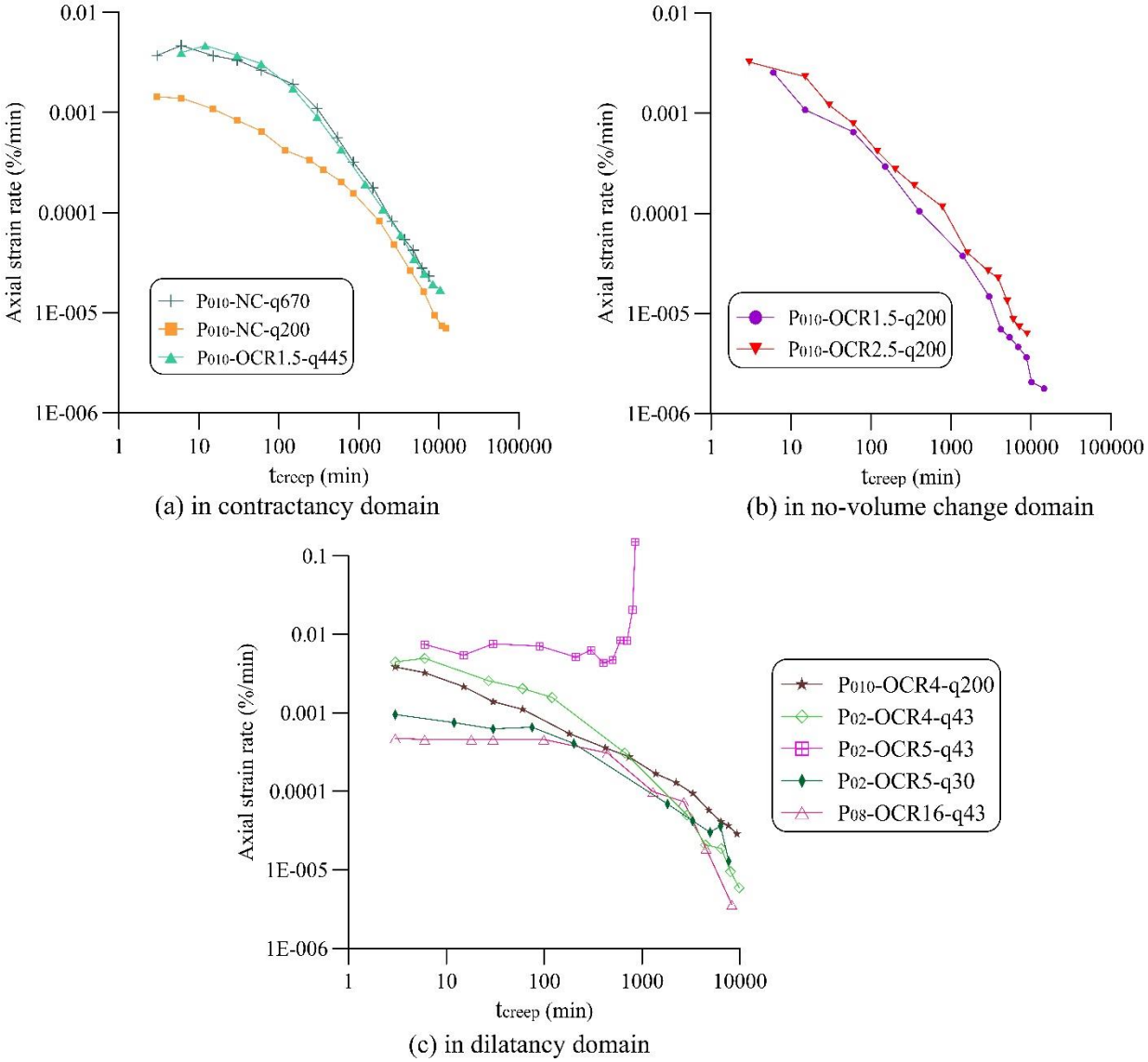

(a) in contractancy domain

(b) in no-volume change domain

(c) in dilatancy domain

Figure 3.36 Relationship of axial strain rate as a function of time

For tests performed under critical state, the strain rates decrease with time generally. The relationships of $log\dot{\varepsilon}_1$-log t are almost linear after about a certain period, and varies from each other within variations of stress conditions. It is noticeable that, in the later period of creep, the $log\dot{\varepsilon}_1$-log t curves for overconsolidated specimens at lower deviatoric stress (q= 30 and 43 kPa in Figure 3.36c) are slightly scattered. The scattered tendency is similar to that reported by Bishop and Lovenbury (1969) on Pancone clay and by Tavenas et al. (1978) on Saint-Alban clay in both triaxial tests and oedometer test. And the "S" shape was interpreted as a limited instability that reflects the modification in soil structure by Bishop and Lovenbury (1969), which is also agreed by Tavenas et al. (1978).

3.4.1.2 Evolution of axial strain rate with stress ratio

The relationship of axial strain rate with a widely parameter η (stress ratio $\eta=q/p'$) at different times is shown in Figure 3.37. It is seen that at a certain t_{creep}, the axial strain rate varies in a limited range with the variation of η, although the tests results are a little scattered, a linear tendency is still identified at a given time. The test points can be fitted approximately by a straight line in the tested range of η. The slope of fitted line is steeper in the later times than that of line in the early time (e.g. t_{creep}=10 min), which shows an opposite tendency that identified by Tian et al. (1994) on marine sediments from Gulf of Mexico in drained creep tests and and by Zhu (2007) in drained creep tests on Hong Kong marine sediments.

This non-linear dependency of the slope on time may indicates that the Equation 1.3 ($\dot{\varepsilon} = Ae^{\alpha D}(\frac{t_1}{t})^m$) proposed by Singh & Mitchell (1968) cannot be used directly for fitting the drained creep test data after the purely deviatoric stress path on remolded Kaolin K13.

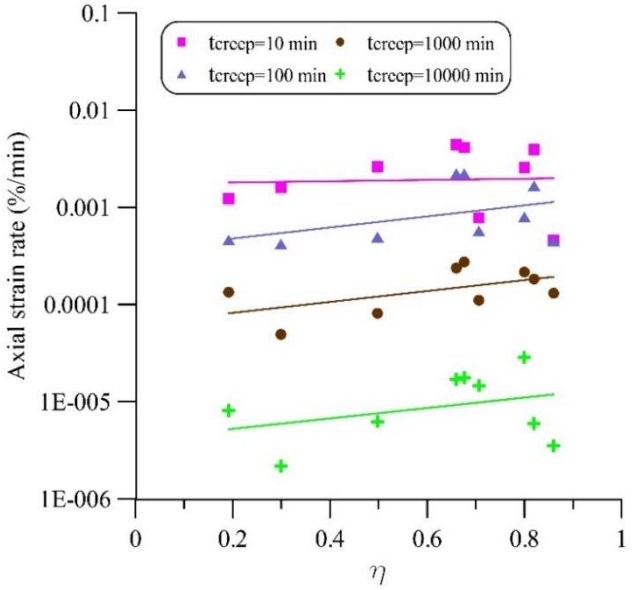

Figure 3.37 Relationship of axial strain rate versus stress ratio at different times

3.4.1.3 Creep parameter m_1 in primary creep

The linear part of each curve in Figure 3.36 during primary stage of creep is used to compute the creep parameter *m* (Singh & Mitchell, 1968). For clarity, we define the creep parameter *m* in

the form of m_1, which is the slopes of the straight lines on log axial strain rates versus log time, being:

$$m_1 = -\frac{\Delta \log \dot{\varepsilon}_1}{\Delta \log t_c} \tag{3.15}$$

Since the creep parameter m has been widely used in creep of analysis, the values of m_1 are obtained here to compare the results of Kaolin to the values of other soils. The values of m_1 here varies from 0.83~1. 4, with most values over than 1.0, differ from the typical values identified by Singh and Mitchell (1968), wherein m_1 were found to fall between 0.75 and 1.0. As reported in literatures, higher values are obtained in drained conditions than those in undrained conditions (Augustesen et al., 2004). A relatively higher range of m_1 corresponds to weaker viscous effects (Zhu, 2007), the intrinsic viscous bonding for the remolded kaolin particles could be inferior, thus the rearrangement activities occur easier and exhibits higher strain rates when the sample was compressed continuously under constant stress.

It is seen in Figure 3.37 that the evolution of axial strain rate increase with stress ratio at a given time generally, which shows a stress-dependency. The stress-dependency of axial strain rate can be further investigated through the parameter m_1 as a function of stress ratio, as shown in Figure 3.38, wherein the numbered line indicates tests under a certain stress condition in common, the same as in Figure 3.28 and Figure 3.33.

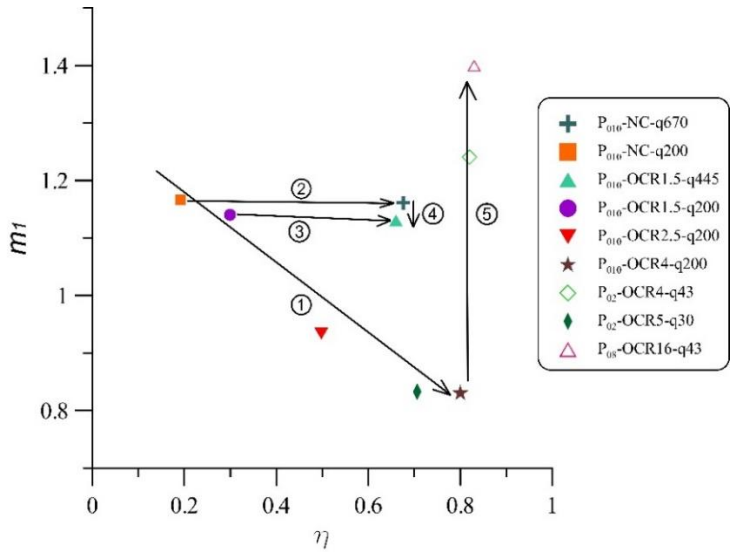

Figure 3.38 Parameter m_1 as a function of stress ratio, η

From Figure 3.38, it can be seen that the parameter m_1 varies with different stress conditions, the results show globally that:

Under the same deviatoric stress (q = 200 kPa translated by line ① in Figure 3.28 and Figure 3.38), the evolution of creep parameter m_I decreases from 1.17 to 0.83. This trend demonstrates that the increment of axial strain is slowed down with the increase of stress ratio when the stress condition varies from contractancy domain to dilatancy domain via the pseudoelastic volumetric domain.

Under the same OCR, the parameter m_I for normally consolidated samples seems insensitive to the variation of stress condition. Comparing test P_{010}-NC-q200 and q670 in contractancy domain (line ② condition in Figure 3.28 and Figure 3.38), the values of m_I are quite close with obvious variation of η from 0.2 to 0.67. Similar results have been found on lightly overconsolidated specimens of test P_{010}-OCR1.5-q200 and q445 (line ③ in Figure 3.28 and Figure 3.38), m_I remains almost constant (=1.14) with the increase of η, while the stress condition varies from pseudoelastic domain to contractancy domain.

Under the same stress ratio, for tests performed in contractancy domain (line ④ condition), the axial strain rate was slowed down slightly by the overconsolidation history, leading to a smaller value of m_I for normally consolidated specimen (P_{010}-NC-q670) than the lightly overconsolidated one (P_{010}- OCR1.5-q445). However, an opposite trend was observed for tests in dilatancy domain, the values of m_I shows an increase tendency with the increase of OCR, corresponding to a quicker dilatant deformation at higher OCR. The positive correlation between m_I and OCR is shown by tests along line ⑤, wherein m_I =1.4 for test P_{08}-OCR16-q43 while m_I =1.2 for test P_{02}-OCR4-q43, and a much smaller m_I (=0.83) for test P_{010}-OCR4-q200. This apparent difference of m_I for highly overconsolidated samples echoes with the fact that the evolution of axial strain is more susceptible to the variation of stress (see Figure 3.34).

3.4.1.4 Secondary creep

In addition to the decrease tendency of log axial strain rate versus log time during the primary creep, the constant tendency of strain rates was obtained in the secondary creep stage for test P_{02}-OCR5-q43 in Figure 3.36, where the stress level is beyond the critical state. The constant tendency was held about 600 minutes, at a constant axial strain rate $\dot{\varepsilon}_1 \approx 0.006$. Afterwards, an accelerating of creep rate appeared and ended up in creep rupture within around 200 minutes. The elapsed time before the showing up of accelerating creep (t_f) is unique related to the minimum strain rate in the form of $t_f.\dot{\varepsilon}_{min} = C$, as proposed by Campanella and Vaid (1973) through undrained creep on

Haney clay. The constant C represents strain magnitude before creep rupture, and for kaolin in drained creep test the value of C is 4.2, which is higher than the value in undrained creep test ($0.2 < C < 2.8$).

3.4.2 Volumetric strain rate

It has been widely accepted that in one dimensional consolidation, the creep rate is almost independent of vertical effective stress for normally consolidated clays (Bjerrum, 1967), same findings have been identified for Kaolin in oedometric path (Figure 1.12). Moreover, in triaxial condition, the axial strain rate is found to be related to the stress condition in this study, distinguishing from the assumptions by Borja & Kavazanjian (1985), and Yin & Graham (1999).

3.4.2.1 Evolution of volumetric strain rate in different domains

Based on the detected volumetric strain in creep phase in Section 3.3, the evolution of volumetric strain rate versus time thus be computed and is plotted in double logarithmic plane in Figure 3.39, where the absolute values were used for $\dot{\varepsilon}_v$ due to negative value of ε_v in dilation.

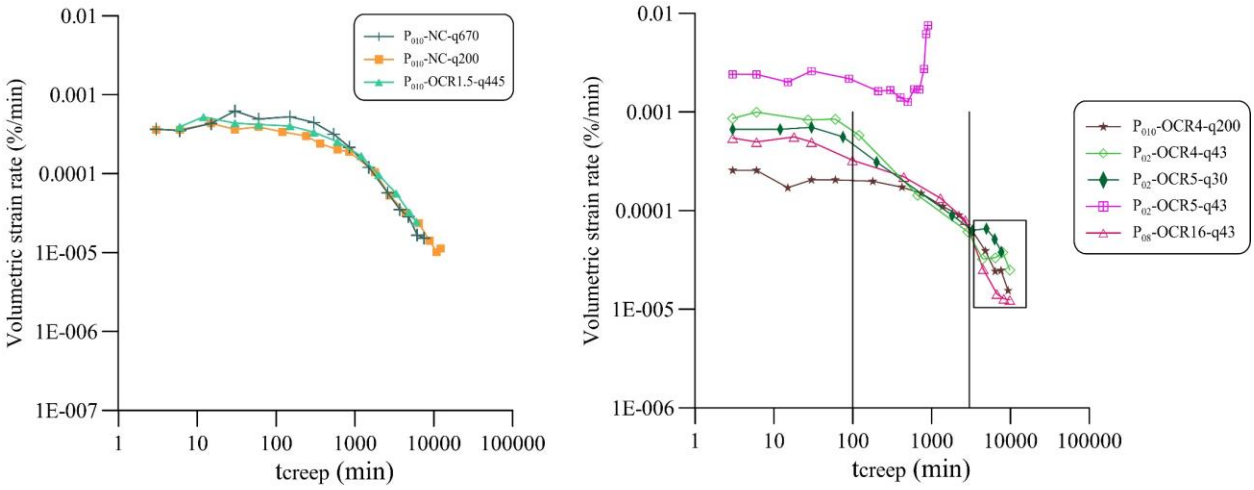

Figure 3.39 Relationship of volumetric strain rate as a function of time

The results show globally that:

- In contractancy domain (Figure 3.39a), the volumetric strain rates for normally consolidated and lightly overconsolidated specimens are approximately constant (≈0.0007%/min) at the beginning. Then a linear tendency is observed after about 1000 minutes, which corresponds to the

primary creep. Tian at al. (1994) obtained similar results on normally consolidated marine sediments of Gulf of Mexico and by Zhu (2007) with Hong Kong marine sediments.

- In dilatancy domain (Figure 3.39b), the time-dependency of $\dot{\varepsilon}_v$ of overconsolidated specimens under critical state is similar with that of normally consolidated ones in contractancy domain. Moreover, larger differences were found for the initial values of $\dot{\varepsilon}_v$, ranging from 0.0003 to 0.001 %/min. Afterwards, the points from different tests are distributed within a narrow band and shows linear tendency after t_c=100 minutes, this unified tendency of $\dot{\varepsilon}_v$ inverse verified the generalized dilation for highly overconsolidated specimens in dilatancy domain (Figure 3.34). It is noteworthy particularly that, after t_c=3000 minutes, the "abrupt" variations in $\dot{\varepsilon}_v$ were detected. Results of Tavenas et al. (1978) further showed that the "abrupt" variations of $\dot{\varepsilon}_1$ and $\dot{\varepsilon}_v$ occur under higher stress level after σ'_3=constant loading, and only $\dot{\varepsilon}_1$ occur under higher stress level after p'=constant loading. However, for test results in this research, the "abrupt" variations were obtained in both $\dot{\varepsilon}_1$ and $\dot{\varepsilon}_v$ of overconsolidated specimens under the purely deviatoric loading. The changes in $\dot{\varepsilon}_v$ are more obvious than that of $\dot{\varepsilon}_1$ in dilatancy domain, which implies that the particular behavior of clay structure in performance of "abrupt" variations of strain rate may be associated with the stress condition, and will be induced after a certain stress path within a certain stress condition.

It is noted in Figure 3.36 and Figure 3.39 that the variations of $log\ \dot{\varepsilon}_1$and $log\ \dot{\varepsilon}_v$ versus *log t* are curved before the linear tendency in primary creep. This is probably because of the dissipation of transient excess porewater dissipation and/or the actual creep behavior of Kaolin. Considering the relatively minor variation of porewater pressure (as shown in Figure 2.20) and the results by Tian et al. (1994) and Zhu (2007), it is very likely that the shape in Figure 3.36 and Figure 3.39 can be taken as the real relationship of $log\ \dot{\varepsilon}_1$and $log\ \dot{\varepsilon}_v$ versus *log t* for Kaolin.

3.4.2.2 Evolution of volumetric strain rate with stress ratio

The changes of volumetric strain rate versus stress ratio at different times is shown in Figure 3.40. Corresponding to a given time, a higher stress ratio results in a higher volumetric strain rate at the early period of creep. Similar to the variations of axial strain rate in Figure 3.37, the changes of volumetric strain rate with stress ratio may be fitted by straight lines, and the slope of fitting results becomes flatter as time passes. At t_{creep}≥10000 minutes, the fitting line is almost horizontal, whereas obvious scatting points are found at the early time of creep.

This non-linear dependency of the slope on the time indicates that after the purely deviatoric stress path, the evolution of volumetric strain rate in drained creep tests cannot be fitted directly by the equation proposed by Singh & Mitchell (1968), Further research are still called for fitting the development of strain rate that dominated by the strain domain mechanisms.

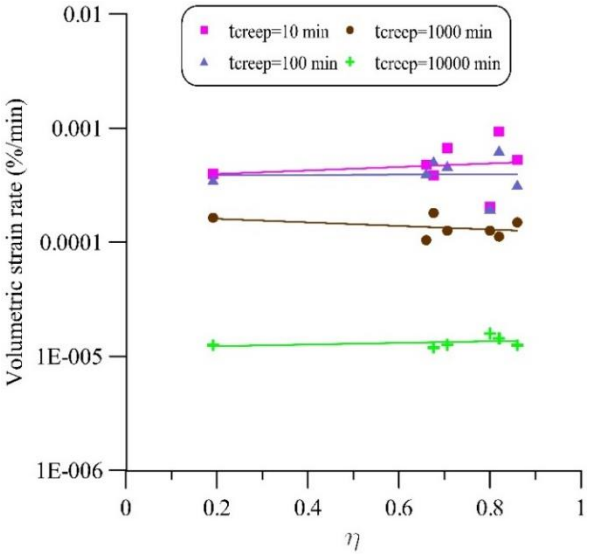

Figure 3.40 Relationship of volumetric strain rate versus stress ratio at different times

3.4.2.3 Creep parameter m_v in primary creep

Even though the linear tendency for $log\ \dot{\varepsilon}_v$ - *log t* curve (Figure 3.39) is generally not apparent as for ($log\ \dot{\varepsilon}_1$ - *log t)* curve (Figure 3.36), linear fitting lines could still be deduced on normally consolidated specimens (Figure 3.39a) and the straight parts for overconsolidated samples (between t_{creep}=100 and 1000 minutes in Figure 3.39b). Similar to Equation 3.15, we define the parameter m_v that is the slopes of the straight lines on log volumetric strain rates versus log time being:

$$m_v = -\frac{\Delta \log \dot{\varepsilon}_v}{\Delta \log t_c} \tag{3.16}$$

The values of m_v was found to be varies from 0.37 to 1.26, in a rage that lower but wider than values of m_1 (0.83~1.4), which implies that the evolution of volumetric strain rate may more sensitive to the variation of stress conditions.

The relationship of parameter m_v versus stress ratio is represented in Figure 3.41. It is noted that for test group P_{010}, there values of m_v remains in relatively high magnitude. However, lower

values of m_v were found for test group P_{02} and P_{08}, where the tests were performed at lower magnitude of stress. One can see in Figure 3.41 that:

Under the same deviatoric stress (line ① condition), the values of m_v for normally consolidated sample in contractancy domain (P_{010}-NC-q200) and highly overconsolidated one in dilatancy domain (P_{010}-OCR4-q200) are quite close, differing from the tendency of m_1 identified in Figure 3.38.

In contractancy domain (line ② condition), similar slight variation of m_v was detected as for m_1 in Figure 3.38, and m_v increases slightly with the increase of η.

In dilatancy domain, under the close stress ratio (line ⑤ condition), values of m_v vary less regularly with the magnitude of the stress.

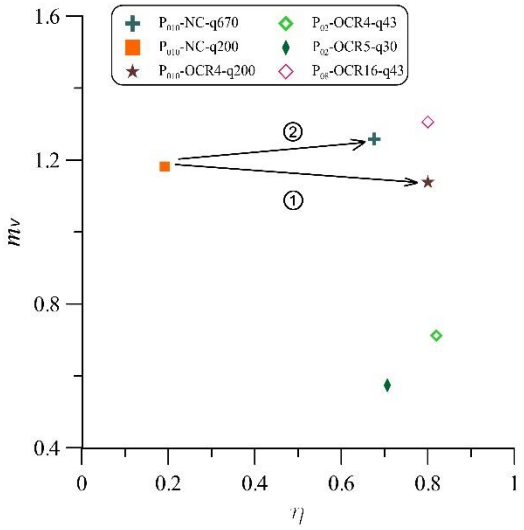

Figure 3.41 Parameter mv as a function of stress ratio, η

3.5 Evolution of deviatoric strain

Deviatoric creep, as mentioned in Section 1.2.2, often accompanies volumetric creep. In drained triaxial condition, the deviatoric strain is obtained from the axial strain and volumetric strain by Equation 1.4 ($\varepsilon_d = \varepsilon_1 - \frac{\varepsilon_v}{3}$). Based on the axial and volumetric creep strain identified in Section 3.3, the deviatoric strain within creep phase thus could be computed, and its variation with time is shown in Figure 3-3 in Annexes Chapter 3.

For tests performed under the critical state, the interaction between volumetric and deviatoric strain during creep is shown in Figure 3.42. The time-dependent of the interaction of these two

coponents for Kaolin after constant p' stress path is similar to that observed by Walker (1969) under multi stage constant σ'_3 tests.

The flatter linear tendency maybe fitted after a curved section at the beginning. For example, the curve of test P_{010}-NC-q670 after point A (at t_{creep}=150 min) is almost linear, which corresponds to the beginning of primary creep stage (see Figure 3.39a). The curved part before point A is more inclined to be the primary consolidation that is controlled by the dissipation of pore pressures after loading.

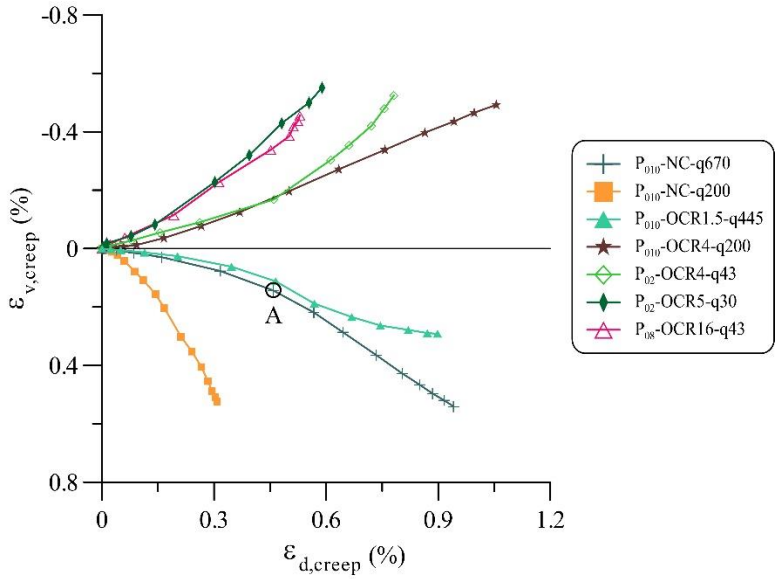

Figure 3.42 Interaction between volumetric and deviatoric strain during creep within the critical state

For test creeping over the critical state (test P_{02}-OCR5-q43), a clear linear tendency was found from the beginning (Figure 3.43), which corresponds to the constant strain rate state in the secondary creep (Figure 3.39b). Moreover, after about 600 minutes, rapid creep deformation was developed and ended at the creep failure.

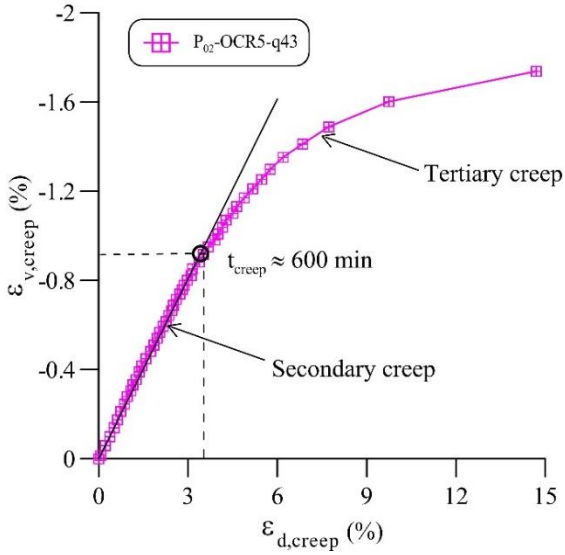

Figure 3.43 Development of volumetric and deviatoric strains with time

3.6 Summary and discussion

3.6.1 Dilatancy rate

The physical manifestation of dilatancy for clay has been widely discussed (Equations 1.7-1.10 in Section 1.2.1). Some stress dilatancy equations are also applied to the dilatancy of clay during undrained creep. The dilatancy equations usually take the form of the ratio of volumetric plastic strain increment ($d\varepsilon_v^p$) to the deviatoric plastic strain increment ($d\varepsilon_d^p$) as a function of M and η.

$$\frac{d\varepsilon_v^P}{d\varepsilon_d^P} = f(M,\eta) \tag{3.17}$$

The interaction between the volumetric strain and deviatoric strain ($\varepsilon_d=\varepsilon_1-\varepsilon_v/3$) is plotted in Figure 3.42 for tests creeping in contractancy and dilatancy domains. Under constant stress, the evolution of ε_v-ε_d consists of the viscoplastic flow. This flow rule (or dilatancy equations) is characterized by the ratio of strain increments in Figure 3.44.

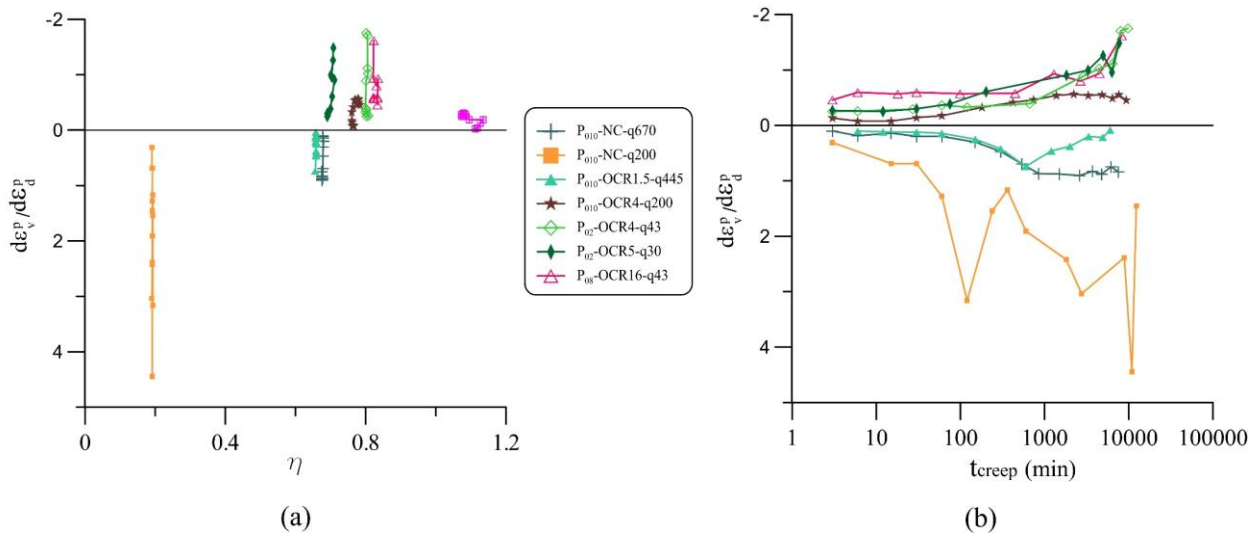

Figure 3.44 Ratio of strain increment during creep: (a) with stress ratio (b) with time

It is seen in Figure 3.44 that under lower stress ratio, the ratio of $d\varepsilon_v^p/d\varepsilon_d^p$ is larger (case of P_{010}-NC-q200), which agrees with the rules by terms of Equation 3.17 in elastoplastic constitutive models. The ratio of $d\varepsilon_v^p/d\varepsilon_d^p$ should be constant under constant η in drained creep. However, the fluctuation curves identified here conflict with the rules in those models. This just confirms that the development of plastic strain under constant stress will further induce anisotropy.

Therefore, elasto-viscoplastic constitutive models accounting for the feature of anisotropy (e.g., Dafalias 1987; Wheeler et al., 2003) is accepted. The dilatancy equation can be generally expressed in Equation 1.10 ($\frac{d\varepsilon_v^P}{d\varepsilon_d^P} = \frac{M^2-\eta^2}{2(\eta-\alpha)}$). The value of α corresponds to the degree of plastic anisotropy of the soil. With α=0 the soil behaves isotropically and Equation 1.10 corresponds to the flow rule of MCC as Equation 3.17, and α=M/3 in critical state when η =M.

The development of erasure of anisotropy with plastic strains can be described by the rotational hardening law (Wheeler et al., 2003), which is expressed as

$$d\alpha = \mu\left[\left(\frac{3\eta}{4} - \alpha\right)\langle d\varepsilon_v^p\rangle + \beta\left(\frac{\eta}{3} - \alpha\right)\left|d\varepsilon_d^p\right|\right] \tag{3.18}$$

where the Macaulay bracket mean that this law would be used for the condition of contractancy with a positive $d\varepsilon_v^p$. A hardening law accounting for the feature of negative $d\varepsilon_v^p$ is still needed to be developed.

As shown in Figure 3.44b, the evolution of $d\varepsilon_v^p/d\varepsilon_d^p$ results in the induced anisotropy. On the other hand, the current anisotropy tendency will evolve towards an equilibrium state causing

variations of $d\varepsilon_v^p$ and $d\varepsilon_d^p$ in the next moment. This kinematic hardening process will terminate theoretically, according to the anisotropic elastoplastic model by Wheeler et al., 2003, when the yield locus and the stress point coincide.

For sample creeping at the critical state (P_{02}-OCR5-q43), the viscoplastic deformation continuously increase with time until tertiary creep (Figure 3.43 in Section 3.5 of Chapter 3). In this condition, the stress dilatancy by Equation 1.10 with $\alpha=M/3$ can describe satisfactorily the viscoplastic flow before rupture.

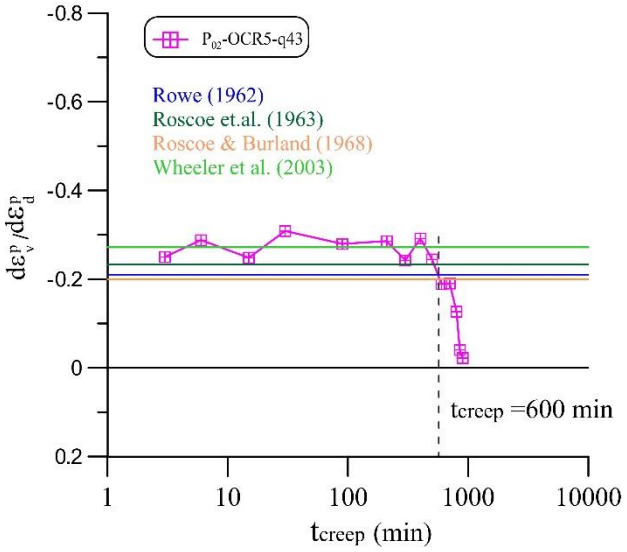

Figure 3.45 Ratio of strain increment versus time over critical state during creep

The plastic flow rules accounts for the induced anisotropy in drained creep, especially the dilatancy for highly overconsolidated soils are still called.

3.6.2 Viscoplasticity evolution

The non-linear volumetric creep strain evolution is part of the time-dependent viscous behavior of the clay. The volumetric strain increment in the scale of sample can be decomposed into a reversible part and a viscoplastic part

$$d\varepsilon_{v,creep} = d\varepsilon_v^{rev} + d\varepsilon_v^{vp} \tag{3.19}$$

The onset of the viscoplastic strain increment depends on the stress location in the (p'-q) plane. When the state of stress lies within the contractancy domain, for example for normally consolidated specimens, positive values of $d\varepsilon_v^{vp}$ develop with time, showing by the structural anisotropy and compression of pore diameter. The cumulative $d\varepsilon_v^{vp}$ corresponds to a strain

hardening, which can be used as a hardening parameter in the construction of viscoplastic soil models.

Similarly, for highly overconsolidated soils creeping in the dilatancy domain, negative values of the viscoplastic volumetric strain develop with time, resulting in strain softening.

Moreover, when the stress level is located above the critical state (case of test P_{02}-OCR5-q43), an accumulating large dilation causes a significant decrease of the soil density. This viscoplastic softening leads to a shrinkage of the maximum strength envelope. The time-dependent ς curve will hence evolve in the direction of the stress point, eventually leading to the collapse of the specimen when the maximum strength envelope and the stress point coincide. When the stress state is located under the critical state, creep strains develop at a decreasing strain rate leading to a stable state of the specimen.

For lightly overconsolidated specimens creeping in the pseudo-elastic volumetric domain, no time-dependent volumetric strain takes place. Relative limited positive/negative $d\varepsilon_v$ appear alternatively, corresponding to a slight fluctuation of p' and q due to the GDS system; a null volumetric change can be assumed in this volumetric domain (see Figure 3.22 and 3.23 in Section 3.2.2 of Chapter 3).

Further quantitative characterizations, at macroscopic as well as microscopic level, are needed before these experimental results can be introduced within a constitutive model for clay.

3.6.3 Summary

The analysis on creep behavior of kaolin undertaken in this research highlights some mechanical characteristics related to the volumetric domain in (p'-q) plane. The creep phenomenon was investigated under the purely deviatoric stress paths. The results clearly show that creep development strongly depends on the stress history and on the behavior during the triaxial loading stage. According to the stress location in the plane of (p'-q), the following conclusions can be drawn:

In the contractancy domain for normally consolidated samples: creep contractancy is observed whatever the stress level in (p'-q) plane. The stress level influences, on the other side, the amount of the creep contractancy; the creep deformation appears as isochronous greater under higher stress level.

In the dilatancy domain for overconsolidated samples: creep dilatancy is clearly observed for high overconsolidated samples whatever the stress level in the dilatancy domain. The volumetric strains are greater for the higher stress level. A total collapse of the sample during creep is obtained when the stress level is over the critical state approaching the failure envelop.

In the pseudoelastic domain: more complex volumetric strains are obtained from the lightly overconsolidated specimens. Alternating contractancy/dilatancy appears during the creep stage in a relatively small range that might be admitted to be due to the monitoring GDS program in maintaining the given stress level. In this domain, no volumetric strain changes can be assumed.

Three creep stages are identified in different tests. Under the critical state, all specimens show the primary stage, the secondary and tertiary stage are rarely seen except in one test beyond the critical state. The relationships of creep log strain rate versus log time are not always linear as proposed by Singh & Mitchell (1968). The ($log\ \dot{\varepsilon} - \log t$) curve varies in different domains, and the parameter m fitted by the linear part of the strain rate curve is not constant. The values of m_1 (m value for axial strain) varies in 0.83 to1.40; values of m_v (m value for volumetric strain) changes from 0.37 to 1.26. Parameter m_v is more sensitive to the variation of magnitude of stress.

As consequence, the stress level and the OCR seem to be the two parameters that strongly govern the creep deformation, and can be detected in both axial and volumetric strain creep variations. The stress ratio seems to more or less influence the volumetric strains. The strain rate variation with time indicates an induced anisotropy and this process may need further micro investigations.

Chapter 4 Microscopic characterization of clay related to creep

The study of soil microstructure involves the study of the arrangement of solid particles as well as the pore space variation. The study of the pore space can be performed by the mercury porosimetry, while the use of Scanning Electron Microscope can provide information on the shape, orientation and concentration of particles, as well as on the pore space.

We aim in this chapter to try to identify the changes of the microstructure evolving during the creep performed at different stress conditions. The approach allows a better understanding the mechanisms governing the creep behavior of clayey materials.

The experimental method consisted of performing a series of triaxial tests and investigating afterwards the microstructural state. Each test was performed twice (along exactly the same stress path and stress level), the first one test being on purely deviatoric stress path (triaxial shear test) up to a given stress level, the other on the same stress path followed by creep test, as explained in section 2.2.1.3 of Chapter 2 (tests series P_{010}).

In this respect, we studied, after each mechanical test (shear only and shear + creep), the evolution of the particle orientation and the pore space related to different stress states and loading history.

4.1 Quantitative analysis of clay structure evolution

In this part, we aim to characterize the evolution of the orientation of the particles under shear and shear + creep, and then we try to define the deformation mechanisms evolving on a microscopic scale.

4.1.1 In contractancy domain

4.1.1.1 Normally consolidated samples

In contractancy domain, the soil behave in contraction in the constant p' stress path triaxial test. This contraction continues to develop under constant sustained stress during creep (Figure 4.1).

The statistical results of particle orientation, through the method developed in Section 2.3.4.1, are shown in Figure 4.2. The figure shows the percentage of particles versus their orientation. The orientation 0° means particles oriented towards the horizontal plane (perpendicular to the axial triaxial effective stress). D line means perfect isotropic orientation of a fictional material.

These results were developed on the results of 14 photos with 7227 particles of sample after creep $(P_{010}\text{-NC-q200})_{creep}$ and 10 photos with 4347 particles of soil after monotonic loading $(P_{010}\text{-NC-q200})_{shear}$. We find that the kaolinite particles are mainly oriented in a direction band from 150° to 165°. 23.8% of the particles are in this preferential direction after shear, while 30.8% of particles oriented in this angle band after creep. All the structural orientation information are listed in **Erreur ! Source du renvoi introuvable.** in Annex Chapter 4.

The higher percentage peak value after creep (point **P** in Figure 4.2) presents the microstructure evolution within the creep phase, i.e., more individualized particles tend to parallel to each other in this preferential direction, resulting in more stable face-face contact accompanied by the decrease of void ratio in creep contractancy. Meanwhile, under the constant sustained stress, the structural anisotropy is highlighted, with a lower value of orientation index I_{or} after creep. The parameter I_{or} can vary from 1 for an isotropic structure to 0 for a perfectly anisotropic structure, as explained in the in Section 2.3.4.1 of Chapter 2 (see the Function 2.19).

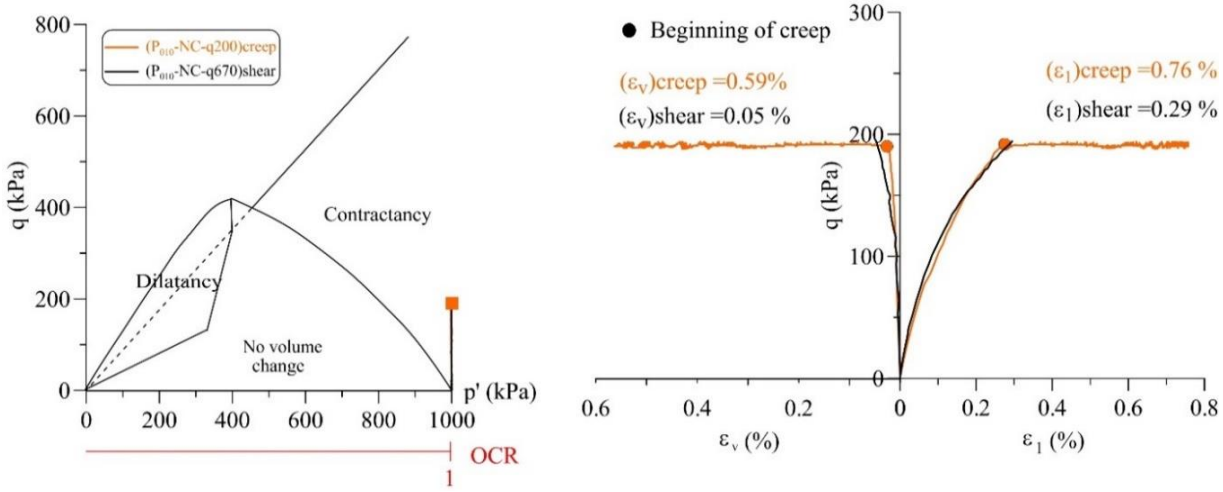

(a) (b)

Figure 4.1 Tests P_{010}-NC-q200 in contractancy domain: (a) in *(p'-q)* plane (b) strain evolution

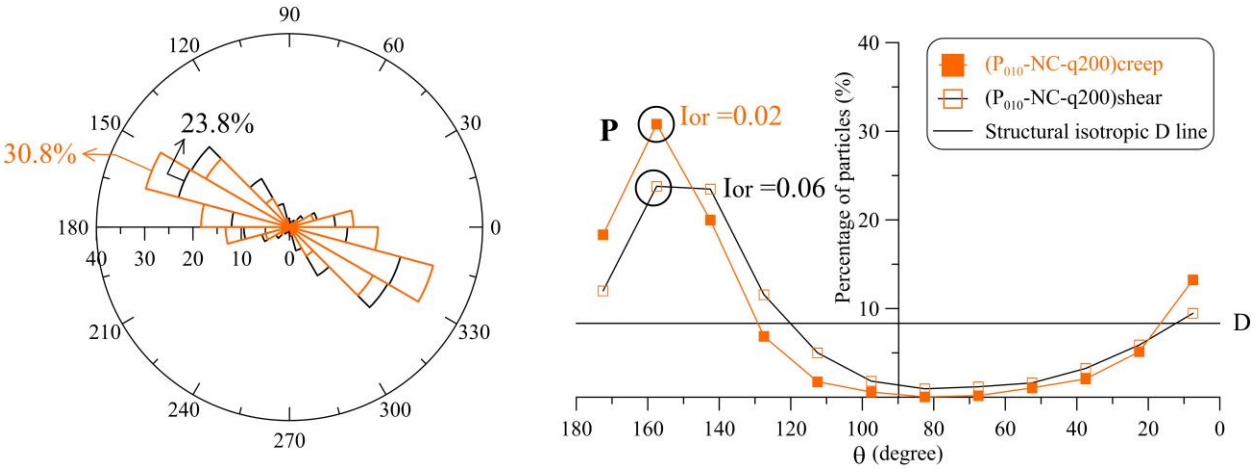

Figure 4.2 Angular orientation of the edge view particles for tests P_{010}-NC-q200

Figure 4.3 presents the representative SEM photos of tests P_{010}-NC-q200 in contractancy domain after shear and after creep, where the red dotted line indicates examples of particle groups giving the microfabric-oriented information. We can see in Figure 4.3 that the vast majority of isolate particles are plate shaped and form aggregates with a maximum diameter of about 10 μm. The mean size of an individual particle is about 1.5 μm in length of edge. Generally, the particles are face-face associations showing by thin layers in the side view of SEM photos. Furthermore, as we can see in this example, it appears that the soil particles tend to more orientated after a period of creep time (Figure 4.3b) than that of after shear (Figure 4.3a).

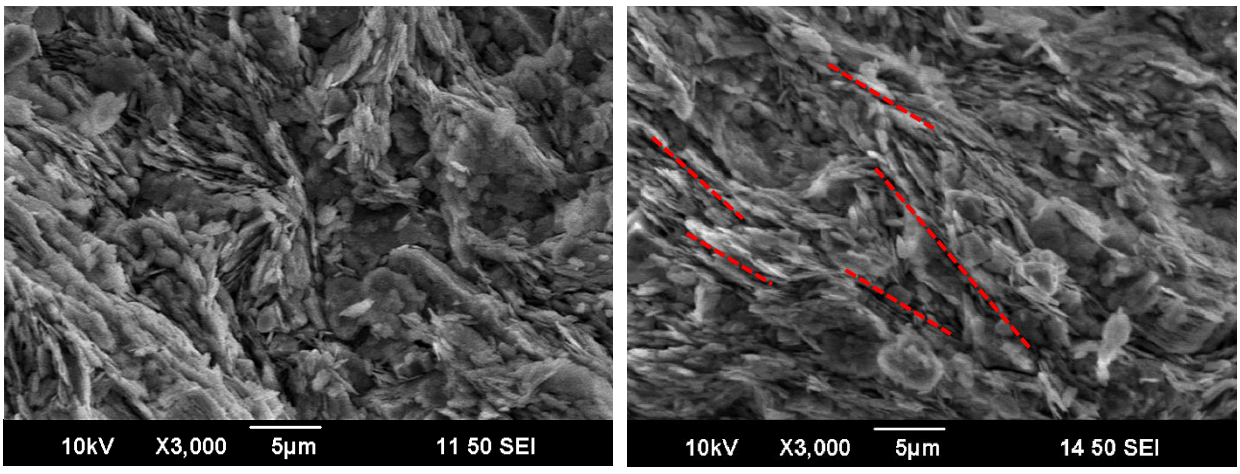

(a) (b)

Figure 4.3 Microfabric of tests P_{010}-NC-q200 in contractancy domain: (a) after shear (b) after creep

Similar results were obtained for normally consolidated specimens under higher stress level of tests P_{010}-NC-q670 (see Figure 4-1 to Figure 4-2 in Annex Chapter 4). The percentage of particles oriented in the band of 150° to 165°, and the structural anisotropy developed within creep phase.

4.1.1.2 Lightly overconsolidated samples

For lightly overconsolidated samples located in contractancy domain (Figure 4.4), the contraction evolves as for the normally consolidated samples.

Based on the statistical results developed on 15 SEM images for each test, we plot the angular orientation pf particles for the lightly overconsolidated sample after shear and after creep in Figure 4.5. It is seen that the preferential direction for these lightly overconsolidated material is from 150° to 165°, same as the normally consolidated samples in this contractancy domain. The less anisotropy trend, with a higher value of orientation index I_{or} after creep, resulting from the reorientation of particles under this loading history. These results can be explained by the fact that some groups of particles tend to rearranged at small crossed angle, this tendency indicating the influence of stress history. It is seen in Figure 4.6b that more side-face associations are identified on the sample after creep than that just after shear (Figure 4.6a), although face-face associations are still the predominance contact pattern in this stress condition.

As we can see in the SEM photo represented in Figure 4.6, the observations are slightly different from the normally consolidated ones (Figure 4.3).

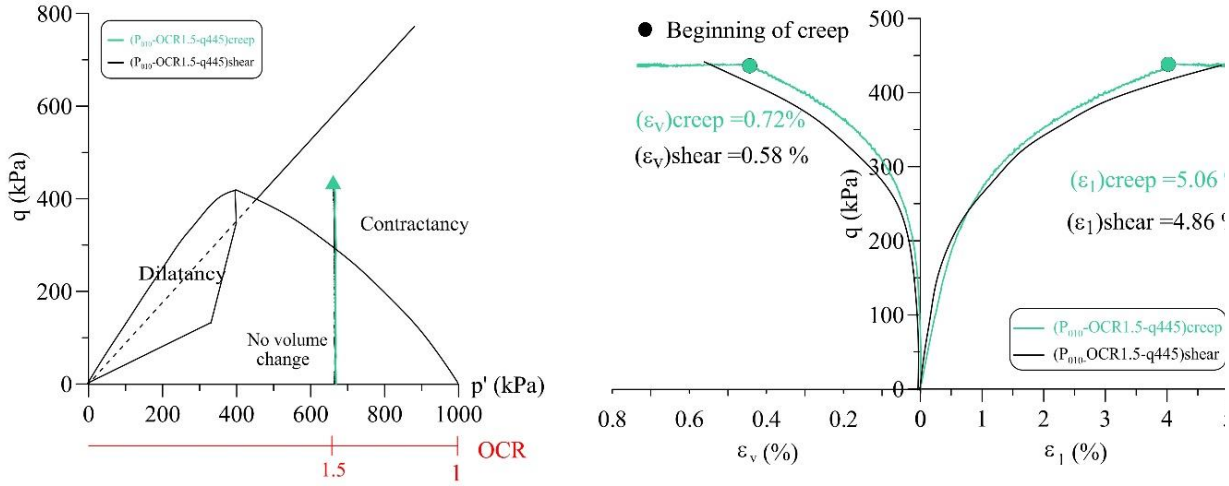

(a) (b)

Figure 4.4 Tests P_{010}-OCR1.5-q445 in contractancy domain: (a) in *(p'-q)* plane (b) strain evolution

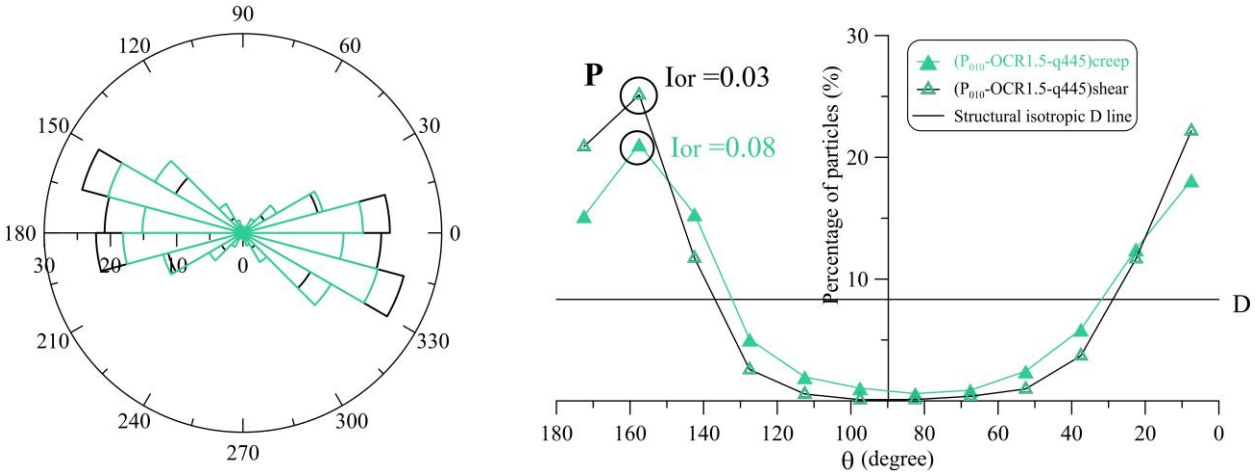

Figure 4.5 Angular orientation of the edge view particles for tests P_{010}-OCR1.5-q445

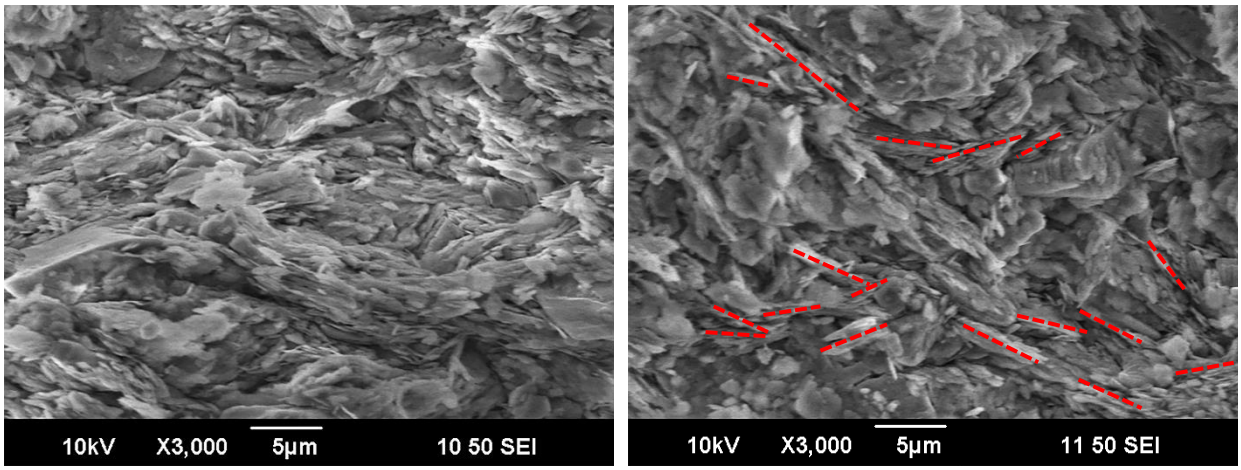

(a) (b)

Figure 4.6 Microfabric of tests P_{010}-OCR1.5-q445 in contractancy domain: (a) after shear (b)after creep

4.1.2 In pseudo-elastic domain

For lightly overconsolidated soil in pseudo-elastic domain, very limited strain develop in constant p' stress loading path, and we assume that no volumetric creep strain will evolve in this domain as explained in Section 3.2.2 of the Chapter 3. Figure 4.7 presents the strain evolutions of lightly overconsolidated specimens (P_{010}-OCR2.5-q200) in this volumetric domain before and after creep.

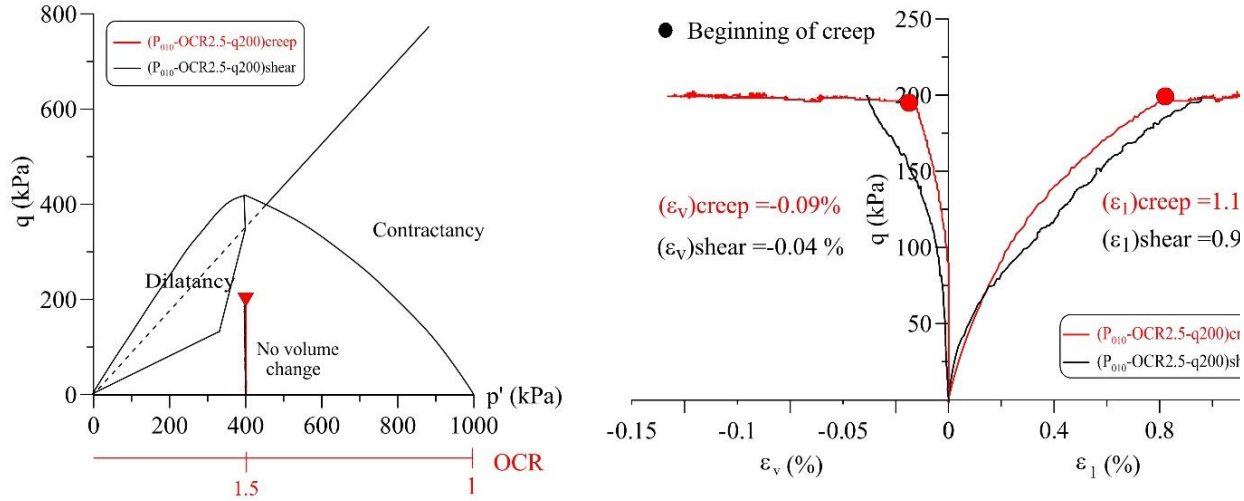

Figure 4.7 Tests P_{010}-OCR2.5-q200 in pseudo-elastic domain: (a) in *(p'-q)* plane (b) strain evolution

Quantitative analysis on the particle orientation developed on SEM images is shown in Figure 4.8. Quite consistent tendency of the particle orientation for these two tests is observed, which demonstrates that very limited structure rearrangement evolved during creep. The main percentage of particles oriented in 150° to 165° band for the two samples.

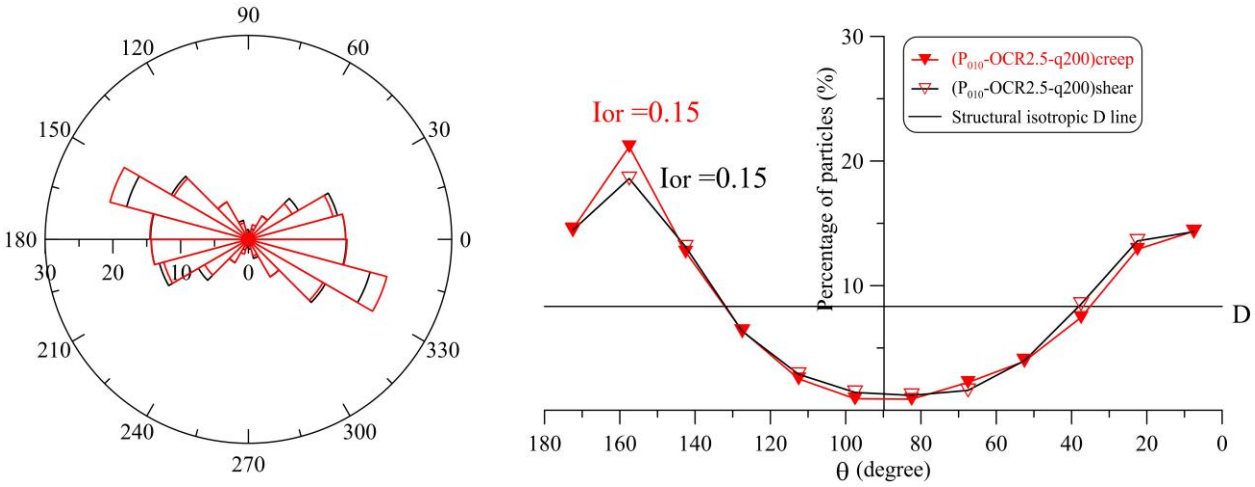

Figure 4.8 Angular orientation of the edge view particles for tests P_{010}-OCR2.5-q200

Figure 4.9 shows the representative SEM images of sample whose stress condition located in this pseudo-elastic domain. We can see that the state of the clay structure after shear and after creep are in similar. The two-slip plane pattern of particles results from the microstructural rearrangement under this constant p' stress path.

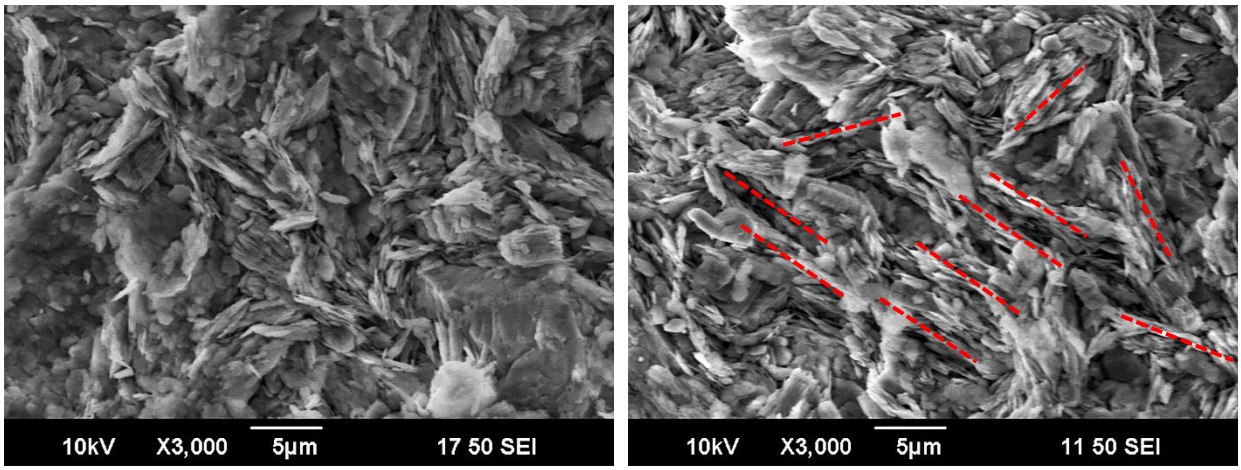

(a) (b)

Figure 4.9 Microfabric of tests P_{010}-OCR2.5-q200 in contractancy domain: (a) after shear (b)after creep

Similar results are obtained for lightly overconsolidated specimens with OCR=1.5 in the pseudo-elastic domain, see Figure 4-4 to Figure 4-5 in Annex Chapter 4.

4.1. 3 In dilatancy domain

When the stress condition locates in the dilatancy domain, the shear dilatancy evolves within the monotonic loading and the dilatancy continues to develop under constant sustained stress (Figure 4.10).

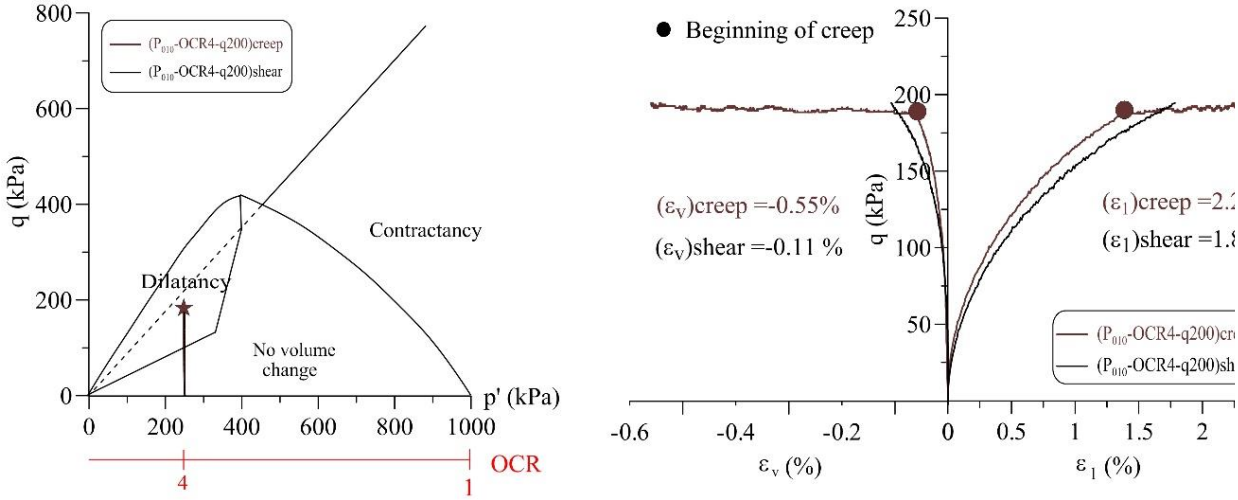

(a) (b)

Figure 4.10 Tests P_{010}-OCR4-q200 in dilatancy domain: (a) in *(p'-q)* plane (b) strain evolution

Figure 4.11 presents the statistical results of percentage of particle orientation of soil after shear and after creep, respectively. Unlike the samples in contractancy domain, less strong preferential

orientation are identified for soils in dilatancy domain. The percentage of particles oriented towards the isotropic structure, this tendency evolve with the dilatancy and creep, resulting in a percentage line closer to the structural isotropic D line. The representative SEM images in Figure 4.12 can give an explanation to these results. The photos show the appearance of structural isotropy tendency develops from dilatancy in creep phase, locally we observe groups of particle arrangement (see the red dotted line in Figure 4.12b) forming random open micro-cracks inside the material (see the blue circles in Figure 4.12b).

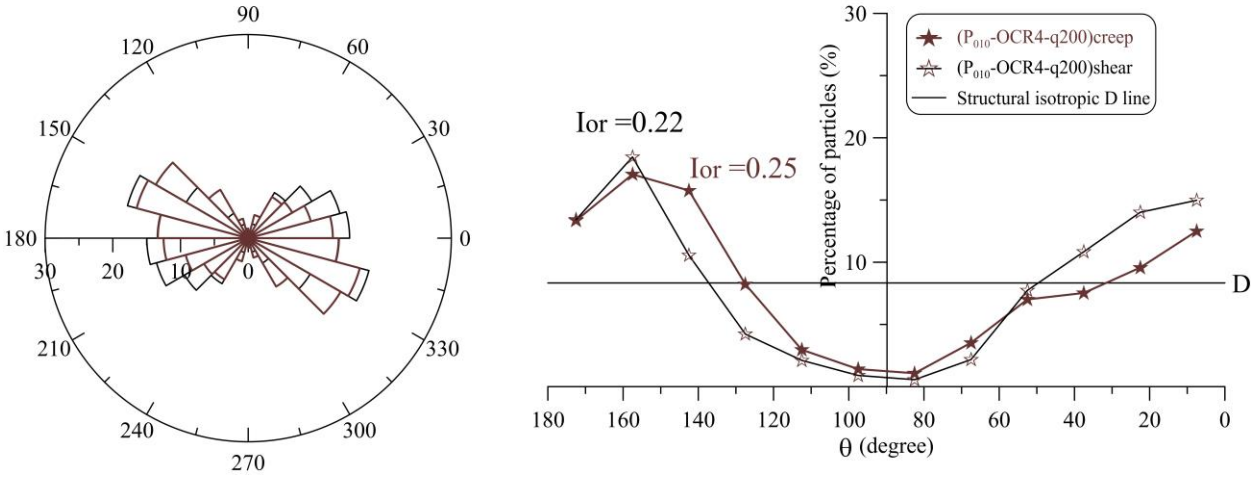

Figure 4.11 Angular orientation of the edge view particles for tests P_{010}-OCR4-q200

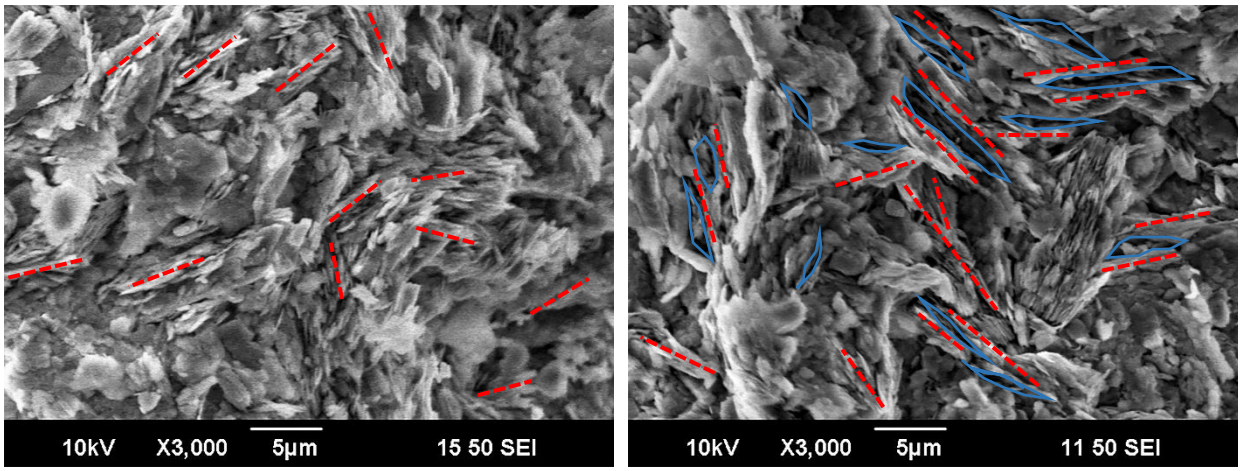

(a) (b)

Figure 4.12 Microfabric of tests P_{010}-OCR4-q200 in dilatancy domain: (a) after shear (b) after creep

4.1.4 Structure evolution with the variation of stress

4.1.4.1 Under the same deviatoric stress

For samples loaded until the same q (= 200kPa), along condition of line ① in Figure 4.13.

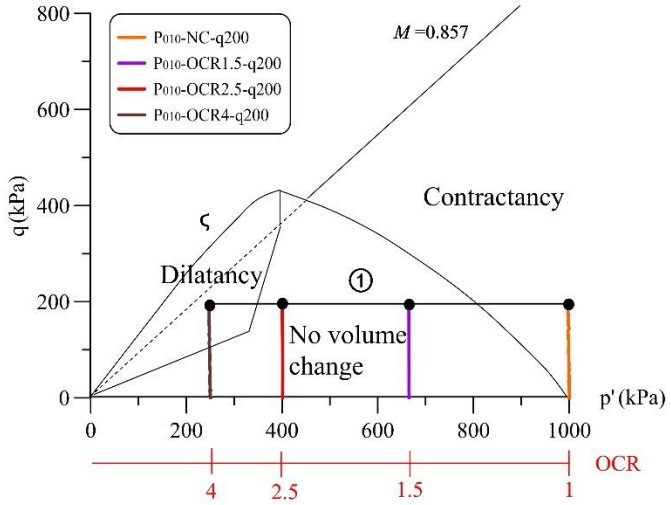

Figure 4.13 Tests under the same deviatoric stress in (p'-q) plane

The microstructure evolution is shown in Figure 4.14. After monotonic loading, we can observe the structural anisotropy for the normally consolidated sample in contractancy domain (P_{010}-NC-q200) in Figure 4.14a. The maximum percentage of particles are in the band of 135° to 165°. The structural anisotropy evolves with the OCR towards an isotropic fabric, which is called the depolarization mechanism according to Hattab & Fleureau (2010), resulting in a curve closer to the **D** line for highly overconsolidated sample in dilatancy domain.

At the end of monotonic loading, the stress was maintained constant for a certain duration, i.e., creep condition, the structure evolution can be highlighted in the specimens after creep (Figure 4.14b). For normally consolidated specimen, we can see a strong structural anisotropy through the principal orientation model (**P**) curve with 30.8% of particles oriented in 150° to 165°. While for the highly overconsolidated sample (P_{010}-OCR4-q200), the orientation curve is closer to the structure isotropic **D** line than the highly overconsolidated sample after shear, due to the dilatancy developed in creep phase.

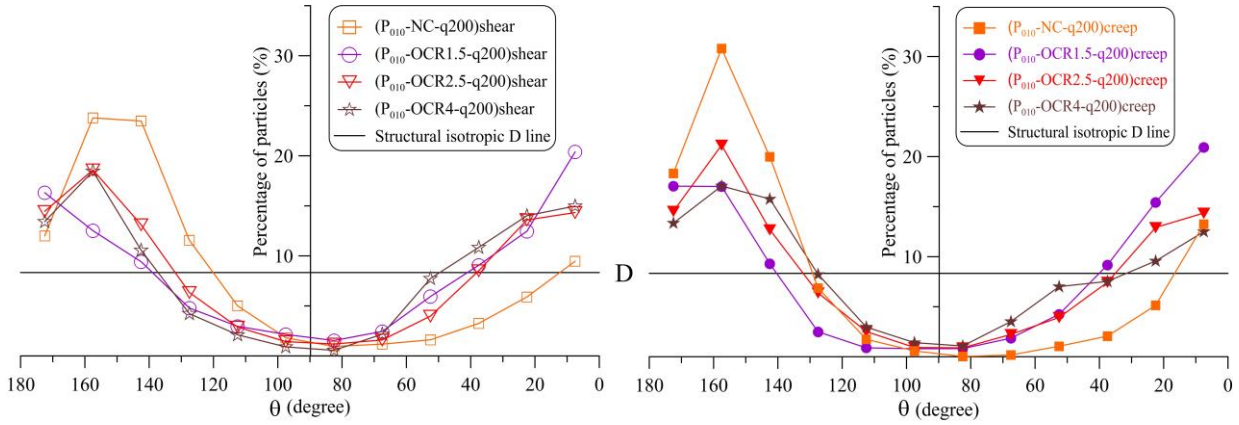

(a) (b)

Figure 4.14 Microstructural evolution under the same deviatoric stress: (a) after shear (b) after creep

The structure evolution can be further qualified in the relation with isotropic index in Figure 4.15. The depolarization in soil structure with the consolidation history can be seen clearly in the relationship of I_{or} versus OCR. That is, I_{or} increase with OCR for both the series of shear tests and creep tests, corresponds to the depolarization tendency from normally consolidated to highly overconsolidated state of the material.

As it is revealed in Figure 4.14b, the structural evolution with OCR continue to develop within the creep phase. For example, I_{or} =0.06 for sample $(P_{010}\text{-NC-q200})_{shear}$ with ε_1=0.29% at the end of shear phase, the structural anisotropy develops within creep phase with I_{or} =0.02 for sample $(P_{010}\text{-NC-q200})_{creep}$ at ε_1=0.76%. For highly overconsolidated sample (OCR=4), high value of I_{or} (=0.22) for shear sample is obtained corresponding to the structural anisotropy in this stress condition, while a higher value of I_{or} (=0.25) can be obtained for the specimen after creep. In this condition, we obtain the dilation at the scale of sample due to the random microstructural orientation of open micro-cracks, this tendency continue to develop within creep.

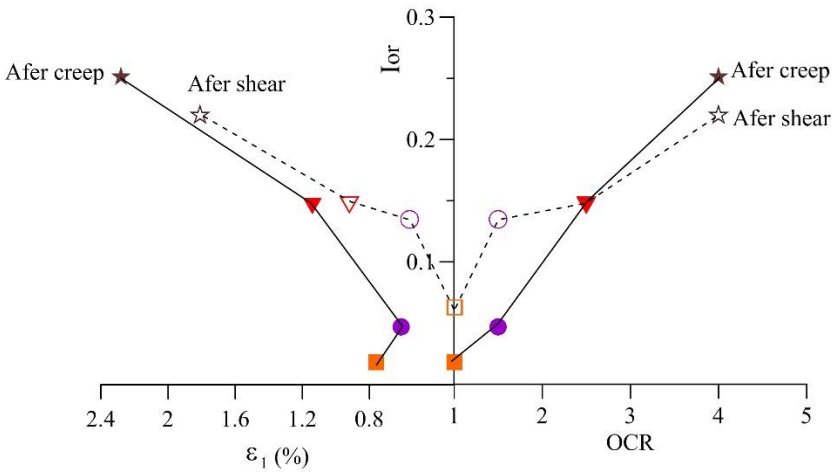

Figure 4.15 Evolution of isotropic index as a function of OCR and axial strain

4.1.4.2 Under the same OCR

Following the same constant p' stress path in monotonic loading, the test series under different stress levels are shown in Figure 4.16.

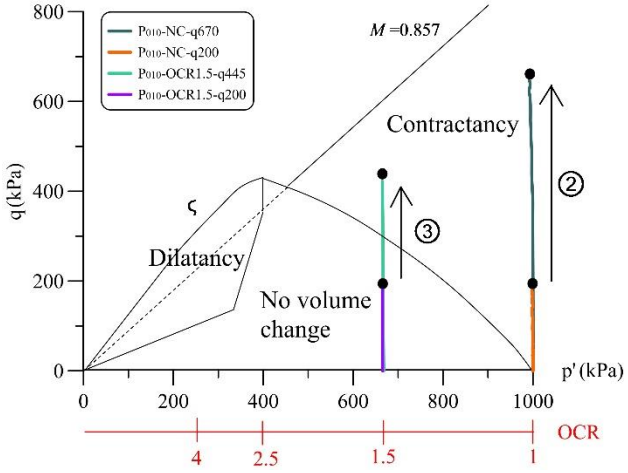

Figure 4.16 Test series under different stress levels in (p'-q) plane

We observe the structural anisotropy in normally consolidated samples (along condition ② in Figure 4.16), showing by the clear U-shape curves in Figure 4.17a. For sample under higher stress level (q=670 kPa), the principal orientation falls in 150° to 165° and 0° to 15°. While for sample with lower stress level (q=200 kPa), the privileged direction are between 150° to 165°.

As explained above, the structural continue to develop during creep. Therefore, the U-shape with higher peak value curves are obtained for samples after creep (Figure 4.17b). The principal

orientation is located between 150° to 165° for the two samples. This can be explained by the fact that, locally in the material, more particles tends to rotate to this direction under constant sustained stress, which represents the induced anisotropy developed during creep.

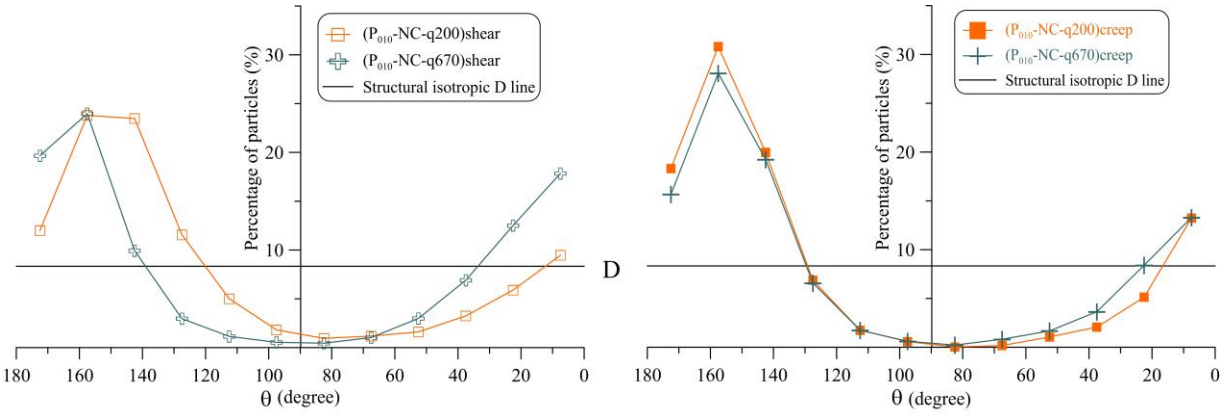

(a) (b)

Figure 4.17 Microstructural evolution with stress level for OCR=1: (a) after shear (b) after creep

The evolution of isotropic index further confirms the development of structural anisotropy during creep (see Figure 4.18). We obtain lower values of I_{or} for samples after creep under different stress levels.

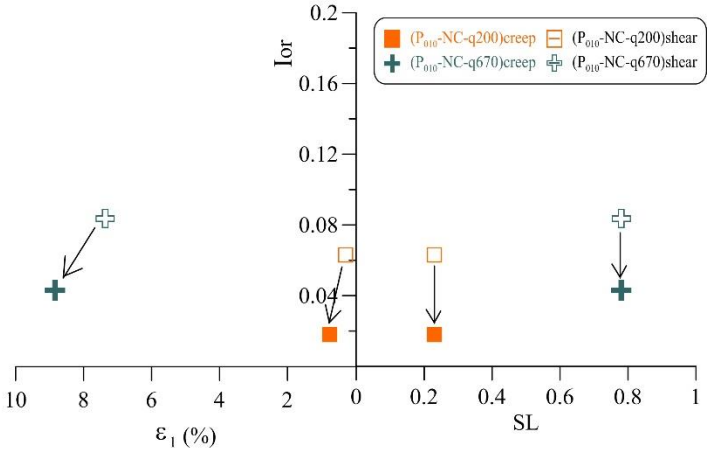

Figure 4.18 Evolution of isotropic index versus *SL* and axial strain for normally consolidated samples

For the lightly overconsolidated samples loading up to different stress levels (condition of line ③ in Figure 4.16), the structural evolution seems to be a little different from the normally consolidated soils. For sample after shear (Figure 4.19a), the structural anisotropy is increased when q is loaded up to the contractancy domain (test P_{010}-OCR1.5-q445); while less anisotropy trend is observed with sample under lower stress level in pseudo-elastic domain (test P_{010}-OCR1.5-q200). After creep, the orientation curves for these two samples are closer (Figure 4.19b), resulting

from a slightly depolarization for sample in the contractancy domain and the structural anisotropy enhancement of soil in pseudo-elastic domain (Figure 4.20).

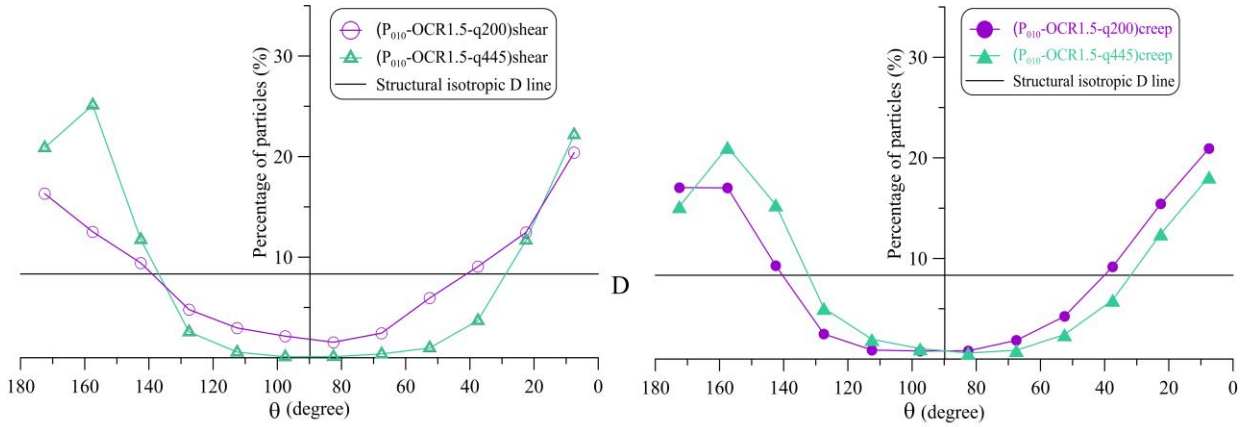

(a) (b)

Figure 4.19 Microstructural evolution with stress level for OCR=1.5: (a) after shear (b) after creep

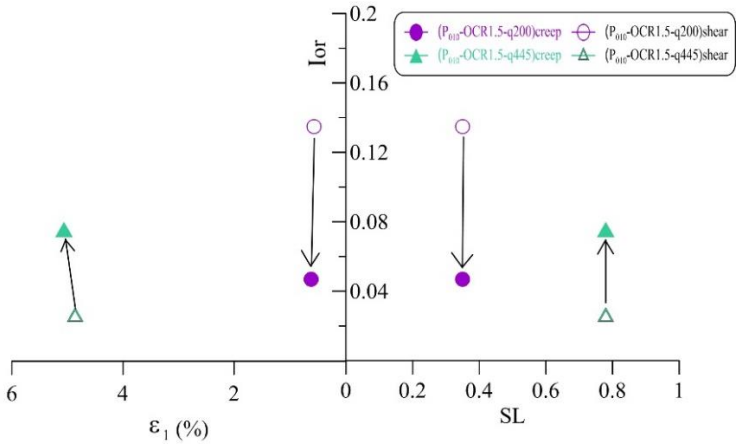

Figure 4.20 Evolution of isotropic index versus SL and axial strain for lightly overconsolidated samples

4.1.4.3 Under the same stress ratio

For samples under the same stress ratio in contractancy domain (condition of line ④ in Figure 4.21), the microstructural evolution for the normally consolidated sample and lightly overconsolidated sample are in quite consistency at the end of monotonic loading (Figure 4.22a). While for samples after creep (Figure 4.22b), the differences is enlarged likely due to the particle rearrangement within the creep phase under different loading history. For normally consolidated sample, more particles tend to rotate in parallel to each other in the privileged direction (150° to 165°), showing by higher peak curve of the percentage particles but with lower I_{or}. For lightly

overconsolidated sample, the particles tends to rearrange towards the isotropic fabric (Figure 4.23), although the privileged direction (150° to 165°) is still maintained.

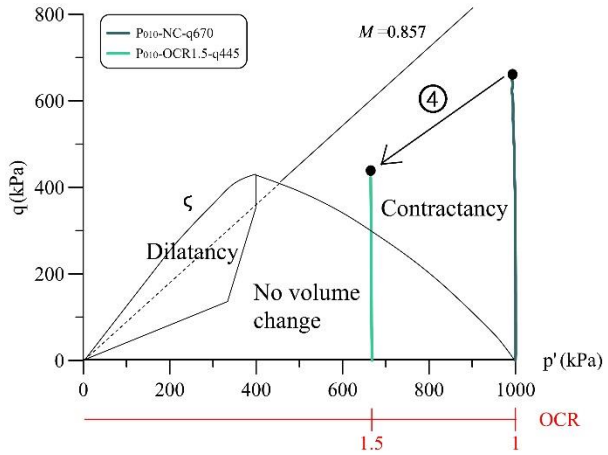

Figure 4.21 Tests under the same stress ratio

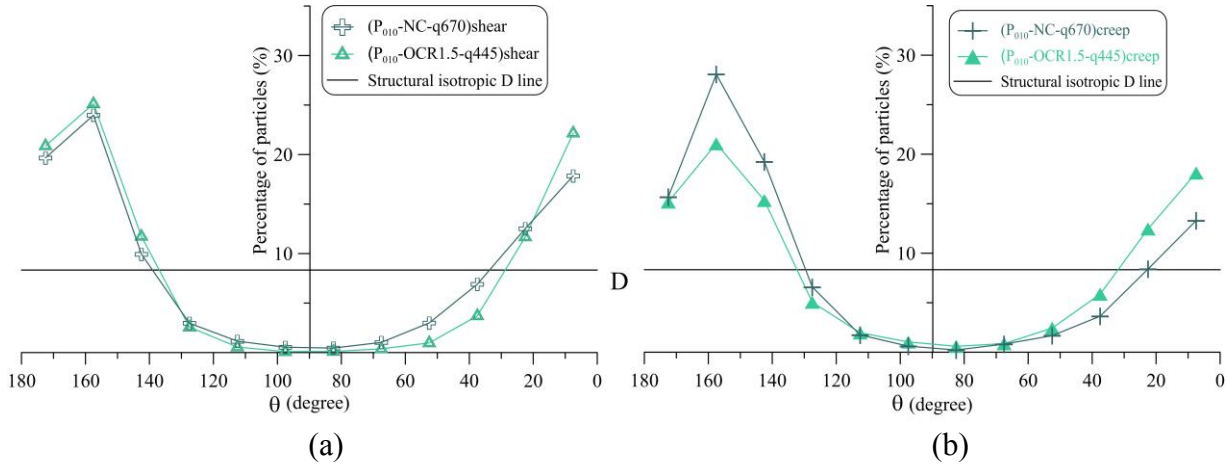

(a) (b)

Figure 4.22 Microstructural evolution under the same stress ratio in contractancy domain: (a) after shear (b) after creep

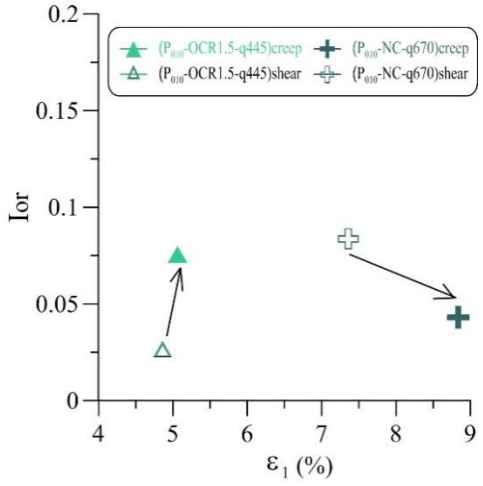

Figure 4.23 Evolution of isotropic index under the same stress ratio in contractancy domain

4.1.5 Discussion

The preferential orientation of particles corresponds to the contraction of normally consolidated soil in contractancy domain becomes more precise during the creep. A complex random orientation, in form of a special organization of particles, occurs for the highly overconsolidated specimens. These results allow highlighting the microstructure mechanism of the dilatancy phenomenon. The phenomenon appears locally with the development of numerous open micro-cracks crossing the material in random directions. During creep, the random orientation of the micro-cracks seems to reinforce.

More generally, the evolution of microstructure of kaolin in creep, under the purely deviatoric stress path, seems to strongly depend on the overconsolidation state, more than the stress level. For the normally consolidated creep samples, the orientation of soil with q=200 kPa and 670 kPa became quite coincide after a certain creep duration, although obviously difference can be found in the samples after monotonic loading. Similar tendency are observed on lightly overconsolidated samples (OCR=1.5) with q=200 kPa and 445kPa. The initial difference of structural orientation, under different stress levels at the end of shear, tends to be minimized in creep phase. This tendency may indicate that under a certain consolidation state, a certain equilibrium structural state exits, and the structural under different stress levels will evolve with time towards this state.

4.2 Evolution of the pores

In respect to the image processing to obtain the pore space, the used technique is deeply described in Section 2.3.4.2 in Chapter 2, the post-processing of the SEM image consisting in defining the pore space, diameter and orientations that identified in the images and, for that, we make some hypotheses:

The photo is considered as a surface; the black part represents the pores because there is no reflection of the secondary electrons. Therefore, we delineate the surfaces representative pores in order to perform the treatment that mentioned in Chapter 2 (§2.3.4.2).

We consider that the pores are ellipsoids and that the image in the vertical plane represents the front projection. In this case, we can consider that the length of the secondary axis represents the

diameter of pore. The orientation of the pores is defined by the angle of main axis from the horizontal.

4.2.1 Pore orientation

Figure 4.24 presents the results of pore space identification fitting by ellipses developed on the SEM images, take the example of three test P010-NC, OCR2.5 and 4-q200 in three volumetric domains. We can see that the majority of pores for normally consolidated specimen $(P_{010}\text{-NC-q200})_{creep}$ are preferentially oriented, showing by the flatted ellipses (Figure 4.24b). While for the highly overconsolidated specimen $(P_{010}\text{-OCR4-q200})_{creep}$, the pores are more randomly oriented (Figure 4.24f), corresponding to the structural isotropy in dilation. For the lightly overconsolidated specimen $(P_{010}\text{-OCR2.5-q200})_{creep}$ in pseudo-elastic domain, a transformation pattern from anisotropy to isotropy of pore orientation can be seen (Figure 4.24d).

The particles in movement during mechanical loading tend to have a certain preferred orientation in space, and the corresponding inter-particle pore spaces give orientation information of the structural rearrangement. Figure 4.25 presents the orientation of pores identified through the semi-automatic methods by Image J. Generally, the pore orientation under different stress conditions are in quite consistency with the orientation of particles that identified manually. For example, we observe significant structural anisotropy (**P** model) for the normally consolidated samples (Figure 4.25a and Figure 4.25b). For highly overconsolidated samples (OCR=4 in Figure 4.25f), the depolarization is introduced which means a random pore organization (**D** model).

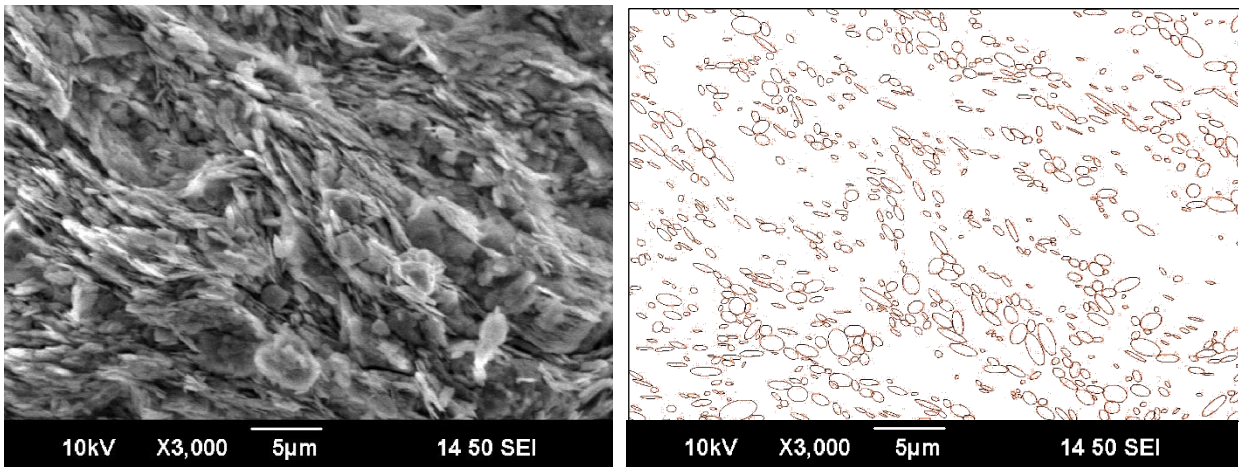

(a) (b)

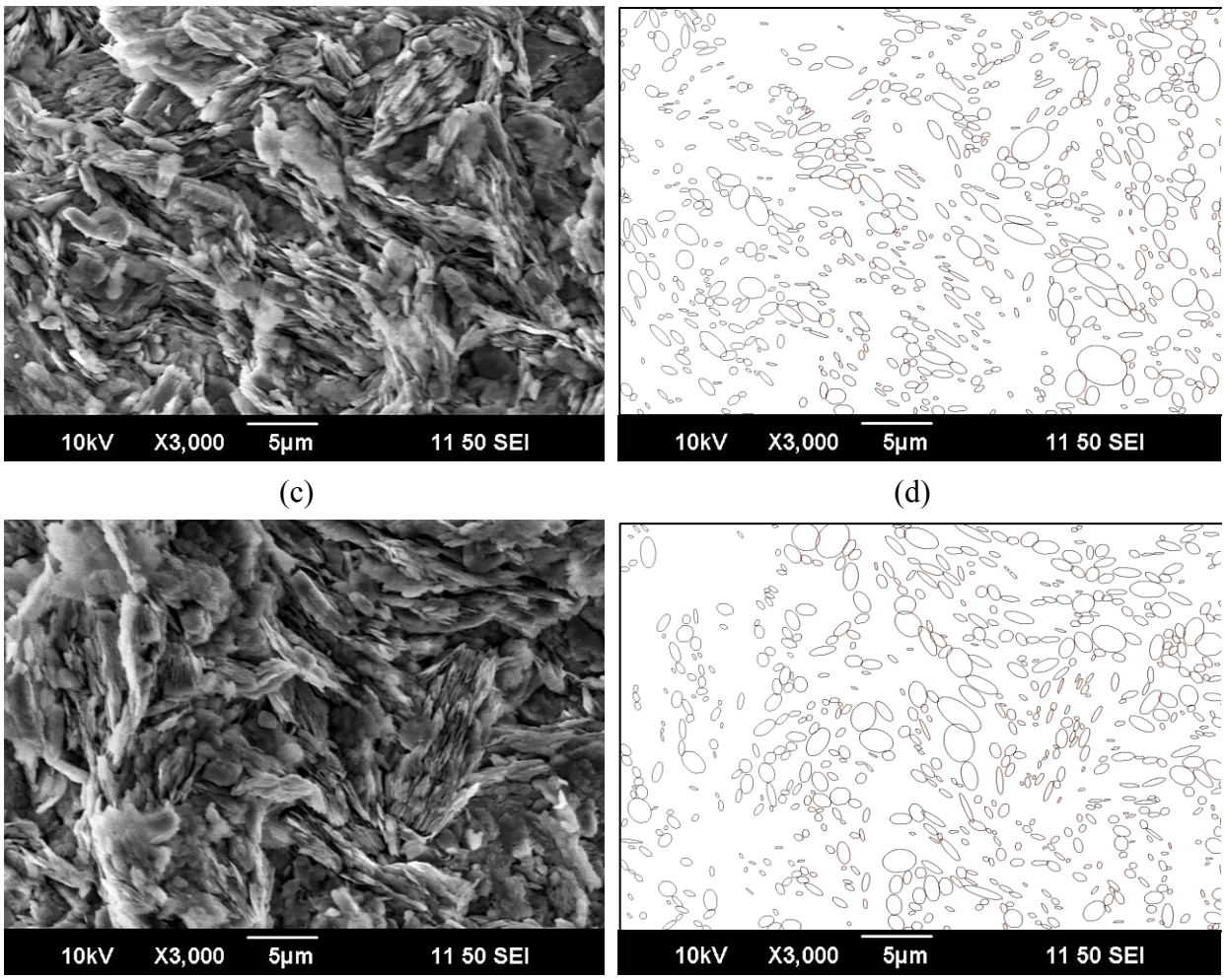

Figure 4.24 Pore space identification: (a), (c) and (e) are representative SEM images for creep tests P_{010}-NC, OCR2.5 and 4 -q200; (b), (d) and (f) are pore spaces fitted by ellipse

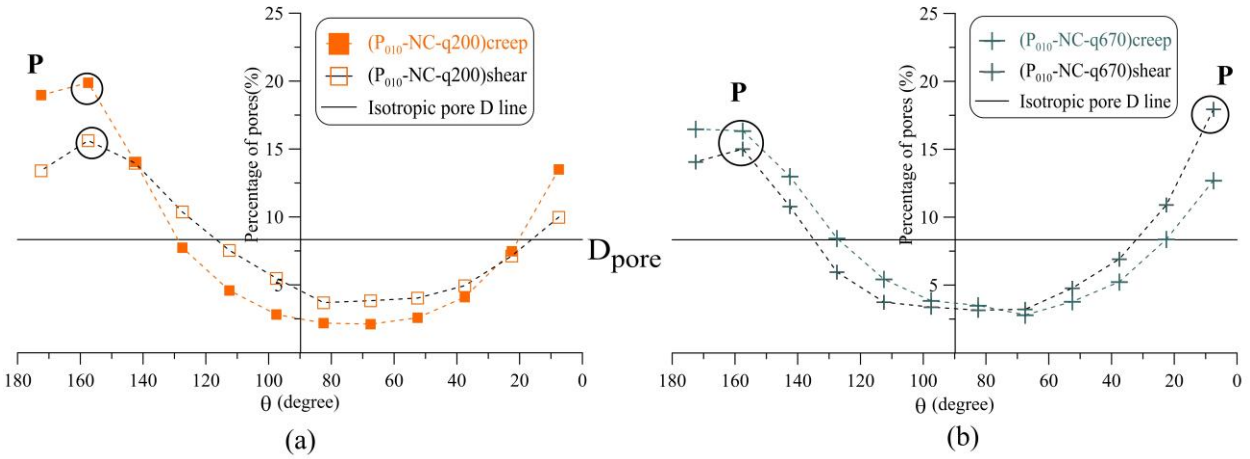

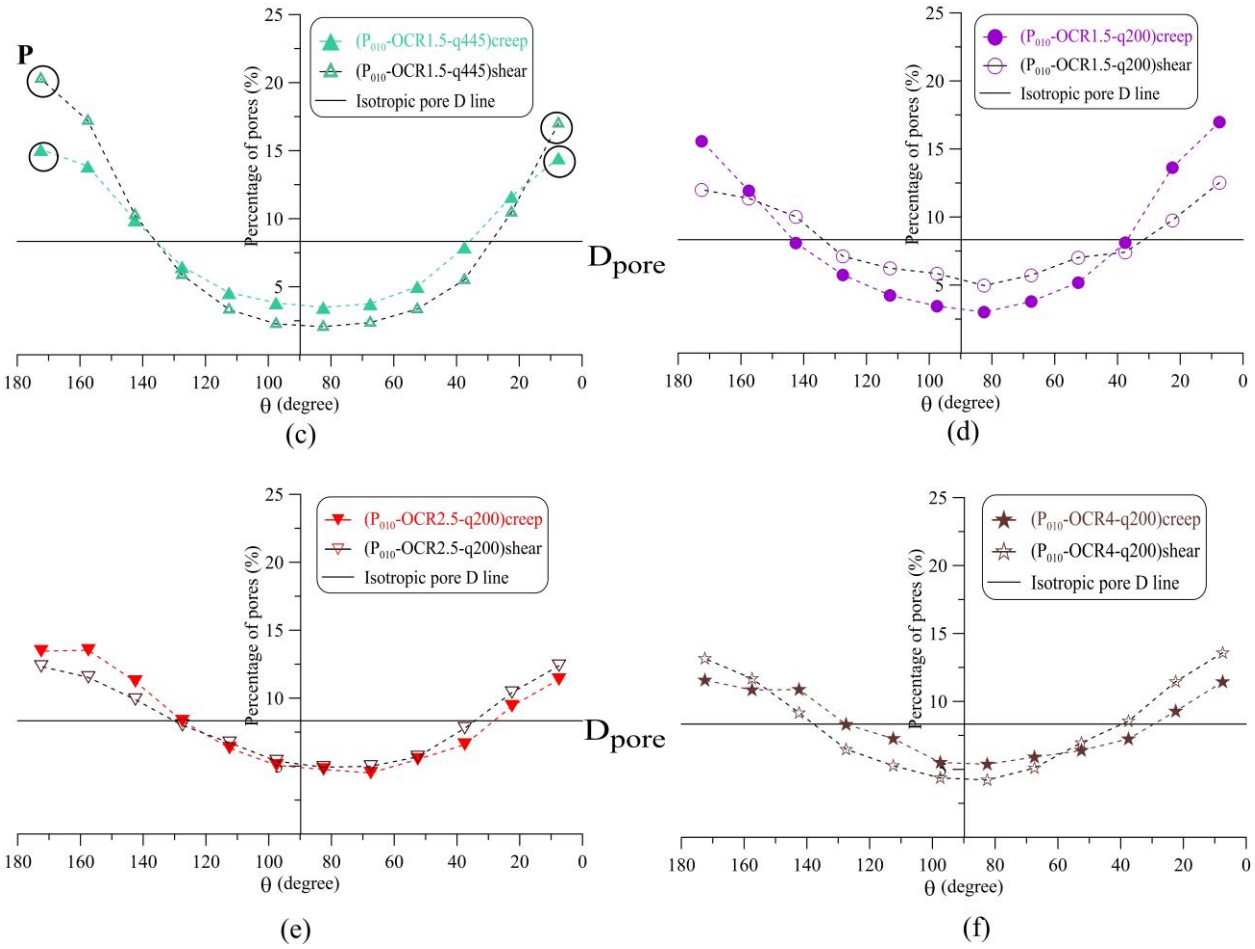

Figure 4.25 Pore orientation of samples after shear and after creep: (a) tests P_{010}-NC-q200 (b) tests P_{010}-NC-q670 (c) tests P_{010}-OCR1.5-q445 (d) tests P_{010}-OCR1.5-q200 (e) tests P_{010}-OCR2.5-q200 (f) tests P_{010}-OCR4-q200

The evolution of pores are discussed separately thereafter according to different stress conditions, and all the information of pore orientation are summarized in **Erreur ! Source du renvoi introuvable.** in Annex Chapter 4.

4.2.1.1 Under the same deviatoric stress

For the four tests loaded until the same deviatoric stress (q = 200kPa), the evolution of pore orientation after monotonic loading is shown in Figure 4.26a. We can see that the pores behave towards structural isotropy when the soil from normally consolidated to highly overconsolidated state. Based on this initial state at the end of monotonic loading, the structure of soils continue to evolve under constant sustained stress in creep phase, showing by an increase in structural

anisotropy in normally consolidated and lightly overconsolidated samples and an increase in structural isotropy in highly overconsolidated soil (Figure 4.26b).

Thereafter, we can calculate the isotropic index based on the percentage of pores through Equation 2.19 in Chapter 2, the same as the calculation of I_{or} for structural orientation in Section 4.1. Figure 4.26c presents the relations of the isotropic index I_{or} versus OCR as well as the volumetric strain. It can be seen clearly that after creep I_{or} decreases with ε_v for OCR = 1 sample, and increase with the dilatancy in OCR = 4 material. For the lightly overconsolidated soil (OCR = 1.5 and 2.5), although there is almost no volume change occurs within creep, the structure anisotropy is also observed as for the normally consolidated soil in contractancy domain.

The orientation of pores is associated to the rearrangement of particles or particle groups under the external load. The quite consistent results on the orientation of particles (Figure 4.14 and Figure 4.15) and pores, identified manually and semi-automatically, confirms a reliable structural result developed on the SEM photos.

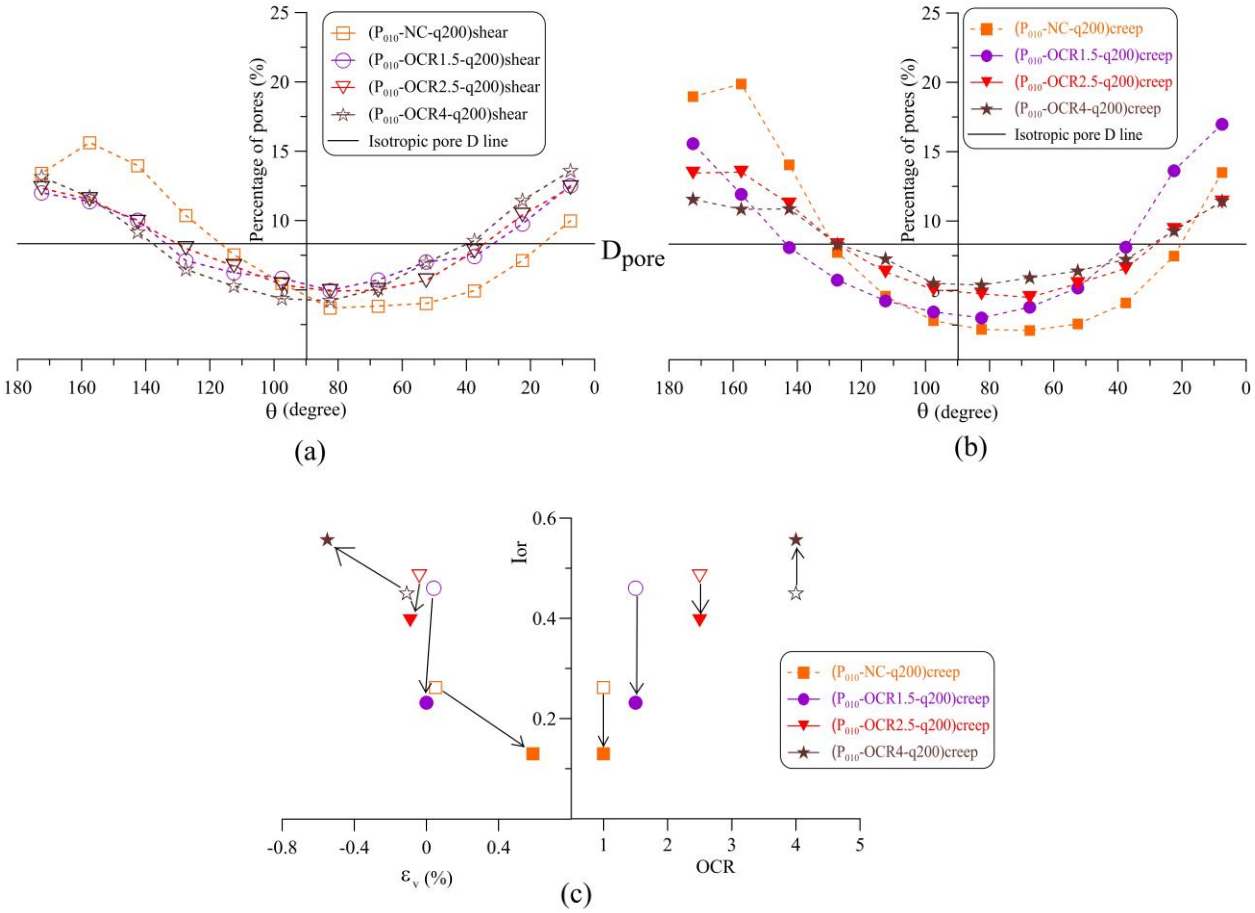

Figure 4.26 Pore orientation under the same deviatoric stress: (a) after shear (b) after creep (c) evolution of isotropic index

4.2.1.2 Under the same OCR

Following the same stress path, the distribution pattern of pores in soil depends on the magnitude of stress applied to the soil. The structural anisotropy is increased under higher stress level for both the normally consolidated samples in Figure 4.27a and lightly overconsolidated ones in Figure 4.28a, where we can see apparent differences in the percentage curves under different stress levels.

After certain durations in creep phase, the differences in the orientation of pores under different deviatoric stresses decrease. We can see in Figure 4.27b that the structural anisotropy increase for the two normally consolidated samples after creep, and the preferred orientations are in the same range (150° to 165°) with q = 200 kPa and 670 kPa. For lightly overconsolidated samples after creep (Figure 4.28b), structural isotropic evolved for sample with q = 445kPa while a structural anisotropy developed for soil with q = 200 kPa, resulting in a quite coincide orientation pattern which towards the horizontal.

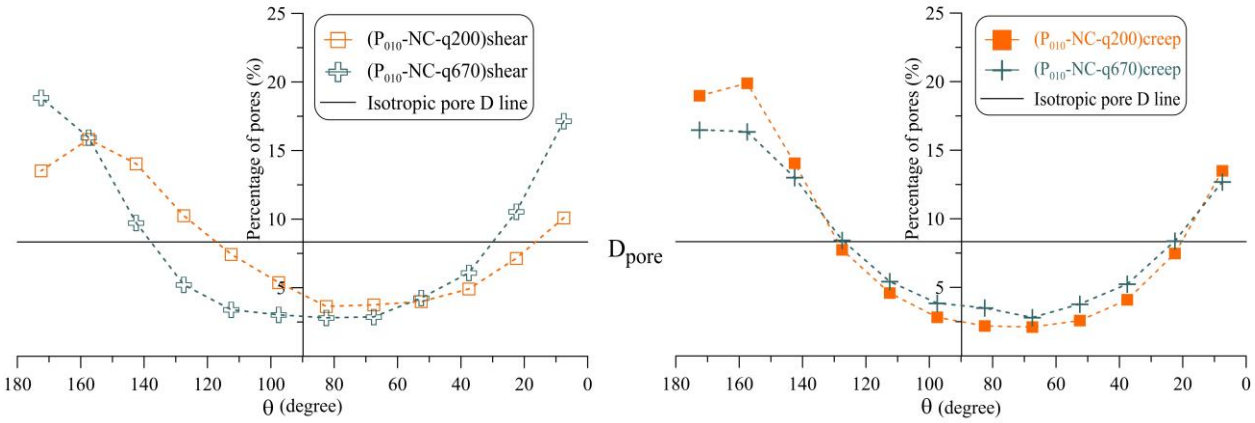

(a) (b)

Figure 4.27 Pore orientation versus stress level with OCR=1: (a) after shear (b) after creep

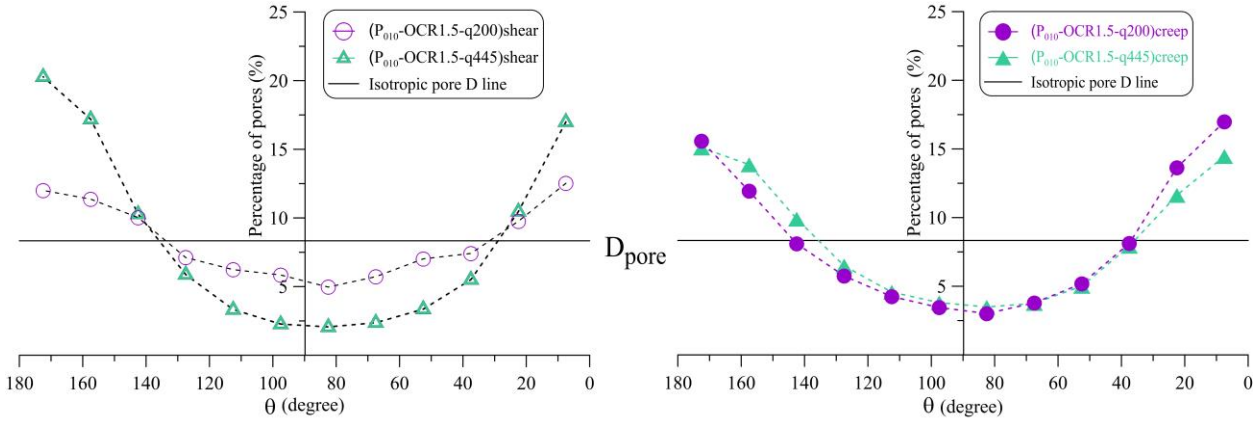

(a) (b)

Figure 4.28 Pore orientation versus stress level with OCR=1.5: (a) after shear (b) after creep

4.2.1.3 Under the same stress ratio

For samples loaded until the same stress ratio (at η = 0.67) in the contractancy domain, the percentage of particles for test P_{010}-NC-q670 and test P_{010}-OCR1.5-q445 are very close (Figure 4.29a), the principle orientation locate mainly in 0° to 15° and 150° to 180°.

While for samples after creep (Figure 4.29b), the differences between these two tests increase. It is most likely that the different loading history tends to change the direction of pore rearrangement within creep phase.

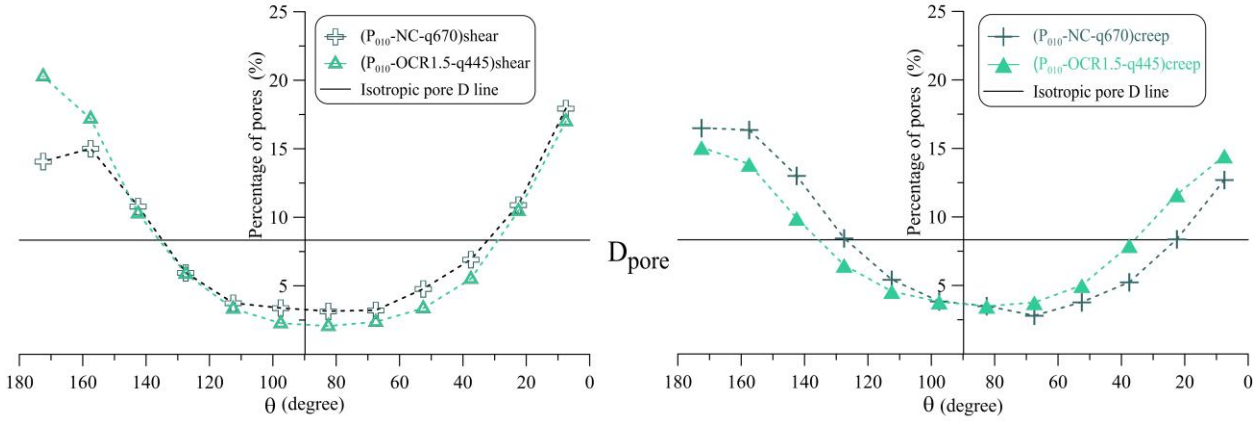

(a) (b)

Figure 4.29 Pore orientation under the same stress ratio: (a) after shear (b) after creep

Generally, the results of pore orientation under different stress conditions are in quite consistency with the orientation of particles. These results further conform the microstructure evolution, after the purely deviatoric stress path in monotonic loading, are obviously related to its

stress condition in (p'-q) plane. That is, the preferential orientation of pores occurred in contraction and isotropic pattern of pores evolved in dilation. The specific pore structure formed after monotonic loading continue to evolve in creep phase.

The random orientation of pores occurs for the highly overconsolidated specimens. The phenomenon appears locally results from the complicated orientation of particles, and the rearrangement of groups of particles accounts for the pore orientation. During creep, the random orientation of the group of pores (or micro-cracks) seems to reinforce.

4.2.2 Pore space by SEM and MIP techniques

4.2.2.1 In the contractancy domain

Following the same stress path, at the end of shear phase the void ratio of samples after shear and after creep (tests P_{010}-NC-q200) are quite close, with e = 0.639 and 0.638 respectively. In the following creep phase, the global void ratio for the sample in creep test is decreased, with e = 0.629 at the end of creep measurement. The evolution of the differential and cumulative mercury intrusion volumes versus pore diameter for these two tests are shown in Figure 4.30.

The differential and cumulative pore volume versus log pore diameter are obtained from the mercury intrusion porosimetry as explained in Section 2.3.2.2 in Chapter 2, while the pore area curves are developed on the SEM images through the method presented in Section 2.3.4.2 in Chapter 2. We can see that for samples after shear and after creep, only one group of pores emerged showing by single peak curves in Figure 4.30a. The most frequent diameter is the same (D_{peak} = 0.161 μm), the same value of D_{peak} mean that creep does not modify significantly the predominant diameter of the pores. For pore diameter lager than D_{peak}, the cumulative volumes of mercury for sample after creep is slightly less that that after shear; whereas for pore diameter less that D_{peak} (especially for D<0.1 μm), almost no difference in the volume can be found between samples after shear and after creep.

The differential pore area, which developed on the front projection area of the pores in the observed section of SEM images is shown in the relation of log pore diameter in Figure 4.30a. Only pore groups whose diameter is larger than 0.1 μm are identified on SEM images subjecting to the resolution restrictions. Therefore, the magnitude of 2D pore groups identified in SEM is larger than those identified by MIP. We can see that the most frequent diameter is smaller for the

sample after creep than that after shear, due to the continuous contraction within creep phase in the scale of sample.

Figure 4.30b shows the cumulative volume of mercury introduced into the sample. The volume of mercury gradually decreases for the sample after creep than that after shear, due to the decrease in porosity within creep contractancy. The cumulative pore area identified on SEM images presents the same tendency, where we can calculate the void ratio per μm^2 e_S by the Equation 2.21 in Section 2.3.4.2 of Chapter 2. The void ratio per gram identified in MIP (e_M) can be calculated by Equation 2.18 ($e_M = V_{intru} \cdot \rho_s$), where e_M = 0.646 for sample after shear and 0.599 after creep, respectively. The equals to 0.267 and 0.247 after shear and after creep.

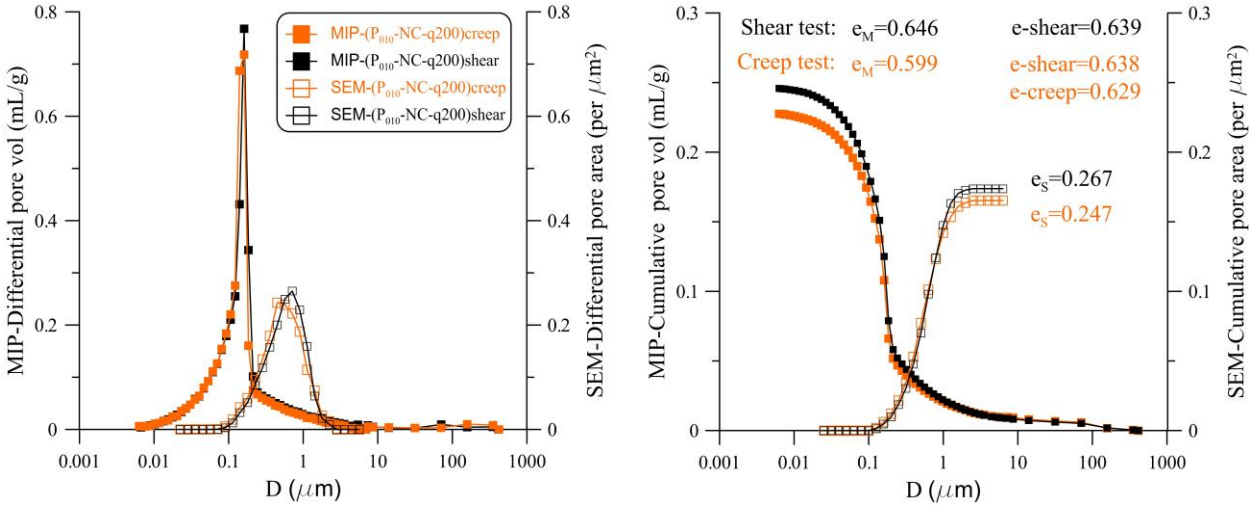

Figure 4.30 Evolution of pore space for test P_{010}-NC-q200 after shear/creep

Comment: test results for the other two group of tests in this domain are illustrated in Figure 4-7 and Figure 4-8 in Annex Chapter 4.

4.2.2.2 In pseudo-elastic domain

After the monotonic loading, the global void ratio for the tests P_{010}-OCR2.5-q200 after shear and after creep in the pseudo-elastic domain are substantially the same. Along 154 hours in creep phase, we observe no volume change of the material on macroscopic level in pseudo-elastic domain. Consequently, no variation occurs in the global void inside the soil in creep.

From Figure 4.31a, we can see that the most frequent diameter of samples, identified in MIP, after shear and after creep are the same (D_{peak}=0.161 μm). The main pore diameter are in a range

between 0.01 μm to 1 μm. Moreover, the differential pore volume for these two samples are quite close. Consequently, we may assume that the state of the porosity before and after creep is equivalent, i.e., no obvious pore space evolve in creep phase.

Differential curves developed on the 2D SEM images show a consistent trend, with larger predominant pore diameter (D_{peak}=0.713) by this technique.

The quite coincide results on the differential and cumulative pore volume/area for sample after and after creep reveals that, in the pseudo-elastic domain, no further variations occur in the pores during creep.

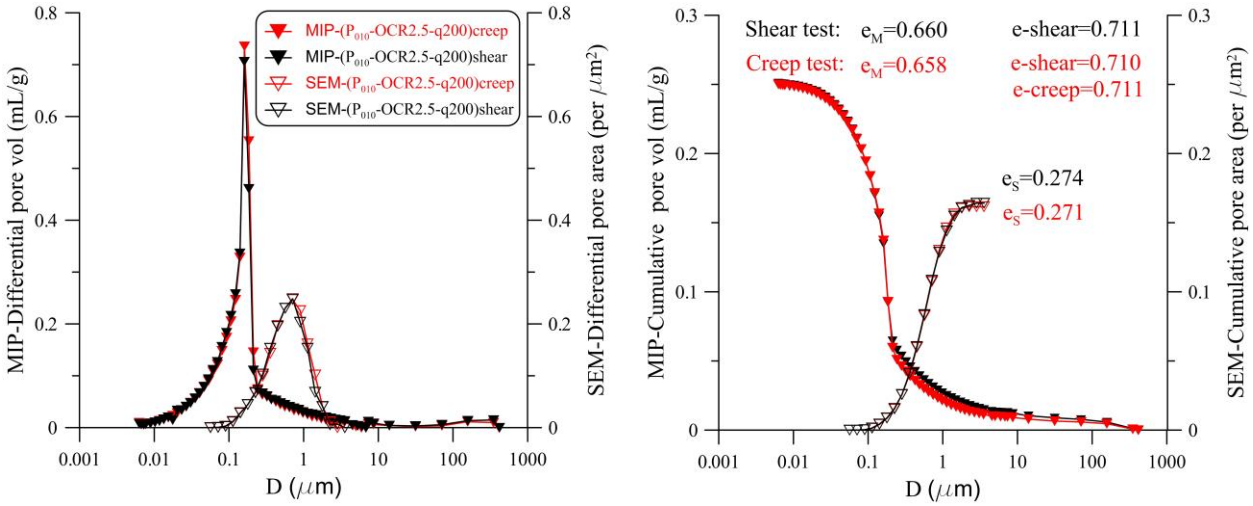

Figure 4.31 Evolution of pore space for test P_{010}-OCR2.5-q200 after shear/creep

Another group of tests in this domain (P_{010}-OCR2.5-q200) is shown in Figure 4-9 in Annex Chapter 4. The larger pore space of sample after creep than that after shear is due to its initial higher void ratio.

4.2.2.3 In the dilatancy domain

For highly overconsolidated samples in dilatancy domain, we observe the continuous dilation within creep phase in macroscopic (see Figure 4.10). Figure 4.32 presents the evolution of pore space for sample before and after creep in this volumetric domain. We can see (Figure 4.32a) that the most frequent diameter of sample after creep (D_{peak}=0.185 μm) is a little bit higher than that after shear (D_{peak}=0.161 μm). Around D_{peak}, for each magnitude of diameter, the pore space of sample after creep is higher than that after shear, which means that the dilatancy in creep is due to

the increase in the pore space whose diameter is between 0.07 μm and 0.3 μm. The differential pore areas identified through the SEM images translate a similar tendency.

Figure 4.32b shows the cumulative volume of mercury introduced into the sample. The volume of mercury gradually increase when D < 0.3 μm for the sample after creep than that after shear, due to more micropores whose size are in this range generate in creep phase.

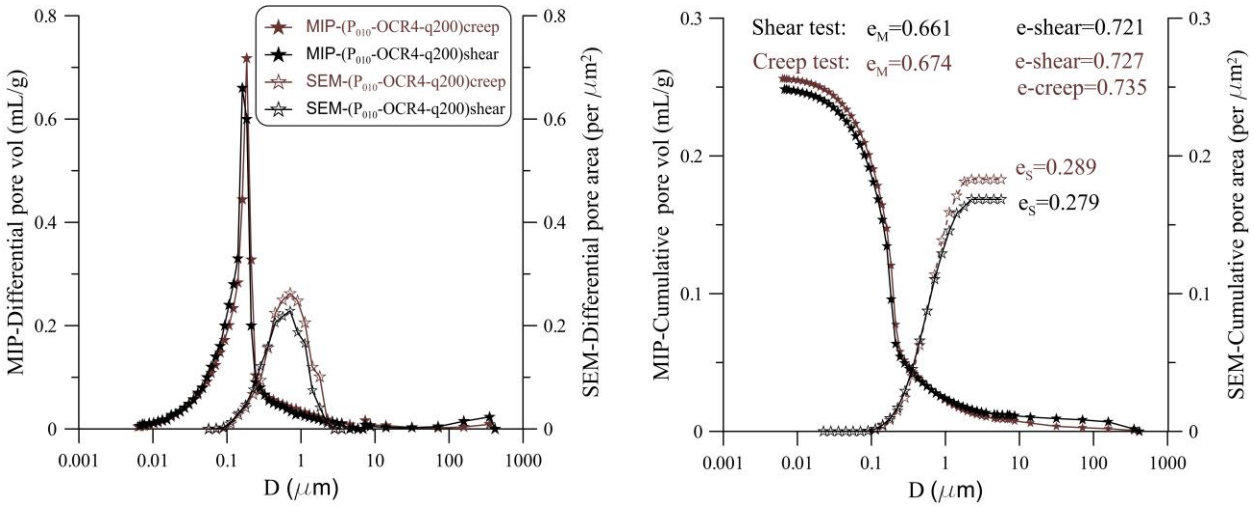

Figure 4.32 Evolution of pore space for test P_{010}-OCR4-q200 after shear/creep

The pore spaces identified through MIP and SEM technique for all tests are summarized in Table 4.1, for tests under certain common conditions will be discussed separately in the following section.

Table 4.1 Summary of pore space for samples after shear and after creep

Test	Shear test					Creep test					
	e-shear	MIP		SEM		e-shear	e-creep	MIP		SEM	
		D_{peak} (μm)	e_M	D_{peak} (μm)	e_S			D_{peak} (μm)	e_M	D_{peak} (μm)	e_S
P_{010}-NC-q200	0.639	0.161	0.646	0.566	0.267	0.638	0.629	0.161	0.599	0.450	0.247
P_{010}-NC-q670	0.645	0.140	0.596	0.713	0.259	0.658	0.648	0.140	0.596	0.713	0.258
P_{010}-OCR1.5-q445	0.665	0.161	0.650	0.713	0.255	0.697	0.693	0.161	0.643	0.713	0.272
P_{010}-OCR1.5-q200	0.707	0.161	0.687	0.897	0.269	0.671	0.671	0.161	0.640	0.713	0.264

P_{010}-OCR2.5-q200	0.711	0.161	0.660	0.713	0.274	0.710	0.711	0.161	0.658	0.713	0.271
P_{010}-OCR4-q200	0.721	0.161	0.661	0.713	0.279	0.727	0.735	0.185	0.674	0.713	0.289

The evolution of pore spaces after shear/creep differs from each other under different stress conditions in different volumetric domains. For normally consolidated specimens in contractancy domain, the mean pore diameter and cumulative pore volume/area after creep are smaller than that after shear corresponds to the contraction within creep. For highly overconsolidated soils in dilatancy domain, an opposite trend is observed due to the dilation within creep which is quite consistent with the orientation of particles analyses. The variations of pore spaces are main occur in the larger pores, while the smaller pores remain unchanged yet. Moreover, the changes of pore space after shear and after creep for lightly overconsolidated materials in pseudo-elastic domain are quite limited.

4.2.2.4 Evolution of pore spaces under different stresses

- Under the same deviatoric stress

Figure 4.33 presents mercury intrusion volumes versus pore diameter of 4 shear tests under the same deviatoric stress. From Figure 4.33a, we can see that the differential curves for the 4 samples are quite close where the most frequent diameter D_{peak}=0.161 μm. This means that the pore distribution with different OCR does not change much.

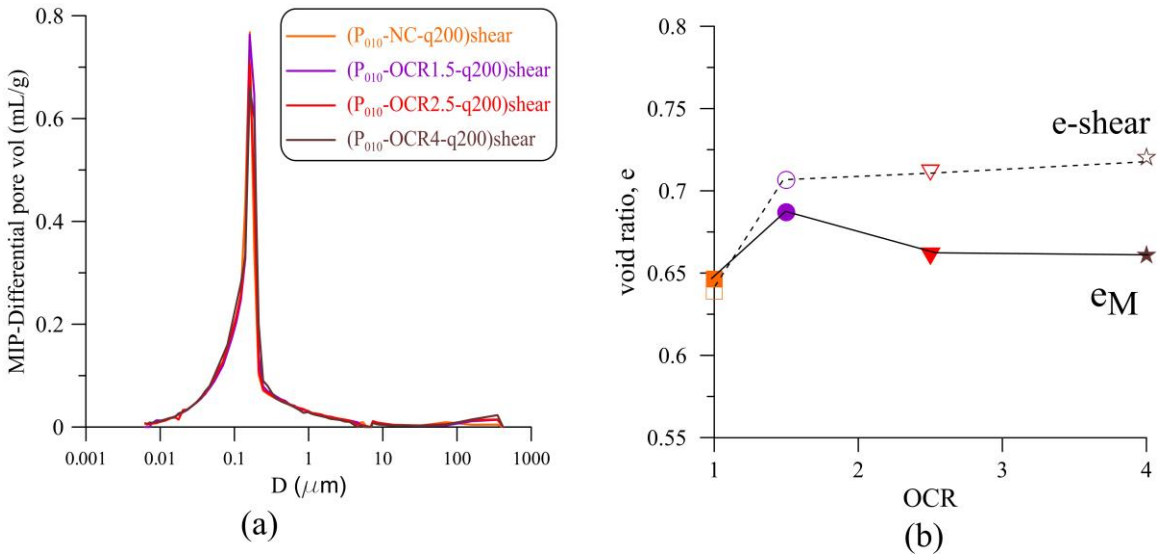

Figure 4.33 Evolution of pore space for shear tests with q = 200 kPa

Figure 4.34 shows the results of 4 creep tests under the same q. From the differential curves in Figure 4.34a, we can see that the most frequent diameter increase from the normally consolidate condition (D_{peak} = 0.161 μm) to highly overconsolidated condition (D_{peak} = 0.185 μm). The variation of pore diameter under different overconsolidation states occurs in the pore groups whose diameter are larger than 0.07 μm. For pore diameter smaller than 0.07μm, under long-term constant stress in different stress condition, the diameter of pores remains unchanged.

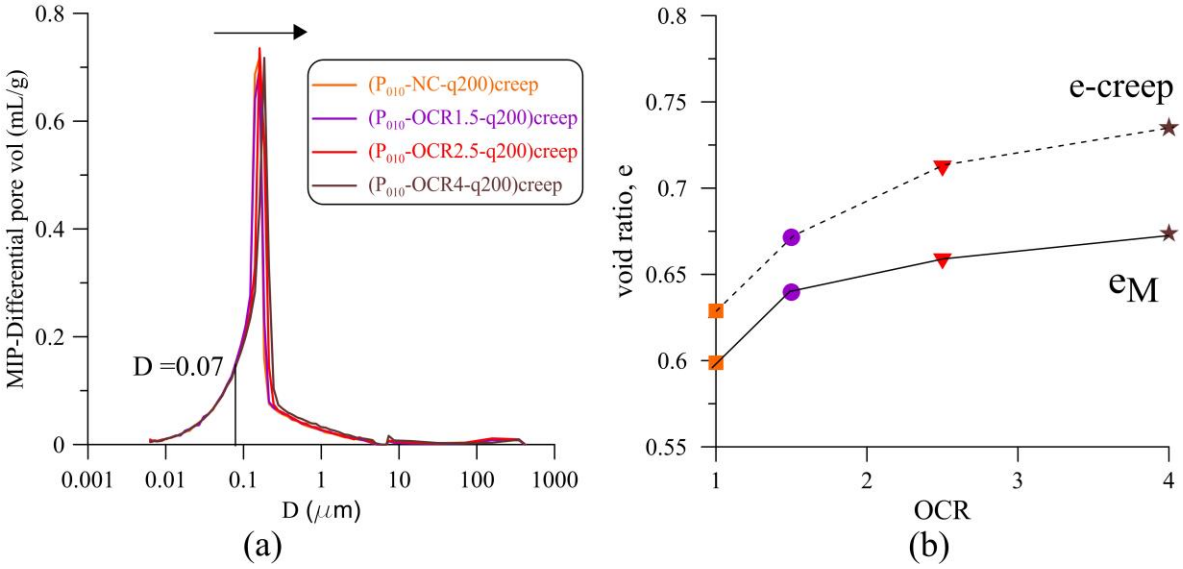

Figure 4.34 Evolution of pore diameter for creep tests with q=200 kPa

The results of differential and cumulative pore area versus pore diameter by SEM images are shown in Figure 4-10 in Annex Chapter 4. The results are generally consist with the global void ratio calculated after mechanical loading.

- Under the same OCR

Figure 4.35 shows mercury intrusion volumes versus pore diameter for normally consolidate specimens under different deviatoric stress after shear/creep. From Figure 4.35a and Figure 4.35b, we can see that after shear the most frequent diameter is smaller under higher stress level, the samples after creep (Figure 4.35c and Figure 4.35d) confirms this tendency. This phenomenon corresponds to higher magnitude of compression under higher stress level at the scale of sample and in the mechanical properties at a macroscopic level (Figure 3.30).

The results developed on SEM images here show that, on this scale of investigation, the variation of pore spaces investigated through this method does not account for the fact that the pore space is reduced along different stress levels for normally consolidated materials.

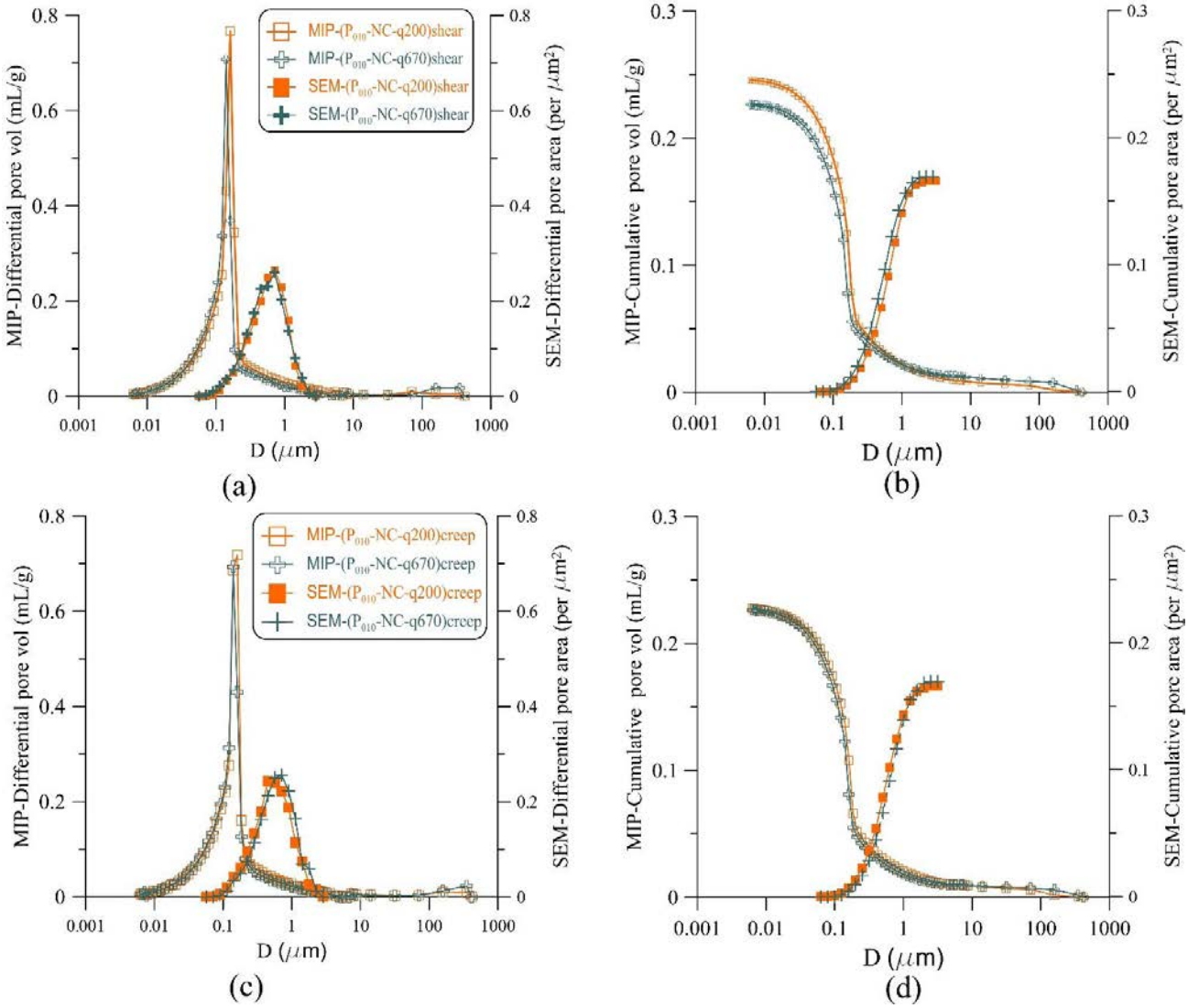

Figure 4.35 Evolution of pore spaces for tests with OCR=1: (a) (b) shear tests; (c), (d) creep tests

Results of the pore space evolution for lightly overconsolidated samples (OCR=1.5) with different stress levels are shown in Figure 4-11 in Annex Chapter 4.

- Under the same stress ratio

Figure 4.36 presents the evolution of pore spaces in normally consolidated and lightly overconsolidated soils after shear/creep under the same stress ratio (η=0.67) in the contractancy domain. We can see that the most frequent pore diameter after shear/ after creep for normally

consolidated material are lightly smaller than the lightly overconsolidated ones (Figure 4.36a and Figure 4.36c). Consequently, the cumulative pore volume/area decrease according to the increase in contraction in the normally consolidated specimens (Figure 4.36b and Figure 4.36d). The results developed on MIP and SEM images are quite consistent with the tendency of void ratio at the scale of sample.

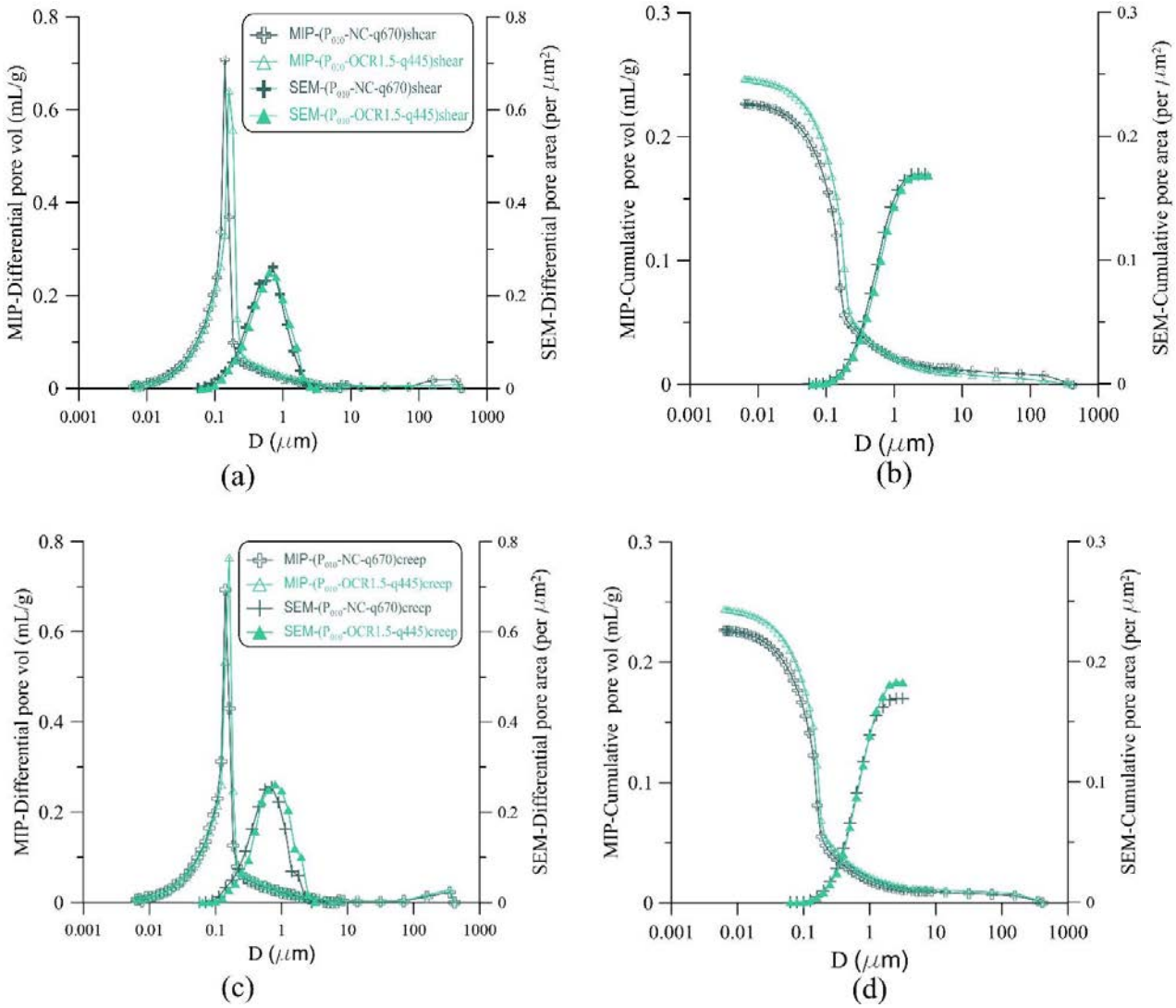

Figure 4.36 Evolution of pore spaces for tests with η=0.67: (a) (b) shear tests; (c), (d) creep tests

By comparing and combining the results of pore spaces by SEM and MIP techniques, we can obtain more clear tendencies of pores for tests in different condition. Under the same deviatoric stress, the difference of creep samples with different OCRs are highlighted among samples after creep, due to the contraction/dilation of normally consolidated and highly overconsolidated

specimens. The variation of pore spaces under different stress levels and OCRs are more revealed on the samples after creep.

4.2.3 Pore shape

As mentioned above and illustrated by Figure 4.25, the pores identified in SEM images are represents by ellipses.

The shape characteristic of the pore thus can be evaluate through the roundness of the fitted ellipse by Equation 2.20 (R_s=B/A), where A is the main axis and B is the secondary axis of the ellipse, i.e., the diameter of pores. Therefore, R_s = 1 means circle shape of the pore.

The aim of this section is characterize the evolution of pore shape before and after creep, as well as to investigate how the contraction and dilation occurs in macroscopic level behaves in the scale of micropores morphology.

4.2.3.1 In contractancy domain

Figure 4.37 presents the variation of normally consolidated specimens in contractancy domain. From Figure 4.37a we can see that the percentage of mean roundness before and after creep is the same (Rs=0.45). For pore roundness higher than this mean value, the percentage of pore roundness for creep sample is smaller than the value of shear sample, whereas for Rs< 0.45, a contrary tendency can be found. This means that the shape of pores inside the soil sample tends to be more flat after subjecting to constant sustained stress in creep stage. The variation of pore shape occur mainly in the size of pore diameter (see Figure 4.37c), where the mean pore diameter for creep sample is smaller than the value of shear sample, meanwhile, the length of pores before and after creep remains almost unchanged (Figure 4.37b).

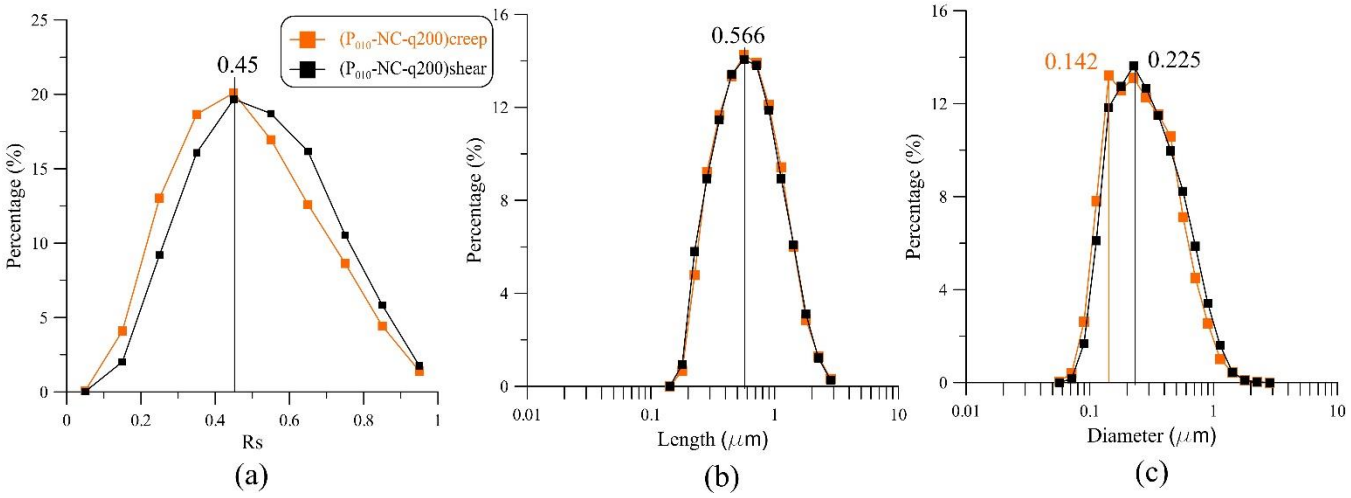

Figure 4.37 Evolution of pore shape for tests P_{010}-NC-q200 in contractancy domain

Figure 4.38 shows the relationship between the pore roundness and pore diameter. In general, the roundness of pores increase with the pore diameter. We can see that the difference between creep sample and shear sample is mainly in the range of D>0.14 μm, which indicates that the large pores are more likely to be contracted in creep whereas the small or the flat pores remains unchanged yet in this test condition.

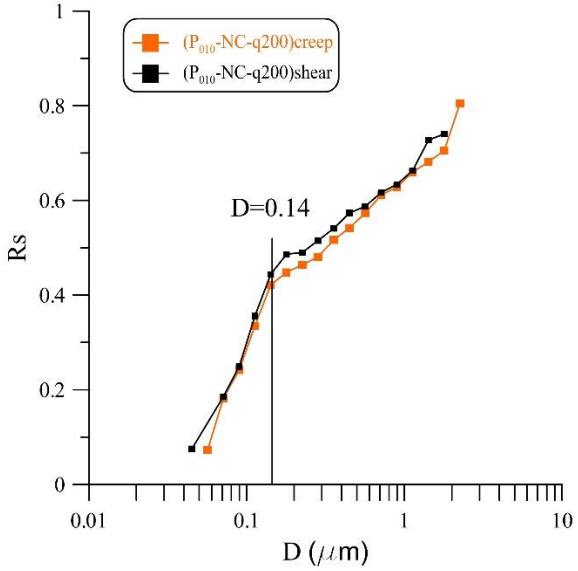

Figure 4.38 Pore roundness versus pore diameter for tests P_{010}-NC-q200

The evolution of pore shapes for the other two group of samples in this domain (P_{010}-NC-q670 and P_{010}-OCR1.5-q200) are shown in Figure 4-12 and Figure 4-13 in Annex Chapter 4.

4.2.3.2 In pseudo-elastic domain

The evolution of pore shapes for tests P_{010}-OCR2.5-q200 is shown in Figure 4.39. For this group of tests, the void in shear sample and creep sample after the mechanical loading are substantially the same. Within creep phase, there is no volume change occur at the macroscopic level (see Figure 3.23), the pore shape after creep seems also to remain generally unchanged. The mean roundness of pore is 0.45, and the mean pore diameter is 0.179 μm.

There is quite slightly differences between the shear sample and creep sample, with a tiny smaller increase of percentage in the length of large pores (Figure 4.39b) and a slightly decrease of percentage in the main diameter range (Figure 4.39c) for the creep sample. Consequently, the pore roundness of pores in the sample after creep is a little smaller than the one after shear (Figure 4.39a). Although we observe no volume variation in the macroscopic level and no further variation in the structure orientation within creep, it seems that the pore shape tends to evolve slightly in a complicate way, which needs more investigations.

The development of pore shapes for the lightly overconsolidated specimens (P_{010}-OCR1.5-q200) in this domain is represented in Figure 4-14 in Annex Chapter 4.

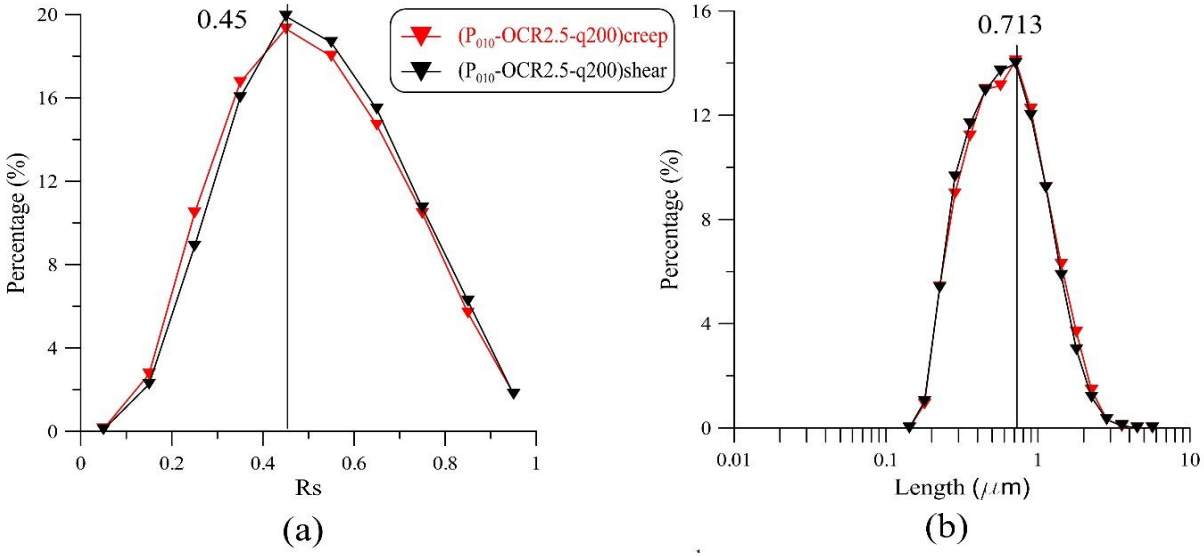

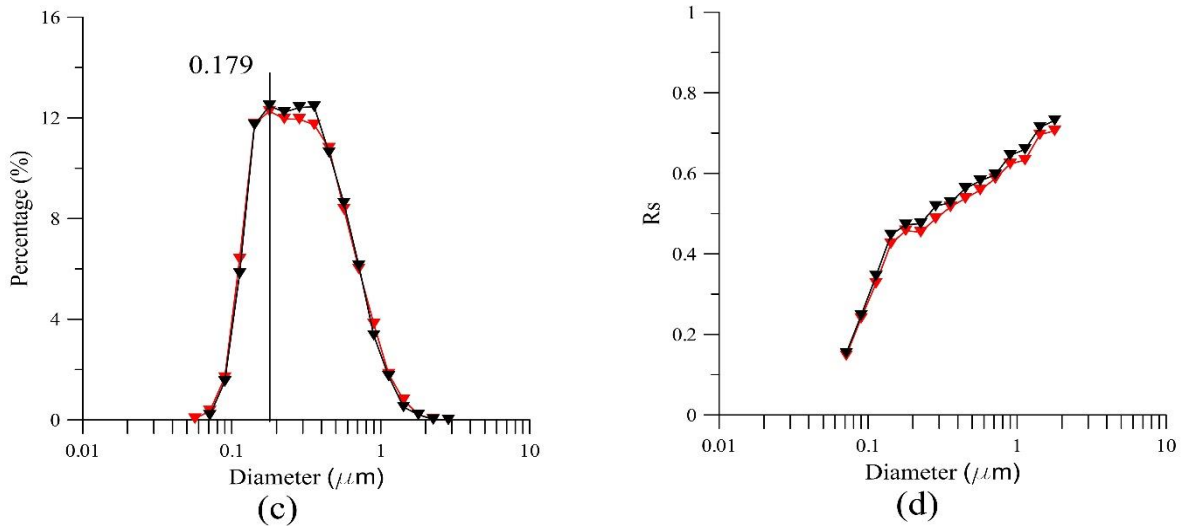

Figure 4.39 Evolution of pore shape for tests P_{010}-OCR2.5-q200 in pseudo-elastic domain

4.2.3.3 In dilatancy domain

For highly overconsolidated specimens in dilatancy domain, the evolution of pore shape for tests with OCR=4 after shear and after creep is represented in Figure 4.40.

We can see the mean pore roundness increase after creep (Figure 4.40a), the variation of pore shape after creep results from the expansion in the length as well as the diameter. For pore length larger than 0.713 μm (Figure 4.40b), the percentage of pore length for creep sample is isochronously higher than the value of shear sample. This result indicates that the large pores were more likely to extend during creep, This might suggest the opening of micro-cracks in the material. Similarly, in Figure 4.40c, we can see that the percentage of large pore diameter (D > 0.358 μm) increase after creep.

It can be noted that the expansion in the pore diameter and pore length occurred within creep phase tends to begin in the large pores, as represented in Figure 4.40d. For pore diameter smaller than 0.358 μm, the percentage versus pore diameter for creep sample and shear sample are quite coincide, which means that the small pores did not contribute yet for the dilatancy of creep in our research.

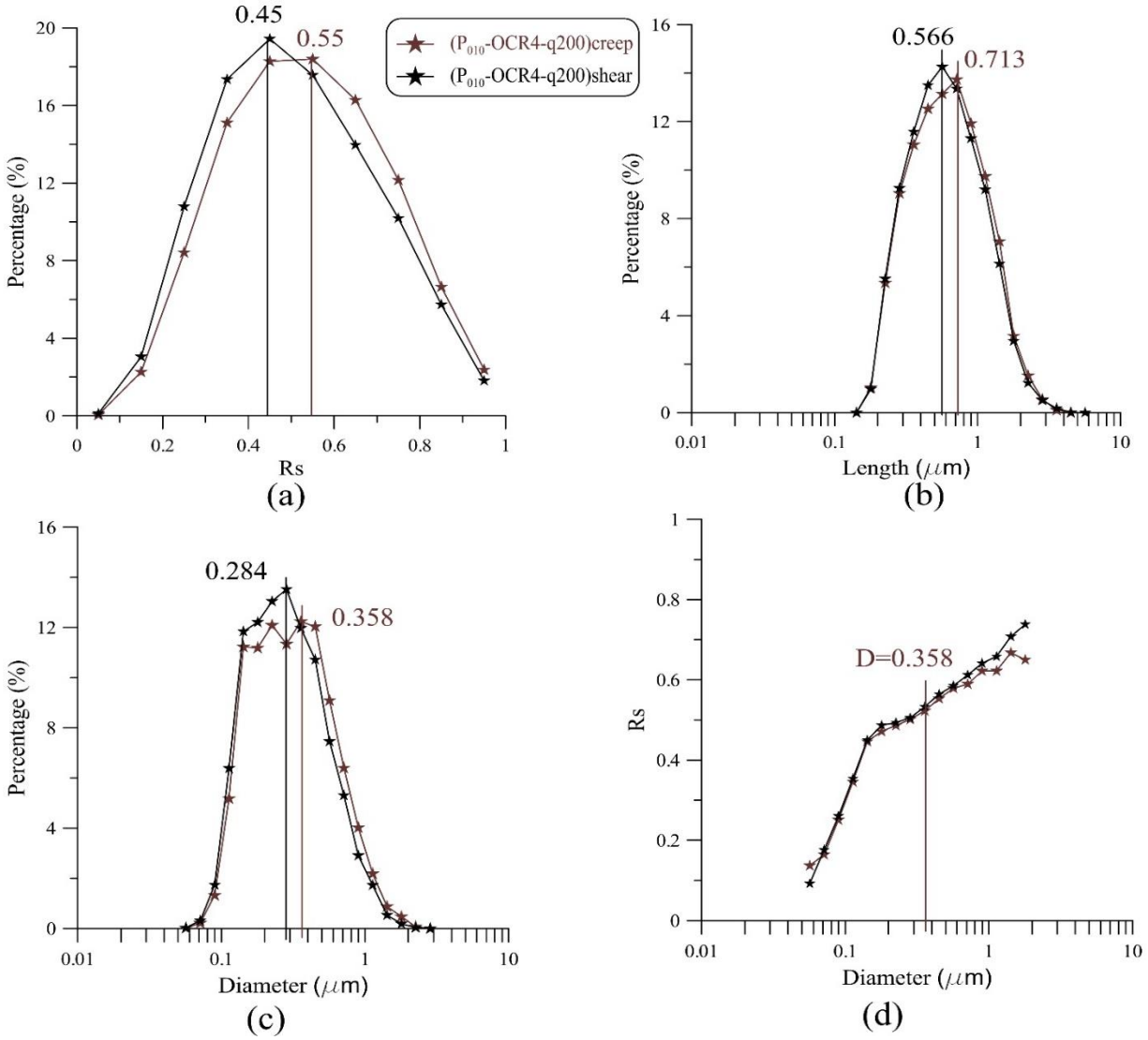

Figure 4.40 Evolution of pore shape for tests P_{010}-OCR4-q200 in dilatancy domain

The results of pore roundness provide supplementary information about how the micropores evolve in the mechanical loading. The creep contractancy on normally consolidated specimens is due to the compression in the diameter of large pores, and the creep dilatancy occurs in highly overconsolidated specimen results from the expansion in both the diameter and length of large pores. That exactly what orientation of particles highlighted from the SEM analyses, we observed opening micro-cracks forming after shear and developing themselves during creeps. Meanwhile, the smaller pore remains almost unchanged yet during creep.

For lightly overconsolidated soils, in pseudoelastic domain, the differences of pore shape for creep sample and shear sample are quite close, and quite limited variations occurred in creep

samples along the observation in this research. The results show that the pseudo-elastic domain remains an open issue, which needs to be more explored at the different levels.

4.2.3.4 Study of the pore shape evolution under different stresses

The development of mean pore shapes for all the 12 samples are listed in Table 4.2.

Table 4.2 Summary of pore shape for samples after shear and after creep

Test	Mean Roundness *Rs*	Percent of mean roundness (%)	Mean length (μm)	Percent of mean length (%)	Mean diameter (μm)	Percent of mean diameter (%)
$(P_{010}\text{-NC-q200})_{creep}$	0.45	20.1	0.566	14.3	0.142	13.6
$(P_{010}\text{-NC-q200})_{shear}$	0.45	19.7	0.566	14.1	0.225	13.7
$(P_{010}\text{-NC-q670})_{creep}$	0.45	19.5	0.566	13.9	0.284	12.5
$(P_{010}\text{-NC-q670})_{shear}$	0.45	18.4	0.713	13.4	0.284	12.5
$(P_{010}\text{-OCR1.5-q445})_{creep}$	0.45	19.0	0.713	14.1	0.284	12.6
$(P_{010}\text{-OCR1.5-q445})_{shear}$	0.45	19.1	0.713	14.1	0.179	12.7
$(P_{010}\text{-OCR1.5-q200})_{creep}$	0.55	18.9	0.713	20.6	0.357	19.75
$(P_{010}\text{-OCR1.5-q200})_{shear}$	0.55	20	0.713	20.7	0.357	20.32
$(P_{010}\text{-OCR2.5-q200})_{creep}$	0.45	19.3	0.713	14.1	0.179	12.3
$(P_{010}\text{-OCR2.5-q200})_{shear}$	0.45	19.9	0.713	14.0	0.179	12.5
$(P_{010}\text{-OCR4-q200})_{creep}$	0.55	18.4	0.713	13.7	0.358	12.2
$(P_{010}\text{-OCR4-q200})_{shear}$	0.45	19.4	0.566	14.3	0.284	13.5

It can be seen that the evolution of pore shapes with stress are more obvious through the changes of mean pore diameter. For the normally consolidated specimens (P_{010}-NC-q200) in contractancy domain, the mean pore diameter after the mechanical loading are small (D= 0.225 μm), and a much smaller value (D = 0.142 μm) can be found for sample after creep. For highly overconsolidated samples (P_{010}-OCR4-q200) in dilatancy domain, an obvious expansion in the mean pore diameter as well as pore length was highlighted for creep sample, resulting in the dilation at the macroscopic scale of sample.

However, the influence of stress level on the pore shape, tests P_{010}-NC-q200 and q670 and tests P_{010}-OCR1.5-q200 and q445, no general conclusions can be drawn at present.

The relationship of pore roundness versus pore diameter for all the 12 tests are shown in Figure 4.41. For pore diameter larger than 0.18μm, a general linear relationship can be fitted on the *Rs-log D* plot. For D lower than this value, the relation of pore roundness versus pore diameter are quite consistent, which indicates that the small pores inside the soil are insensitive to the change of external stress.

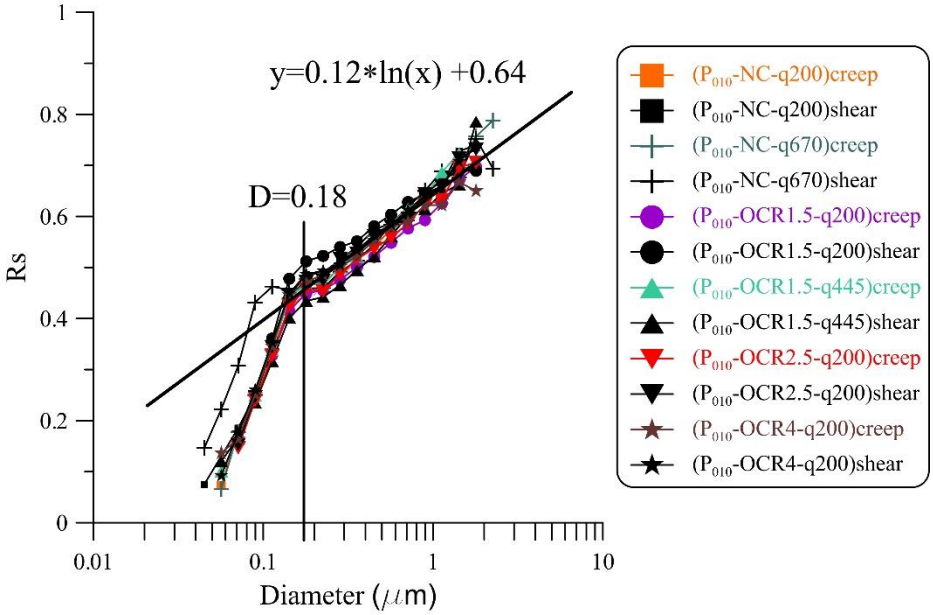

Figure 4.41 Pore roundness versus pore diameter under different stresses

4.3 Conclusions

In attempting to relate the mechanical creep behaviour to the structural characteristics of clay samples, we have used different experimental techniques to describe these relationships before and after creep. The experimental approach consists in performing MIP tests in order to study the variation of the porosity, as well as quantitative and qualitative analyses developed on SEM photographs to reveal the evolution of particles and voids. The following conclusions may be derived from the results of the tests:

In the contractancy domain for normally consolidated samples: the microfabric analysis on samples after monotonic loading indicates the anisotropy of fabric, with a preferential orientation of the particles between 150˚ and 165˚. The group of particles orient generally parallel to each other in one plane. Based on this initial state, the particles continue to rearrange under constant sustained stress in creep phase, resulting in higher percentage of particles oriented in this preferential direction. The structural anisotropy is increased after creep. The orientation of pores

confirms this tendency. Moreover, the evolution of pore space indicates that the mean pore diameter is smaller along with smaller cumulative pore volume/area of creep sample.

In the dilatancy domain for overconsolidated samples: the structural depolarization developed after shear, showing by the assembly of groups of particles oriented in an isotropic manner. Based on this microfabric state, the structural isotropy continue to develop in the orientation of directions, formed by groups of particles that are more random. Similar results are obtained on the analysis of pore orientation. The mean pore diameter and cumulative pore volume/area for creep sample is higher than the shear sample, corresponding to the dilation in macroscopic level.

In the pseudo-elastic domain: the microfabric of lightly overconsolidated soils are in the intermediate state. The evolution of particles and pores after shear and after creep are quite close, which is particularly clear for tests OCR=2.5. This result indicates that the microstructural evolution within creep in this domain is quite limited.

The pores in triaxial loading are generally elliptical; the large pores are more sensitive to the variation of stress. In contractancy domain, the contraction occurred within creep is mainly due to the compression in diameter of large pores, resulting from the enhanced face to face contact pattern of solid particles. In the dilatancy domain, the pores in dilation specimen tend to become more round after creep due to the dilatancy mechanism, with the expansion in diameter and length of the large pores. The expansion of micropores together results in the opening of microcracks inside the material that contributes to the dilation in the scale of sample. This results highlight precisely the mechanism of dilatancy in clayey materials. Whereas for lighted overconsolidated specimen in pseudo-elastic domain, no obvious difference are identified on the pores between samples after shear and after creep yet.

Generally, the microfabric evolution of soils in creep phase depends on the structural pattern developed in monotonic loading, which is strongly influenced by the OCR. The variation of pores identified through mercury intrusion and SEM images show logical results that are consistent with the global void ratio at the scale of sample and in the mechanical properties at a macroscopic level.

Conclusions and perspectives

Summary and conclusions

The creep behavior of clayey soils is starting to be progressively significant in theoretical and practical geotechnical engineering. Increasing building activities on the soft clay foundations demand a better understanding and more precise prediction of the creep phenomenon.

The main contribution of this thesis is the presentation of the time-dependent behaviour of a typical clayey material (kaolin) submitted, at macroscopic scale, to different stress conditions in a long-term drained condition and in following the microstructural evolution within creep. The triaxial creep tests were performed along the constant mean effective stress path by high-precision GDS triaxial system, which could capture accurately the volume change inside the material. After the mechanical loading, the clay samples were prepared particular care to avoid as far as possible distributing the microstructure during observation. The microstructural research was carried out, by means of scanning electronic microscope and mercury intrusion porosimetry on specimens prepared after shear and after creep, to reveal the particle and void evolution related to creep. The main conclusions can be drawn on macroscopic and microscopic in the following

Macroscopic results on clays

The analysis of the creep behavior of a kaolinite highlighted some mechanical characteristics related to the stress state in the (p'-q) plane. The results clearly show that, under constant p' stress path, the strain evolution during creep strongly depends on the behavior during the initial loading stages. The time-dependent as well as the stress-dependent viscoplastic strain evolutions are controlled by the volumetric domain mechanisms.

In the contractancy domain for normally consolidated samples: a creep contractancy was obtained for any stress level. The magnitude of the creep contractancy was influenced by the creep stress state, i.e., the creep strains were bigger under higher stress levels. A time-dependent viscoplastic hardening developed continuously at a decreasing strain rate.

In the dilatancy domain for overconsolidated samples: a creep dilatancy was clearly observed for highly overconsolidated samples for any stress level in this domain. The dilative volumetric strain was greater for a higher stress level.

In the pseudo-elastic domain, more complex volumetric strain evolutions were obtained for the lightly overconsolidated specimens. Alternating small contractancy/dilatancy amplitudes appeared during the creep stage. These results were assumed to be the consequence of small stress variations when the GDS program was trying to maintain a given stress level. In this domain, no volumetric strain change can be assumed during creep.

Three creep stages are identified in different tests. Under the critical state, all specimens show the primary stage, the secondary and tertiary stage are rarely seen except in the test beyond the critical state. The creep rupture in tertiary stage was due to a viscoplastic softening, leading to the decrease of the maximum strength with the decrease of the soil density.

The evolution of creep strain rate are partially different from the general pattern proposed by Singh & Mitchell (1968). The ($log\,\dot{\varepsilon} - \log t$) curve varies in different volumetric domains, and the parameter *m* fitted by the linear part of the strain rate curve is not always constant. Parameter *m* related to volumetric strain is more sensitive to the variation of magnitude of stress.

Microscopic results on clays

The aim of the microscopic research is to establish a link between the macroscopic creep performance of clay and their microfabric. The results of microstructure show that the adjustment of structure within creep depends on the structural state at the end of monotonic loading stage. The microstructural variation of particles and pores identified through SEM images and mercury intrusion show logical results that are consistent with tendency at the scale of sample.

In the contractancy domain for normally consolidated samples: the microfabric analysis on samples after monotonic loading indicates the anisotropy of fabric for any stress level. The particles orient generally parallel to each other in one plane with a preferential orientation between 150˚ and 165˚. Within creep, the larger inter-particle pores whose diameter is over than 0.3 μm were firstly compressed in diameter, while the smaller pores remained unchanged yet. Meanwhile, the length of pores inside the sample after shear and after creep were almost the same, we may assume that the sliding movements between particles are negligible. The compression of pores along with the rearrangement of particles resulting in the increase of percentage of particles in the preferential orientation. Consequentially, the structural anisotropy is increased with the creep contractancy.

In the dilatancy domain for highly overconsolidated samples: a clear structural isotropy formed at the end of monotonic loading, showing by the assembly of groups of particles oriented in an isotropic manner. The pores in dilatant specimen are generally more round than those in contractive sample. Based on this microfabric state, the structural isotropy continue to develop in the orientation of directions, formed by groups of particles that are more random. Similar results are obtained on the analysis of pore orientation. The mean pore diameter and cumulative pore volume/area for creep sample is larger than the shear sample, corresponds to the dilation in macroscopic level. The expansion of micropores together results in the opening of microcracks inside the material that contributes to the dilation in the scale of sample.

In the pseudo-elastic domain: the microfabric of lightly overconsolidated soils are in the intermediate state. The evolution of particles and pores after shear and after creep are quite close, which is particularly clear for tests OCR=2.5. This result indicates that the microstructural evolution within creep in this domain is quite limited.

It is noticeable that the evolution of microstructure of kaolin in creep, under the purely deviatoric stress path, depends on the overconsolidation state more than the stress level. For the normally consolidated creep samples, the orientation of soil with q=200 kPa and 670 kPa became quite coincide after a certain creep duration, although obviously difference can be found in the samples after monotonic loading. Similar tendency are observed on lightly overconsolidated samples with q=200 kPa and 445kPa. The initial difference of structural orientation under different stress levels at the end of shear tend to be minimized in creep phase. This tendency may indicates that under a certain consolidation state, a certain equilibrium structural state exits, and the structural under different stress levels will evolve with time towards this state.

Perspectives

In this PhD work, a comprehensive experimental study was conducted on the time-dependent behavior of kaolin. We hope we have brought some ideas to a better understanding of the mechanical characteristics of clay, and enrich the modeling of the time-dependent behavior of clayey materials. There are many aspects for future research.

(1) Creep tests with different overconsolidation ratios and different stress levels in pseudo-elastic domain. In this research, we obtained two creep test results with OCR=1.5 and 2.5 under q=200 kPa in this domain. It will be interesting to study the volumetric creep behavior with other

OCRs and stress levels, to determine the complete boundary conditions of no-volume change volumetric domain.

(2) To perform creeps tests under different stress path terminated in the same stress location in the pseudo-elastic domain. In this research, the volumetric domains are determined with reference to the constant p' stress path. The volumetric creep strain after different stress paths can be very helpful to investigate the mechanisms in this domain.

(3) Other microstructure investigation technique can be very promising to reveal the structural evolution within creep. For example, the microtomography and Focused Ion Beam Scanning Electron Microscopes (FIB-SEM), which can give 3D information of the pores, especially the micro cracks development with time in the dilatant samples.

(4) Constitutive modelling of creep accounting for OCR effects and considering the microstructure of soft soils.

References

A:

Aboshi, H. (1973). An experimental investigation on the similitude in the consolidation of a soft clay, including the secondary creep settlement. *Proceeding of the 8th International Conference on Soil Mechanics and Foundation Engineering*, Moscow, 4(3), 88.

Ahmed, S., Lovell, C.W., Diamond, S. (1974). Pore size and strength of compacted clay. Journal of Geotechnical and Geoenvironmental Engineering, 101, 407-425.

Akagi, H. (1994). A physico-chemical approach to the consolidation mechanism of soft clays. *Soils and foundations*, 34(4), 43-50.

Al-Mukhtar M., Belanteur N., Tessierb, D. Vanapallic S.K. (1996). The fabric of a clay soil under controlled mechanical and hydraulic stress states. *Applied Clay Science*, 11 (2-4), 99-115.

Arulanandan, K., Shen, C. K., Young, R.B. (1971) Undrained creep behavior of a coastal organic silty clay. *Géotechnique*, 21(4). 359-375.

Augustesen, A., Liingaard, M., Lade, P. (2004). Evaluation of time-dependent behavior of soils. *International Journal of Geomechanics*, 4(3), 137-156.

B:

Baguelin, F., Jezequel, J.F., Shields, D.H. (1978). The pressuremeter and foundation engineering (Rock & Soil Mechanics Series). Trans. Tech. Publications

Bahar, R., Cambou, B., Fry, J.J. (1995). Forecast of creep settlements of heavy structures using pressuremeter tests. *Computers and Geotechnics*, 17(4), 507-521.

Bai X., Smart P. (1997). Change in microstructure of kaolin in consolidation and undrained shear. *Géotechnique*, 47(5), 1009-1017.

Barden, L. (1969). Time-dependent deformation of normally consolidated clays and peats. *Journal of the Soil Mechanics and Foundations Division*, 95 (SM1), 1-31.

Beaufort, D., Cassagnabere, A., Petit, S., Lanson, B., Berger, G., Lacharpagne, J.C., Johansen, H. (1998). Kaolinite-to-dickite reaction in sandstone reservoirs. *Clay Minerals*, 33, 297-316.

Benchabane, A. (2006). Etude du comportement rhéologique de mélanges argiles-polymères: Effets de l'ajout de polymères. Thèse de Doctorat, Université Louis Pasteur-Strasbourg, France.

Bergaya F., Lagaly G. (2006). General introduction: clays, clays minerals, and clay science. Handbook of Clay Science, Developments in Clay Science, 1, 1-18.

Berre, T., Iversen, K. (1972). Oedometer tests with different specimen heights on a clay exhibiting large secondary compression. *Géotechnique*, 17 (1), 53-70.

Berry, P.L., Poskitt, T.J. (1972). The consolidation of peat. *Géotechnique*, 22(1), 27-52.

Bjerrum, L. (1967). Engineering geology of Norwegian normally-consolidated marine clays as related to settlements of buildings. *Géotechnique*, 17(2), 83-118.

Bjerrum, L. (1972). The effect of rate of loading on the p'_c value observed in consolidation tests on soft clay. *Norwegian Geotechnical Institute Publication*, 95.

Bishop A. W., Henkel, D.J. (1957). The measurement of soil properties in the triaxial test. London: Arnold E.

Bishop, A. W., Lovenbury, H. T. (1969). Creep characteristics of two undisturbed clays. *Proceedings of the 7th International Conference on Soil Mechanics and Foundation Engineering*, Mexico, 1, 29-37.

Bishop, A. W., Wesley, L. D. (1975) A hydraulic triaxial apparatus for controlled stress path testing. Géotechnique, 25(4), 657-670.

Biarez, J., Hicher, P. Y. (1994). Elementary mechanics of soil behaviour: saturated remoulded soils. A.A. Balkema, Rotterdam Netherlands.

Brunke, O., Brockdorf, K., Drews, S., Müller, B., Donath, T., Herzen, J., Beckmann, F. (2008). Comparison between x-ray tubebased and synchrotron radiation-based µCT, Developments in X-Ray Tomography VI, edited by: Stock, S. R., Proceedings of SPIE, 7078.

Brandl, H. (2013). Consolidation/Creeping of Soils and Pre-treated Sludge. *5th Biot Conference on Poromechanics*, ASCE, Vienna, 1346-1357.

BS 1377. (1990). British Standard Methods of test for Soils for civil engineering purposes: Part 8. Shear strength tests (effective stress). BSI, London, UK.

Buisman, A.S.K. (1936). Results of long duration settlement test. *Proceeding of the 1st International Conference on Soil Mechanics and Foundation Engineering*, Harvard University, 1, 103-106.

Bouziri, S. (2007). Etude des mécaniques de déformation dans les argiles surconsolidées. Thèse de doctorat. Ecole centrale Paris.

Borja, R.I., Kavazanjian, E. (1985). A constitutive model for the stress-strain-time behavior of wet clays. *Géotechnique*, 35(3), 283-298.

C:

Cady, J. G., Wilding, L. P., Dries, L. R. (1986). Petrographic microscope techniques. In: Methods of Soil Analysis, 2nd ed., American Society of Agronomy, Madison, Part1, Chapter 8.

Campanella, R.G., Vaid, Y. P. (1973) Triaxial and plane strain creep rupture of an undisturbed clay. Canadian Geotechnical Journal, 11(1), 1-10.

Carlos A. Leon y Leon. (1998). Particle size distribution of carbon blacks by mercury porosimetry. Rubber chemistry and technology, 71 (5), 988-997.

Carroll, D. (1970). Clay minerals: a guide to their X-ray identification. Geological Society of America, Boulder, CO, Special Paper 126.

Casagrande, A., Wilson, S. D. (1951). Effect of rate of loading on strength of clays and shales at constant water content. *Géotechnique*, 2(3), 251-263.

Chapman, D.L. (1913). LI. A contribution to the theory of electrocapillarity. *Philosophical Magazine*, 25(148), 475-481.

Christidis, G.E. (2011). Industrial Clays. Chapter in European Mineralogical Union Notes in Mineralogy, 9, 341-414.

Christie, I.F., Tonks, D.M. (1985). Developments in the time line theory of consolidation. *The 11th international conference on soil mechanics and foundation Engineering*, San Francisco, 423-426.

Crawford, C. B. (1986). State of the art: Evaluation and interpretation of soil consolidation tests. *Consolidation of soils: Testing and evaluation, R. N. Young and F. C. Townsend, eds., ASTM Special Technical Publication*, 892, 71-103.

Collins, K., McGown, A. (1974). The form and function of microfabric features in a variety of na tural soils. *Géotechnique*, 24(2), 223-254.

Crooks, J.H.A., Becker, D. E., Jerreries, M.G., McKenzie, K. (1984) Yield behaviour and consolidation. I: pore water response. *Proceedings, Symposium on sedimentation consolidation models: prediction and validation.* SanFrancisco, ASCE, 356-381.

Cui, Z-D, Tan, J. (2014). Analysis of long-term settlements of Shanghai Subway Line 1 based on the in situ monitoring data. *Natural Hazards*, 75(1), 465-472.

D:

Dees, P.-J., Polderman, J. (1981). Mercury porosimetry in pharmaceutical technology. Powder Technology, 29 (1), 187-197.

D'Elia, B. (1991). Deformation problems in the Italian structurally complex clay soils. *Proceedings of the 10th International Conference on Soil Mechanics and Foundation Engineering*, Firenze, 4, 1159-1170.

De Jong, G.J., Verruijt, A. (1965). Primary and secondary consolidation of a spherical clay sample. *Proceeding of the 6th international conference soil mechanic and foundation engineering*, Montreal, 254-258.

De Jonge, N., Ross, F.M. (2011). Electron microscopy of specimens in liquid. *Nature Nanotechnology*. 6, 695-704.

Delage, P., Lefebvre, G. (1984). Study of the structure of a sensitive Champlain clay and of its evolution during consolidation. *Canadian Geotechnical Journal*, 21(1), 21-35.

Den Haan, E. J., Edil, T. B. (1994). Secondary and tertiary compression of peat. *Proceedings of the International Workshop on Advances in Understanding and Modelling the Mechanical Behaviour of Peat*, 16-18 June 1993, Balkema, Rotterdam, The Netherlands, 49-60.

Diamond, S. (1971). Microstructure and pore structure of impact-compacted clays. *Clays and Clay Minerals*, 19(4), 239-249.

Dudoignon P., Pantet A., Carrara L., Velde B. (2001). Macro–micro measurement of particle arrangement in sheared kaolinitic matrices. *Géotechnique*, 51(6), 493-499.

Duncan, J. M., Rajot, J. P., and Perrone, V. J. (1996). Coupled analysis of consolidation and secondary compression. *The 2nd International Conference On Soft Soil Engineering*, Nanjing, 3-27.

E:

Evans, B.W., Guggenheim, S. (1988). Talc pyrophyllite and related minerals. Hydrous Phyllosilicates (Exclusive of Micas). *Reviews in Mineralogy*, 19, 225-280.

F:

Flavigny, E., Reveillet, M. (1983). Un appareillage simple pour l'étude des sols. Journées AUGC, Nancy, 31.

Feda, J. (1992). Creep of soils and related phenomena, Development in geotechnical engineering, Elsevier Science, North Holland, Amsterdam, The Netherlands.

Fesharaki, O., Garcia-Romero, E., Cuevas-Gonzalez, J., Lopez-Martinez, N. (2007). Clay mineral genesis and chemical evolution in the Miocene sediments of Samosaguas, Madrid Basin, Spain.

Clay Minerals, 42, 187-201.

Fodil, A., Aloulou, W., Hicher, P-Y. (1997). Viscoplastic behaviour of soft clay. *Géotechnique*, 47(3), 581-591.

G:

Gai, P.L., Boyes, E.D. (2009). Advances in atomic resolution in situ environmental transmission electron microscopy and 1A aberration corrected in situ electron microscopy. *Microscopy Research and Technique*, 72, 153-164.

Graham, J., Yin, J-H. (2001). On the time-dependent stress-strain behaviour of soft soils. *Proceedings of the 3rd International Conference on Soft Soil Engineering*, Hong Kong, 13-24.

Graham, J., Tanaka, N., Crilly, T., Alfaro, M. (2001). Modified cam clay modelling of temperature effects in clays. *Canadian Geotechnical Journal*, 38, 608-621.

Garlanger, J.E. (1972). The consolidation of soils exhibiting creep under constant effective stress. *Géotechnique*, 22(1), 71-78.

Geuse, E.C.W.A., Tjong-Kie, T. (1953). The mechanical behaviour of clays. Proceeding of then *Proceedings of the 2nd International Congress on Rheology*, London, 247-259.

Ghezzehei T.A., Or, D. (2001). Rheological properties of wet soils and clays under steady and oscillatory stresses. *Soil Science Society of America Journal*, 65(3), 624-637.

Giesse, R.F. Jr. (1988) Kaolin minerals: structures and stabilities. Reviews in Mineralogy, 19. Mineralogical Society of America Book Crafters Inc. Chelsea, Michigan 1988, 29-66.

Gillott, J. E. (1968). Clay in Engineering Geology, Elsevier Science, New York.

Guillot, X., Al-Mukhtar, M., Bregaya, F., Fleureau, J.-M. (2002). Estimation de la porosité dans un matériau argileux, Géoscience, 334, 105-109. (in French)

Goldstein, M., Ter-Stepanian, G. (1957). The long-term strength of clays and depth creep of slopes. *Proceedings of the 4th International Conference on Soil Mechanics and Foundation Engineering*, London, 2, 311-314.

Gould, M. D., Taylor, C., Wolff, S.K., Chandler, G.S., Jayatilaka, D. (2008). A definition for the covalent and ionic bond index in a molecule. *Theoretical Chemistry Accounts*,119(1-3), 275-290.

Graham, J., Crooks, J. H. A., Bell, A. L. (1983). Time effects on the stress-strain behaviour of natural soft clays. *Géotechnique*, 33(3), 327-340.

Griffiths F.J. Joshi R.C. (1990).Clay fabric response to consolidation. *Applied Clay Science*, 5, 3 7-66.

Grim, R.E. (1962). Applied clay mineralogy, International series in the earth and planetary sciences. Mc Graw Hill, New York.

Grimshaw, R.W. (1971). The Chemistry and Physics of Clays. Wiley-Inter science, New York.

Gupta, B. (1964). Creep of saturated soil at different temperatures. PhD Thesis, The University of British Columbia, Canada.

H:

Hammad, T. (2010). Comportement des sédiments marins de grande profondeur: approche multiéchelle. Doctoral dissertation, Ecole Centrale Paris, France. (in French)

Hammad, T., Fleureau, J-M., Hattab, M. (2014). Kaolin/montmorillonite mixtures behaviour on oedometric path and microstructural variations. European Journal of Environmental and Civil Engineering, 17(9), 826-840.

Hattab, M., Hicher, P.-Y. (2004). Dilating behavior of overconsolidated clay. *Soils and Foundations*, 44(4), 27-40.

Hattab, M., Bouziri-Adrouche, S., Fleureau, J-M. (2010). Évolution de la microtexture d'une matrice kaolinitique sur chemin triaxial axisymétrique. *Canadian Geotechnical Journal,*47(1), 34-48. (in French)

Hattab, M., Fleureau, J-M. (2011). Experimental analysis of kaolinite particle orientation during triaxial path. *International Journal for Numerical and Analytical Methods in Geomechanics,* 35(8), 947- 968.

Head, K. H. (1992). Manual of soil laboratory testing. Vol. 3, Pentech Press, London.

Henkel, D. J. (1956). The effect of overconsolidation on the behaviour of clays during shear. *Géotechnique,* 6(4), 139-150.

Hicher, P-Y. (1985). Mechanical behavior of saturated clays on various paths monotonic and cyclic loads. Application modeling elastoplastic and viscoplastic. Doctoral dissertation, University of Paris VI. (in French)

Hicher P.Y.,Wahyudi H., Tessier, D. (2000).Microsturctural analysis of inherent and induced ani sotropy in clay. *Mechanics of Cohesive-frictional Materials*, 5, 341-371.

Hinchberger, S.D., Rowe, R. (1998). Modelling the rate-sensitive characteristics of the Gloucester foundation soil. *Canadian Geotechnical Journal*, 35, 769-789.

Holzer, T.L., Hoeg, K., Arulanandan, K. (1973). Excess pore pressure during undrained clay creep. *Canadian Geotechnical Journal*, 10(1), 12-24.

Horowitz, S., Trievel, R.C. (2012). Carbon-oxygen hydrogen bonding in biological structure and function. *Journal of Biological Chemistry*, 287(50), 41576-41582.

Hounsfield, G.N. (1973). Computerized transverse axial scanning(tomography): Part 1. Description of system. British Journal of Radiology, 46, 1016-1022.

I:

Ighil Ameur, L. (2016). Étude expérimentale du phénomène de l'endommagement et de la fissuration d'une matrice poreuse. Doctoral dissertation, Université de Lorraine, France. (in French)

K:

Kabbaj, M., Oka, F., Leroueil, S., Tavenas, F. (1986). Consolidation of natural clays and laboratory testing. *Consolidation of soils: Testing and evaluation, ASTM Special Technical Publication, 892, R. N. Young and F. C. Townsend, eds.,* ASTM, Philadelphia, 378-404.

Kaczmarek, L. (2016). Rheometer use in analysis of soil creep behaviour. *16th International Multidisciplinary Scientific Geo Conference SGEM 2016*, 1(3), 237-244.

Karstunen, M., Yin, Z-Y. (2010). Modelling time-dependent behaviour of Murro test embankment. *Géotechnique*, 60(10). 735-749.

Kaufhold, A., Halisch, M., Zacher, G., Kaufhold, S. (2016). X-ray computed tomography investigation of structures in Opalinus Clay from large-scale to small-scale after mechanical testing. *Solid Earth*, 7, 1171-1183.

Kavazanjian, E., Mitchell, J.K. (1977). A general stress-strain time formulation for soils. *Proceedings of the 9th International Conference on Soil Mechanics and Foundation Engineering*, Specialty Session 9, 113-120.

Kavazanjian, E., Mitchell, J.K. (1980). Time-dependent deformation behavior of clays. *Journal of Geotechnical Engineering Division, ASCE*, 106(6), 611-630.

Kjartanson, B.H., Shields, D.H., Domaschuk, L., Man, C.S. (1988). The creep of ice measured with the pressuremeter. Canadian Geotechnical Journal, 25(2),250-261.

Komamura, F. (1981). Time dependent behavior of soil during direct shear creep. Journal of the Japan Society of Landslide, 17(4), 20-27.

Kong L-W, Zhang, X-W, Guo, A-G, Cai, Y. (2011). Creep behavior of Zhanjiang strong structured clay by drained triaxial test. *Chinese Journal of Geotechnical Engineering*, 30(2), 365-372. (in Chinese)

Kirby, J.M., Blunden, B.G. (1991). Interaction of soil deformations, structure and permeability. *Australian Journal of Soil Research*, 29(6), 891-904.

Kuhn, M.R., Mitchell, J.K. (1993). New perspectives on soil creep. *Journal of Geotechnical Engineering*, 119(3), 507-524.

Kwan, D. (1971). Observation of the failure of a vertical cut in clay at Welland, Ontario. *Canadian Geotechnical Journal*, 8(2), 283-298.

L:

Ladanyi, B., Johnston, G.H. (1973). Evaluation of in-situ creep properties of frozen soils with the pressuremeter. Proceedings of the 2nd International Conference of Permafrost, Yakutsk, 310-318.

Ladd, C. C., Foott, R., Ishihara, K., Schlosser, F., Poulos, H. J. (1977). Stress-deformation and strength characteristics. *Proceeding of the 9th International Conference on Soil Mechanics and Foundation Engineering*, Japan, 2, 421-494.

Ladd, C. C., Preston, W. B. (1965). On the secondary compression of saturated clays. MIT Research Rep. R65-59, Massachusetts Institute of Technology, Cambridge, Mass.

Lade, P. V., Liu, C.-T. (1998). Experimental study of drained creep behavior of sand. *Journal of Engineering Mechanics, ASCE*, 124 (8), 912-920.

Lafleur, J., Silvestri, V., Asselin, R., Soulié, M. (1988). Behaviour of a test excavation in soft Champlain Sea clay. *Canadian Geotechnical Journal*, 25(4),705-705.

Lagaly, G. (2006) Colloid clay science. Handbook of Clay Science. Developments in Clay Science, 1. Elsevier, Amsterdam, 141-245.

Lambe, T.W., Whitman, R.V. (1969). Soil mechanics. *John Wiley & Sons*, New York.

Le, T. M., Fatahi, B., Khabbaz, H. (2012). Viscous behaviour of soft clay and inducing factors. *Geotechnical and Geological Engineering*, 30 (5), 1069-1083.

Landis, E.N., Nagy, E.N., Keane, D.T., Nagy, G. (1999). A technique to measure three-dimensional work-of-fracture of concrete in compression. *Journal of Mechanical Engineering*,125, 599-605.

Landis, E. N., Keane, D.T. (2010). X-ray microtomography. *Materials characterization*, 61(12), 1305-1316.

Lanier, L. (1989). Recent trends in laboratory testing. Geomaterials: constitutive equations and modelling, Edited by Darve, F. Elsevier Applied Science, 7-26.

Le, TM., Fatahi, B., Khabbaz, H. (2012). Viscous behaviour of soft clay and inducing factors.

Geotechnical and Geological Engineering, 30(5), 1069-1083.

Lenoir, N., Bornert, M., Desrues, J., Bésuelle, P., Viggiani, G. (2007). Volumetric digital image correlation applied to X-ray microtomography images from triaxial compression tests on argillaceous rock. Strain, 43, 193-205.

Leonards, G. A., Girault, P. (1961). A study of one-dimensional consolidation test. *Proceeding of the 5th International Conference on Soil Mechanics and Foundation Engineering*, 1, 213-218.

Leroueil, S., Kabbaj, M., Tavenas, F., Bouchard, R. (1985). Stress-strain-strain rate relation for the compressibility of sensitive natural clays. *Géotechnique*, 35(2), 159-180.

Li, J-S., Lin, Y-M. (2000). Singh-Mitchell creep model of Shanghai very soft silt clay. *Rocks and Soil Mechanics*, 21(4), 363-366.

Liam Finn, W.D., Shead, D. (1973). Creep and creep rupture of a sensitive clay. *Proceeding of the 8th International Conference on Soil Mechanics and Foundation Engineering*, Moscow, 1.1

Liingaard, M., Augustesen, A., Lade, P. V. (2004). Characterization of models for time-dependent behavior of soils. *International Journal of Geomechanics*,4 (3), 157-177.

Luckham, P.F., Rossi, S. (1999). Colloidal and rheological properties of bentonite suspensions. *Advances in Colloid and Interface Science*, 82(1-3), 43-92.

Luo, Q-Z, Chen, X-P. (2014). Experimental Research on Creep Characteristics of Nansha Soft Soil. *The Scientific World Journal*, 2014, 1-8.

Lånsivaara, T., Nordal, S. (2000). Strain rate approach to creep evaluations. *13th Nordic Geotechnical Conference NGM-2000*, 25-32.

M:

Marshall, C. E. (1964). The physical chemistry and mineralogy of soils. Soil Materials, Wiley, New York.

Maslov, N.N. (1935). Problems in Geotechnical Investigations. Svirstroy Publications, Leningrad, 4.

Mckyes, E., Yong, R.N. (1971). Three techniques for fabric viewing as applied to shear distortion of a clay. *Clays and Clay Minerals*, 19, 289-293.

Mejia, C. A., Vaid, Y. P., Negussey, D. (1988). Time dependent behaviour of sand. *International Conference on Rheology and Soil Mechanics*, Elsevier Applied Science, London, 312-326.

Meschyan, S.R. (1995). Experimental rheology of clayey soils. Geotechnika13, A.A. Balkema Publishers, Rotterdam, Netherlands.

Mesri, G. (1973). Coefficient of secondary compression. *Journal of the geotechnical engineering division, ASCE*, 99 (SM1), 9515, 123-137.

Mesri, G. (2003). Primary compression and secondary compression. *Geotechnical special publication*, ASCE, Reston, 119, 122-166.

Mesri, G., Castro, A. (1987). C_α/Cc concept and K_0 during secondary compression. *Journal of Geotechnical Engineering*, 113(3), 230-247.

Mesri, G., Choi, Y. K. (1985). The uniqueness of end-of-primary (EOP) void ratio-effective stress relationship. *Proceeding of the 11th International Conference on Soil Mechanics and Foundation Engineering*, 2, 587-590.

Mesri, G., Godlewski, P. M. (1977). Time and stress-compressibility interrelationship. *Journal of the Geotechnical Engineering Division*, 103(5), 417-430.

Mitchell, J. K. (2003). Fundamentals of soil behavior. John Wiley & Sons Inc., New York.

Mitchell, J.K., Soga, K. (2005). Fundamentals of soil behavior (Third edition). John Wiley and Sons, New York.

Monroy, R., Zdravkovic, L., Ridley, A. (2007). Fabric changes in compacted London Clay due to variations in applied stress and suction. *Experimental Unsaturated Soil Mechanics*, 41-48.

Moon, C.F. (1972). The microstructure of clay sediments. Earth-Science Reviews, 8(3), 303-321.

Murayama, S., Shibata, T. (1958). On the rheological characteristics of clays. Disaster Prevention Research Institute, Kyoto, Japan. I (26).

Moore, D. M., Reynolds, R. C., Jr. (1997). X-ray diffraction and the identification and analysis of clay minerals, 2nd ed., Oxford University Press, New York.

Morgenstern, N. R., Tchalenko, J. S. (1967). Microscopic structures in Kaolin subjected to direct shear. Géotechnique, 17(4), 309-328.

Murayama, S., Shibata, T. (1961). Rheological properties of clays. *Proceeding of the 5th International Conference on Soil Mechanics and Foundation Engineering*, 1, 269-274.

Murayama, S., Michihiro, K., Sakagami, T. (1984) Creep characteristics of sands. *Soils and foundations*, 24(2), 1-15.

Myriam,M., Suarez,M., Martin-Pozas,J.M. (1998). Structural and textural modifications of palygorskite and sepiolite under acid treatment. *Clays and Clay Minerals*, 46, 225-231.

N:

Navarro, V., Alonso, E.E. (2001). Secondary compression of clay as a local dehydration process. *Géotechnique*, 51(10), 859-869.

NF (Norme Française) P 94-074 (1994). Sols : reconnaissance et essais- Essais à l'appareil triaxial de revolution. Association française de normalisation, Paris, France.

NF (Norme Française) P 94-090-1 (1997). Sols : reconnaissance et essais - Essai oedométrique - Partie 1 : essai de compressibilité sur matériaux fins quasi saturés avec chargement par paliers. Association française de normalisation, Paris, France.

Nguetnkam, J.P., Kamga, R., Villieras, F., Ekodeck, G.E., Razafitianamaharavo, A., Yvon, J. (2005). Assessment of the surface areas of silica and clay in acid leached clay materials using concepts of adsorption on heterogeneous surfaces. *Journal of Colloid and Interface Science*, 289, 104-114.

Nicholson P.G., Russell P.W., Fujii C. F. (1996). Soil creep and creep testing of highly weathered tropical soils. Geotechnical Special Publication, 61, 195-213.

Nimmo, J. R. (2013). Porosity and Pore Size Distribution. Reference Module in Earth Systems and Environmental Sciences, Elsevier, 1-9.

O:

O'Reilly, M. P., Mair, R. J, Alderman, G H. (1991). Long-term settlements over tunnels: an eleven-year study at Grimsby. Proceedings of Tunnelling. London, UK, 55-64.

Olsen, H.W., (1962). Hydraulic flow through saturated days. *Proceedings of the 9th National Conference on Clays and Clay Minezals,* West Lafayette, Indiana, 131-161.

Oualmakran, M., Mercatoris, B.C.N., François, B. (2016). Pore-size distribution of a compacted silty soil after compaction, saturation, and loading. *Canadian Geotechnical Journal*, 53(12), 1902-1909.

P:

Pacios, L. F. (1991). A simplified representation of atomic electron densities and electrostatic potentials. *The Journal of Physical Chemistry*, 95, 10653-10658.

Penumadu, D., Dean, J. (2000). Compressibility effect in evaluating the pore-size distribution of kaolin clay using mercury intrusion porosimetry. *Canadian Geotechnical Journal*, 37(2), 393-405.

Prashant, A., Penumadu, D. (2007). Effect of microfabric on mechanical behavior of kaolin clay using cubical true triaxial testing. *Journal of Geotechnical and Geoenvironmental Engineering*, 133, 433-444.

Pruett, R.J., Murray, H.H. (1993). The mineralogical and geochemical controls that source rocks impose on sedimentary kaolins. *Clay Minerals Society*, 149-170.

Pusch, R. (1970). Microstructural changes in soft quick clay at failure. *Canadian Geotechnical Journal*, 7(1), 1-7.

R:

Rangeard, D. (2002). Identification des caractéristiques hydro-mécaniques d'une argile par analyse inverse des essais pressiométriques. Doctoral dissertation, Ecole Centrale de Nantes et l'Université de Nantes.

Rangeard, D, Hicher, P-Y, Zentar, R. (2003). Determining soil permeability from pressuremeter tests. *International Journal for Numerical and Analytical Methods in Geomechanics*, 27(1),1-24.

Raymond, G. P. (1965). Prediction of settlements and pore pressures beneath a highway embankment at New Liskeard, Ontario. O.J.H.R.P. report.

Reeves, G., Sims, I., Cripps, J. (2006). Clay materials used in construction, The Geological Society.

Reynolds, O. (1985). On the dilatancy of media composed of rigid particles in contact, with experimental illustration. Philosophical Magazine, 5(20), 469-481.

Ritter, H.-L., Drake, L.-C. (1945). Pressure porosimeter and determination of complete macro pore-size distributions. Ind. Eng. Chem. Anal. Ed., 17 (12), 782-786.

Rootare, H.-M., Prenzlow, C.-F. (1967). Surface areas from mercury porosimeter measurements. The Journal of physical chemistry, 71 (8), 2733-2736.

Roscoe, K.H., Burland, J. (1968). On the generalized stress-strain behavior of wet clay. *Engineering Plasticity*, 535-609.

Roscoe, K., Schofield, A., Thurairajah, A. (1963). Yielding of clays in states wetter than critical. *Géotechnique*, 13 (3), 211-240.

Rowe, P. W. (1962). The stress-dilatancy relation for static equilibrium of an assembly of particles in contact. *Proceedings of the Royal Society of London A: Mathematical, Physical and Engineering Sciences*. The Royal Society, 500-527.

Rowe, R., Hinchberger, S.D. (1998). The significance of rate effects in modelling the Sackville test embankment. *Canadian Geotechnical Journal*, 35, 500-516.

S:

Saito, M. (1965). Forecasting the time of occurrence of a slope failure. *Proceeding of the 6th International Conference on Soil Mechanics and Foundation Engineering*, Quebec, 2, 537-541.

Saito, M. (1969). Forecasting of time of slope failure by tertiary creep. *Proceeding of the 7th International Conference on Soil Mechanics and Foundation Engineering*, 2, 667-683.

Saito, M., Uezawa, H. (1961). Failure of soil due to creep. *Proceeding of the 5th International Conference on Soil Mechanics and Foundation Engineering*, 1, 315-318.

Sachan, A., Penumadu, D. (2007). Effect of microfabric on shear behavior of kaolin clay. *Journal of Geotechnical and Geoenvironmental Engineering,* 10.1061/(ASCE)1090-0241(2007) 133:3(306).

Sachan, A., Penumadu, D. (2009). Effect of shear deformation on microfabric of clay using XRD Technique. *Geotechnical and Geological Engineering*, 27(2), 249-264.

Schulten, H.-R., Schnitzer, M. (1997). The chemistry of soil organic nitrogen: a review. *Biology and Fertility of Soils*, 26(1), 1-15.

Sekiguchi, H. (1973). Flow characteristics of clays. *Soils and foundations*, 13, 45-60.

Sergeyev, Y. M., Grabowska-Olszewska, B., Osipov, V. I., Sokolov, V. N., Kolomenski, Y. N. (1980). The classification of microstructures of clay soils. *Journal of Microscopy*, 120(3), 237-260.

Sheahan, T.C. (1995). Interpretation of undrained creep tests in terms of effective stresses. *Canadian Geotechnical Journal*, 32, 373-379.

Shear, D.L., Olsen, H.W., Nelson, K.R. (1992). Effects of desiccation on the hydraulic conductivity versus void ratio relationship for a natural clay. Transport. Res. Record, 1369, 130-135.

Shen, C.K., Arulanandan, K., Smith, W.S. (1973). Secondary consolidation and strength of a clay. *Journal of the Soil Mechanics and Foundations Division*, ASCE, 99(SM1), 95-110.

Shibata, T., Karube, D. (1969) Creep rate and creep strength of clays. *International conference on soil mechanics and foundation engineering*, 1, 361-367.

Shimizu, M. (1982). Effect of overconsolidation on dilatancy of a cohesive soil. *Soils and Foundations*, 22(4), 121-133.

Shirlaw, J.N. (1995). Observed and calculated pore pressures and deformations induced by an earth balance shield: Discussion. *Canadian Geotechnical Journal*. 1995, 32,181-189.

Schofield, A. N., Worth, C. P. (1968). Critical state soil mechanics. McGraw Hill, New York.

Silva, A. J., Moran, K., Akers, S. A. (1983). Stress-strain-time behavior of deep sea clays. *Canadian Geotechnical Journal*. 20, 517-531.

Singh, A., Mitchell, J. K. (1968). General stress-strain-time function for soils. *Journal of the Soil Mechanics and Foundation Division*, 94(1), 21-46.

Singh, A., Mitchell, J.K. (1969). Creep potential and creep rupture of soils. *Proceeding of the 7th International Conference on Soil Mechanics and Foundation Engineering*, Mexico, 1, 379-384.

Sivakomar, V., Doran, I.G., Graham, J. (2002). Particle orientation and its influence on the mechanical behavior of isotropically consolidated reconstituted clay. Engineering Geology, 66(3-4), 197-209.

Snead, D.E. (1970). Creep rupture of saturated undisturbed clays. Doctoral dissertation, University of British Columbia, Vancouver.

Sparks D. L. (2003). Environmental Soil Chemistry. Second Edition, Elsevier Science, 367.

Sridharan, A., Rao, G.V. (1973). Mechanisms controlling volume change of saturated clays and the role of effective stress concept. *Géotechnique*, 23(3), 359-382.

Sridharan, A. (2001). Engineering behaviour of clays: influence of mineralogy. Chemo mechanical coupling in clays: from nano-scale to engineering applications, Swets&Zeitlinger, Maratea.

Stepanian, G.Ter. (1975). Creep of a clay during shear and its rheological model. *Géotechnique,* 25(2), 299-320.

Sun, J. (2007). Rock rheological mechanics and its advance in engineering applications. *Chinese Journal of Rock Mechanics and Engineering*, 26(6), 1081-1106.

Suklje, L. (1957). The analysis of the consolidation process by the isotaches method. *Proceeding of the 11th International Conference on Soil Mechanics and Foundation Engineering*, 1, 200-206.

Sun, D., You, G., Zhou, A., Sheng, D. (2016). Soil-water retention curves and microstructures of undisturbed and compacted Guilin lateritic clay. *Bulletin of Engineering Geology and the Environment*, 75(2), 781-791.

Swindell, W., Barrett, H.H. (1977). Computerized tomography: taking sectional X-rays. *Physics Today*, 30, 32.

T:

Tavenas, F., Leroueil, S., La Rochelle, P., Roy, M. (1978). Creep behaviour of an undisturbed lightly overconsolidated clay. *Canadian Geotechnical Journal*, 15(3), 402-423.

Taylor, D.W. (1942). Research on consolidation of clays. Department of Civil and Sanitation Engineering, Massachusetts Institute of Technology, Report 82.

Taylor, D.W., Merchant, W.A. (1940) A theory of clay consolidation accounting for secondary compression. *Journal of Mathematical Physics*, 19,167-185.

Terzaghi, K. (1941) Undisturbed clay samples and undisturbed clays. *Journal of the Boston Society of Civil Engineers*, 29(3), 211-231.

Tian, W.-M., Silva, A. J., Veyera, G. E., Sadd, M. H. (1994). Drained creep of undisturbed cohesive marine sediments. *Canadian Geotechnical Journal*, 31(6), 841-855.

Tovey, D., Wong, K-Y. (1973). The preparation of soils and other geological materials for the S.E.M. Proc Int. Symp. Soil Structure, Gothenburg, 59-67.

V:

Velde B. (1995). Origin and mineralogy of clays. Clays and the environment. Springer Berlin Heidelberg.

Vialov, S., Skibitsky, A. (1957). Rheological processes in frozen soils and dense clays. *Proceedings of the 4th International Conference on Soil Mechanics and Foundation Engineering*, London, 1, 120-124.

Vyalov, S.S. (1986). Rheological fundamentals of soil mechanics. Developments in Geotechnical Engineering, Elsevier.

W:

Wahls, H. E. (1962). Analysis of primary and secondary consolidation. *Journal of the Soil Mechanics and Foundations Division*, 88 (SM6), 207-234.

Walker, L. K., Raymond, G. P. (1968). The prediction of consolidation rates in a cemented clay. *Canadian Geotechnical Journal*, 5(4), 192-216.

Walker, L.K. (1969a). Discussion. *Proceedings of the American Society of Civil Engineers*, 95(SM1), 409-415.

Walker, L.K. (1969b). Undrained creep in a sensitive clay. *Géotechnique*, 19(4), 515-529.

Walker, L. K. (1969c). Secondary compression in the shear of clays. *Journal of the Soil Mechanics and Foundations Division*, ASCE, 95(SM 1), 167-188.

Wang, Y.H., Xu, D. (2006). Dual porosity and secondary consolidation. *Journal of Geotechnical and Geoenvironmental Engineering*, 133(7), 793-801.

Washburn, A.-L. (1956). Classification of Patterned Ground and Review of Suggested Origins. Geological Society of America Bulletin, 67(7), 823-865.

Wahyudi, H. (1991). Etudedes propriétés mécaniques des matériaux argileux en relationavec leur organisation à différentes échelles. Thèse de doctorat, Ecole centrale Paris.

Wei, X. (2014). Etude micro-macro de la fissuration des argiles soumises à la dessiccation. Doctoral dissertation, Ecole Centrale Paris, France.

Wheeler, S. J., Näätänen, A., Karstunen, Minna, Lojander, M. (2003). An anisotropic elastoplastic model for soft clays. *Canadian Geotechnical Journal*, 40(2), 403-418.

Whittig, L. D., Allardice, W. R. (1986). X-Ray Diffraction Techniques. In: Klute, A., Ed., Methods of Soil Analysis, Part 1: Physical and Mineralogical Methods, American Society of Agronomy, Madison, 331-362.

Wilson, M. J., Wilson, L., Patey, I. (2014). The influence of individual clay minerals on formation damage of reservoir sandstones: a critical review with some new insights. *Clay Minerals*, 49, 147-164.

Winkerkorn, H. W. (1943). The condition of water in porous systems. *Soil Science*, 56(2),109-116.

Wu, H-W, Li, Q, Liu, G-B. (2011). Characteristics of one-dimensional compressibility of Shanghai clay. *Chinese Journal of Geotechnical Engineering*, 33(4), 630-636. (in Chinese)

Y:

Yang, S.L., Schjetne, K., Kvalstad, T. (2010). Application of X-ray computed tomography in marine clays. Proceedings of the 12th International Offshore and Polar Engineering Conference, Beijing, China.

Yin, J-H., Graham, J. (1989). Viscous-elastic-plastic modelling of one dimensional time-dependent behaviour of clays. *Canadian Geotechnical Journal*, 26, 199-209.

Yin, J-H. (1999). Non-linear creep of soils in oedometer tests. *Géotechnique*, 49(5), 699-707.

Yin, J-H. (2002). Calculation of settlements of foundation soils considering creep. *Proceedings of the Nakase Memorial symposium on soft ground engineering in coastal areas*, Yokosuka, Japan, 205-211.

Yin, Z-Y. (2006). Modélisation viscoplastique des argiles naturelles et application au calcul de remblais sur sols compressibles. Thèse de Doctorat, Ecole Centrale de Nantes, France.

Yin, Z-Y., Hicher, P-Y. (2008). Identifying parameters controlling soil delayed behaviour from laboratory and in situ pressuremeter testing. *International Journal for Numerical Methods in Geomechanics*, 32, 1515-1535.

Yin, Z-Y, Zhang, D-M, Hicher, P-Y, et al. (2008). Modeling of the time-dependent behavior of soft soils using a simple elasto-viscoplastic model. *Chinese Journal of Geotechnical Engineering*, 30(6), 880-888.

Yin, Z-Y, Zhu, Q-Y, Zhu, J-G. (2008). Experimental investigation on creep behavior of soft clays: review and development. Rocks and soil mechanics, 34(2), 1-17. (in Chinese)

Yin, Z-Y, Chang, C S. (2009). Microstructural modelling of stress-dependent behaviour of clay. *International Journal of Solids and Structures*, 46(6), 1373-1388.

Yin, Z-Y, Chang, C S, Hicher, P-Y., Karstunend, M. (2009). Micromechanical analysis of kinematic hardening in natural clay[J]. International Journal of Plasticity, 25(8),1413-1435.

Yin, Z-Y, Chang, C S, Karstunen, M., Hicher, P-Y. (2010). An anisotropic elastic-viscoplastic model for soft clays. *International Journal of Solids and Structures*, 47(5), 665-677.

Yin, Z-Y, Karstunen, M., Arstunen, M., Hicher, P-Y. (2010). Evaluation of the influence of elasto-viscoplastic scaling functions on modelling time-dependent behaviour of natural clays. *Soils and Foundations*, 50(2), 203-214.

Yin, Z-Y, Karstunen, M. (2011). Modelling strain-rate-dependency of natural soft clays combined with anisotropy and destructuration. *Acta Mechanica Solida Sinica*, 24(3),216-230.

Yin, Z-Y, Karstunen, M., Chang, C S, M. ASCE, Koskinen, M., Lojander, M. (2011). Modeling time-dependent behavior of soft sensitive clay. *Journal of Geotechnical and Geoenvironmental Engineering*, 137(11), 1103-1113.

Yin, Z-Y, Karstunen, M., Wang, J-H, et al. (2011). Influence of features of natural soft clay on the behavior of embankment. *Journal of Central South University of Technology*, 18(5),1667-1676.

Yin, Z-Y, Wang, J-H. (2012). A one-dimensional strain-rate based model for soft structured clays. *Science China Technological Sciences*, 55(1), 90-100.

Yin, Z-Y, Xu, Q., Yu, C. (2012). Elastic viscoplastic modeling for natural soft clays considering nonlinear creep. *International Journal of Geomechanics*, 15(5), 1-10.

Yong, R.N., Sheeran, D. (1973). Fabric unit interaction and soil behavior. *Proceedings of the International Symposium on Soil Structure*, Gotheubmg, Sweden, 176-183.

Z:

Zeevaart, L. (1986). Consolidation in the inter granular viscosity of highly compressible soils. *ASTM Special Technical Publication*, Philadelphia, 257-281.

Zentar, R. (1999). Analyse inverse des essais pressiométrique, application à l'argile de Saint-Herblain. Doctoral dissertation, Ecole Centrale de Nantes et l'Université de Nantes.

Zhu, F., Duan, Z-Y, Wu, Z-Y, Wu, Y-Q, Li, T-L, Cai, Y-D. (2014). Experimental study on direct shear creep characteristics and long-term strength of red layer sliding zone soil in Southern Hunan. *Advanced Materials Research*, 842, 782-787.

Zhu, J-G, Yin, J-H, Luk, S-T. (1999). Time-dependent stress-strain behavior of soft Hong Kong marine deposits. *ASTM geotechnical testing journal*, 22(2), 118-126.

Zhu J.-G. (2007). Rheological behavior and elastic viscoplastic modeling of soil. Science Press, Beijing, China.

Acknowledgments

First and foremost, I want to thank my advisor Professor Mahdia Hattab. It has been an honor to be her Ph.D student. I appreciate all her contributions of time, ideas, and patience to make my Ph.D. experience productive and stimulating. The enthusiasm and rigorous working attitude she has for research is contagious and motivational for me, especially during tough times when I was frustrated by the failure of tests. I am also thankful for the excellent example she has provided as a successful woman geotechnologist and professor.

I would like to thank my co-director Professor Zhenyu Yin. I am very grateful for his guidance, suggestions and patience during my graduate studies in France. His enthusiasm, motivation and immense knowledge in soil rheology, taken together, make him a great mentor.

I extend my deepest gratitude to Professor Pierre-Yves Hicher, whose support and guidance in the analysis of experimental results. He has been actively interested in my work and has been available to advise me in every possible discussion. I would like to sincerely thank he and his wife for their selfless help in improving my English writing.

My sincere gratitude is reserved for my graduate advisor Professor Jianlin Ma. He is the most honorable and chivalrous teacher I have ever met. He led me into the field of geotechnical six years ago and encouraged me to start the Ph.D research. It is my honor to have his encouragement and help all the time.

I owe my gratitude to Professor Jean-Marie Fleureau and Mr. Thomas Reiss, in MSSMat, Ecole Centrale Paris, for their helpful in drying samples. I would also like to thank Mr. Mohamad Jrad in LEM3 for his help in solve the devise problems, and Mr. Lamine Ighil-Lameur in LEM3 for teaching me how to operate the GDS apparatus. The aid of Dr. Yudong Zhang, Mr. Jean-Sébastien Lecomte and Mr. Jérôme Slowensky in LEM3 on microstructural observation are highly appreciated. I am special thankful to my colleague Mr. Qianfeng Gao for helping me manage the MIP and SEM observations. I am also thankful to Ms. Ouardia Sediki for the help in the measurement of grain size distribution.

I would like to thank all the jury members for taking time out of their busy schedules to achieve my dissertation defense, and special gratitude to Professor Yujun Cui and Professor Irini Djeran-Maigre for their constructive suggestions and comments on my dissertation.

I gratefully acknowledge the funding sources that made my Ph.D. work possible. I was funded by the China Scholarship Council for 3 years.

My time at LEM3 was made enjoyable in large part due to the many friends and groups that became a part of my life. I am grateful for time spent with Ms. Xia Huang, Ms. Chunqing Lin, Ms. Wen Chen, Ms. Jing Wen, Ms. Yuting Huang, Ms. Xiaomeng Liu, Ms. Meishuai Liu, and the gentlemen Mr. Cai Chen, Mr. Chunyang Zhang, Mr. Zhengtian Yang, Mr. Ling Zeng, Mr. Tao Liu, Mr. Hanbing Bian, Mr. Yuqi Zhang, Mr. Qun Huang, Mr. Shun Xu, Mr. Yajun Zhao, Mr. Rui Xu, Mr. Xiaolei Chen.

Last but not least, I would like to express my deep love and gratitude to my parents and my families who have always been loving, helping, encouraging and supporting me in my life. My special thanks go to my beloved husband Mr. Bin Hu, he has always supported and encouraged me in every way I could be. I hope that I can make him proud of me as I always proud of him.

Thanks to all the loves that bring me to life.

Dan ZHAO

November 2017

In Metz

Annex

Annex Chapter 1

1. Oedometric apparatus

The schematic diagram in Figure 1-1 represents the used oedometer apparatus. The soil specimen is placed inside a steel rigid ring. Drainage is achieved by two porous stones located on the top and the bottom. The bottom stone functions as a base and the top one is next to a piston, transmitting an external load to the specimen A thin layer of silicone grease was smeared on the internal surface of the metal ring to reduce the friction between the soil and the steel ring. During the whole test, the soil specimen was immersed in water.

According to the France Norm (NF P94-090-1), the height of the oedometer ring should fulfill $10mm \leq H \leq 0.4D$, and according to the British Standards (BS1377), the height should be at least 2 cm and the rate of diameter/height should between 3 and 4. Two dimensions of oedometer rings were selected for this research accordingly; 50 mm in diameter × 20 mm in height and 80 mm in diameter × 20 mm in height, with the diameter/height ratio is 2.5 and 4 respectively.

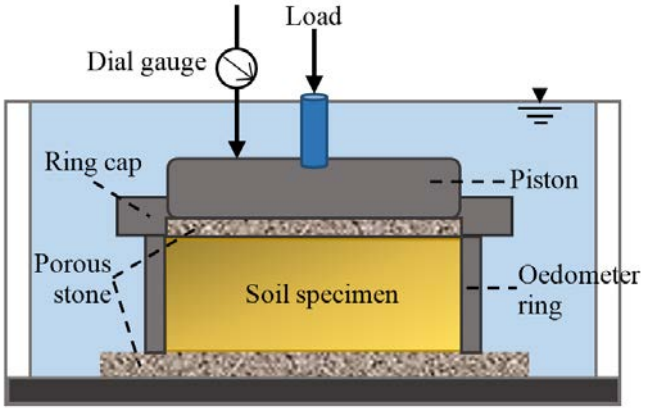

Figure 1-1 Basic scheme of the oedometer ring

Figure 1-2 gives the photos of the used oedometer apparatus, marked by Controlab.fr, which total dimension is L 200 x D 750 x H 500 mm (H = 1300 mm with bench), the 3-speed levers are 9: 1, 10: 1 and 11: 1, equipped with an adjustable counterweight and the maximum load for each lever is 64 kg.

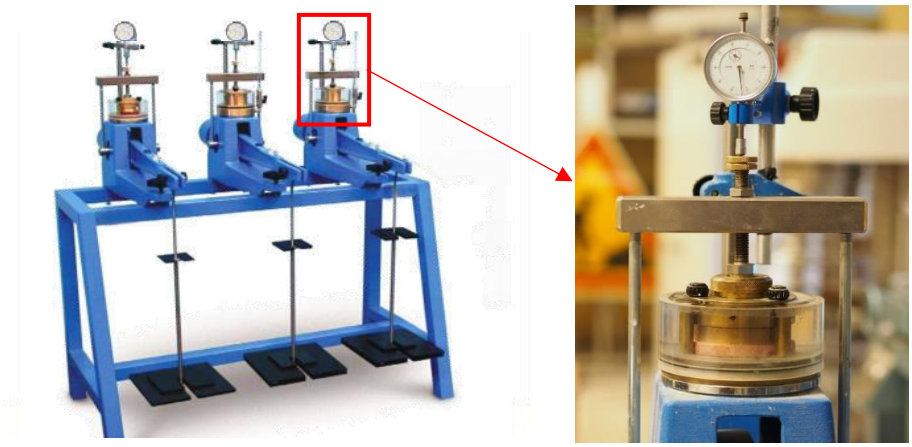

(a) (b)

Figure 1-2 Photos of the oedometer apparatus: (a) overview photo; (b) photo of oedometer cell

2. Oedometer testing program

As conducted in the critical oedometer test, the loading and unloading are performed by steps. The duration of each step is 24 hours, except for loads at 400 kPa and 800kPa in which the duration has been longer, 10 days and 7days, for the observation of creep development (Table 1-1). The loading rate is defined by the Equation 1-1 below (Wu et al., 2011; Zhou and Chen, 2006).

$$\overline{\sigma_l} = \frac{\sigma_i - \sigma_{i-1}}{\sigma_{i-1}} \tag{1-1}$$

Table 1-1 Program of oedometer test

Loading cell (Diameter/mm × Height/mm)	50×20; 80×20								
Loading steps (kPa)	12.5	25	50	100	200	**400** **(10 days)**	600	**800** **(7 days)**	1000
Loading rate $\overline{\sigma_i}$	-	1.0	1.0	1.0	1.0	1.0	0.5	0.33	0.25

3. Mechanical behavior on oedometric path

The initial void ratio of saturated soil specimen

$$e_{00} = w \cdot G_s \tag{1-2}$$

Where $w=1.5 \cdot w_L$; specific gravity $G_s=\frac{\gamma_s}{\gamma_w}$

The void ratio before loading can be calculated by the measured deformation at the end of applying the piston as following

$$e_0 = e_{00} - (1 + e_{00}) \frac{\Delta H_{piston}}{H_{00}} \quad (1\text{-}3)$$

Where H_{00}: the initial height of specimen, H_{00}=20 mm for all specimens.

Similarly, one can calculate the void ratio after each load

$$e_i = e_0 - (1 + e_0)\, \varepsilon_1 \quad (1\text{-}4)$$

Where ε_1: the axial strain, $\varepsilon_1 = \frac{\Delta H_i}{H_0}$ (ΔH_i: the compaction corresponding to load 'i'; H_0: the height of specimen before loading)

After all the compression points are plotted in (*e-log* σ'_v) plane. The compression index *Cc* and the swelling index *Cs* may be obtained by fitting the linear part for loading or unloading stage (see Figure 1-3). The identified C_c is 0.28 and C_s is 0.09 for Kaolin, both are normally values for low plasticity soil, these results are consistent with the values found in the literature on the same material (Ighil-Ameur, 2016). The identified *Cc*= 0.35 and *Cs* = 0.04 for Shanghai clay.

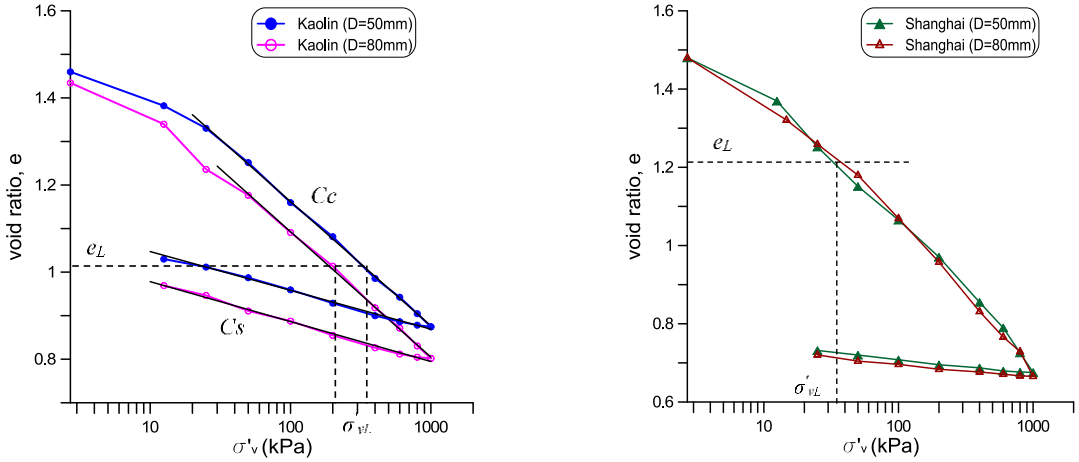

Figure 1-3 Oedometric path in *e-logt* plane

The variations of void ratio with time during the whole multiple loading for both Kaolin and Shanghai clay are represented in Figure 1-4 and 1-5, where the fitting line shows the identification of $C_{\alpha e}$, and the arrow at the beginning corresponds to time node of t_{100}.

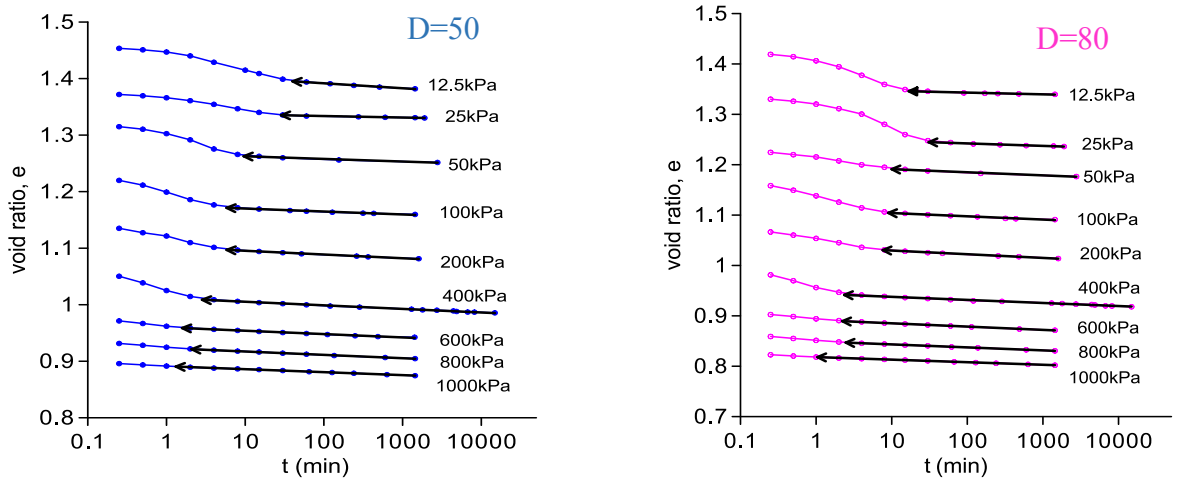

(a) D=50 mm (b) D=80 mm

Figure 1-4 Void ratio, *e* as a function of logarithm time for Kaolin

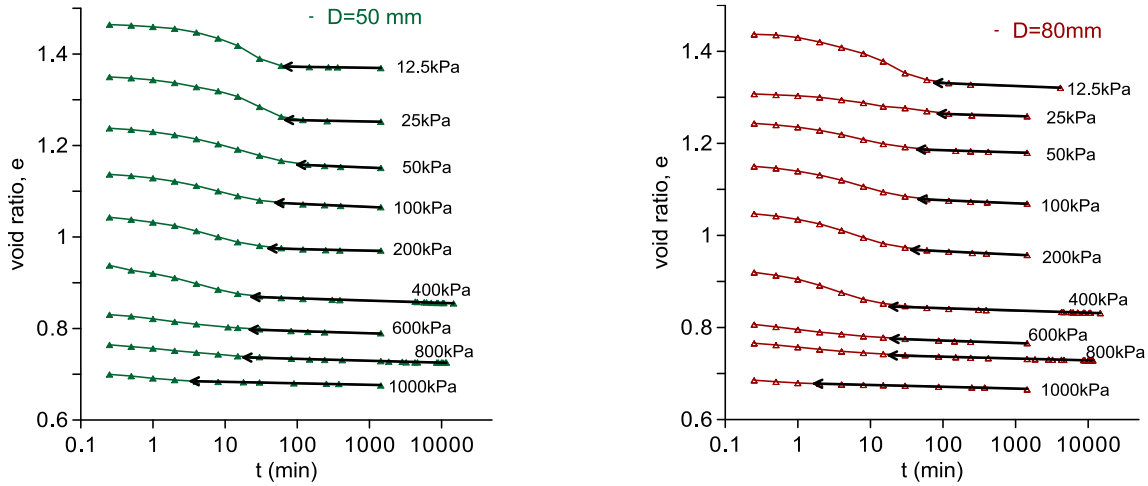

(a) D=50 mm (b) D=80 mm

Figure 1-5 Void ratio, *e* as a function of logarithm time for Shanghai clay

The values of t_{100} and $C_{\alpha e}$ at each loading stage of Kaolin and Shanghai clay are summarized in Table 1-2 and Table 1-3.

Table 1-2 Results of curve fitting for t_{100} and $C_{\alpha e}$ of Kaolin

Sample	σ'_v (kPa)	12.5	25	50	100	200	400	600	800	1000
D=50 mm	t_{100} (min)	31.2	28.7	9.6	5.8	5.8	2.9	1.6	2.1	1.3
	$C_{\alpha e}$	0.0038	0.0027	0.0046	0.0052	0.0066	0.0063	0.0059	0.0059	0.0053
	R^2	0.9827	0.9623	0.9715	0.9726	0.9927	0.9955	0.9888	0.9985	0.9989
D=80 mm	t_{100} (min)	17.8	30.9	9.5	9	7.6	2.4	2.2	2.5	1.0
	$C_{\alpha e}$	0.0035	0.0049	0.0027	0.0065	0.0073	0.0061	0.0065	0.0059	0.0051
	R^2	0.9053	0.9672	0.9717	0.9799	0.9930	0.9920	0.9981	0.9993	0.9992

Table 1-3 Results of curve fitting for t_{100} and $C_{\alpha e}$ of Shanghai clay

Soil	σ'_v (kPa)	12.5	25	50	100	200	400	600	800	1000
D=50 mm	t_{100} (min)	65.2	67.9	90.8	50.4	40.3	23.3	22.2	26.6	3.4
	$C\alpha e$	0.0022	0.0031	0.0064	0.0070	0.0037	0.0050	0.0049	0.0042	0.0032
	R^2	0.9676	0.9058	0.9327	0.9544	0.9017	0.9752	0.9117	0.9591	0.9785
D=80 mm	t_{100} (min)	75.5	86.8	43.6	45.7	36.4	18.2	19.0	18.6	1.7
	$C\alpha e$	0.0062	0.0046	0.0049	0.0068	0.0075	0.0049	0.0054	0.0040	0.0039
	R^2	0.9769	0.9212	0.9678	0.9590	0.9789	0.9712	0.9498	0.9798	0.9802

Annex Chapter 3

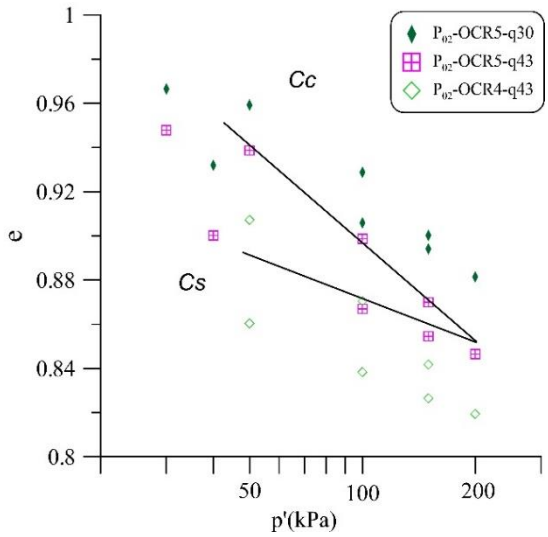

Figure 3-1 Identification of *Cc* and *Cs* for group P_{02} during isotropic path

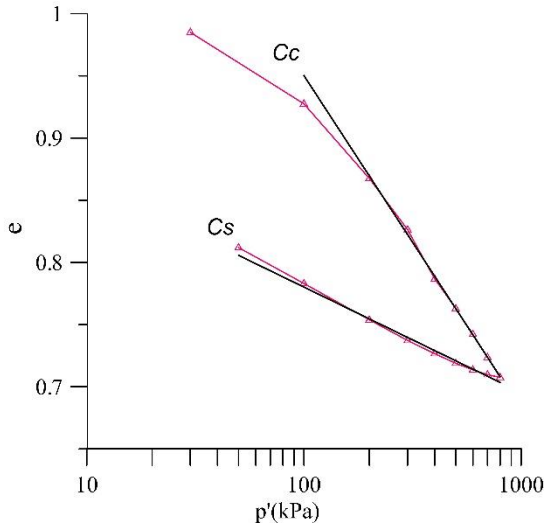

Figure 3-2 Identification of *Cc* and *Cs* for test P_{08}-OCR16-q43 during isotropic path

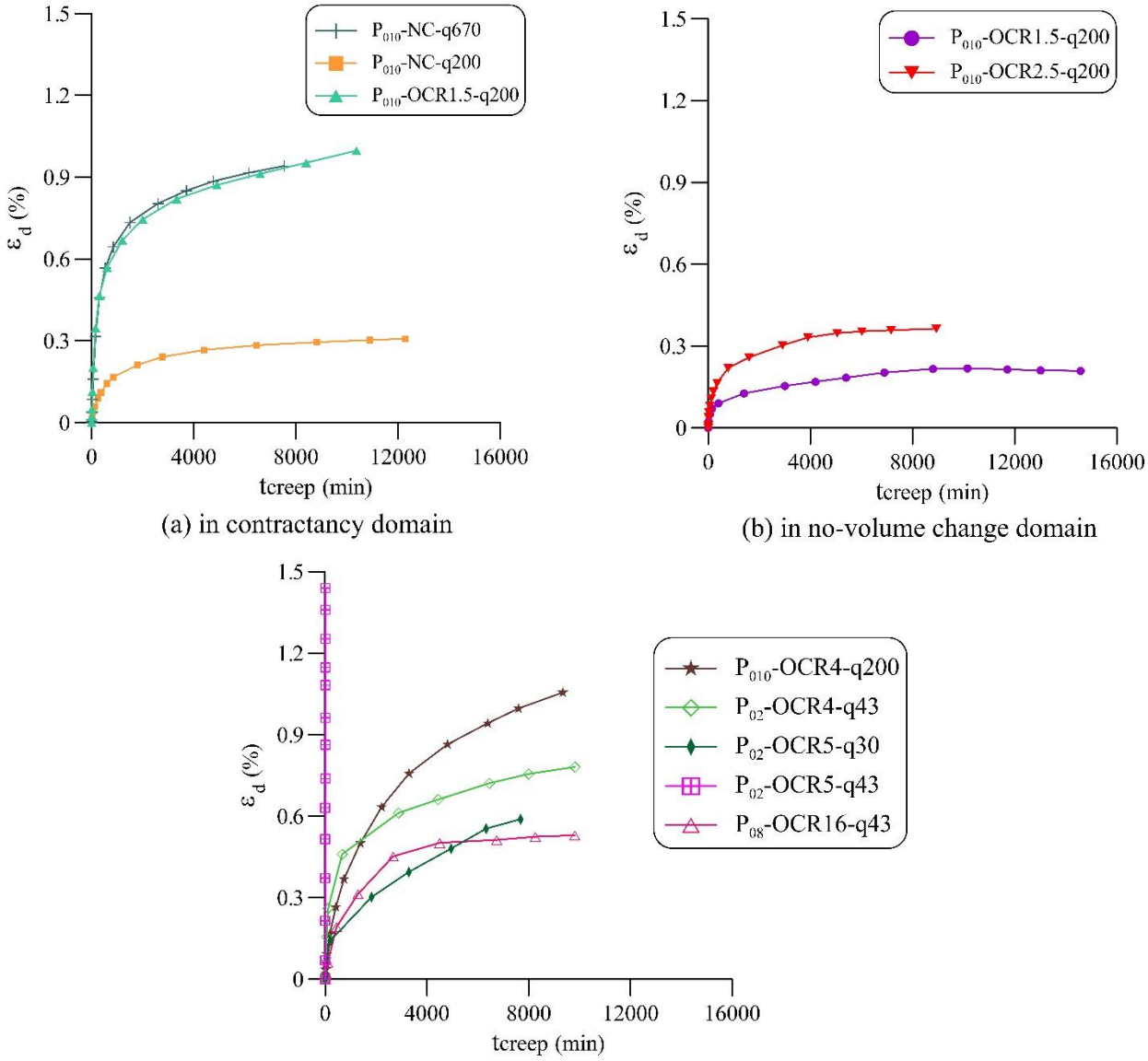

(a) in contractancy domain

(b) in no-volume change domain

(c) in dilatancy domain

Figure 3-3 Evolution of deviatoric strain with time during creep phase in different domains

Annex Chapter 4

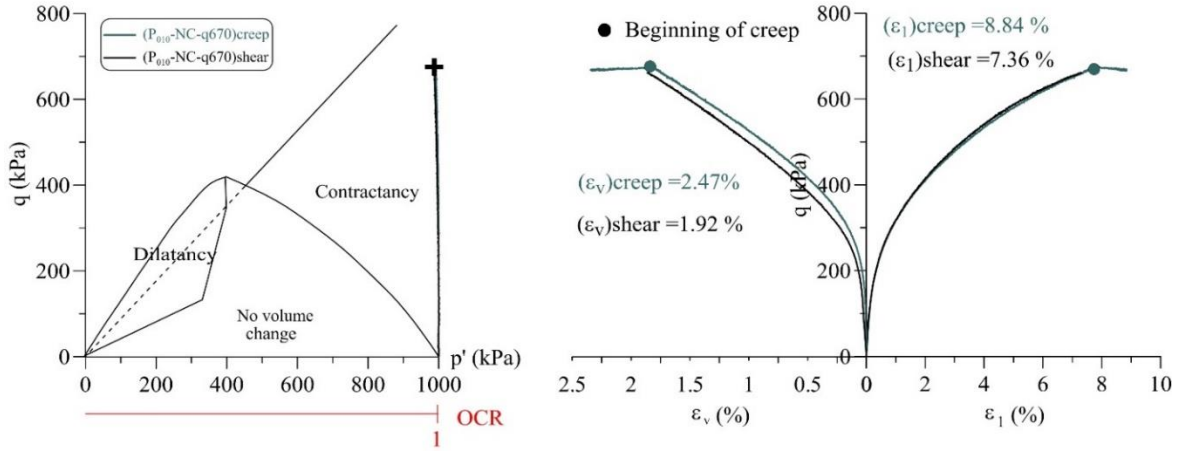

(a) (b)

Figure 4-1 Tests P_{010}-NC-q670 in contractancy domain:(a) in *(p'-q)* plane (b) strain evolution

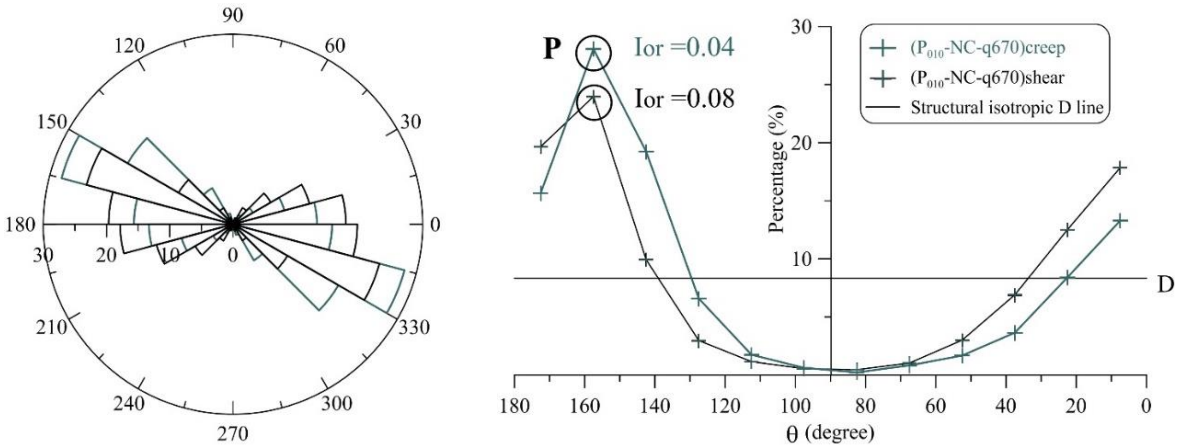

Figure 4-2 Angular orientation of the edge view particles for tests P_{010}-NC-q670

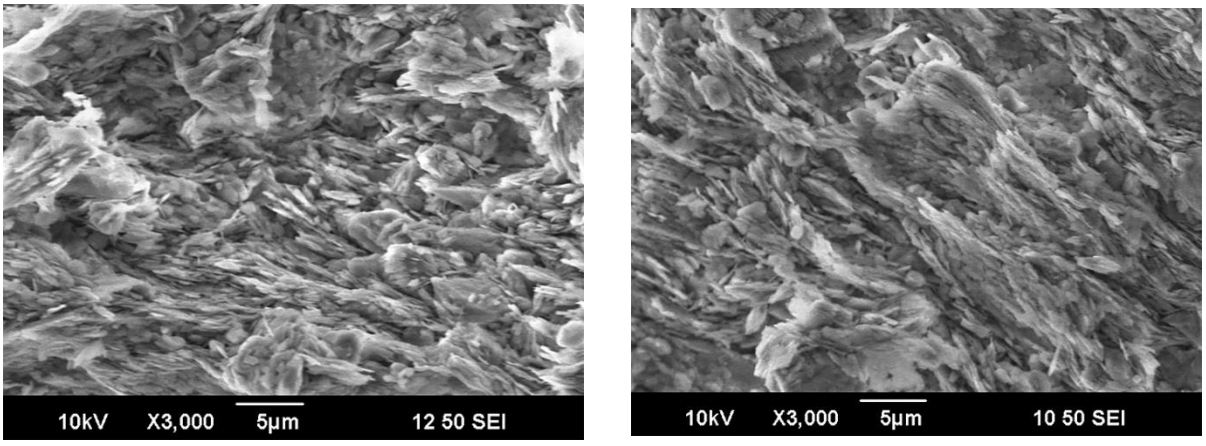

(a) (b)

Figure 4-3 Microfabric of tests P_{010}-NC-q670 in contractancy domain: (a) after shear (b)after creep

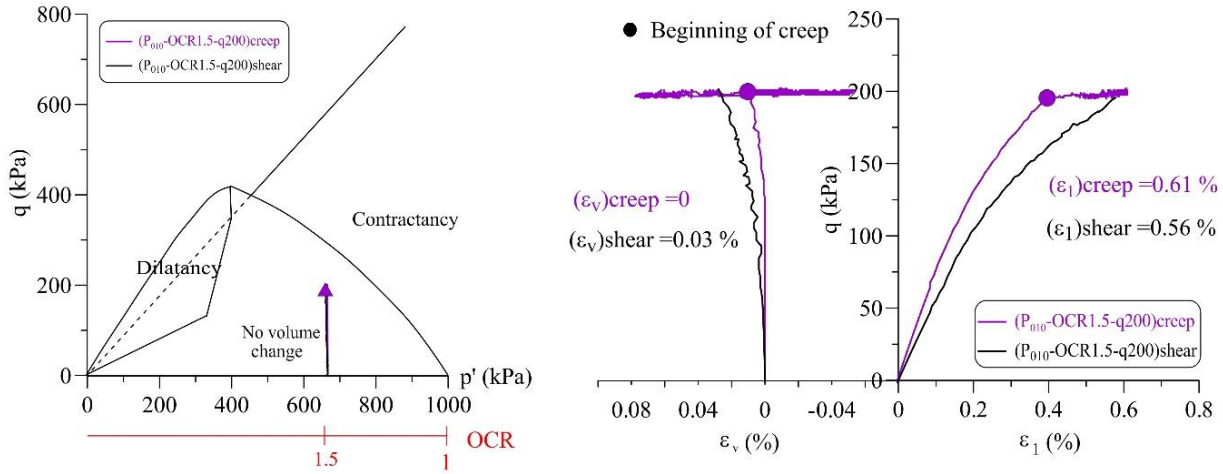

(a) (b)

Figure 4-4 Tests P_{010}-OCR1.5-q200 in pseudo-elastic domain: (a) in *(p'-q)* plane (b) strain evolution

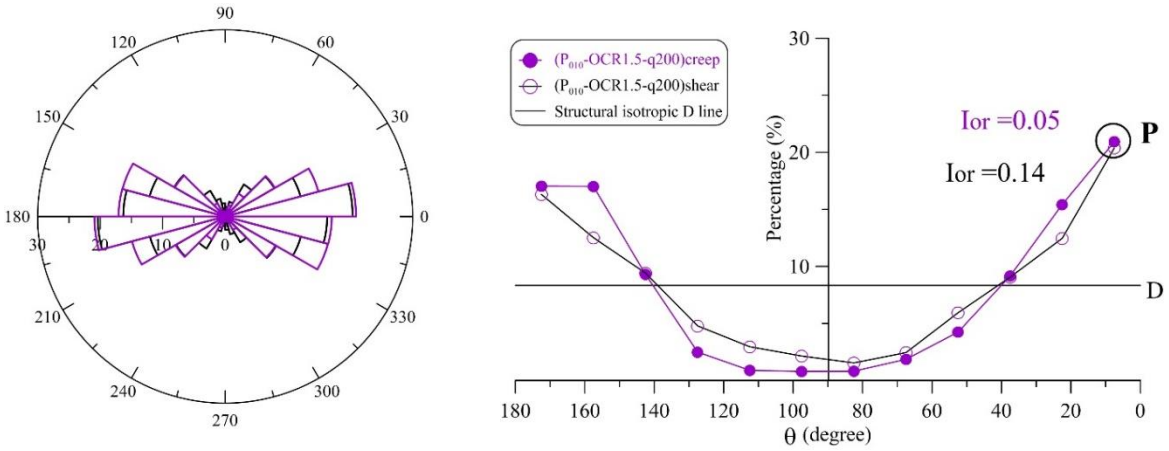

Figure 4-5 Angular orientation of the edge view particles for tests P_{010}-OCR1.5-q200

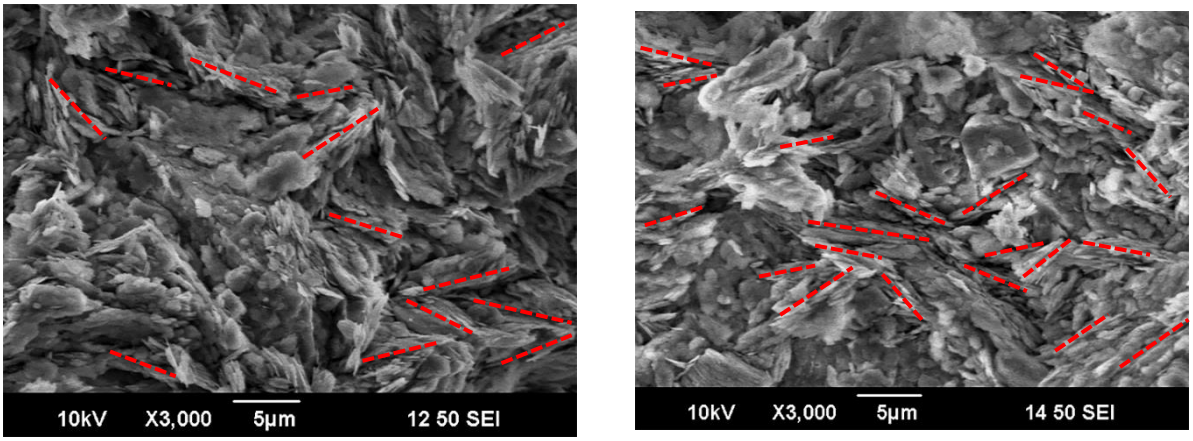

(a) (b)

Figure 4-6 Microfabric of tests P_{010}-OCR1.5-q200 in pseudo-elastic domain: (a) after shear (b)after creep

Table 4-1 Microstructure orientation of particle and void

Test	ε_1 (%)	ε_v (%)	Number of image	**Particle**				**Void**			
				Number	Preferred angle θ (˚)	Percentage of θ (%)	I_{or}	Number	Preferred angle (˚)	Percentage of θ (%)	I_{or}
$(P_{010}\text{-NC-q200})_{creep}$	0.76	0.59	14	7227	150~165	30.8	0.02	11255	150~165	20.1	0.13
$(P_{010}\text{-NC-q200})_{shear}$	0.29	0.05	10	4347	150~165	23.8	0.06	8472	150~165	15.8	0.26
$(P_{010}\text{-NC-q670})_{creep}$	8.84	2.47	20	7570	150~165	28.1	0.04	15609	165~180	16.5	0.19
$(P_{010}\text{-NC-q670})_{shear}$	7.36	1.92	14	5735	150~165	24	0.08	11395	150~165	15.1	0.22
$(P_{010}\text{-OCR1.5-q445})_{creep}$	5.06	0.72	15	6530	150~165	21.1	0.08	12731	165~180	11.6	0.25
$(P_{010}\text{-OCR1.5-q445})_{shear}$	4.86	0.58	15	7156	150~165	25.1	0.03	13132	165~180	20.3	0.12
$(P_{010}\text{-OCR1.5-q200})_{creep}$	0.61	0	16	6617	0~15	20.9	0.05	12607	0~15	17	0.23
$(P_{010}\text{-OCR1.5-q200})_{shear}$	0.56	0.04	17	6739	0~15	20.4	0.14	11737	0~15	12.5	0.46
$(P_{010}\text{-OCR2.5-q200})_{creep}$	1.14	-0.09	18	5953	150~165	21.2	0.15	13421	150~165	13.5	0.40
$(P_{010}\text{-OCR2.5-q200})_{shear}$	0.92	-0.05	15	4195	150~165	18.6	0.15	11356	0~15	12.4	0.48
$(P_{010}\text{-OCR4-q200})_{creep}$	2.28	-0.55	10	3296	150~165	17.1	0.25	7400	165~180	11.6	0.56
$(P_{010}\text{-OCR4-q200})_{shear}$	1.81	-0.11	11	3418	150~165	18.5	0.22	8630	0~15	13.6	0.45

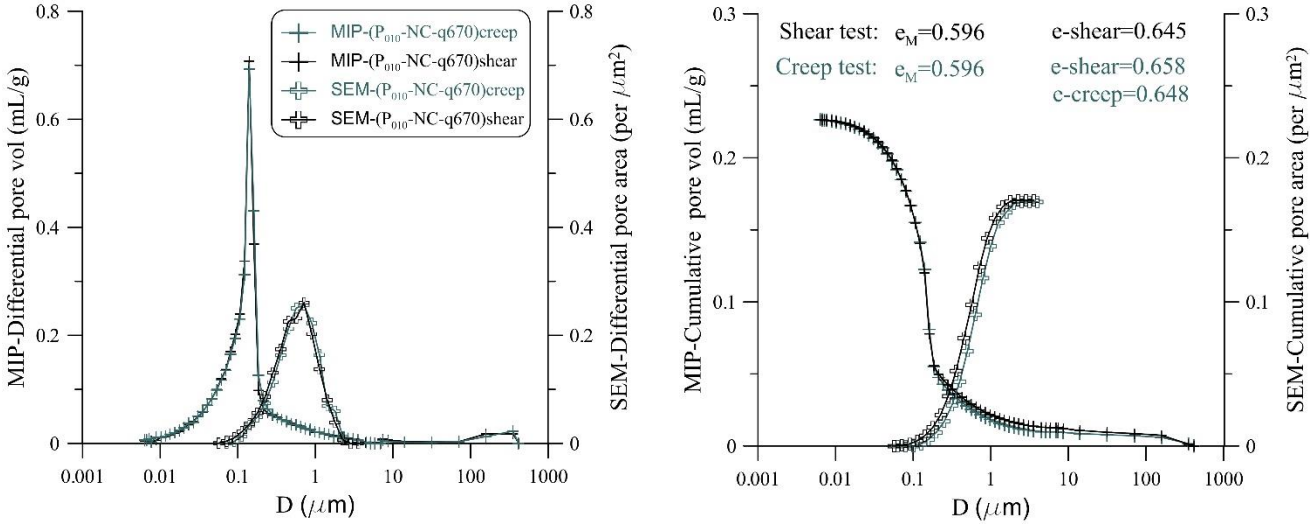

(a) (b)

Figure 4-7 Evolution of pore space for test P_{010}-NC-q670 after shear/creep in contractancy domain

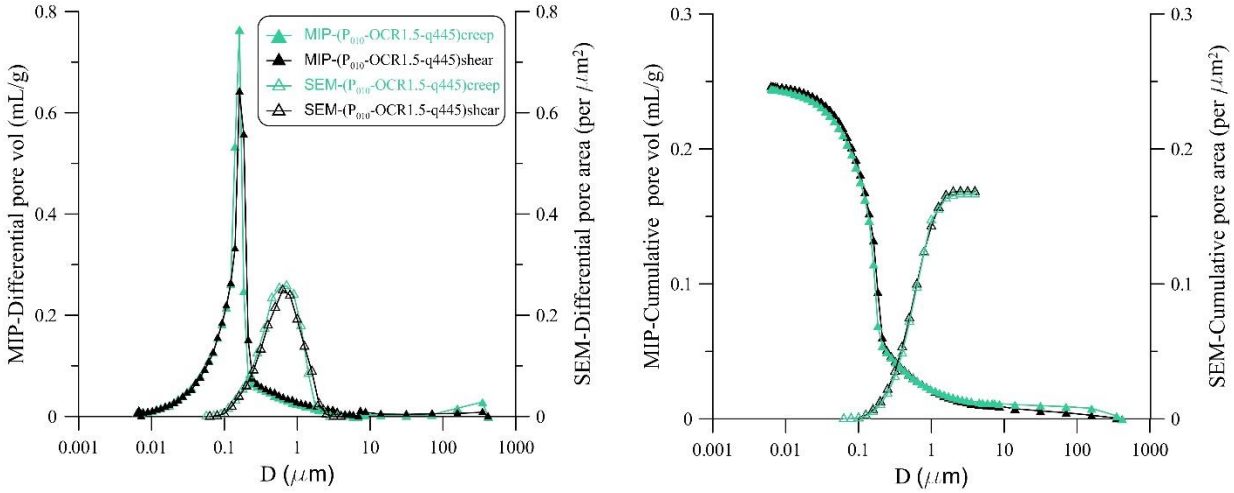

(a) (b)

Figure 4-8 Evolution of pore space for test P_{010}-OCR1.5-q445 after shear/creep in contractancy domain

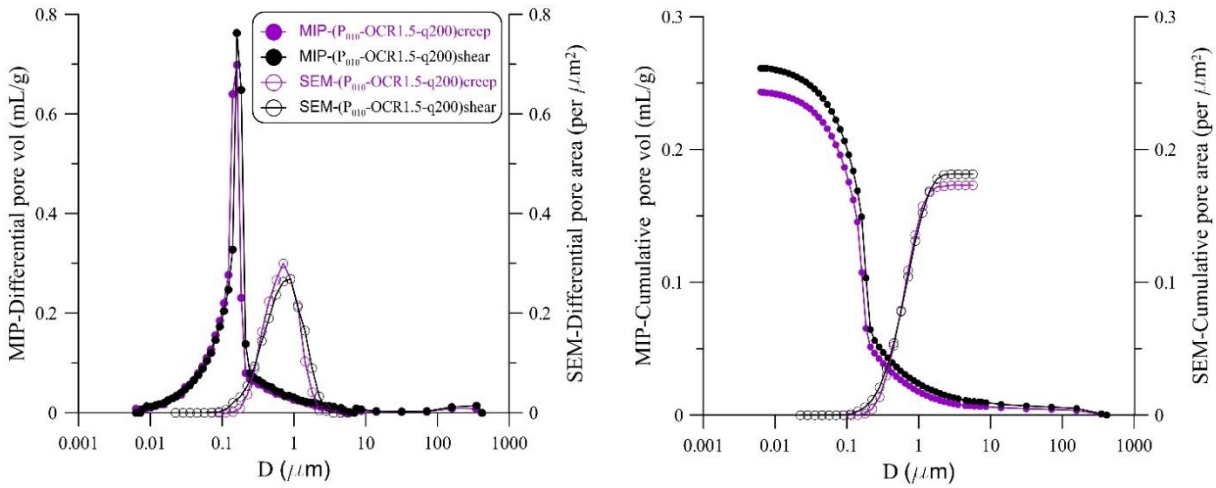

Figure 4-9 Evolution of pore space for test P_{010}-OCR1.5-q200 after shear/creep in pseudo-elastic domain

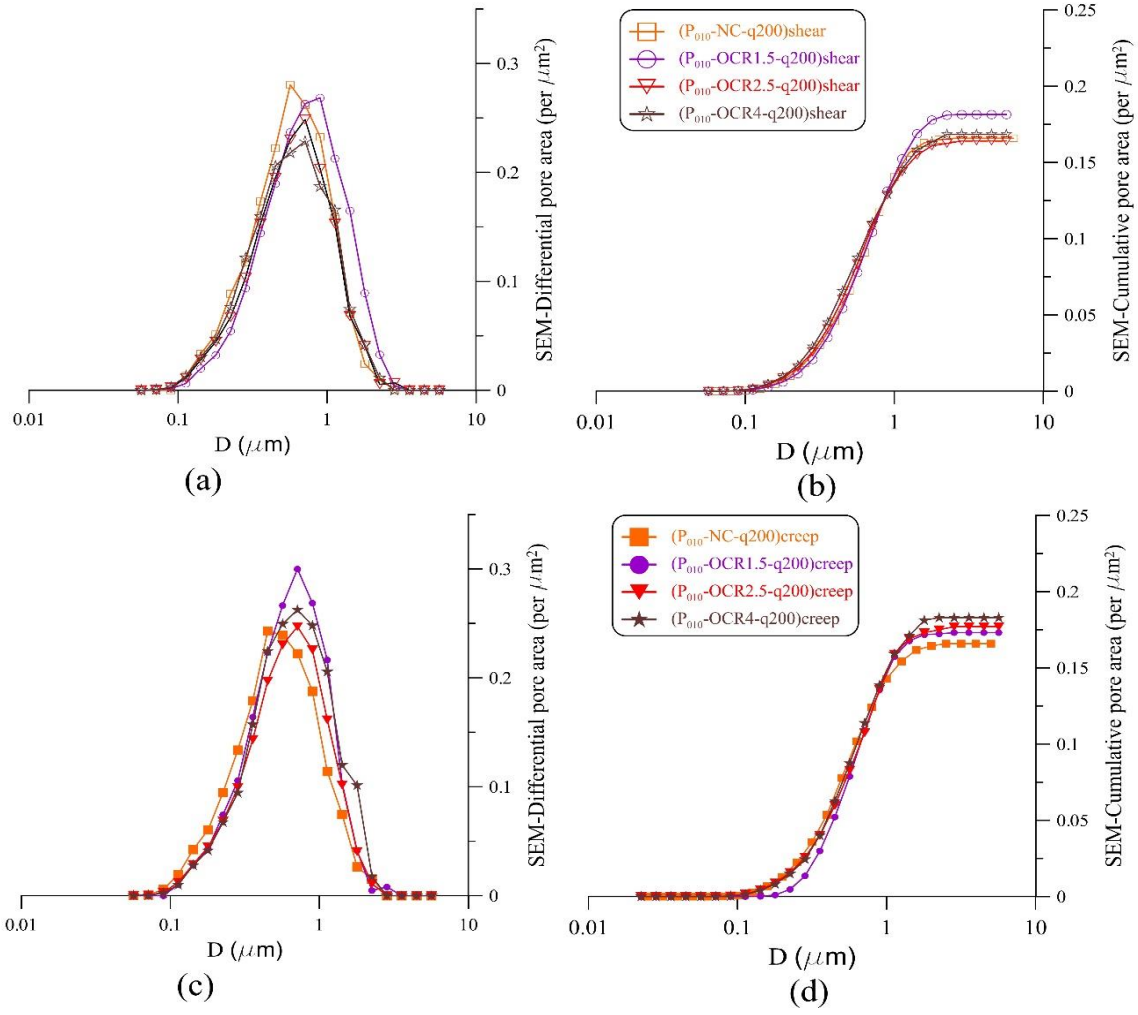

Figure 4-10 Evolution of pore area for tests with OCR=1: (a) (b) shear tests; (c), (d) creep tests

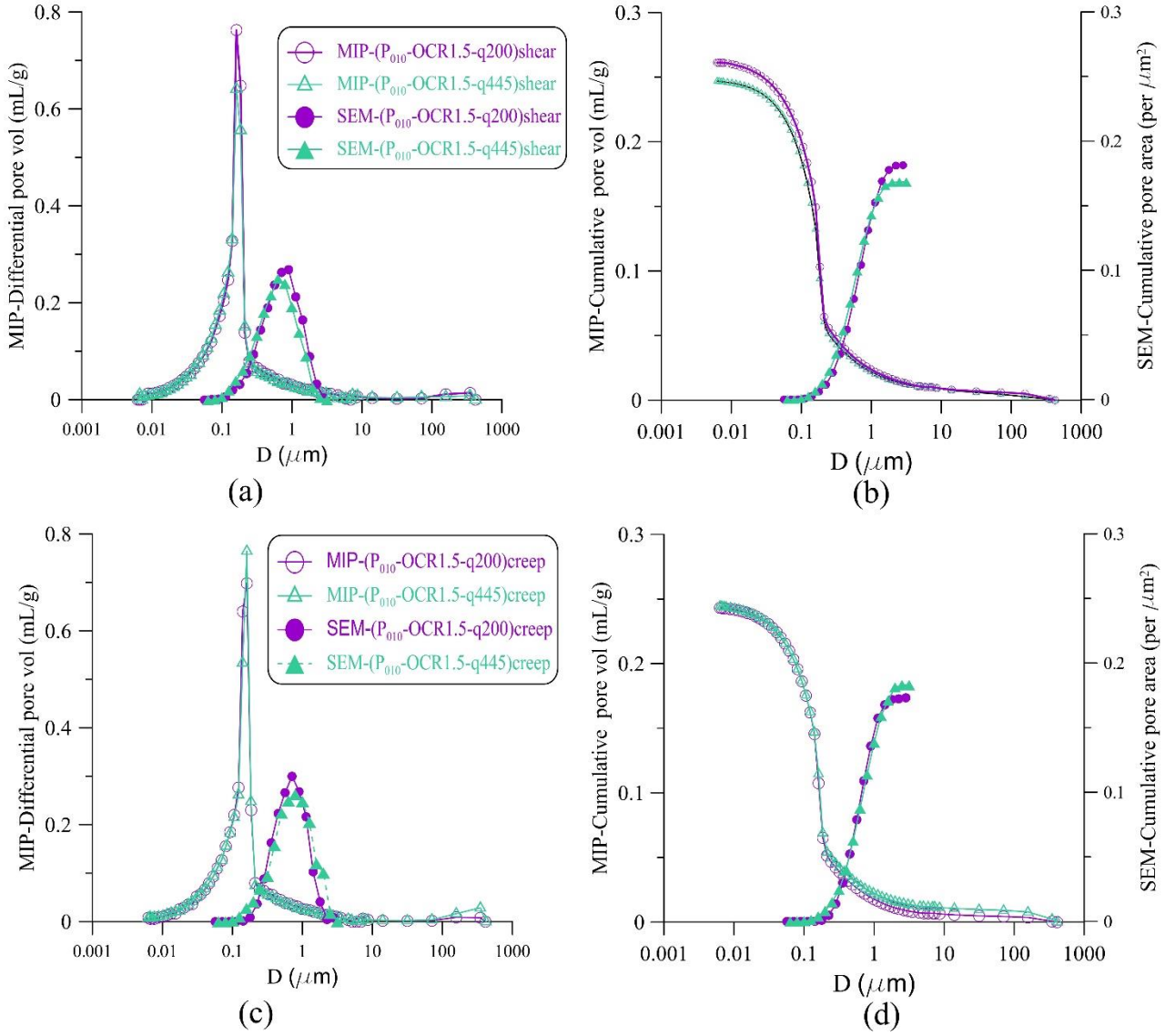

Figure 4-11 Evolution of pore area for tests with OCR=1.5: (a) (b) shear tests; (c), (d) creep tests

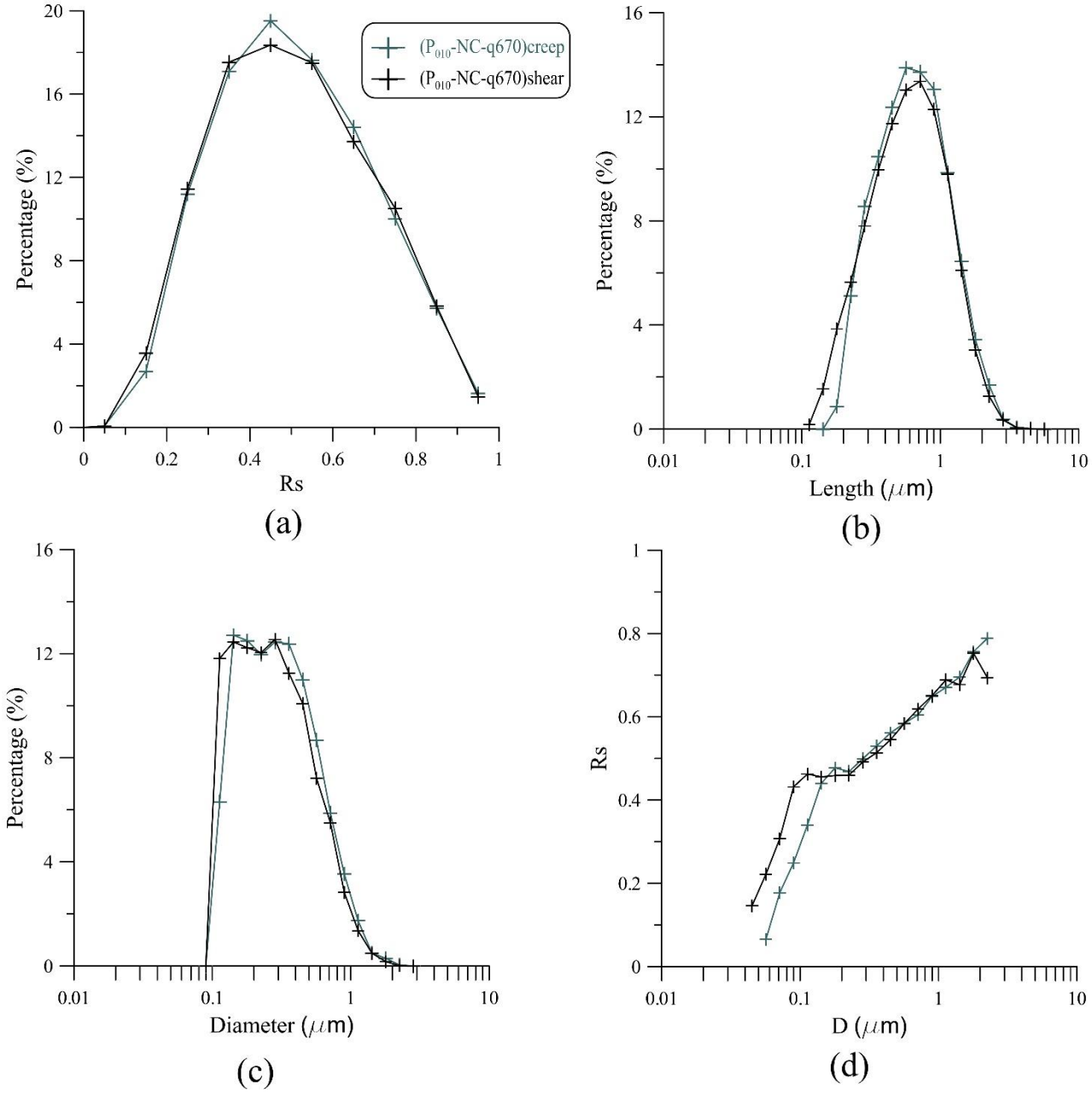

Figure 4-12 Evolution of pore shape for tests P_{010}-NC-q670 in contractancy domain

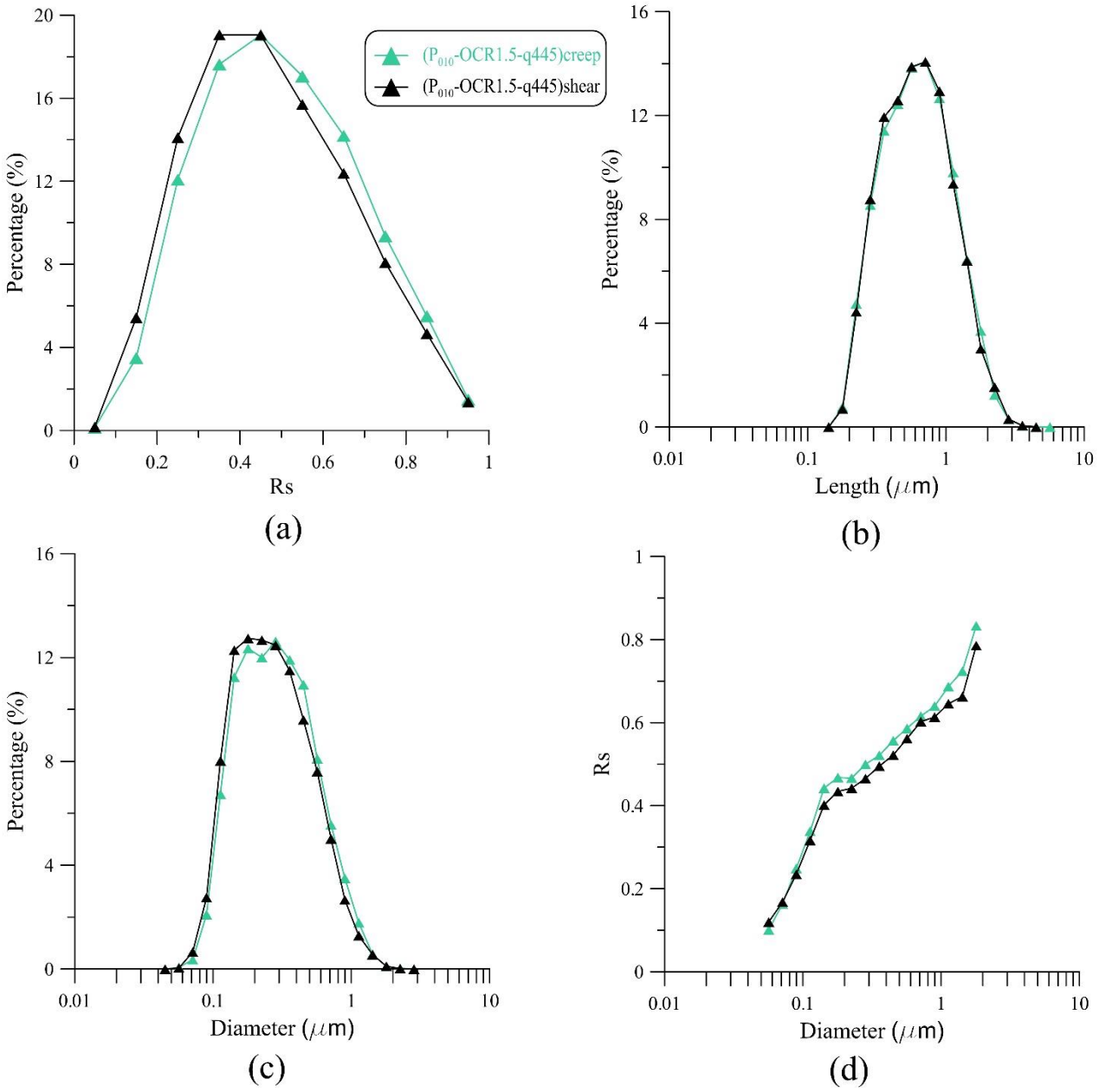

Figure 4-13 Evolution of pore shape for tests P_{010}-OCR1.5-q445 in contractancy domain

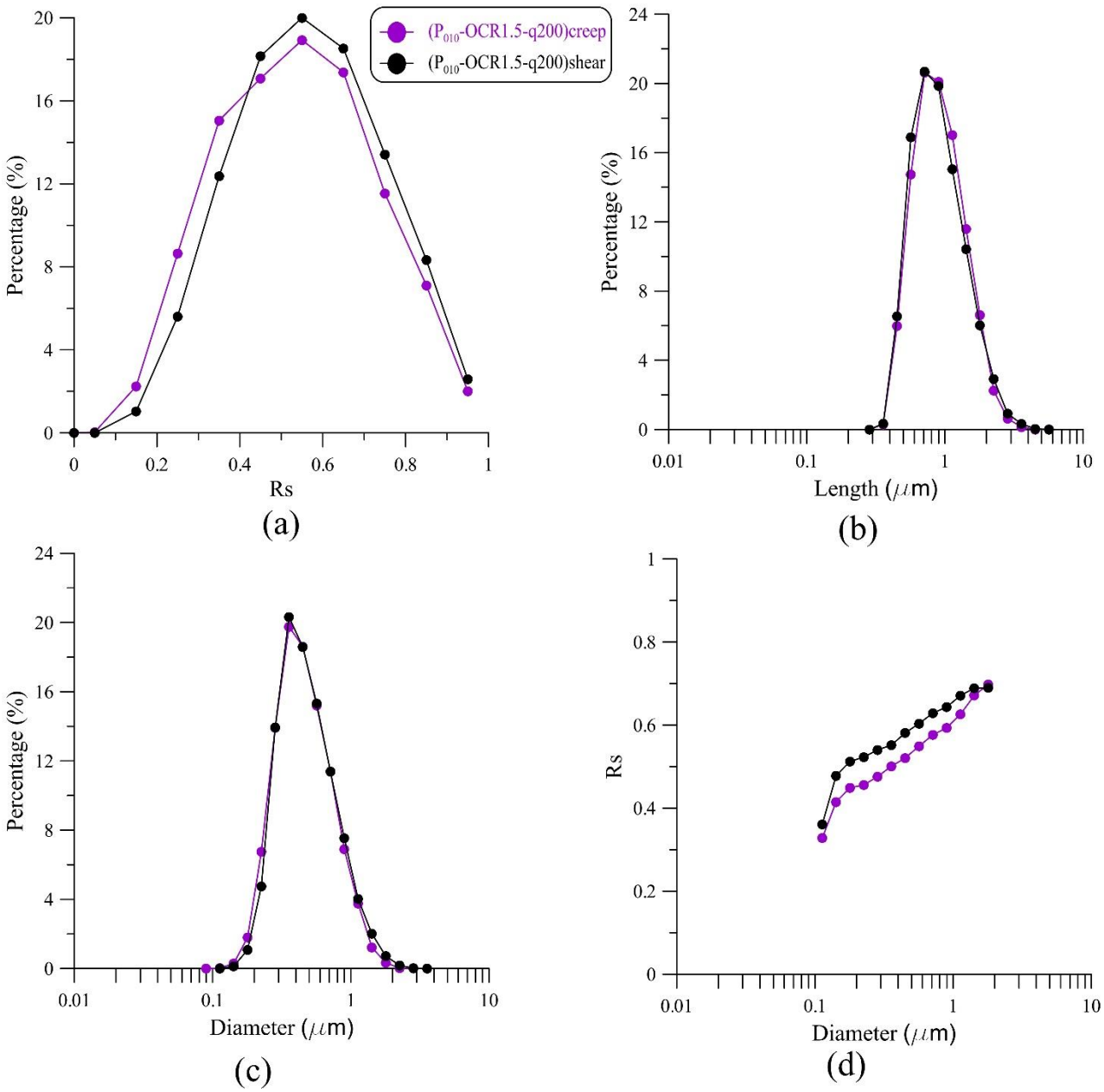

Figure 4-14 Evolution of pore shape for tests P_{010}-OCR1.5-q200 in pseudo-elastic domain